Modeling and Estimation of Linear and Nonlinear Piezoelectric Systems

Sai Tej Paruchuri

Dissertation submitted to the Faculty of the
Virginia Polytechnic Institute and State University
in partial fulfillment of the requirements for the degree of

Doctor of Philosophy
in
Mechanical Engineering

Andrew J. Kurdila, Chair
Pablo A. Tarazaga
John A. Burns
Steve C. Southward
Jeffrey T. Borggaard

September 11, 2020
Blacksburg, Virginia

Keywords: Oscillator Arrays, Broadband Attenuation, RKHS, Adaptive Estimation.

Modeling and Estimation of Linear and Nonlinear Piezoelectric Systems

Sai Tej Paruchuri

(ABSTRACT)

A bulk of the research on piezoelectric systems in recent years can be classified into two categories, 1) studies of linear piezoelectric oscillator arrays, 2) studies of nonlinear piezoelectric oscillators. This dissertation derives novel linear and nonlinear modeling and estimation methods for such piezoelectric systems. In the first part, this work develops modeling and design methods for Piezoelectric Subordinate Oscillator Arrays (PSOAs) for the wideband vibration attenuation problem. PSOAs offer a straightforward and low mass ratio solution to cancel out the resonant peaks in a host structure's frequency domain. Further, they provide adaptability through shunt tuning, which gives them the ability to recover performance losses because of structural parameter errors. This dissertation studies the derivation of governing equations that result in a closed-form expression for the frequency response function. It also analyzes systematic approaches to assign distributions to the nondimensional parameters in the frequency response function to achieve the desired flat-band frequency response. Finally, the effectiveness of PSOAs under ideal and nonideal conditions are demonstrated in this dissertation through extensive numerical and experimental studies. The concept of performance recovery, introduced in empirical studies, gives a measure of the PSOA's effectiveness in the presence of disorder before and after capacitive tuning. The second part of this dissertation introduces novel modeling and estimation methods for nonlinear piezoelectric oscillators. Traditional modeling techniques require knowledge of the structure as well

as the source of nonlinearity. Data-driven modeling techniques used extensively in recent times build approximations. An adaptive estimation method, that uses reproducing kernel Hilbert space (RKHS) embedding methods, can estimate the underlying nonlinear function that governs the system's dynamics. A model built by such a method can overcome some of the limitations of the modeling approaches mentioned above. This dissertation discusses (i) how to construct the RKHS based estimator for the piezoelectric oscillator problem, (ii) how to choose kernel centers for approximating the RKHS, and (iii) derives sufficient conditions for convergence of the function estimate to the actual function. In each of these discussions, numerical studies are used to show the RKHS based adaptive estimator's effectiveness for identifying linearities in piezoelectric oscillators.

Modeling and Estimation of Linear and Nonlinear Piezoelectric Systems

Sai Tej Paruchuri

(GENERAL AUDIENCE ABSTRACT)

Piezoelectric materials are materials that generate an electric charge when mechanical stress is applied, and vice versa, in a lossless transformation. Engineers have used piezoelectric materials for a variety of applications, including vibration control and energy harvesting. This dissertation introduces (1) novel methods for vibration attenuation using an array of piezoelectric oscillators, and (2) methods to model and estimate the nonlinear behavior exhibited by piezoelectric materials at very high mechanical forces or electric charges. Arrays of piezoelectric oscillators attached to a host structure are termed piezoelectric subordinate oscillator arrays (PSOAs). With the careful design of PSOAs, we show that we can reduce the vibration of the host structure. This dissertation analyzes methodologies for designing PSOAs and illustrates their vibration attenuation capabilities numerically and experimentally. The numerical and experimental studies also illustrate the robustness of PSOAs. In the second part of this dissertation, we analyze reproducing kernel Hilbert space embedding methods for adaptive estimation of nonlinearities in piezoelectric systems. Kernel methods are extensively used in machine learning, and control theorists have studied adaptive estimation of functions in finite-dimensional spaces. In this work, we adapt kernel methods for adaptive estimation of functions in infinite-dimensional spaces that appear while modeling piezoelectric systems. We derive theorems that ensure convergence of function estimates to the actual function and develop algorithms for careful selection of the kernel basis functions.

Dedication

Dedicated to my mother who gave me the freedom to pursue my dreams.

Acknowledgments

I want to express my sincere gratitude to Dr. Andrew Kurdila, my doctoral advisor, for his patient guidance, continuous encouragement, and useful critique of my research work. I would also like to thank my doctoral committee members, Dr. Pablo Tarazaga, Dr. John Burns, Dr. Steve Southward, and Dr. Jeff Borggaard. The advice given by them has been a great help in adding a new perspective to my research and improving my work quality. I wish to acknowledge the knowledge and experience given to me by Mr. Jia Guo and Dr. Parag Bobade, my research colleagues, which significantly accelerated my research on RKHS. I want to thank Mr. Nathan Powell, my labmate, for giving his valuable time to review and scrutinize the lengthy derivations on piezoelectric oscillators. I want to offer my special thanks to Dr. Sriram Malladi and other VAST lab members for their guidance while conducting the experiments. Their practical expertise made a tremendous difference in the successful completion of the experimental studies. Special thanks should be given to Dr. Joseph Vignola and Dr. John Sterling, my research collaborators at the Catholic University of America, for their useful input and constructive suggestions on piezoelectric oscillator array studies.

Contents

List of Figures

List of Tables

Chapter 1

Introduction

The smart materials community has explored various piezoelectric systems extensively in the past three decades. Some of the primary motivations for these studies have been vibration attenuation, energy harvesting, and high-precision actuator or sensor systems. Two recent trends in the research on piezoelectric systems have focused on using arrays of piezoelectric systems to improve beyond the limitations of an individual oscillator's effectiveness, and the investigation of the inherent nonlinearity of piezoelectric systems to achieve better performance. This dissertation introduces a number of new results related to these two emerging topics of research: the study of 1) broadband vibration attenuation using an array of linear piezoelectric oscillators, and 2) modeling and estimation of nonlinear piezoelectric oscillators.

1.1 Passive Piezoelectric Subordinate Oscillator Arrays (Chapter 2)

Many specific research topics motivate the investigations in this dissertation. For example, we can think of state-switched piezoelectric vibration absorbers as systems that were inspired by classical dynamic vibration absorbers. State-switched absorbers exploit the inherent capabilities of a piezoelectric system to modify parameters dynamically and thereby expand the capability of mechanical DVAs. It is important to note that while making this argument, one should be very careful not to trivialize the complexity involved in constructing

the smart material systems based on classical mechanical solutions for vibration attenuation. For instance, the DVAs are linear systems, whereas state-switched piezoelectric absorbers are nonlinear. In recent times, researchers have explored the effect of multiple DVAs on a host structure's frequency response. By careful choice of the DVA properties, one can achieve broadband vibration attenuation. The first topic discussed in this dissertation can be thought of as a generalization of classical DVAs. Piezoelectric Subordinate Oscillator Arrays, or PSOAs, are the smart material equivalent of Subordinate Oscillator Arrays, a class of vibration attenuation systems that have been studied over the past decade. PSOAs consist of an array of piezoelectric bimorphs with shunt circuits. By choosing the nondimensional frequency distribution carefully, one can cancel resonant peaks of a host structure and achieve a flat frequency response. Such systems have low mass ratios and provide broadband attenuation, in contrast to classical DVA designs. Furthermore, one can retune the parameters of a PSOA to reduce the effects of modeling errors and disorder. Refer Chapter 2 for a detailed discussion on the advantages of using PSOAs.

In this dissertation, the dynamics of a PSOA attached to a host is modeled using a block structure that permits the derivation of a closed-form expression for the frequency response function from input to host response. Such an expression enables one to simplify the problem of designing an array of piezoelectric oscillators for broadband vibration attenuation by choosing a nondimensional frequency distribution of the whole array. Even though recent studies have explored arrays of piezoelectric oscillators, none of them pose the problem of broadband attenuation using such arrays as the choice of frequency distributions, and here lies one of the novel contributions of this study. Further, this work explores the ability to vary shunt capacitances to achieve the desired frequency distribution and hence, the desired flat band frequency response. Finally, this work explores the performance recovery capabilities of a PSOA when its performance has degraded due to disorder in structural parameters. Such

robustness and retuning aspects of oscillator arrays are yet to be discussed in the literature.

Chapter 2 of this dissertation explores the theory, design, and experimental study of PSOAs. Section 2.1 of the chapter motivates the study of PSOAs. Section 2.2 covers an extensive literature review of piezoelectric systems that have been developed over the past three decades. Section 2.3 reviews the fundamentals of SOAs. It has been included because of the similarity of SOAs to PSOA systems. Sections 2.4 and 2.5 in the chapter discuss the derivation of the governing equations and a closed-form expression for the FRF of PSOAs, respectively. The derivation of a closed-form expression for the FRF of PSOAs is possible only under certain assumptions (capacitive shunts, for example), the details of which are given in Section 2.5. The methodologies for PSOA design are discussed in detail in the same section. Section 2.6 lists the experimental procedure used to validate the vibration attenuation capabilities of PSOAs. Sections 2.7 and 2.8 give an account of the extensive numerical and experimental studies conducted to illustrate the effectiveness of PSOAs. The appendix at the end of the chapter covers some of the finer details of the derivation in Sections 2.4 and 2.5.

The major contributions of the research work summarized in Chapter 2 are as follows:

1. This dissertation derives a theory for modeling of PSOA systems that results in a closed-form expression of the FRF from input to host response.

2. This dissertation develops design methods based on the assignment of distributions for nondimensional electromechanical parameters. These techniques do not require optimization to achieve strong results in vibration attenuation.

3. This dissertation illustrates the effectiveness and robustness of PSOA systems under ideal as well as non-ideal conditions through numerical studies. The topic of robustness has not been studied systematically for piezoelectric systems prior to this dissertation.

4. This dissertation validates and verifies the analysis through experiments.

5. Finally, the dissertation introduces a novel robustness metric, one that characterizes the performance recovery abilities of PSOAs in the presence of disorder through experiments.

Much of this chapter has been published in the following refereed journal article.

Sai Tej Paruchuri, John Sterling, Vijaya V N Sriram Malladi, Andrew Kurdila, Joseph Vignola, and Pablo Tarazaga. Passive piezoelectric subordinate oscillator arrays. Smart Materials and Structures*, 28(8):85046, August 2019. ISSN 0964-1726. doi: 10.1088/1361-665x/ab2f5a. URL http://dx.doi.org/10.1088/1361-665X/ab2f5a*

Other contributions on subordinate oscillator arrays described in Chapter 2 have appeared in the following conference proceedings and journal articles.

1. Sai Tej Paruchuri, Vijaya V N Sriram Malladi, Pablo A Tarazaga, and Andrew J Kurdila. Expanding the Teaching of Single Frequency Vibration Absorption to Broadband Attenuation using Subordinate Oscillator Arrays via Fettuccine Pasta, April 2020. URL https://doi.org/10.31224/osf.io/qb4up

2. Sai Tej Paruchuri, Andrew Kurdila, and Joseph Vignola. Estimation of Distribution Errors in Piezoelectric Subordinate Oscillator Arrays, November 2018. URL https://doi.org/10.1115/SMASIS2018-8065

3. Sai Tej Paruchuri, John Sterling, Andrew Kurdila, and Joseph Vignola. Piezoelectric composite subordinate oscillator arrays and frequency response shaping for passive vibration attenuation. volume 2017-January, pages 702–707. IEEE, August 2017. doi: 10.1109/CCTA.2017.8062544. URL http://ieeexplore.ieee.org/document/

8062544/

4. Sai Tej Paruchuri, Andrew J. Kurdila, John Sterling, Amelia Vignola, John Judge, Joe Vignola, and Teresa Ryan. Thermodynamic Variational Formulations of Subordinate Oscillator Arrays (SOA) With Linear Piezoelectrics. In *ASME. International Design Engineering Technical Conferences and Computers and Information in Engineering Conference, Volume 8: 29th Conference on Mechanical Vibration and Noise ():V008T12A068.*, volume 8, 2017. ISBN 9780791858226. doi: 10.1115/DETC2017-68056. URL http://dx.doi.org/10.1115/DETC2017-68056

5. John A. Sterling, Joseph F. Vignola, Teresa J. Ryan, and Sai T. Paruchuri. Analysis of increased damping in arrays of attached resonators. *The Journal of the Acoustical Society of America*, 145(3):1824, March 2019. ISSN 0001-4966. doi: 10.1121/1.5101664. URL https://doi.org/10.1121/1.5101664

6. John Sterling, Joseph Vignola, Jenna Gietl, Teresa Ryan, Noah Sonne, and Sai Tej S.T. Paruchuri. Effect of Increased Damping in Subordinate Oscillator Arrays. *Journal of Physics: Conference Series*, 1149(1):12006, 2018. ISSN 1742-6588. doi: 10.1088/1742-6596/1149/1/012006. URL http://dx.doi.org/10.1088/1742-6596/1149/1/012006

7. John Sterling, Sai Tej Paruchuri, Teresa Jean Ryan, Joseph Vignola, and Andrew J Kurdila. Subordinate Oscillator Arrays: Physical Design and Effects of Error, April 2020. URL https://doi.org/10.31224/osf.io/kpv3r

8. John Sterling, Sai Tej Paruchuri, Pablo Tarazaga, Joseph Vignola, Andrew Kurdila, V.V.N. Sriram Malladi, Teresa Ryan, Vijaya V N Sriram Malladi, and Teresa Ryan. Piezoelectric Subordinate Oscillator Arrays: Performance Recovery and Robustness to

Uncertainty, August 2019. URL https://doi.org/10.1115/DETC2019-98092

9. Joseph Vignola, John Judge, John Sterling, Teresa Ryan, Andrew Kurdila, Sai Tej Paruchuri, and Aldo Glean. On the Use of Shunted Piezo Actuators for Mitigation of Distribution Errors in Resonator Arrays. In *Proceedings of the 22nd International Congress on Acoustics*, 2016

10. Campbell R Neighborgall, Karan Kothari, V V N Sriram Malladi, Pablo Tarazaga, Sai Tej Paruchuri, and Andrew Kurdila. Shaping the Frequency Response Function (FRF) of a Multi-Degree-of-Freedom (MDOF) Structure Using Arrays of Tuned Vibration Absorbers (TVA). In *Conference Proceedings of the Society for Experimental Mechanics Series*, pages 317–326. Springer International Publishing, 2020. ISBN 978-3-030-12684-1. doi: 10.1007/978-3-030-12684-1_33

1.2 RKHS Embedding Methods for Adaptive Estimation (Chapters 3, 4 and 5)

The second topic presented in this dissertation is an entirely novel approach to modeling and estimating nonlinearities in piezoelectric systems. Irrespective of the application, many studies on piezoelectric systems have used linear models. However, for high field strengths, these systems are best approximated by nonlinear models. The restriction to linear models implies that we can only operate in the linear regime, which corresponds to low excitation or field levels in the piezoelectric governing equations. Further, it also implies that the nonlinearity in these systems cannot be exploited to achieve better performance.

The traditional approach to modeling nonlinear systems generally involves the inclusion of higher-order terms in the electric enthalpy density. However, this inclusion implies prior

knowledge of the structure of the nonlinearity in the system. Quite recently, researchers have tried using data-driven approaches to model nonlinear systems. Data-driven modeling eliminates, or relaxes, the need for strong assumptions on the exact form or structure of the underlying nonlinearity. However, a majority of these data-driven approaches fit linear models to nonlinear systems. Further, it is well known that most data-driven models studied in literature often ensure state convergence, but not parameter convergence. The convergence of parameters, under additional constraints, can ensure that the model predicts the dynamics beyond the scope of the input data.

In Chapters 3, 4 and 5, we introduce the RKHS based embedding approach for adaptive estimation of nonlinearities in piezoelectric oscillators. In all these chapters, the kernel embedding approach is used to represent the unknown nonlinear function/model as an element of a Reproducing Kernel Hilbert space (RKHS). Such an embedding allows one to use the properties of the RKHS when estimating the system. Adaptive estimators are then used to estimate the unknown function in this infinite-dimensional space. Such a technique has never been used before to model piezoelectric oscillators. This technique, along with suitably defined persistence of excitation conditions, ensures convergence of the function estimate to the true function. Further, the source of nonlinearity does not affect the effectiveness of this approach. That is, it does not matter if the nonlinearity arise in the constitutive laws, the boundary conditions, or elsewhere in the governing equations.

1.2.1 RKHS Embedding for Estimation of Nonlinear Piezoelectric Systems (Chapter 3)

Chapter 3 focuses on formulating the RKHS embedding adaptive estimator for the piezoelectric oscillator problem. In particular, this chapter considers the case when the unknown nonlinear function $f : \mathbb{R} \to \mathbb{R}$.

The motivation behind the RKHS embedding and adaptive estimation approach is given in detail in Section 3.1 of the chapter. The nonlinear governing equations of motion are discussed in Section 3.2. The governing equations derived in this section were used in the numerical simulations to represent the actual system. Section 3.3 covers the theory behind the RKHS embedding and adaptive estimation in infinite-dimensional spaces. Section 3.4 presents the algorithm for adaptive estimation using RKHS embedding methods. This section also covers the sufficient conditions for convergence of function estimates. Section 2.7 goes over the numerical results that validate the effectiveness of the estimator.

The following are the primary contributions of the research presented in Chapter 3.

1. This chapter studies the RKHS embedding strategy for adaptive estimation of nonlinearities in the governing equations of autonomous system. The approach is then modified to estimate the nonlinearities in piezoelectric oscillator models, which are nonautonomous systems.

2. The chapter studies convergence of state estimates of the RKHS embedding method to actual states.

3. The chapter also analyzes conditions that guarantee estimated function convergence to the true function in state-space.

4. The chapter illustrates the effectiveness of the adaptive estimator when the unknown nonlinear function $f : \mathbb{R} \to \mathbb{R}$.

The contributions of this chapter have appeared in the following peer-reviewed journal article.

Sai Tej Paruchuri, Jia Guo, and Andrew Kurdila. Reproducing kernel Hilbert space embedding for adaptive estimation of nonlinearities in piezoelectric systems. Nonlinear Dynamics, *101*

(2):1397–1415, 2020. ISSN 1573-269X. doi: 10.1007/s11071-020-05812-2. URL https://doi.org/10.1007/s11071-020-05812-2

1.2.2 Kernel Center Adaptation in the Reproducing Kernel Hilbert Space Embedding Method (Chapter 4)

In Chapter 3, the unknown nonlinear function is assumed to be a mapping $f : \mathbb{R} \to \mathbb{R}$. While implementing the RKHS adaptive estimator, it is important to choose the finite-dimensional RKHS which approximates the infinite-dimensional RKHS in which the function f is contained. This amounts to choosing kernel centers in the positive limit set. The distribution of the kernel centers directly affect the approximation error of the function estimate. When it is assumed that $f : \mathbb{R} \to \mathbb{R}$, choosing evenly distributed kernel centers is fairly straightforward. This is evident from the numerical example given in Chapter 3. However, when $f : \mathbb{R}^d \to \mathbb{R}$, it is not easy to choose evenly distributed kernel centers in the positive limit set that is contained in $\mathbb{R}^d$. Chapter 4 introduces two algorithms that enable us to choose evenly distributed kernel centers in the positive limit set in a (semi-) automated strategy.

Section 4.1 of Chapter 4 introduces the motivation behind the kernel center selection problem. Section 4.2 goes over the theory of RKHS embedding for adaptive estimation. This section also reviews the criteria for kernel center selection more generally in RKHS embedding methods and illustrates the importance of choosing evenly distributed kernel centers using the piezoelectric oscillator example. Sections 4.3 and 4.4 introduce algorithms for kernel center selection based on centroidal Voronoi partitions and Kohonen self-organizing maps, respectively. In Section 4.5, we use these algorithms for center selection in practical examples.

The contributions of the work in Chapter 4 are as follows.

1. We develop criteria for kernel center selection for RKHS embedding methods for a class of nonlinear systems.

2. We develop centroidal Voronoi tessellations based kernel center selection algorithm, which can be implemented for systems for which we can sample the positive limit set. This algorithm inherently make sure that the kernel centers are evenly distributed.

3. We develop kernel center selection algorithm based on Kohonen self-organizing maps, which can be implemented for a generic class of nonlinear systems. This method can be applied to many types of systems, including systems where the state-trajectory is not contained in the positive limit set.

4. We illustrates the effectiveness of these algorithms for two different nonlinear systems, including the piezoelectric oscillator example.

This work has been submitted for publication in a peer-reviewed journal. The reference of the preprint on arxiv is given below.

Sai Tej Paruchuri, Jia Guo, and Andrew Kurdila. Kernel Center Adaptation in the Reproducing Kernel Hilbert Space Embedding Method. September 2020. URL http://arxiv.org/abs/2009.02867

1.2.3 Sufficient Conditions for Parameter Convergence over Embedded Manifolds using Kernel Techniques (Chapter 5)

Persistence of excitation refers to a sufficient condition for convergence of the function estimate error in adaptive estimation methods. In this chapter, we derive sufficient conditions for persistence of excitation of RKHS of functions defined over manifolds. We study the implication of this sufficient conditions when the RKHS is finite and infinite-dimensional.

Section 5.1 of the chapter discusses the motivation behind the study of sufficient conditions for persistence of excitation. Section 5.2 reviews some of the theory behind RKHS embedding methods for adaptive estimation. In Section 5.3, we derive the sufficient conditions that ensure persistence of excitation. Section 5.4 discusses the implications of using the sufficient condition, when the RKHS is infinite-dimensional. Section 5.5 illustrates the implementation of the sufficient condition in a practical example.

The primary contributions of this work are as follows:

1. We derive sufficient condition for persistence of excitation in a finite-dimensional RKHS.

2. We show that when the actual function belongs to the finite-dimensional space, the sufficient condition implies convergence of the function estimate to the actual function.

3. We prove that when the actual function belongs to an (infinite-dimensional) RKHS, the sufficient condition implies that the function estimate error is ultimately bounded by a constant. The constant depends on the approximation error between the infinite-dimensional RKHS and the finite-dimensional RKHS.

4. We illustrate the effectiveness of the sufficient conditions using a piezoelectric oscillator example.

The work in this chapter was submitted for publication in a peer-reviewed journal. The preprint is available on arxiv, whose reference is given below.

Sai Tej Paruchuri, Jia Guo, and Andrew Kurdila. Sufficient Conditions for Parameter Convergence over Embedded Manifolds using Kernel Techniques. September 2020. URL https://arxiv.org/abs/2009.02866

1.2.4 Other Contributions

Some of the other contributions on RKHS embedding methods for adaptive estimation have appeared or under review in the following conference proceedings and journal articles.

1. Andrew J. Kurdila, Jia Guo, Sai Tej Paruchuri, and Parag Bobade. Persistence of Excitation in Reproducing Kernel Hilbert Spaces, Positive Limit Sets, and Smooth Manifolds. September 2019. URL http://arxiv.org/abs/1909.12274

2. Jia Guo, Sai Tej Paruchuri, and Andrew J. Kurdila. Persistence of Excitation in Uniformly Embedded Reproducing KernelHilbert (RKH) Spaces (ACC). In *American Control Conference*, 2020

3. Jia Guo, Sai Tej Paruchuri, and Andrew J. Kurdila. Persistence of Excitation in Uniformly Embedded Reproducing Kernel Hilbert (RKH) Spaces. February 2019. URL https://arxiv.org/abs/2002.07963

4. Jia Guo, Sai Tej Paruchuri, and Andrew J. Kurdila. Approximations of the Reproducing Kernel Hilbert Space (RKHS) Embedding Method over Manifolds. July 2020. URL http://arxiv.org/abs/2007.06163

Chapter 2

Passive Piezoelectric Subordinate Oscillator Arrays

Abstract

Subordinate Oscillator Arrays (SOAs) attached to a host structure have been shown to achieve flat attenuation of the frequency response over a band around a target natural frequency of the host. Due to their sensitivity to disorders that can arise from sources such as fabrication errors, as well as uncertainties in their structural properties or that of the host, SOAs can be challenging to implement in some applications. To overcome this shortcoming, Piezoelectric Subordinate Oscillator Arrays (PSOAs) are studied in this chapter. This chapter models PSOAs using variational principles to facilitate the analysis and development of design strategies. A closed-form expression for the frequency response function of the host structure *is then used to design the PSOAs with and without uncertainties. This chapter shows that the flat attenuation over a frequency band around a harmonic of the host can be achieved by assigning a distribution to the mechanical, electrical, or electromechanical properties of the PSOAs. For instance, it is shown that choosing a distribution of capacitive shunt circuits can achieve essentially the same qualitatively flat attenuation as that of classical SOAs. In this sense, the approach in this chapter generalizes the results attained for conventional SOAs. Finally, the chapter investigates the robustness of PSOAs, that is, their relative insensitivity to types of uncertainties. It is shown that PSOAs afford the chance to ameliorate some types*

of sensitivities that prove problematic for SOAs that are purely mechanical in nature. The notion of performance recovery *is introduced; this measure quantifies how much attenuation loss due to uncertainty in an initial SOA or PSOA design can be recovered by modification of the electrical properties alone.*

2.1 Introduction

The vibrations community has studied vibration attenuation of a host structure of given structural properties using attached substructures for decades. One classic example is a dynamic vibration absorber (DVA) attached to a host structure, which now appears as a typical example in vibration textbooks [1]. By analyzing the frequency response function, one can conclude that a DVA is a simple yet effective method for vibration attenuation. However, DVAs achieve attenuation only in a narrow frequency band around a particular frequency of operation. Any variation in the driving frequency can render the DVA ineffective, and it is known that the response is amplified at some nearby, off-resonance driving frequencies. Thus, if the driving frequency changes, a classical DVA has to be re-tuned, that is it must be re-built, to match the new input frequency.

It is well-known that these potential disadvantages of a classical DVA have been addressed in many ways. To achieve a broader frequency range of vibration reduction, damped vibration absorbers have been used. Many investigators have proposed methods which optimize parameters of damped vibration absorbers [2, 3, 4, 5, 6]. Researchers have tried to overcome these limitations by attaching the host structure to an array of linear vibration absorbers whose natural frequencies form a band in the frequency domain [7, 8, 9, 10, 11]. This is possible when the frequency band of the array is spaced around the host structure's natural frequency. These arrays of oscillators have been referred to in the literature as Subordinate

Oscillator Arrays, or SOAs. At first, designing an SOA might look like a complicated task since designers are forced to choose the structural properties of multiple absorbers. Vignola et al. in [11] show that simple "closed form" design strategies, ones that do not require optimization, that prescribe distributions representing the structural properties of the SOA makes implementing SOAs much more straightforward in practice.

At the same time, a large number of piezoelectric systems have been studied to achieve a variety of engineering goals. Some of the most recent are summarized in Table 2.1. In Section 2.2 we review these references in more detail, but here we note that many of these references seek to develop passive and active vibration absorbers. Other papers in the table obtain vibration attenuation as a byproduct of their research: methods for energy harvesting from structures naturally induce attenuation of structural response.

Perhaps surprisingly, there is little or no formal overlap between the study of mechanical domain SOAs and the literature on composite piezoelectric systems to achieve vibration attenuation. In particular, none of the references in Table 2.1 discuss, or even refer to, the notion of introducing distributions or mixtures of properties (as in [7, 8, 9, 10, 11]) of attached piezoelectric arrays connected to a host. In view of this fact, one of the overall and guiding aims of this chapter is to explore how the philosophy of design for SOAs in [11] in terms of distributions of properties can be extended to arrays of Piezoelectric SOAs or PSOAs.

The answer to this general question is that assigning distributions of electromechanical properties of PSOAs defines a theoretically sound, closed form, simple, effective strategy to achieve vibration attenuation in a host structure. From a technical standpoint, the efficacy of the method can be traced to finding a closed form expression for the frequency response function from input excitation to the host response. In this expression, which is valid for

an arbitrary number of attached piezoelectric elements, all the electromechanical degrees of freedom of the PSOA have been eliminated. It is the specific zero-nonzero block structure of the coupled equations governing the PSOA and the (non-piezoelectric) host (see Equations 2.12 below) that allow the elimination of all piezoelectric states.

To be sure, the governing equations for a PSOA coupled to a host are indeed a very special type of linear piezoelectric system, and such a simple reduction cannot be carried out in general linearly elastic piezoelectric systems. Note that this zero-nonzero block structure does not, in general, arise for instance in modal or finite element approximations of "monolithic" linear, distributed piezoelectric continua models such as used for beams, plates, or shells, such as those modeled in a general form in [12], or in many of the references in Table 2.1. It is conceivable that such a block structure, and subsequent elimination of the piezoelectric states, could be carried out with the introduction of static or Guyan reduction, the definition of independent and dependent coordinates or other component mode synthesis approaches [13]. See the comments following Equation 2.13. However, this process amounts to another level of approximations beyond and in addition to discretization, one that is nontrivial and sometimes impossible to carry out. In any event, it is the specific block structure of the PSOA and host equations that enables the closed form expression for the FRF of the host to be derived.

In the remainder of this chapter, we begin with a careful literature review of related electromechanical modeling of piezoelectric systems in Section 2.2. Section 2.3 summarizes the relevant technical background for SOAs. Section 2.4 describes models for PSOAs, while Section 2.5 summarizes the derivation of the frequency response function from the input to the host response when it is equipped with a PSOA. The closed form design strategies, including the specific discussion of mass-distribution-only and capacitance-distribution-only methods, is given in Section 2.5. The experimental setup is introduced in Section 2.6, Section 2.7

summarizes the numerical simulations of the experiment, and 2.8 reviews the experimental results. The conclusions of the chapter are given in Section 2.9

2.2 Piezoelectric Structures Literature Review

General Type	Reference(s)
SOAs	[10] 2012, [11] 2009, [14] 2012, [15] 2016, [8] 2005, [7] 1996, [16] 2001, [17] 1997, [9] 2005
Qualitative, numerical, and experimental study of piezoelectric systems with shunt circuits	[18] 1990, [19] 2000, [20] 2000, [21] 2001, [22] 2001, [23] 2006, [24] 2010, [25] 2011, [26] 2011, [25] 2011, [27] 2011, [28] 2011, [29] 2012, [30] 2012, [31] 2012, [30] 2012, [31] 2012, [32] 2013, [33] 2014, [34] 2014, [35] 2016, [36] 2016, [37] 2017
Mechanical SDOF or MDOF system, state switched or semi-active piezoelectric DVAs	[38] 1999, [39] 1999, [40] 2000, [41] 2000, [42] 2001, [43] 2001, [44] 2002, [45] 2004, [46] 2006, [47] 2006, [48] 2008, [49] 2009, [50] 2010, [51] 2011, [52] 2012
Gain scheduled or operating mode switched piezoelectric composite DVAs	[53] 1997, [54] 1998, [55] 2000,
Optimization-Based DVA analysis and design	[56] 2003, [57] 2012, [58] 2014,
Piezoelectric energy harvesting, unswitched or switched	[53] 1997, [54] 1998, [55] 2000, [59] 2010, [60] 2009, [61] 2007, [62] 2013, [63] 2006, [64] 2005, [65] 2009, [66] 2012, [67] 2012, [68] 2012, [69] 2003,
Metamaterials and Wave propagation design and tailoring	[70] 2011, [71], [72] 2013, [73] 2013, [74] 2015, [75] 2016, [76] 2016, [77] 2017, [78] 2017, [79] 2017, [80] 2017

Table 2.1: Relevant Piezoelectric Systems Literature Summary

Researchers have studied active and passive structures based on piezoelectric materials for vibration attenuation for some time, and an extensive literature on this topic has accumulated over the years. The term piezoelectric system covers a wide range of nuanced systems that vibration engineers and researchers have used for a variety of applications. Just within the

field of vibration attenuation, we can classify piezoelectric systems into multiple categories based on the methodology used to achieve attenuation. The objective of this section is to highlight the similarities and the differences of such systems described in the literature with the one discussed in this chapter.

Indeed, one glaring difference between many studies of composite piezoelectric systems and that tackled in this chapter is that the latter system is made up of a family of linear oscillators that are connected to the host structure. That is, the piezoelectric components are only connected to the host, not to each other. Even though the oscillators in the PSOA are not coupled to each other, the coupling arises through the host. Thus, the response of the PSOA in itself is not of particular interest in this context, and the primary focus of this chapter is on the input-output response of the host structure coupled with a PSOA. This fact stands in stark contrast to many models of distributed active piezoelectric systems that are studied in the literature. Furthermore, as mentioned above, the nature of the PSOA connection to the host creates a coupled linear ODE that enables the derivation of a closed-form expression for host frequency response function. This expression makes it easier to develop well-defined design techniques with predictable performance.

Further, some of the topics that are not traditionally discussed in papers on linear piezoelectric systems, but are addressed here, include: (1) the effect of robustness and uncertainty on the performance of a design; (2) the development of a simple general design approach that relies on the distributions of electromechanical properties of the PSOA; and (3) an analysis of the performance recovery ability of a PSOA.

Because of the sheer number of studies of piezoelectric systems for vibrations attenuation, the only the most relevant categories of research are reviewed here. Table 2.1 shows each general category and a corresponding list of papers that fall under a category. Of course,

some of these studies can fall under multiple categories. Such studies have been classified based on the authors' assessment of the principal features of the approach. Piezoelectric systems have been studied for more than half a century, and one of the earliest references is [81]. However, most of the papers presented in Table 2.1 are from studies conducted in the past 25 years. In addition to the piezoelectric systems shown in Table 2.1, SOAs have been included as a category due to its similarity to the system presented in this chapter. PSOAs can be seen as a generalization of SOAs or as a particular case of coupled linearly piezoelectric systems. Discussions on these systems appear regularly in this chapter since these systems have inspired PSOAs.

The largest category in Table 2.1 is the one that contains piezoelectric equivalents of DVAs. The papers in the category include qualitative, numerical and experimental studies of piezoelectric oscillators with shunt circuits. In the studies, the mechanical part of the systems has been modeled using lumped (both single degree of freedom and multi-degree of freedom) as well as distributed parameter systems. The associated shunt circuits have been modeled as passive (using RLC circuits) and active systems. When passive electrical circuits are attached, these can be understood either as attempts to change the effective properties of the whole system or to induce (additional) poles and harmonics into the system response of the original structure. The papers in this category have discussed the modeling and design of piezoelectric systems. While these systems provide a theoretical framework for the design and analysis of PSOAs, they do not exploit the specific structural advantages of the PSOA and host system. Further, these papers do not discuss the robustness of the systems and performance recovery using shunt tuning. In essence, the PSOA systems can be thought of as a combination of SOAs and the piezoelectric systems in this category.

The third category in Table 2.1 includes the systems that use state switching to achieve parameter shifts in electromechanical properties of a structure. For example, it is well-

known that by switching between two capacitances, one can change the effective stiffness and hence the natural frequency of the system. These systems are sometimes considered as semi-active systems since these systems switch between passive circuits, at the expense of the relatively low energy consumed to power the switches, in contrast to modulating voltage or current in the shunt circuit. Several studies in Table 2.1 investigating this effect can be found in the past two decades. However, a general study of robustness of these systems has not been undertaken in these references. We will argue that the use of flat-band solutions like PSOAs can be an effective alternative to some of these systems, especially when the frequency band of operation is known and restricted to a fewer number of resonant peaks. This is demonstrated in particular in the conclusions in Section 2.9.

Another recent class of systems which have attracted the interest of the vibrations community are those that are associated with metamaterials and waveguide design. Metamaterials are composed of an identical array of substructures that are periodically distributed along the length of the host structure. By doing so, a bandgap is created in the frequency response of the host structure. Since the study of these systems is a relatively recent innovation, most of the relevant studies have been focused on analyzing the basic effect of metamaterials in the frequency domain, analyzing the limiting behavior, or on optimizing the placement of the piezoelectric oscillators on the host structure. Issues like robustness or sensitivity to perturbation in the location or the parameters of the piezoelectric oscillators are yet to be fully understood. Furthermore, the host systems considered in most of the relevant studies are monolithic beams, plates, or shell structures. Because of the nature of the problem of synthesizing metamaterials, it is reportedly more difficult to generalize the synthesis of metamaterial structures to arbitrary geometry. This can be attributed to the fact that metamaterials rely heavily on the periodicity of the substructures which can be hard to define in complex structures. Theoretically, the governing equations of metamaterials systems and

PSOAs look very similar. However, there are significant differences in the models as well as in the intended goals of the overall system after synthesis. One primary difference is that substructures are generally identical in metamaterials, whereas, parameter distributions dictate the mix of material properties of the piezoelectric substructures in PSOAs. Metamaterials create bandgaps by essentially moving existing resonant peaks outside of the frequency band of interest. Whereas PSOAs extend the effect of DVAs to cancel an existing resonant peak in the frequency response. This implies that modal spillover is very minimal in case of PSOAs as opposed to that of metamaterials. However, it is important to note that the frequency band of metamaterial systems are typically larger (spanning over multiple resonant peaks), and sometimes much larger, than that of the PSOAs.

2.3 Subordinate Oscillator Arrays

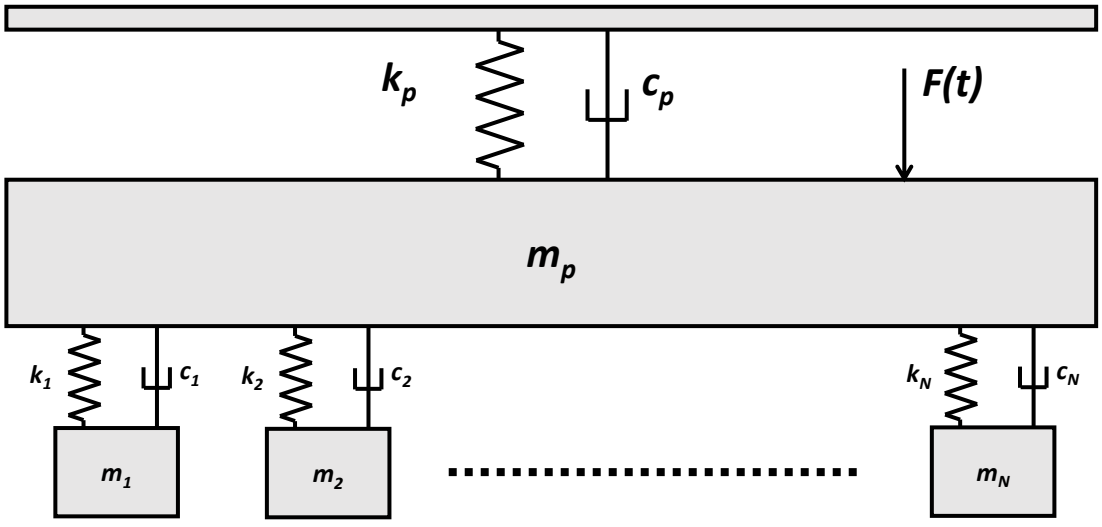

Figure 2.1: Array of single degree of freedom oscillators attached to a host structure.

Figure 2.1 shows a simple SOA, consisting of N mass-spring-damper oscillators, attached to a host structure of mass m_p, stiffness k_p, damping c_p and natural frequency ω_p [11, 14, 15]. The mass, stiffness and the damping of the n^{th} oscillator in the SOA are denoted by m_n, k_n

and c_n, respectively. Since the PSOA approach used in this chapter is very similar to the one used in [11], a brief summary of relevant theory is presented here. Vignola et al. in [11] derived a closed form equation for the frequency response function (FRF) of the map from the applied external force F_p to motion of the primary x_p. The frequency response at a given nondimensional frequency Ω can be calculated using the function

$$\frac{X_p(\Omega)k_p}{F_p(\Omega)} = \left(1 - \Omega^2 + \frac{i\Omega}{Q_p} + \sum_{n=1}^{N} \alpha_n \left(\frac{-\Omega^2\left(1 + \frac{i\Omega}{\beta_n Q_n}\right)}{1 - \left(\frac{\Omega}{\beta_n}\right)^2 + \frac{i\Omega}{\beta_n Q_n}}\right)\right)^{-1}, \tag{2.1}$$

where

$$\Omega := \omega/\omega_p, \quad \alpha_n := \frac{m_n}{m_p}, \quad \beta_n := \sqrt{\frac{\gamma_n}{\alpha_n}}, \quad \gamma_n := \frac{k_n}{k_p}, \quad Q_n := \frac{\sqrt{m_n k_n}}{c_n}. \tag{2.2}$$

In Equations 2.1 and 2.2, the subscript p represents the properties of the primary or host structure, and the subscript n represents the properties of the n^{th} attached substructure. The variable β_n is the nondimensional frequency of each substructure in the SOA. It can be expressed in terms of the nondimensional mass α_n and the nondimensional stiffness γ_n as shown in Equation 2.2. The constants Q_n and Q_p are the quality factors of the substructure and the host structure, respectively. From Equation 2.1, it is evident that the frequency response of the host structure attached to an SOA depends on the distributions of the nondimensional mass, stiffness and frequency denoted by α_n, γ_n and β_n, respectively. This implies that the problem of designing an SOA amounts to a problem of selecting three distributions instead of $3N$ parameters for all the substructures. The interdependence of α_n, β_n and γ_n implies that we have to construct distributions for only two of the three terms.

2.3.1 Nondimensional Frequency Distributions

As mentioned earlier, the design of a flat frequency response using SOAs distributes the frequency band of the SOA around the host structure's natural frequency. This is achieved by assigning an appropriate distribution to the nondimensional frequency β_n. The distribution used in [11] for β_n is represented by equations of the form

$$\beta_n = \begin{cases} \frac{\Delta}{2}\left(\left(\frac{2(n-1)}{N-1}\right)^p - 1\right) + 1 & \text{for } n \leq \frac{N}{2}, \\ \\ \frac{\Delta}{2}\left(1 - \left(\frac{2(N-n)}{N-1}\right)^p\right) + 1 & \text{for } n \geq \frac{(N+1)}{2}. \end{cases} \tag{2.3}$$

The nondimensional frequency distribution defined by Equation 2.3 is a antisymmetric curve centered at 1. The parameter Δ in Equation 2.3 represents the bandwidth of the nondimensional frequency distribution. Figure 2.2 shows the frequency response of the host structure for various values of Δ. The parameter p determines how the substructures are spaced around the center. When $p = 1$, the frequency of the substructures are equally spaced around the natural frequency of the host structure. When $p = 0$, the host structure is attached to a DVA whose nondimensional frequency is 1. Finally, $p = \infty$ corresponds to the case where the host structure is attached to two DVA's with nondimensional frequencies equal to $1 - \Delta/2$ and $1 + \Delta/2$. Later in this chapter, it will be shown that a nondimensional frequency distribution as expressed in Equation 2.3 can be used to design a PSOA.

2.3.2 Effect of Disorder on Performance of SOAs

Disorder or parameter uncertainties in systems can be induced due to fabrication errors in substructures or measurement errors in structural properties of the host. Vignola et al. in [15] studied the effect of disorder on the frequency response of a primary structure

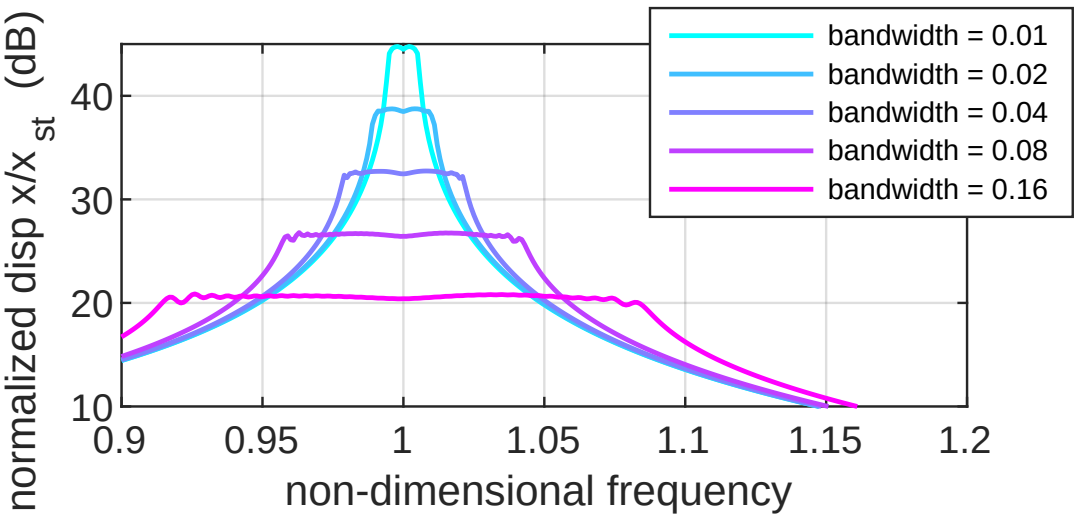

Figure 2.2: Broadband flat attenuation by SOA for varying bandwidths.

attached to an SOA. Figure 2.3 shows the degradation of SOA's performance as the disorder is increased. The figure shows a flat frequency response when uncertainty is low and a

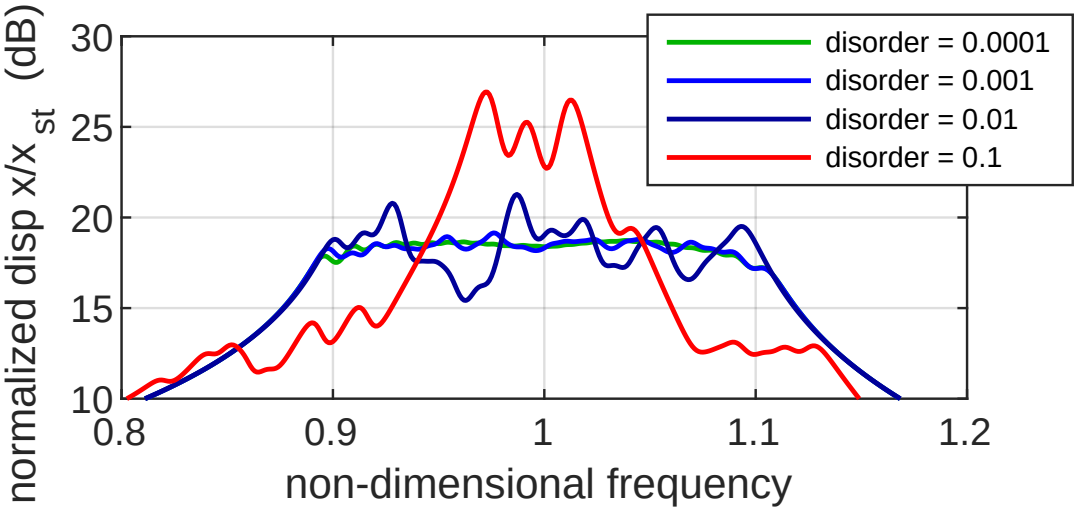

Figure 2.3: Degradation of SOA's performance with disorder.

non-flat response as uncertainty approaches 0.1. These results indicate that SOA's desired performance is limited by the precision of manufacturing and accuracy of measurements of the host's structural properties. One possible solution to overcome some of these issues is to develop a tunable SOA, a PSOA, which potentially allows for effective change of structural

properties after fabrication.

2.4 Host Structure with PSOA Model

In this section, the $\mathcal{H}$ variational principle which is based on extremization of the electric enthalpy and is discussed in A.1, will be used to model a piezoelectric subordinate oscillator array attached to a host structure. The canonical PSOA consists of a series of bimorph beams with shunt circuits connected to them. The shunt circuit of k^{th} bimorph beam in the array consists of a resistor R_k, capacitor $\mathcal{C}_k$ and current source i_k in parallel. Starting with a distributed beam model, finite dimensional approximations are introduced. Ultimately each oscillator in the PSOA is modeled as a single degree of freedom system. Figure 2.4 shows a piezoelectric subordinate array attached to a host structure. The dimensions of each appendage in the PSOA are shown in Figure 2.5. The host structure is assumed to have two inputs, base motion $\mathfrak{z}$ and applied force F_p.

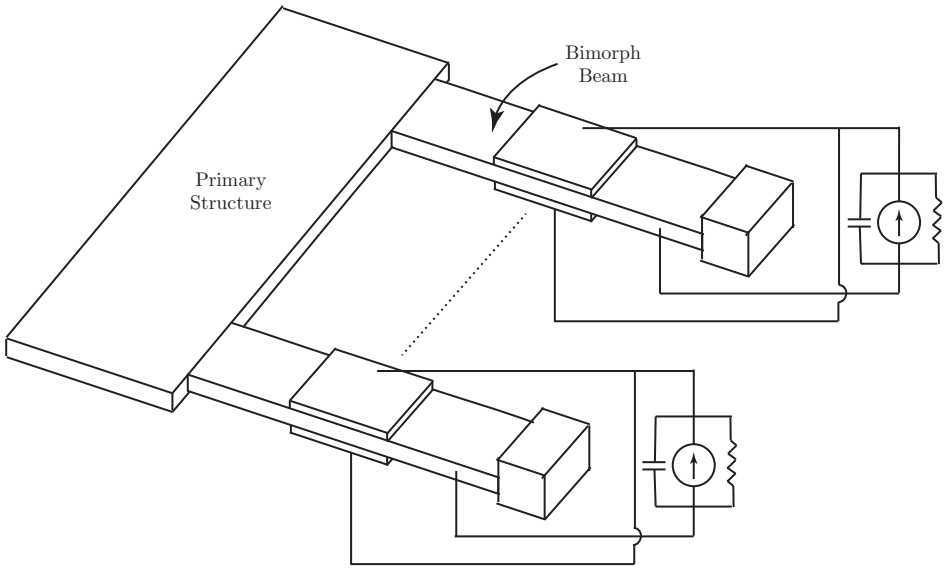

Figure 2.4: A PSOA attached to a host structure.

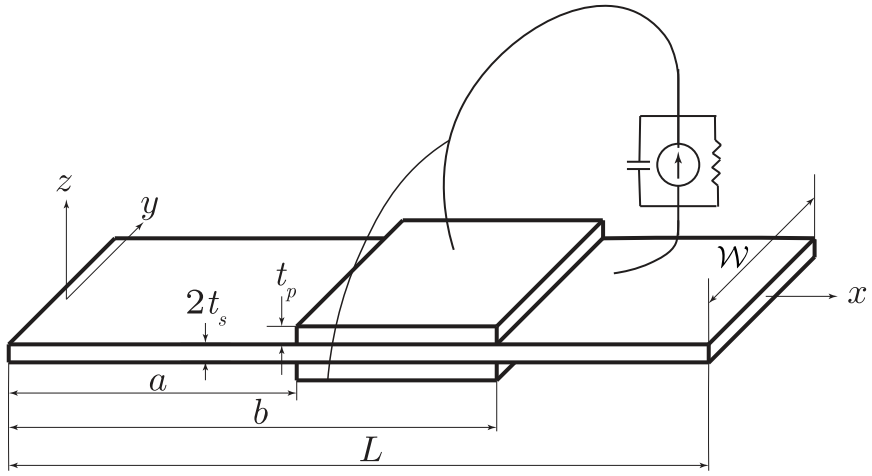

Figure 2.5: Dimensions of a substructure in a PSOA.

If x_p represents the absolute motion of the primary structure and w_i is the relative motion of appendage i in a PSOA with N substructures, the kinetic energy of the system shown in Figure 2.4 can be expressed as

$$T = \underbrace{\frac{1}{2}m_p\left(\dot{x}_p - \dot{\mathfrak{z}}\right)^2}_{\text{I}} + \sum_{i=1}^{N}\Bigg\{\underbrace{\frac{1}{2}\int_0^{L_i}\rho_i A_i\left(\dot{x}_p + \frac{\partial w_i}{\partial t} - \dot{\mathfrak{z}}\right)^2 dx_i}_{\text{II}} + \underbrace{\frac{1}{2}m_i\left(\dot{x}_p + \frac{\partial w_i}{\partial t}(t, L_i) - \dot{\mathfrak{z}}\right)^2}_{\text{III}}\Bigg\}, \tag{2.4}$$

where ρ_i, A_i and L_i are the density, cross sectional area and length of the bimorph, respectively. The cross sectional area is defined as $A_i := 2t_{s,i} \cdot \mathcal{W}_i$, where $2t_{s,i}$ and $\mathcal{W}_i$ are the thickness and width of the substrate as shown in Figure 2.5, respectively. Further, m_i is the tip mass attached to the bimorph, and m_p is the host structure's mass. The terms I, II and III in Equation 2.4 represent the kinetic energy contributions from the primary mass of the host structure, distributed mass of each appendage in the SOA and tip mass of each appendage in the SOA respectively.

After following the steps shown in B, the kinetic energy can be expressed in the quadratic

form

$$T = \frac{1}{2}\left\{ \begin{array}{ccc|c} \dot{\boldsymbol{W}}_1^T & \cdots & \dot{\boldsymbol{W}}_n^T & (\dot{x}_p - \dot{\mathfrak{z}}) \end{array} \right\} \left[\begin{array}{ccc|c} \boldsymbol{M}_{11} & \cdots & \boldsymbol{0} & \boldsymbol{M}_{1p} \\ \vdots & \ddots & \vdots & \vdots \\ \boldsymbol{0} & \cdots & \boldsymbol{M}_{nn} & \boldsymbol{M}_{np} \\ \hline \boldsymbol{M}_{1p}^T & \cdots & \boldsymbol{M}_{np}^T & M_{pp} \end{array} \right] \left\{ \begin{array}{c} \dot{\boldsymbol{W}}_1 \\ \vdots \\ \dot{\boldsymbol{W}}_n \\ \hline (\dot{x}_p - \dot{\mathfrak{z}}) \end{array} \right\}, \tag{2.5}$$

where the vectors $\boldsymbol{W}_1, \ldots \boldsymbol{W}_n$ is defined as the vector of temporal components of the Galerkin approximation $w_i(x,t) = \sum_{j=1}^{n} \Psi_{ij}(x) W_{ij}(t) = \boldsymbol{\Psi}_i^T(x)\boldsymbol{W}_i(t)$. The terms $\boldsymbol{M}_{11}, \ldots, \boldsymbol{M}_{nn}$, $\boldsymbol{M}_{1p}, \ldots, \boldsymbol{M}_{np}$ and M_{pp} are defined in B.

In order to derive an expression for the electromechanical potential, we first derive a representation for the electric enthalpy density. The linear electric enthalpy density of each appendage is calculated from the following expression in [82],

$$\mathcal{H}_i := \frac{1}{2} C_i^E S_i^2 - e_i S_i E_i - \frac{1}{2} \epsilon_i^S E_i^2, \tag{2.6}$$

where E_i is the electric field, C_i^E is the material stiffness at constant electric field, $S_i := -z_i \frac{\partial^2 w_i}{\partial x_i^2}$ is the axial strain in a Bernoulli-Euler beam, e_i is the piezoelectric constant, ϵ_i^S is the permittivity of the piezoelectric material at constant strain. After substituting the expression for electric enthalpy density into Equation 2.35, the total electromechanical potential of a PSOA attached to a host structure will have the form

$$\mathcal{V}_{\mathcal{H}} := \underbrace{\frac{1}{2} K_p x_p^2}_{\text{IV}} + \sum_{i=1}^{N} \underbrace{\mathcal{V}_{\mathcal{H}_i}}_{\text{V}}. \tag{2.7}$$

In the above equation, term IV represents the strain energy of the host structure's spring with stiffness K_p. Further, term V represents the electromechanical potential of each piezoelectric

oscillator in the PSOA and is expressed in the form

$$\mathcal{V}_{\mathcal{H}i} = \frac{1}{2}\boldsymbol{W}_i^T \boldsymbol{K}_{ii} \boldsymbol{W}_i - \boldsymbol{B}_i^T \boldsymbol{W}_i V_i - \frac{1}{2} D_i V_i^2 - \frac{1}{2}\mathcal{C}_i V_i^2, \tag{2.8}$$

Here, D_i is the effective capacitance of the piezoelectric material, $\mathcal{C}_i$ is the shunt capacitance, $\boldsymbol{B}_i^T$ is the control influence matrix and V_i is the voltage across the shunt circuit. The intermediate steps that lead to the above expression are discussed in C. The virtual work done by the nonconservative electromechanical loads will have contributions from the force input, current source, resistor and damping in the system. The virtual work done is expressed in the form

$$\delta W_{nc} = F_p \delta\left(x_p - \mathfrak{z}\right) + \sum_{k=1}^{N} i_k \delta\lambda_k - \sum_{k=1}^{N} \frac{\dot{\lambda}_k}{R_k}\delta\lambda_k + \delta W_{nc,visc}, \tag{2.9}$$

where λ_k is the flux linkage across the shunt circuit, i_k is the current source in the shunt circuit, R_k is the resistor in the shunt circuit and F_p is the force applied to primary mass m_p. The virtual work done by mechanical damping can be derived from $\delta W_{nc,visc} = \delta \boldsymbol{q}^T \mathcal{Q}_{visc}$, where $\mathcal{Q}_{visc}$ is the generalized forces of viscous damping and $\boldsymbol{q}$ is the set of generalized coordinates defined by the vector

$$\boldsymbol{q} = \left\{ \begin{array}{cccccc} \boldsymbol{W_1}^T & \boldsymbol{W_2}^T & \dots & \boldsymbol{W_N}^T & x_p \end{array} \right\}^T.$$

The generalized forces due to damping $\mathcal{Q}_{visc}$ can be derived from the expression $\mathcal{Q}_{visc} = -\frac{\partial \mathcal{F}}{\partial \dot{\boldsymbol{q}}}$ where

$$\mathcal{F} := \dot{\boldsymbol{q}}^T \underbrace{\begin{bmatrix} \mathbb{C} & \boldsymbol{0} \\ \boldsymbol{0}^T & C_p \end{bmatrix}}_{\boldsymbol{C}} \dot{\boldsymbol{q}} \tag{2.10}$$

is the Rayleigh dissipation function. In Equation 2.10, C_p is the damping of the primary structure and $\mathbb{C} := \text{diag}(\boldsymbol{C}_{11}, \boldsymbol{C}_{22}, \ldots, \boldsymbol{C}_{NN})$, where $\boldsymbol{C}_{nn}$ is the damping matrix of the n^{th} oscillator in the PSOA. After simplification, the virtual work done by the viscous damping will have the form

$$\delta W_{nc,visc} = -\delta \boldsymbol{q}^T \boldsymbol{C} \dot{\boldsymbol{q}}. \tag{2.11}$$

The equations of motion is obtained, as discussed in D, by using the $\mathcal{H}$ Variational Principle. The most general finite dimensional model is then given by

$$\begin{bmatrix} \mathbb{M} & \mathbb{M}_p \\ \mathbb{M}_p^T & M_{pp} \end{bmatrix} \begin{Bmatrix} \ddot{\mathbb{W}} \\ \ddot{x}_p \end{Bmatrix} + \begin{bmatrix} \mathbb{C} & \mathbf{0} \\ \mathbf{0}^T & C_p \end{bmatrix} \begin{Bmatrix} \dot{\mathbb{W}} \\ \dot{x}_p \end{Bmatrix} + \begin{bmatrix} \mathbb{K} & \mathbf{0} \\ \mathbf{0}^T & K_p \end{bmatrix} \begin{Bmatrix} \mathbb{W} \\ x_p \end{Bmatrix} - \begin{bmatrix} \mathbb{B} \\ \mathbf{0} \end{bmatrix} \mathbb{V} = \begin{bmatrix} \hat{F}_{p_1} \\ \hat{F}_{p_2} \end{bmatrix}, \tag{2.12}$$

where $\hat{F}_{p_1} = \mathbb{M}_p \ddot{\boldsymbol{\jmath}}$, $\hat{F}_{p_2} = F_p + M_{pp} \ddot{\boldsymbol{\jmath}}$ and

$$\mathbb{B}^T \dot{\mathbb{W}} + \mathbb{D} \dot{\mathbb{V}} + \boldsymbol{\zeta} \dot{\mathbb{\Lambda}} - \mathbb{i} + \boldsymbol{\mathcal{C}} \dot{\mathbb{V}} = \mathbf{0}. \tag{2.13}$$

It should be noted that this equation of motion allows for the possibility of multi-mode approximations of each PSOA appendage.

Also, as a part of comparison, it is known that the actuator equations for a monolithic, distributed, linear piezoelectric composite (such that those that arise from piezoelectric beams, plates, or shells (see [12])) has the form

$$\mathbb{M}_{mono} \ddot{\mathbb{W}} + \mathbb{C}_{mono} \dot{\mathbb{W}} + \mathbb{K} \mathbb{W} = \mathbb{B}_{mono} \mathbb{V}$$

with $\mathbb{M}_{mono}$, $\mathbb{C}_{mono}$, $\mathbb{K}_{mono}$ symmetric, sparse and banded. However, these matrices are not guaranteed to have the block zero structure of Equation 2.12. As mentioned in the in-

troduction, it may be possible using component mode synthesis to drive the equation to a similar form. It we can choose $\mathbb{W} = [\mathbb{W}_I^T \mathbb{W}_D^T]^T = [\Psi_I^T \Psi_D^T]^T$ where $[\Psi_I \Psi_D]\mathbb{K}[\Psi_I^T \Psi_D^T]^T = diag(K_{II}, K_{DD})$ and $[\Psi_I \Psi_D]\mathbb{C}[\Psi_I^T \Psi_D^T]^T = diag(C_{II}, C_{DD})$, then the more general Equation can be cast in a form somewhat similar to Equation 2.12. However, this definition can result in new, nonintuitive definitions of states.

2.5 PSOA Design using Frequency Response Function

In this section, the closed form FRF from the input force F_p to the displacement x_p of the host structure is derived when each subordinate element is modeled with a single degree of freedom. Next, various strategies that can be implemented in the design of the PSOA are discussed. As it will become evident in the current section, the resistor and the current source in the shunt circuit are not necessary for passive PSOAs designed for vibration attenuation. The values R^{-1} and i are assumed to be zero in the subsequent calculations. Further, it is assumed that there is no base excitation to simplify the derivation of the closed-form expression. After making use of these assumptions, integrating Equation 2.13 with zero initial conditions generates an expression for voltage of the form

$$\mathbb{V} = -(\mathbb{D} + \boldsymbol{\mathcal{C}})^{-1} \mathbb{B}^T \mathbb{W} \cdot \tag{2.14}$$

Substituting the expression for voltage into Equation 2.12 and taking the Laplace transform will result in the expression

$$\begin{bmatrix} \mathbb{M}s^2 + \mathbb{C}s + \hat{\mathbb{K}} & \mathbb{M}_p s^2 \\ \mathbb{M}_p^T s^2 & M_{pp}s^2 + C_p s + K_p \end{bmatrix} \begin{Bmatrix} \mathbb{W} \\ x_p \end{Bmatrix} = \begin{bmatrix} \mathbf{0} \\ f_p(s) \end{bmatrix}, \tag{2.15}$$

where

$$\hat{\mathbb{K}} := \mathbb{K} + \mathbb{B}(\mathbb{D} + \boldsymbol{\mathcal{C}})^{-1}\mathbb{B}^T. \tag{2.16}$$

It is evident from the expression for $\hat{\mathbb{K}}$ that the shunt capacitance induces a change in the stiffness of the PSOA. As shown in E, the FRF can be obtained by evaluating this transfer function along the imaginary axis, i.e. by substituting $s = i\omega$. The nondimensionalized frequency response function, obtained by dividing both sides of Equation 2.64 by the stiffness of the host structure K_p, is expressed as

$$\frac{x_p K_p}{f_p} = \left[1 - \Omega^2 + \frac{i\Omega}{Q_p} + \sum_{n=1}^{N} \hat{\alpha}_n \left[\Omega^2 + \frac{-\Omega^2\left(1 + \frac{i\Omega}{\beta_n Q_n}\right)}{1 - (\frac{\Omega}{\beta})^2 + \frac{i\Omega}{\beta_n Q_n}}\right]\right]^{-1}, \tag{2.17}$$

where

$$\Omega = \omega\sqrt{\frac{M_{pp}}{K_p}}, \quad \tilde{\alpha}_n = \frac{M_{nn}}{M_{pp}}, \quad \beta_n = \sqrt{\frac{\gamma_n}{\tilde{\alpha}_n}}, \quad \gamma_n = \frac{\hat{K}_{nn}}{K_p}, \quad Q_n = \frac{\sqrt{M_{nn}\hat{K}_{nn}}}{C_{nn}}, \quad \hat{\alpha}_n = \alpha_n^2\tilde{\alpha}_n. \tag{2.18}$$

The definitions of M_{nn}, C_{nn}, K_{nn} and α_n are available in E. Equation 2.17 is a principal result for electromechanical systems in this chapter and should be compared to Equation 2.1 for purely mechanical systems.

2.5.1 Methodology for PSOA Design

As discussed in the earlier sections, flat broadband attenuation of frequency response can be achieved when the bandwidth of the SOA is distributed around the host structure's natural frequency. The SOA bandwidth is defined as the range of isolated natural frequencies from the smallest possible resonant frequency to the largest resonant frequency. In this subsection,

two systematic approaches to achieve the good designs will be discussed. Figure 2.6 shows a PSOA, designed using the two approaches, attached to a host structure. The equations of motion of piezoelectric oscillator n in the PSOA can be extracted from Equations 2.12 and 2.13. They have the form

$$\boldsymbol{M}_{nn}\ddot{\boldsymbol{W}}_n + \boldsymbol{C}_{nn}\dot{\boldsymbol{W}}_n + \boldsymbol{K}_{nn}\boldsymbol{W}_n - \boldsymbol{B}_n V_n = -\boldsymbol{M}_{np}\ddot{x}_p, \tag{2.19}$$

$$\boldsymbol{B}_n^T\dot{\boldsymbol{W}}_n + (D_n + \mathcal{C}_n)\,\dot{V}_n + \frac{V_n}{R_n} - i_n = 0. \tag{2.20}$$

As mentioned at the beginning of this section, the shunt circuit consists of only a capacitor for each appendage. Hence, the terms corresponding to resistor and current source in Equations 2.20 can be set to zero. Further, using single mode approximation simplifies the vectors $\boldsymbol{M}_{nn}$, $\boldsymbol{M}_{np}$, $\boldsymbol{C}_{nn}$, $\boldsymbol{K}_{nn}$, $\boldsymbol{B}_n$ and $\boldsymbol{W}_n$ in Equations 2.19 and 2.20 to scalars M_{nn}, M_{np}, C_{nn}, K_{nn}, B_n and W_n, respectively. With these assumptions, Equations 2.19 and 2.20 simplify to

$$M_{nn}\ddot{W}_n + C_{nn}\dot{W}_n + K_{nn}W_n - B_n V_n = -M_{np}\ddot{x}_p, \tag{2.21}$$

$$B_n\dot{W}_n + (D_n + \mathcal{C}_n)\,\dot{V}_n = 0. \tag{2.22}$$

Assuming zero initial conditions, Equation 2.22 can be integrated and rewritten as an expression for voltage of the form

$$V_n = -\frac{B_n}{D_n + \mathcal{C}_n}W_n. \tag{2.23}$$

Substituting the expression for voltage into the Equation 2.19 results in

$$M_{nn}\ddot{W}_n + C_{nn}\dot{W}_n + \underbrace{\left[K_{nn} + \frac{B_n^2}{D_n + \mathcal{C}_n}\right]}_{\hat{K}_{nn}} W_n = -M_{np}\ddot{x}_p, \tag{2.24}$$

For a system represented by a second order differential equation as shown in Equation 2.24, the natural frequency will be

$$\omega_n = \sqrt{\frac{K_{nn} + \frac{B_n^2}{D_n + \mathcal{C}_n}}{M_{nn}}} = \sqrt{\frac{\hat{K}_{nn}}{M_{nn}}}. \tag{2.25}$$

Equation 2.25 gives the isolated natural frequency of an oscillator in a PSOA. The system parameters M_{nn}, K_{nn}, B_n, D_n and $\mathcal{C}_n$ of each oscillator are chosen in such a way that the PSOA achieves the desired bandwidth. The following paragraphs discuss two specific strategies for making these choices.

Design by Tip Mass Distribution

The first approach varies the tip mass to achieve the necessary natural frequency distribution. After fixing all the parameters except tip mass, the nondimensional mass distribution $\tilde{\alpha}_n$ can be calculated using the relation given in Equation 2.18. The nondimensional mass of oscillator n is

$$\tilde{\alpha}_n := \frac{\gamma_n}{\beta_n^2} := \frac{M_{nn}}{M_{pp}} = \frac{\mathcal{M}_{nn} + m_{nn}}{m_p + \sum_i (\mathcal{M}_i + m_i)}, \tag{2.26}$$

which can be rearranged as

$$m_1 + m_2 + \cdots + \left(1 - \frac{\Psi(L)^2}{\tilde{\alpha}_n}\right) m_n + \cdots + m_N = \frac{\int_0^L \rho A \Psi(x)^2 dx}{\tilde{\alpha}_n} - (m_p + N\rho AL). \tag{2.27}$$

The tip mass distribution that can achieve the desired frequency distribution can be calculated using the relation

$$\boldsymbol{m} = (\mathrm{I_N} - \mathrm{P})^{-1}\mathrm{Q}, \tag{2.28}$$

with

$$\mathrm{P} := diag\left(\frac{\Psi(L)^2}{\tilde{\alpha}_1}, \frac{\Psi(L)^2}{\tilde{\alpha}_2}, \cdots, \frac{\Psi(L)^2}{\tilde{\alpha}_N}\right) \quad \text{and} \tag{2.29}$$

$$\mathrm{Q} := \begin{bmatrix} \left(\frac{\int_0^L \rho A \Psi(x)^2 dx}{\tilde{\alpha}_1} - (m_p + N\rho AL)\right) \\ \vdots \\ \left(\frac{\int_0^L \rho A \Psi(x)^2 dx}{\tilde{\alpha}_N} - (m_p + N\rho AL)\right) \end{bmatrix}^T. \tag{2.30}$$

Design by Capacitance Distribution

The second approach specifies stiffness properties by varying shunt capacitance while fixing the other parameters. Similar to the first approach, all parameters except the shunt capacitance are kept constant. The nondimensional stiffness of oscillator n

$$\gamma_n := \beta_n^2 \tilde{\alpha}_n := \frac{\hat{K}_{nn}}{K_p}. \tag{2.31}$$

The shunt capacitance of oscillator n that can produce the required nondimensional frequency can be calculated using the relation

$$\mathcal{C}_n = \frac{B_n^2}{\hat{K}_{nn} - K_{nn}} - D_n. \tag{2.32}$$

The advantages and the limitations of both the approaches will be discussed along with the numerical results in Subsection 2.7.1.

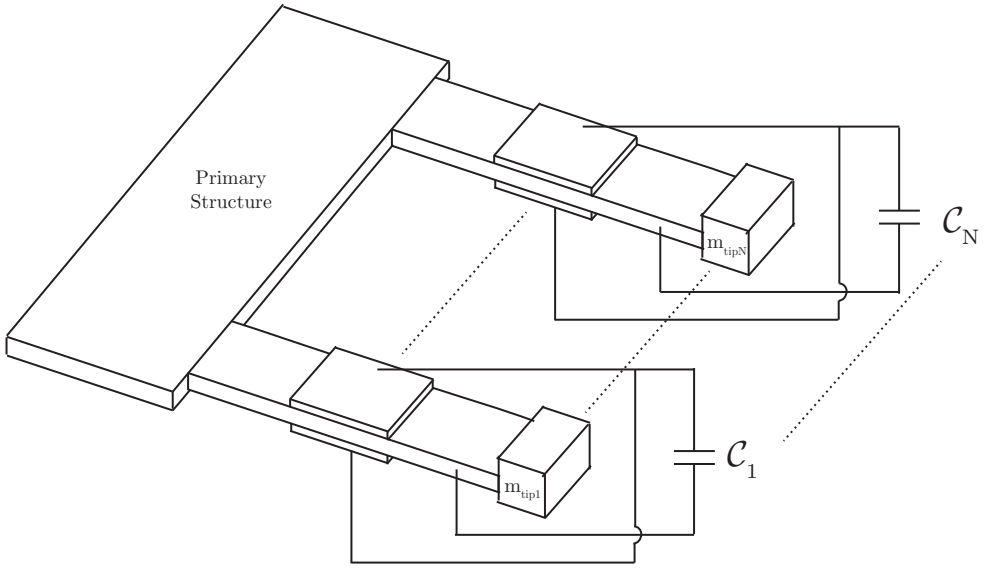

Figure 2.6: PSOA designed using hybrid approach.

2.6 Experimental Procedure

Performance of PSOAs in attenuating resonant peaks was tested on an aluminum beam shown in Figure 2.7. The aluminum beam of dimensions 29.7 cm × 7.67 cm × 1.275 cm ($l \times w \times t$) was clamped at one end, while the bimorphs were attached at its free end. A shaker was attached to the beam at a distance of 13.2 cm from its tip. The frequency response functions of the structure were evaluated between the input force measured by a PCB dynamic force transducer and the tip-velocity measured with a single point laser vibrometer (PSV-100). The attenuation in the resonant peaks of the aluminum beam was monitored from the FRFs measured with an LMS SCADAS DAQ system. Initially, baseline FRF of the host structure (without PSOA) was recorded, which was later compared to FRFs of the modified structure as piezoceramic bimorphs (Part Number: T226-H4-503Y)

were attached to it in succession. The material and geometric properties of these PSOAs are summarized in Tables 2.2 and 2.3. Even though the bimorphs have an aspect ratio that resembles a rectangular plate rather than a beam, the fundamental frequency of the cantilevered bimorphs is the only resonant frequency in the bandwidth of interest. Therefore, each PSOA can be considered as a tuned single degree-of-freedom dynamic oscillator.

The performance of four PSOAs, each with 2, 4, 6, 8 bimorphs, was studied during the experiments. The natural frequencies of the bimorphs in the PSOAs were estimated from the FRFs between the base-acceleration and the tip velocity of the bimorph attached to the host structure. For these experiments, the length of the bimorphs was varied to achieve the desired frequency distribution and tip masses were only added once the maximum length of bimorphs was reached. Because of the geometry of the PSOA, it was not possible to vary tip mass alone: the size of the tip masses would interfere with one another. Thus, the practical constraints in the setup play a critical role in determining the parameters that can be varied to achieve the desired nondimensional frequency distribution. Theoretically, the length and the tip mass variation should be sufficient to tune the natural frequencies of the bimorphs. However, due to uncertainties in the experiments, the length was fixed first, the tip-mass (if required) was added next, and finally, the shunt capacitance was tuned to approach the desired natural frequency.

Furthermore, the performance of the PSOAs with open shunt circuits was evaluated under varying dynamic properties of the host structure. Once a tip-mass was added to the host, the PSOAs were then re-tuned using the shunt capacitances. The performance recovery achieved by the PSOAs after shunt tuning was studied for three different tip masses, 31.60 g, 62.81 g, and 81.29 g. The results of the above-mentioned experiments are discussed in Section 2.8.

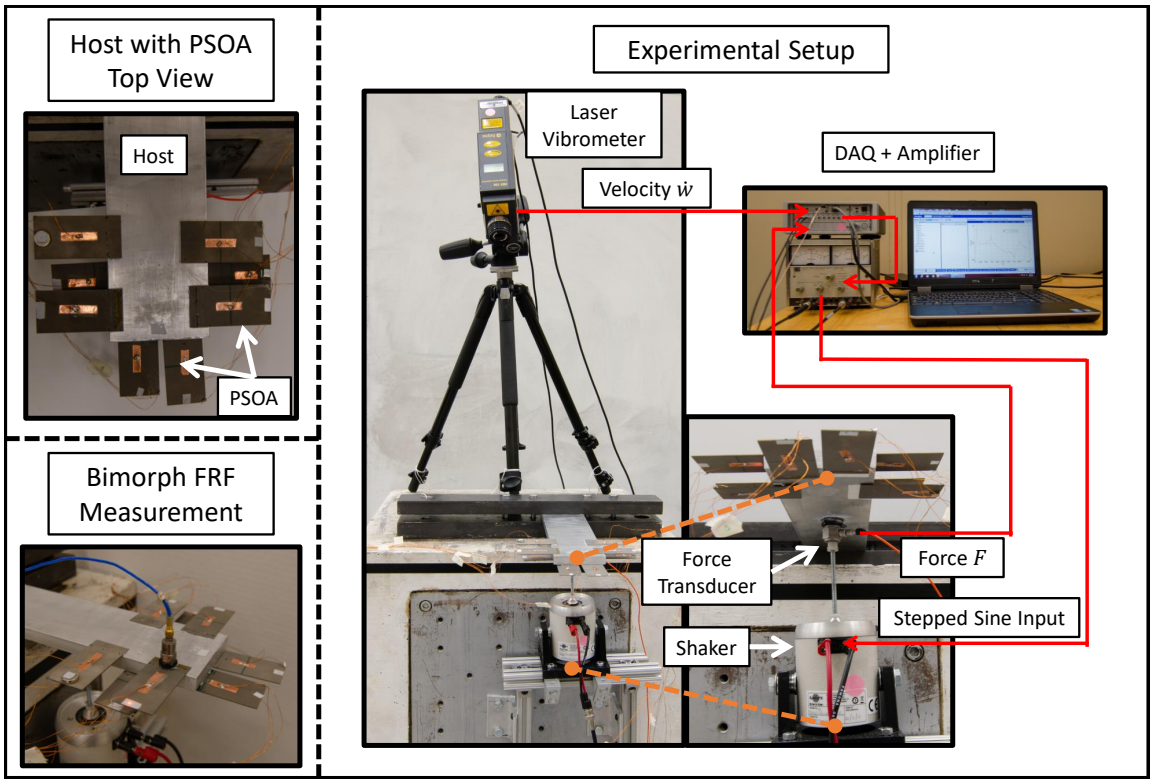

Figure 2.7: Experimental Setup.

2.7 Numerical Results

We simulated the response of the host structure attached to the PSOAs that were designed using approaches presented in the previous sections under ideal as well as non-ideal conditions. To better contrast the simulation results for different cases, the host's structural properties, the nondimensional frequency distribution β_n, the number of substructures N in the PSOA, and majority of the fixed parameters of the PSOA were maintained constant for all simulations. The host structure was assumed to have a mass $m_p = 1000$ kg, stiffness $K_p = 1273300$ N/m and a very low damping ratio $\zeta_p = 0.0001$, which places its natural frequency at 35.68 rad/sec. The nondimensional frequency distribution β_n shown in Figure 2.8 was used for the simulations and was generated using Equation 2.3 with $\Delta = 0.09$ and $p = 0.9$. We assigned the following values to the fixed parameters of the SOA:

$C = 6.9e + 10$ Pa, $\rho_m = 2.3e + 3$ kg/m^3, $N = 25$, $L = 0.5$ m, $\mathcal{W} = 0.025$ m, $2t_s = 0.003$ m, $a = 0.25$ L, $b = 0.75$ L, $e_{31} = -10.4$ C/ m^2, $\epsilon = 13.3$ nF/m, $\zeta_{SOA} = 0.01$. In the following subsections, we will discuss the results we obtained for the various simulation cases.

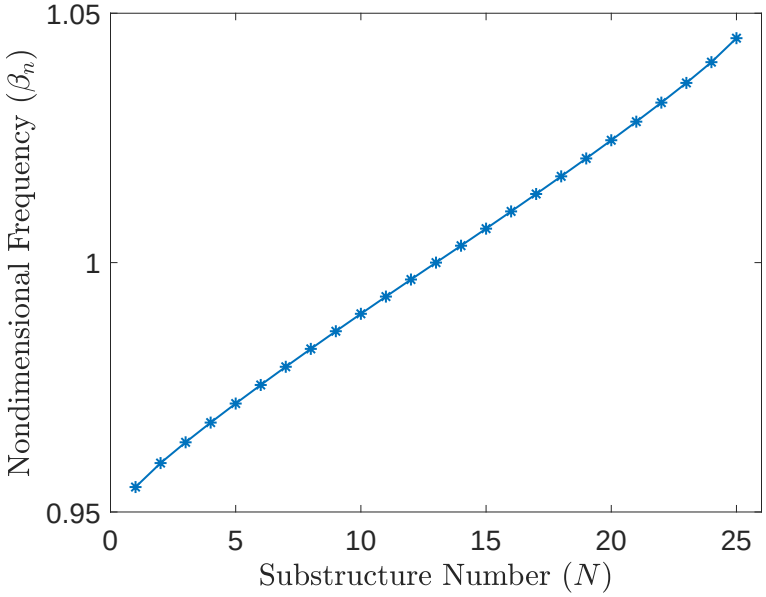

Figure 2.8: Nondimensional frequency distribution obtained using equation 2.3 with $\Delta = 0.09$ and $p = 0.9$.

2.7.1 PSOA Simulations under Ideal Conditions

In the first set of simulations, we assumed that we had perfect knowledge of host structural properties, and the fabricated PSOA adhered strictly to the design specifications.

Implementing the first approach to develop a piezoelectric array of 25 substructures with no shunt circuits resulted in a tip mass distribution as shown in Figure 2.10. This result was obtained for piezoelectric patch thickness of $t_p = 0.0005$ m. When we simulated the effect of PSOA with this tip mass distribution on the host structure, we obtained the frequency response shown in Figure 2.9. As the figure portrays, the addition of the PSOA reduces the steady state displacement of the host structure to approximately 1% of its actual steady state displacement at the resonant frequency. This result indicates that PSOAs can indeed

achieve a reasonably flat bandwidth in the host structure's resonant peak region. Figure 2.9 also shows that the magnitude increase outside this region is negligible. This is a substantial qualitative improvement over a classical DVA.

One of the critical aspects to consider during the design of SOAs, as well as the DVAs, is the maximum displacement of the substructures. We plotted the frequency response from the force input F_p to the displacement of the 13^{th} substructure W_{13}, which can be seen in Figure 2.11. As evident from the figure, to ensure the displacement is within the mechanical limitations, the maximum force input to the host structure should not exceed 10^3 times the maximum displacement allowable in the substructure.

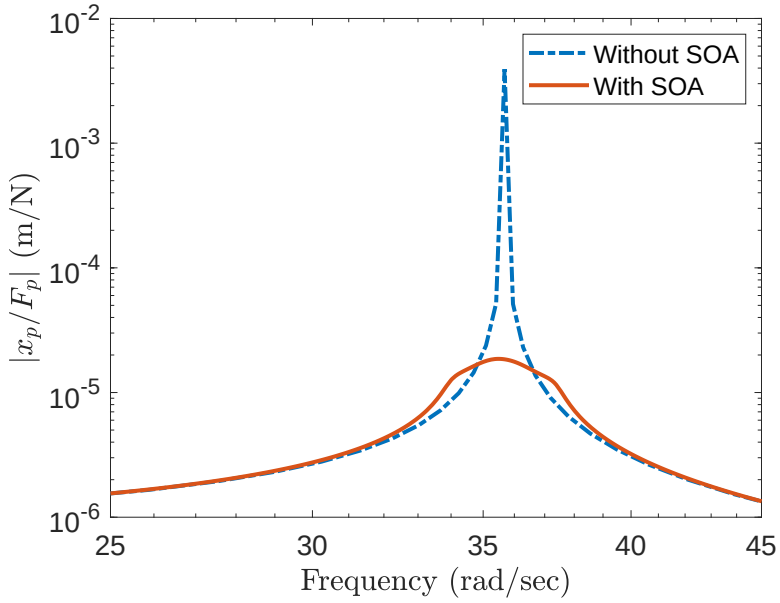

Figure 2.9: Frequency response function from force input F_p to displacement x_p of a host structure with and without a PSOA. The PSOA was designed using first approach.

In the second set of simulations, we tested a PSOA designed using a distribution of capacitive shunts. We calculated the total tip mass of each substructure to be $m_i = 0.06944$ kg from the prescribed total mass ratio $\mu = 4.065 \times 1e - 3$. Assuming the piezoelectric thickness as $t_p = 0.003$ m, we obtained the capacitance distribution shown in Figure 2.13. Figure 2.12 shows the frequency response of the host structure when the shunt capacitors followed

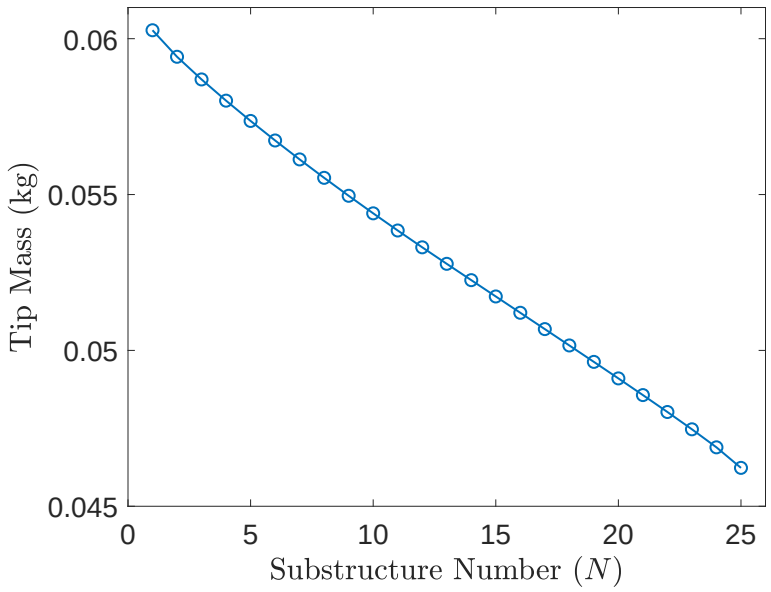

Figure 2.10: Tip mass distribution used to achieve the frequency response shown in Figure 2.9.

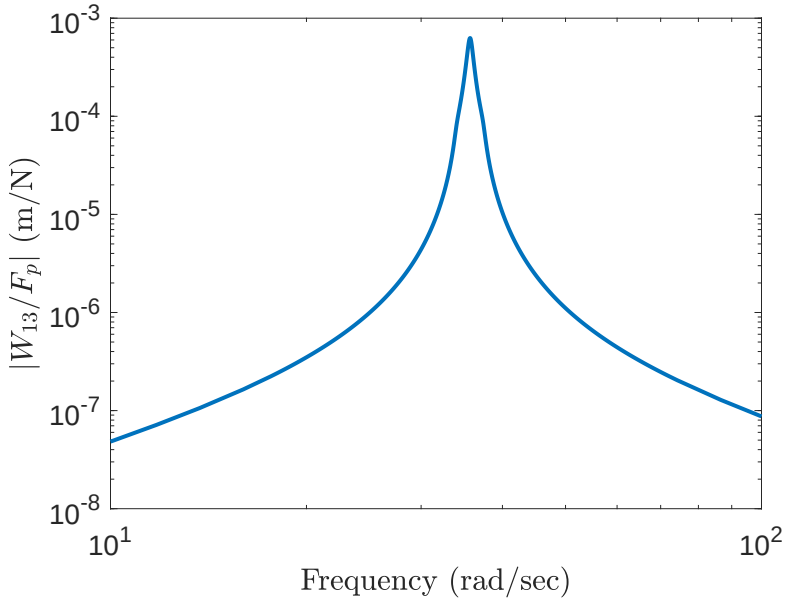

Figure 2.11: Frequency response function from force applied F_p on the host structure to the displacement W_{13} of the 13^{th} substructure in the PSOA designed using first approach.

the distribution shown in Figure 2.13. The primary implication of this result is that it is possible to achieve flat attenuation using mechanically identical oscillators. One of the advantages of using a capacitive shunt distribution is that it allows the designer to impose

a mass ratio. Prescribing an actual mass ratio is problematic in the first approach since the tip masses are unknown during the initial stages of design. Hence, design using the first approach requires an iterative process. On the other hand, it is important to note that the PSOAs designed using the second approach usually require piezoelectric patches whose thicknesses are no longer negligible. In such cases, the model developed using modal shape functions is interpreted as an approximation whose accuracy must be validated. In some instances, individual variations of tip-mass or the capacitance are not sufficient to generate the necessary nondimensional frequency distribution. In such cases, multiple parameters must be simultaneously varied as shown in the experimental results.

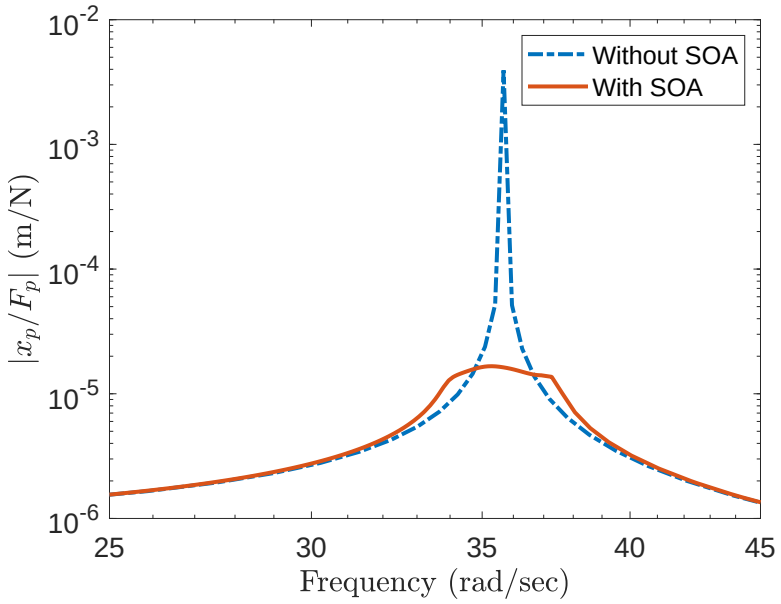

Figure 2.12: Frequency response function from force input F_p to the displacement of the host structure attached to a PSOA designed using second approach.

2.7.2 PSOA Simulations under Non-Ideal Conditions

In the previous subsection, we demonstrated the effectiveness and the advantages of the PSOAs through simulations. But the simulations relied on ideal conditions which entailed

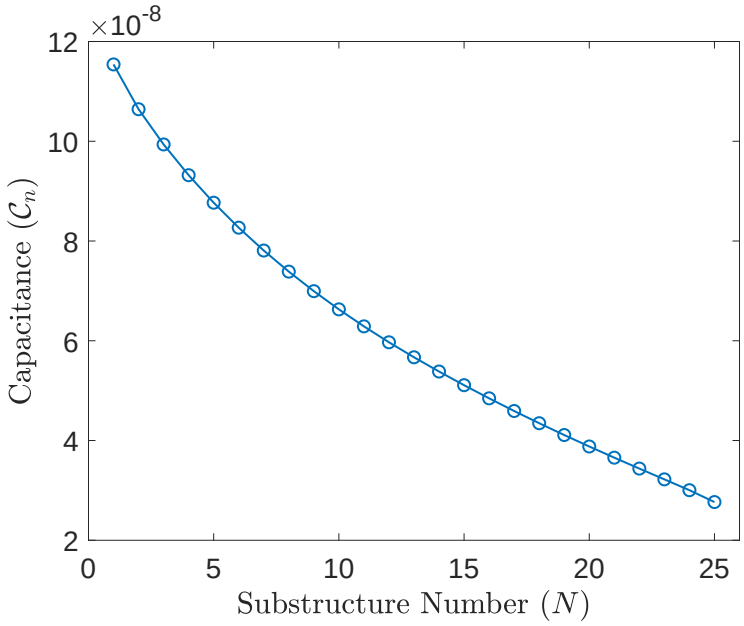

Figure 2.13: Capacitance distribution used to achieve the frequency response shown in Figure 2.12.

perfect knowledge of the host structure's properties and a high level of precision during manufacturing. These assumptions may not be justified in some applications. Further, the structural properties of some systems can degrade or evolve over time which can render the SOA ineffective. In this subsection, we will discuss the performance of the PSOAs under non-ideal conditions and analyze the robustness of PSOA systems in the presence of disorder. In the following set of discussions, we restrict our analysis to the PSOA designed using the first approach. The piezoelectric patch thickness value used for this set of simulations is $t_p = 0.001$ m.

Assume that the host's structural properties used in the previous simulations are inaccurate and the actual host structure has a stiffness which is 10% less than what we measured. Figure 2.14 shows the effect of this error on the frequency response of the host. The PSOA, which has no capacitive shunt, is expected to generate a flat frequency response. However, the presence of error in host structure model induces a peak in the frequency response as

shown in Figure 2.15. The induced peak disappeared, when we attached the PSOA with shunts of capacitance $\mathcal{C}_n = 1$ F. As can be seen in Figure 2.15, we were able to achieve a frequency response very similar to the expected response after shunt tuning.

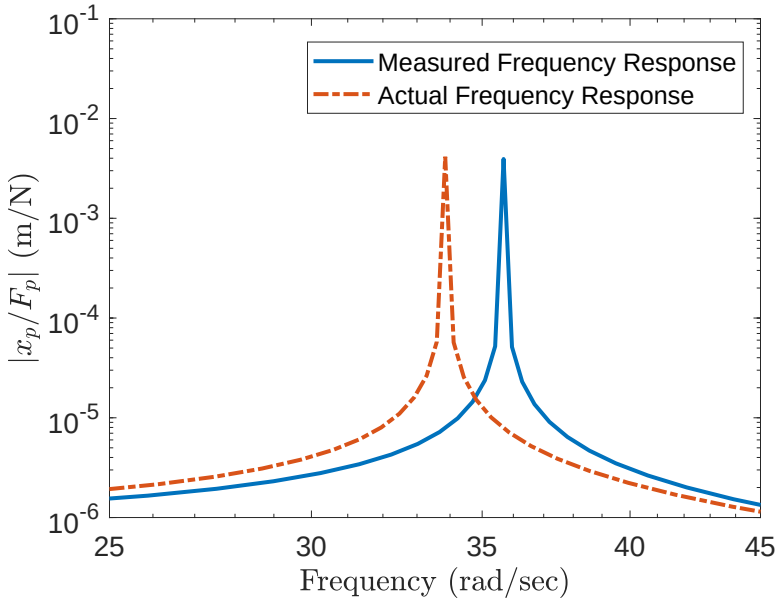

Figure 2.14: Frequency response function from the force applied F_p to the displacement x_p of the host structure. Effect of 10% disorder in host structure's stiffness on the natural frequency can be seen in this plot.

Similarly, let us assume that the fabricated PSOA designed in Subsection 2.7.1 did not comply with the design specifications. To imitate this disparity in the design and fabricated SOA's parameters, we introduced a -10% error in the stiffness $\mathbb{K}$ of the SOA. The ideal PSOA that we designed in Subsection 2.7.1 attached to a shunt capacitance of $\mathcal{C}_n = 1$ F would have produced a spectrally flat response as shown in Figure 2.16. However, the fabrication errors induce a peak in the frequency response as shown in the same figure. After reducing the shunt capacitance to $\mathcal{C}_n = 1e-9$ F, we were able to achieve a frequency response that almost mimics the expected response.

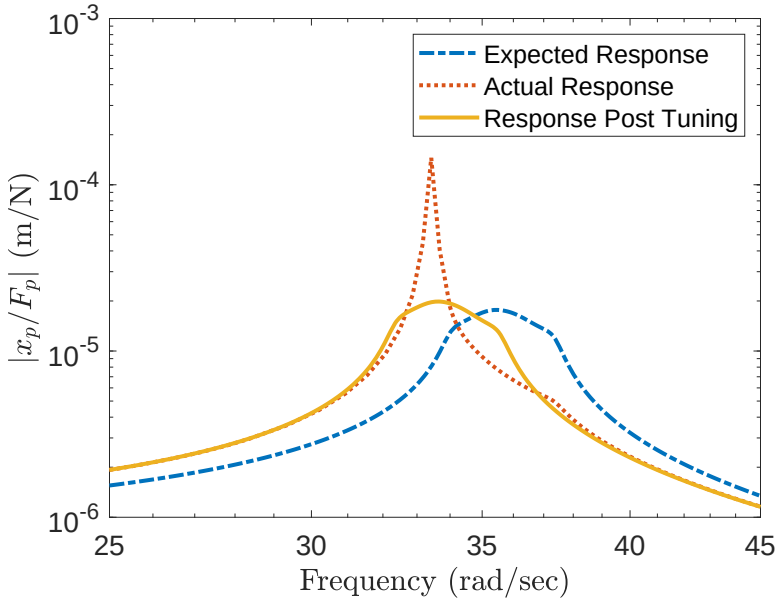

Figure 2.15: Frequency response function from the force applied F_p to the displacement x_p of a host structure. This plot shows that the effect of disorder on the host structure's response can be mitigated by shunt tuning.

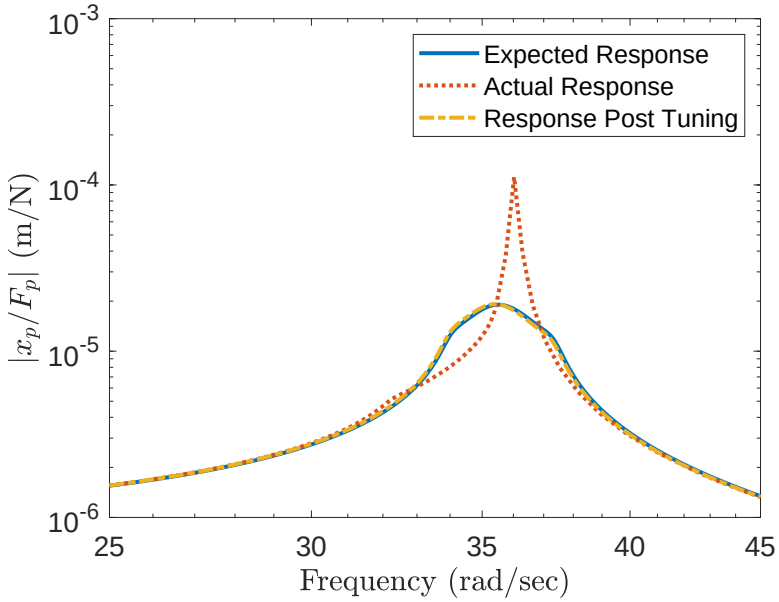

Figure 2.16: Frequency response function from the force applied F_p to the displacement x_p of a host structure attached to a PSOA. An error of -10% in the stiffness of the PSOA deteriorates the host structure's response. However, the effect of error is eliminated after shunt tuning.

2.8 Experimental Results

As discussed in earlier sections, the first natural frequency of an aluminum beam was targeted for experimentally studying the performance of the PSOAs. Figure 2.17 shows the experimental frequency response function of the unmodified host (red) as well as the FRFs of the host with PSOAs. The structural details of the oscillators in the PSOA are tabulated in Table 2.2. While the PSOA with two oscillators was able to achieve a 25 dB reduction, adding more oscillators resulted in a wider flattening of the bandwidth with at least 30 dB attenuation. The natural frequencies of the oscillators in the PSOA were selected such that their nondimensional frequencies would follow the selected distributions shown in Figure 2.18. Revisiting Equation 2.18, the nondimensional frequency is expressed as the ratio of nondimensional stiffness and nondimensional mass, which also included mass of the subordinate oscillators. However, in Figure 2.18, the nondimensional frequency is defined for experimental results as the ratio of the damped natural frequency of the bimorphs to the damped natural frequency of the unmodified host. This definition is a good approximation of the theoretical nondimensional frequency, as it easier to estimate during experimentation.

Based on Figure 2.17, it is evident that increasing the number of oscillators does not always have significant attenuation gains, especially considering the increase in the mass ratio at each step. However, the advantage of having more oscillators in PSOAs comes from an increase in its robustness. The robustness of vibration attenuation via PSOAs is evaluated through artificially changing the host's natural frequency by adding tip mass. Figure 2.19 shows the change in the FRFs of the host structure with addition of tip masses. Consequently, the nondimensional frequency distribution of the PSOA is not tuned for the modified host. Even for a 15 Hz shift in natural frequency (or 13 % change in nondimensional frequency), PSOAs with four and eight oscillators were able to attenuate the resonant peak by about 25 dB, as seen in Figure 2.20. It can also be seen that the PSOA with higher bandwidth (8

No.	No. of Bimorphs	Mass Ratio	Bimorph Ref. (Figure 2.18)	Length (mm)	Tip-mass (g)	Shunt Capacitance	Natural Frequency (Hz)
1	2	2.30%	A, B	53.28, 48.88	0, 0	220 nF, 220 nF	110.25, 123.5
2	4	4.59%	C, A B, D	55.70, 53.28, 48.88, 46.24	0, 0, 0, 0	470 nF, 820 nF, 220 nF, O	94, 108.5, 123.5, 136.5
3	6	7.13%	E, C, A, B, D, F	58.5, 55.70, 53.28, 48.88, 46.24, 44.45	1.75, 0, 0, 0 0, 0	470 nF (BS), 220 nF, 220 nF, 220 mF, 220 mF, O	86.25, 95, 110.25, 119 130.75, 142.75
4	8	9.87%	G, E, C, A, B, D, F, H	58.50, 58.50, 55.70, 53.28, 48.88, 46.24, 44.45, 42.85	3.72, 1.75, 0, 0 0, 0 0, 0	O, O, O, 220 nF, 2.2 mF, C, O, 2.2 mF	79.75, 94, 97.25, 110.25 122.25, 130.75 142.75, 150

(BS) - capacitance between bottom piezo layer and substrate (top piezo layer is not included in the circuit), O - shunt circuit is open, C - shunt circuit is closed.

Table 2.2: Parameters of PSOAs used in the experiments.

Bimorph Properties	
Substrate Material	Brass
Total mass	10.3 (g)
$\mathcal{W}_i$	31.75 (mm)
$t_{p,i}$	0.27 (mm)
$2t_{s,i}$	0.11 (mm)

Table 2.3: Properties of bimorphs used in experiments

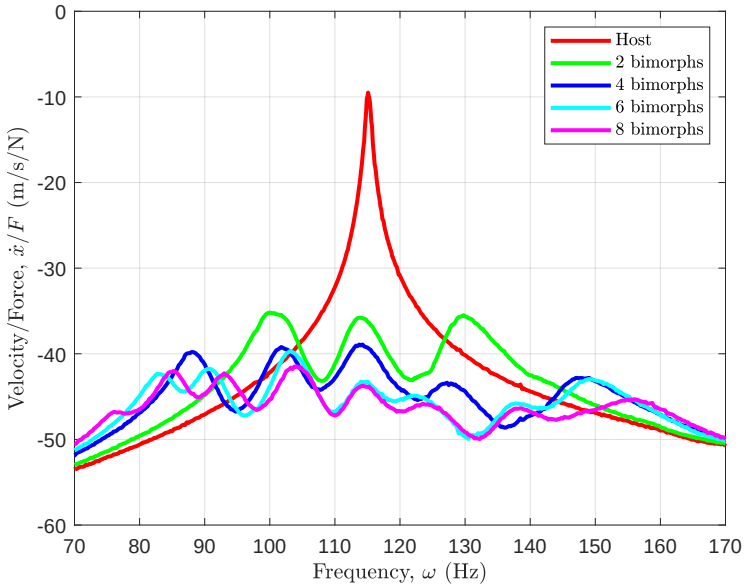

Figure 2.17: Experimental FRF from base acceleration to the tip velocity of the host structure with PSOAs.

oscillator case) resulted in a flatter response; thereby displaying the robustness of PSOAs. Additionally, in case of the PSOA with eight oscillators, shunt tuning was not necessary. On the other hand, shunt tuning improved the performance of the PSOA with four oscillators as shown in Figure 2.21.

In this figure, the red colored line (no tip mass) is the response of the original system with PSOAs. With addition of tip masses to the host, the natural frequency of the host decreases and the magnitude increases at lower frequencies. As the PSOAs are tuned with shunted circuits, the magnitude is partially recovered as pointed out in this figure. While the dashed

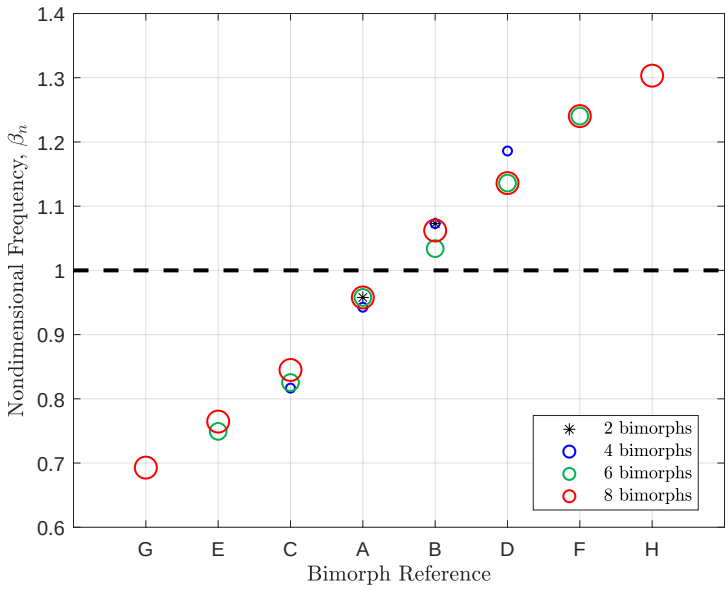

Figure 2.18: Nondimensional frequency distribution of the PSOAs shown in Figure 2.17. The oscillators in the PSOAs are referenced out of order in the x-axis to maintain the symmetry and facilitate comparison of the nondimensional frequency distributions. The properties of all the oscillators can be referred from Table 2.2 based on the oscillator reference.

line correspond to open circuits, the solid lines correspond to the PSOAs with closed shunts. The difference in peak magnitudes gives a measure of the recovered performance. Loci of the peaks of open and closed circuit lines are also seen in Figure 2.21. Extrapolation of these lines provides us with an idea of how the PSOA performs with changes or uncertainty in the dynamics of the host structure. It is important to notice that these lines are not parallel to each other. And this agrees with our intuition since we expect the performance recovery ability of the PSOA to decrease with increasing uncertainty. From a design perspective, we want the performance recovery ability of a PSOA to be as high as possible. This can be achieved by piezoelectric oscillator shunt tuning, which can be achieved by increasing the thickness of the bimorph's piezoelectric patches. Another approach would be to include negative capacitance [52, 83]. In situations where uncertainty can be higher, these factors should be considered, however these discussions are beyond the scope of the current chapter and hence not addressed rigorously.

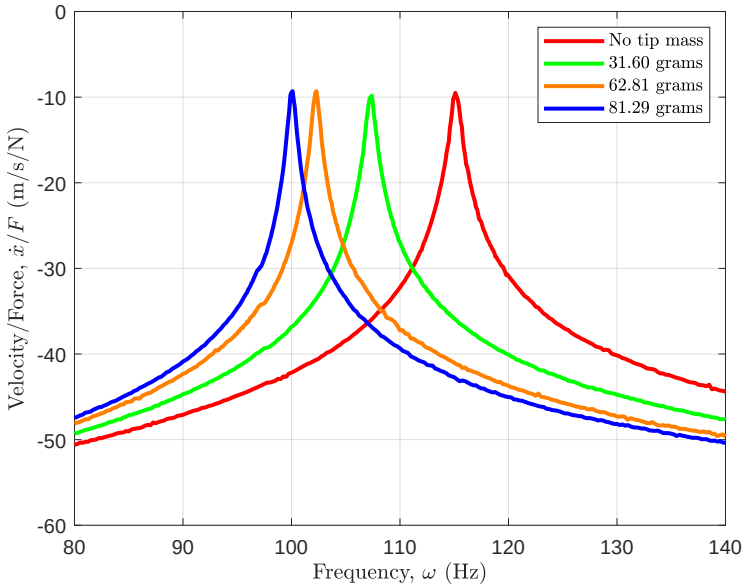

Figure 2.19: The variation of the host structure's FRFs with different tip masses. The tip masses mimic the degradation of host's properties over time.

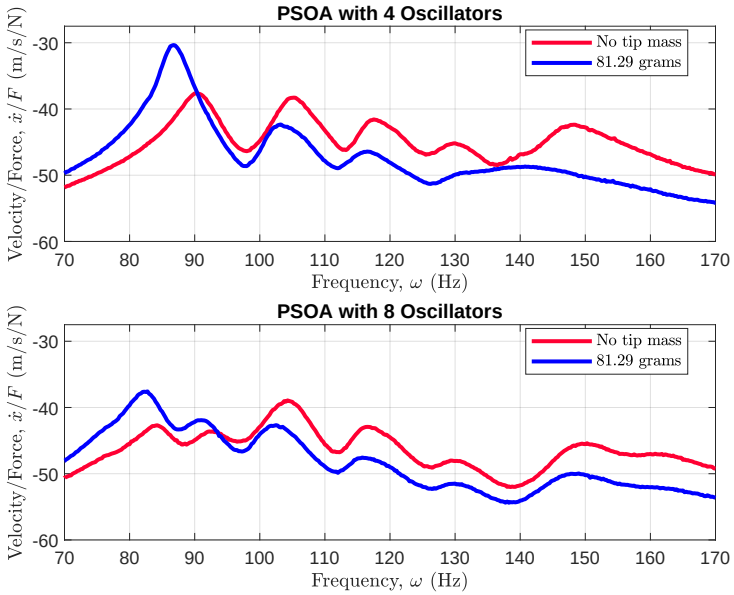

Figure 2.20: Experimental FRF from base acceleration to the tip velocity of the host structure with 4 and 8 oscillator PSOAs.

Figure 2.22 shows the FRFs of the host as well as the host with eight oscillators PSOA up to 2500 Hz. This figure is presented here to show that the amount of modal spillover outside the PSOA bandwidth. The performance deterioration is minimal in the displayed

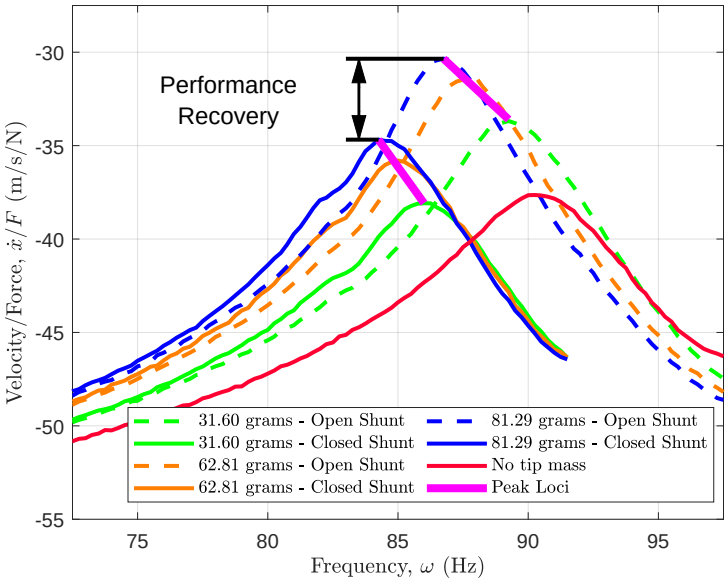

Figure 2.21: Four oscillator PSOA's performance recovery using shunt tuning.

frequency range. Also, the second and third modes have been attenuated by about 10 dB. This can be attributed to the damping of and the absorption of high frequencies energies by the oscillators tuned to the first natural frequency.

2.9 Conclusions

This chapter has shown that PSOAs can realize and improve on the benefits of ordinary SOAs and tunable DVAs. They can be used to achieve a flat response in the frequency domain and have the ability to address uncertainties in structural properties, at the expense of added complexity. The zero-nonzero block structure of the coupled PSOA and host system enables assignment of distributions to nondimensional electromechanical parameters. As shown both numerically and experimentally in this chapter, the assignment of such distributions dramatically simplifies the design process and can eliminate the need for complex optimization methods. Furthermore, the idea of performance recovery is introduced to analyze the ability of PSOA's performance under uncertain structural parameters. It was shown

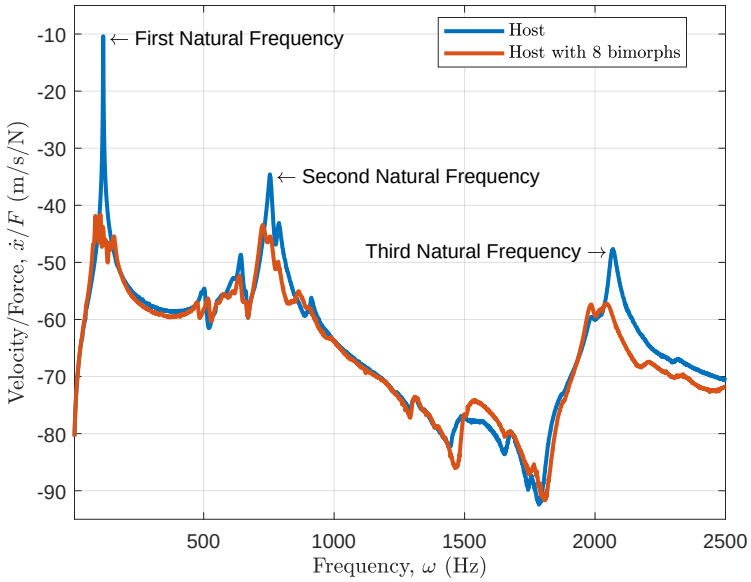

Figure 2.22: Broadband experimental FRF from base acceleration to the tip velocity of the host structure with 8 oscillator PSOA. The FRF shows that the modal spillover across a large frequency range is minimal. Additionally, the second and the third natural frequencies are also attenuated.

experimentally that for limited levels of uncertainty, passive capacitance tuning could recover the PSOA's flat frequency bandwidth after loss due to uncertainty. The tuning techniques described in this chapter are limited to passive methods. As a topic of future study, it would be of interest to analyze how active circuits can also be implemented to tune the PSOAs adaptively.

A Thermodynamic Variational Principles

Modeling of piezoelectric systems has been studied for decades, and various methods have been developed to model linear as well as nonlinear piezoelectric systems. Even though Newtonian techniques can be used to model piezoelectric systems [82], variational principles provide a systematic approach to derive consistent equations of motion when they are subject to nontrivial boundary conditions or couples to other electromechanical systems. In our

problem the piezoelectric systems are attached to shunt circuits with resistors and capacitors. The variational principles for the piezoelectric system involve a modified form of classical Hamilton's principle [81, 82, 84, 85, 86, 87, 88, 89, 90, 91]. The classical form of Hamilton's principle [82, 92] states that any trajectory in the mechanical configuration space must satisfy the variational identity

$$\delta \int_{t_0}^{t_1} (T - \mathcal{V}) dt + \int_{t_0}^{t_1} \delta W_{nc} dt = 0, \tag{2.33}$$

where T is the kinetic energy of the system, $\mathcal{V}$ is the potential energy of the system and δW_{nc} is the virtual work done by the nonconservative mechanical forces acting on the system. The variational formulations for piezoelectric systems use a modified form of Equation 2.33 and are expressed in terms of electric enthalpy density $\mathcal{H}$ or the internal energy density $\mathcal{U}$. The equivalence of the two variational principles is discussed using a simple example in [84].

A.1 $\mathcal{H}$ Variational Principle

According to the $\mathcal{H}$ variational principle, the actual motion of a piezoelectric system attached to a shunt circuit with a resistor, capacitor and current source in parallel must satisfy the variational identity

$$\delta \int_{t_0}^{t_1} (T - \mathcal{V}_{\mathcal{H}}) dt + \int_{t_0}^{t_1} \delta W_{\mathcal{H},nc} dt = 0 \tag{2.34}$$

for all admissible variations of the actual electromechanical trajectory. In Equation 2.34, T is the kinetic energy and $\mathcal{V}_{\mathcal{H}}$ is the electromechanical potential. It includes the potential energy of linearly elastic components and the contribution of the electrical enthalpy. The term δW_{nc} is the nonconservative virtual work done by the electromechanical loads on the

system. The contribution of electric enthalpy to the electromechanical potential is expressed in the form

$$\mathcal{V}_{\mathcal{H}} := \int_{\Omega} \mathcal{H} d\Omega - \frac{1}{2} \sum_{i} \mathcal{C}_i V_i^2. \tag{2.35}$$

In Equation 2.35, $\mathcal{H}$ is the electric enthalpy density of the piezoelectric continua Ω, $\mathcal{C}_i$ is the capacitance of the i^{th} capacitor in the shunt circuit, and V_i is the voltage across the i^{th} shunt circuit. The virtual work done by the nonconservative terms in a piezoelectric system attached to a shunt circuit has the form

$$\delta W_{\mathcal{H},nc} = \delta W_{nc} + \sum_{j} i_j \delta \lambda_j - \sum_{k} \frac{\dot{\lambda}_k}{R_k} \delta \lambda_k, \tag{2.36}$$

where δW_{nc} is the virtual work term shown in Equation 2.33 and λ_k is the flux linkage across the shunt circuit. The terms $\sum_j i_j \delta \lambda_j$ and $-\sum_k \frac{\dot{\lambda}_k}{R_k} \delta \lambda_k$ represent the virtual work contributions from the current source with current output i_k and the resistor with resistance R_k, respectively. The equations of motion obtained using this variational principle are expressed in terms of displacements and voltage/flux linkage as the generalized coordinates.

A.2 $\mathcal{U}$ Variational Principle

The second variational principle used in this chapter is the $\mathcal{U}$ variational principle. It is expressed in terms of internal energy density of the system. According to this principle, the actual motion of a electromechanical system must satisfy the variational statement

$$\delta \int_{t_0}^{t_1} (T - \mathcal{V}_{\mathcal{U}}) dt + \int_{t_0}^{t_1} \delta W_{\mathcal{U},nc} dt = 0 \tag{2.37}$$

for all admissible variations of the actual electromechanical trajectory. In Equation 2.37, T is the kinetic energy, $\mathcal{V}_{\mathcal{U}}$ is the electromechanical potential defined in terms of the internal energy density and $\delta W_{\mathcal{U},nc}$ is the nonconservative work done by the system. The expression for $\mathcal{V}_{\mathcal{U}}$ has the form

$$\mathcal{V}_{\mathcal{U}} := \int_{\Omega} \mathcal{U} d\Omega + \frac{1}{2} \sum_{i} \frac{1}{\mathcal{C}_i} Q_i^2, \tag{2.38}$$

where $\mathcal{U}$ is the internal energy density of the piezoelectric continua Ω, $\mathcal{C}_i$ is the capacitance of the i^{th} capacitor in the shunt circuit, and Q_i is the charge flowing through the shunt circuit. The virtual work done $\delta W_{\mathcal{U},nc}$ is expressed in the form

$$\delta W_{\mathcal{U},nc} = \delta W_{nc} + \sum_{j} V_j \delta Q_j - \sum_{k} R_k \dot{Q}_k \delta Q_k, \tag{2.39}$$

where δW_{nc} is the virtual work done shown in Equation 2.33 and Q_k is the charge flowing through the shunt circuit. The terms $\sum_j V_j \delta Q_j$ and $-\sum_k R_k \dot{Q}_k \delta Q_k$ represent the virtual work contributions from the voltage source V_k and the resistor of resistance R_k respectively. The equations of motion derived using this variational principle are expressed in terms of the displacements and charge as the generalized coordinates.

B Kinetic Energy of a PSOA

The kinetic energy of a PSOA attached to a host structure is given in Equation 2.4. Using separation of variables and Galerkin approximation, an approximation of the transverse displacement of each appendage is constructed as $w_i(x,t) = \sum_{j=1}^{n} \Psi_{ij}(x) W_{ij}(t) = \boldsymbol{\Psi}_i^T(x) \boldsymbol{W}_i(t)$. Substitution of the approximation into the expression for kinetic energy of the distributed

mass of each appendage results in

$$
\begin{aligned}
T_i &:= \frac{1}{2}\int_0^{L_i} \rho_i A_i \left((\dot{x}_p - \dot{\mathfrak{z}}) + \dot{\boldsymbol{W}}_i^T \boldsymbol{\Psi}_i\right)\left((\dot{x}_p - \dot{\mathfrak{z}}) + \boldsymbol{\Psi}_i^T \dot{\boldsymbol{W}}_i\right) dx_i, \\
&= \frac{1}{2}\Bigg(\underbrace{\int_0^{L_i} \rho_i A_i dx_i}_{\mathcal{M}_i}(\dot{x}_p - \dot{\mathfrak{z}})^2 + 2\underbrace{\int_0^{L_i} \rho_i A_i \boldsymbol{\Psi}_i^T dx_i}_{\boldsymbol{\mathcal{M}}_{ip}^T}\dot{\boldsymbol{W}}_i(\dot{x}_p - \dot{\mathfrak{z}}) + \dot{\boldsymbol{W}}_i^T \underbrace{\int_0^{L_i} \rho_i A_i \boldsymbol{\Psi}_i \boldsymbol{\Psi}_i^T dx_i}_{\boldsymbol{\mathcal{M}}_{ii}}\dot{\boldsymbol{W}}_i\Bigg), \\
&= \frac{1}{2}\Bigg(\mathcal{M}_i(\dot{x}_p - \dot{\mathfrak{z}})^2 + 2\boldsymbol{\mathcal{M}}_{ip}^T \dot{\boldsymbol{W}}_i(\dot{x}_p - \dot{\mathfrak{z}}) + \dot{\boldsymbol{W}}_i^T \boldsymbol{\mathcal{M}}_{ii}\dot{\boldsymbol{W}}_i\Bigg). \qquad (2.40)
\end{aligned}
$$

Similarly, substitution of the approximation of the transverse displacement into the expression for kinetic energy of the tip mass of each appendage results in

$$
\begin{aligned}
T_i &= \frac{1}{2} m_i \Bigg((\dot{x}_p - \dot{\mathfrak{z}}) + \dot{\boldsymbol{W}}_i^T \boldsymbol{\Psi}_i(L_i)\Bigg)\Bigg((\dot{x}_p - \dot{\mathfrak{z}}) + \boldsymbol{\Psi}_i^T(L_i)\dot{\boldsymbol{W}}_i\Bigg), \\
&= \frac{1}{2}\Bigg(m_i(\dot{x}_p - \dot{\mathfrak{z}})^2 + 2\underbrace{m_i \boldsymbol{\Psi}_i^T(L_i)}_{\boldsymbol{m}_{ip}^T}\dot{\boldsymbol{W}}_i(\dot{x}_p - \dot{\mathfrak{z}}) + \dot{\boldsymbol{W}}_i^T \underbrace{m_i \boldsymbol{\Psi}_i(L_i)\boldsymbol{\Psi}_i^T(L_i)}_{\boldsymbol{m}_{ii}}\dot{\boldsymbol{W}}_i\Bigg), \\
&= \frac{1}{2}\Bigg(m_i(\dot{x}_p - \dot{\mathfrak{z}})^2 + 2\boldsymbol{m}_{ip}^T \dot{\boldsymbol{W}}_i(\dot{x}_p - \dot{\mathfrak{z}}) + \dot{\boldsymbol{W}}_i^T \boldsymbol{m}_{ii}\boldsymbol{W}_i\Bigg). \qquad (2.41)
\end{aligned}
$$

Thus, the total kinetic energy of the system is expressed as

$$
\begin{aligned}
T &= \frac{1}{2} m_p(\dot{x}_p - \dot{\mathfrak{z}})^2 + \sum_{i=1}^{N} \frac{1}{2}\Bigg(\underbrace{(\mathcal{M}_i + m_i)}_{M_i}(\dot{x}_p - \dot{\mathfrak{z}})^2 + 2\underbrace{(\boldsymbol{\mathcal{M}}_{ip} + \boldsymbol{m}_{ip})}_{\boldsymbol{M}_{ip}}{}^T \dot{\boldsymbol{W}}_i^T(\dot{x}_p - \dot{\mathfrak{z}}) \\
&\qquad + \dot{\boldsymbol{W}}^T \underbrace{(\boldsymbol{\mathcal{M}}_{ii} + \boldsymbol{m}_{ii})}_{\boldsymbol{M}_{ii}}\dot{\boldsymbol{W}}\Bigg), \\
&= \frac{1}{2} m_p(\dot{x}_p - \dot{\mathfrak{z}})^2 + \sum_{i=1}^{N} \frac{1}{2}\Bigg(M_i(\dot{x}_p - \dot{\mathfrak{z}})^2 + 2\boldsymbol{M}_{ip}^T \dot{\boldsymbol{W}}_i(\dot{x}_p - \dot{\mathfrak{z}}) + \dot{\boldsymbol{W}}^T \boldsymbol{M}_{ii}\dot{\boldsymbol{W}}_i\Bigg), \\
&= \frac{1}{2} M_{pp}(\dot{x}_p - \dot{\mathfrak{z}})^2 + \sum_{i=1}^{N} \frac{1}{2}\Bigg(2\boldsymbol{M}_{ip}^T \dot{\boldsymbol{W}}_i(\dot{x}_p - \dot{\mathfrak{z}}) + \dot{\boldsymbol{W}}^T \boldsymbol{M}_{ii}\dot{\boldsymbol{W}}_i\Bigg), \qquad (2.42)
\end{aligned}
$$

where $M_{pp} := m_p + \sum_{i=1}^{N} M_i$.

C Electromechanical Potential of a PSOA

The total electromechanical potential of the system shown in Figure 2.4 can be calculated using Equation 2.35. However, as evident from the electric enthalpy density expression given in Equation 2.6, the electric field E_i has to be calculated before proceeding further. The curl of the electric field across the bimorph beam is approximated as zero in the electrostatic approximation in linear piezoelectricity. Hence, electric field is expressed in the form $E_i(x_i, y_i, z_i) := -\frac{\delta \phi_i}{\delta z_i}$, where ϕ_i is the electric potential function. From the assumption of linear variation of potential across the piezoelectric patch, it follows that

$$E_i = \begin{cases} \frac{V_i}{t_{p,i}} & (x_i, y_i, z_i) \in \text{bottom patch}, \\ -\frac{V_i}{t_{p,i}} & (x_i, y_i, z_i) \in \text{top patch}, \\ 0 & \text{otherwise}. \end{cases} \tag{2.43}$$

In Equation 2.43, V_i and $t_{p,i}$ are the voltage across and thickness of the piezoelectric patch of the i^{th} oscillator in the PSOA. The electromechanical potential can now be expressed using Equation 2.35. It has the form

$$\begin{aligned} \mathcal{V}_{\mathcal{H}i} =& \frac{1}{2}\int_0^{L_i}\left(\int\int C_i^E z_i^2 dy_i dz_i\right)\left(\frac{\partial^2 w_i}{\partial x_i^2}\right)^2 dx_i + \int_0^{L_i}\left(\int\int e_i z_i E_i dy_i dz_i\right)\frac{\partial^2 w_i}{\partial x_i^2} dx_i \\ & - \frac{1}{2}\int_0^{L_i}\left(\int\int \epsilon_i^S E_i^2 dy_i dz_i\right) dx_i - \frac{1}{2}\mathcal{C}_i V_i^2. \end{aligned} \tag{2.44}$$

Assuming the material stiffness to be uniform in the y and z direction, the term $\int\int C_i^E z_i^2 dy_i dz_i$ simplifies to $C_i^E I_i$ where I_i is the area moment of inertia of piezoelectric beam i. Defining the terms $\kappa_i := \kappa_{Ti} - \kappa_{Bi}$ with $\kappa_{Ti} := \int\int_{A_T} z_i dy_i dz_i$ for the top piezoelectric patch and $\kappa_{B_i} := \int\int_{A_B} z_i dy_i dz_i$ for the bottom piezoelectric patch simplifies the expression for the

electromechanical potential to

$$\mathcal{V}_{\mathcal{H}i} = \frac{1}{2}\int_0^{L_i} C_i^E I_i \left(\frac{\partial^2 w_i}{\partial x_i^2}\right)^2 dx_i - \int_0^{L_i} \frac{e_i \kappa_i}{t_{p,i}} \chi_{[a_i,b_i]} \frac{\partial^2 w_i}{\partial x_i^2} dx_i V_i(t) - \frac{1}{2}\frac{\epsilon_i^S 2A_{p,i}(b_i - a_i)}{t_{p,i}^2} V_i^2 - \frac{1}{2}\mathcal{C}_i V_i^2. \tag{2.45}$$

As shown in Figure 2.5, a_i and b_i in the above equation are the left and right piezoelectric patch coordinates, respectively. The piezoelectric cross sectional area is defined as $A_{p,i} := t_{p,i} \cdot \mathcal{W}_i$, where $t_{p,i}$ and $\mathcal{W}_i$ are the thickness and width of the piezoelectric patch, respectively. The function $\chi_{[a_i,b_i]}$ in the Equation 2.45 is called the characteristic function and is defined as

$$\chi_{[a_i,b_i]}(x) := \begin{cases} 1, & \text{if } x \in [a_i, b_i], \\ 0, & \text{otherwise.} \end{cases} \tag{2.46}$$

Substituting the Galerkin approximation for transverse displacement of each substructure $w_i = \sum_{i=1}^n \Psi_i(x) W_i(t) = \boldsymbol{\Psi}_i(x)\boldsymbol{W}_i(t)$ into the above expression generates the expression

$$\mathcal{V}_{\mathcal{H}i} = \frac{1}{2}\boldsymbol{W}_i^T \boldsymbol{K}_{ii} \boldsymbol{W}_i - \boldsymbol{B}_i^T \boldsymbol{W}_i V_i - \frac{1}{2} D_i V_i^2 - \frac{1}{2}\mathcal{C}_i V_i^2, \tag{2.47}$$

where

$$\boldsymbol{K}_{ii} := \int_0^{L_i} C_i^E I_i \boldsymbol{\Psi}_i'' \boldsymbol{\Psi}_i^{'',T} dx_i, \quad \boldsymbol{B}_i^T := \int_0^{L_i} \frac{\kappa_i e_i}{t_{p,i}} \chi_{[a_i,b_i]} \boldsymbol{\Psi}_i^{'',T} dx_i, \quad D_i := \frac{\epsilon_i^S 2A_{p,i}(b_i - a_i)}{t_{p,i}^2}. \tag{2.48}$$

D Host Structure with a PSOA Model

In this section, the steps involved in deriving the equation of motion of a PSOA attached to a host structure are given. Further simplification of the above expressions in Equations 2.4, 2.7 and 2.9 is achieved by introducing the block vectors and matrices

$$\mathbb{W} := \left\{ \begin{array}{ccc} \boldsymbol{W}_1 & \dots & \boldsymbol{W}_N \end{array} \right\}^T, \quad \mathbb{V} := \left\{ \begin{array}{ccc} V_1 & \dots & V_N \end{array} \right\}^T, \quad \mathbb{i} := \left\{ \begin{array}{ccc} \boldsymbol{i}_1 & \dots & \boldsymbol{i}_N \end{array} \right\}^T,$$
$$\mathbb{\Lambda} := \left\{ \begin{array}{ccc} \boldsymbol{\lambda}_1 & \dots & \boldsymbol{\lambda}_N \end{array} \right\}^T, \quad \mathbb{M}_p := \left\{ \begin{array}{ccc} \boldsymbol{M}_{1p} & \dots & \boldsymbol{M}_{Np} \end{array} \right\}^T, \tag{2.49}$$

$$\begin{aligned} \mathbb{M} &:= \text{diag}(\boldsymbol{M}_{11}, \boldsymbol{M}_{22}, \dots, \boldsymbol{M}_{NN}), \quad \mathbb{B} := \text{diag}(\boldsymbol{B}_1, \boldsymbol{B}_2, \dots, \boldsymbol{B}_N), \\ \mathbb{K} &:= \text{diag}(\boldsymbol{K}_{11}, \boldsymbol{K}_{22}, \dots, \boldsymbol{K}_{NN}), \quad \mathbb{D} := \text{diag}(D_1, D_2, \dots, D_N), \\ \boldsymbol{\zeta} &:= diag\left(\frac{1}{R_1}, \frac{1}{R_2}, ..., \frac{1}{R_N}\right) \quad \boldsymbol{\mathcal{C}} := diag\left(\mathcal{C}_1, \mathcal{C}_2, ..., \mathcal{C}_N\right). \end{aligned} \tag{2.50}$$

The final equation for kinetic energy, electromechanical potential energy and virtual work done then has the form

$$T = \frac{1}{2}(M_{pp}\left(\dot{x}_p - \dot{\mathfrak{z}}\right)^2 + 2\left(\dot{x}_p - \dot{\mathfrak{z}}\right)\mathbb{M}_p^T\dot{\mathbb{W}} + \dot{\mathbb{W}}^T\mathbb{M}\mathbb{W}), \tag{2.51}$$

$$\mathcal{V}_{\mathcal{H}} = \frac{1}{2}(K_p x_p^2 + \mathbb{W}^T\mathbb{K}\mathbb{W} - 2\mathbb{V}^T\mathbb{B}^T\mathbb{W} - \mathbb{V}^T\mathbb{D}\mathbb{V} - \mathbb{V}^T\boldsymbol{\mathcal{C}}\mathbb{V}), \tag{2.52}$$

$$\begin{aligned} \delta W_{nc} &= F_p\delta\left(x_p - \mathfrak{z}\right) + \mathbb{i}^T\delta\mathbb{\Lambda} - \dot{\mathbb{\Lambda}}^T\boldsymbol{\zeta}\delta\mathbb{\Lambda} - \delta\boldsymbol{q}^T\boldsymbol{C}\dot{\boldsymbol{q}}, \\ &= F_p\delta\left(x_p - \mathfrak{z}\right) + \mathbb{i}^T\delta\mathbb{\Lambda} - \dot{\mathbb{\Lambda}}^T\boldsymbol{\zeta}\delta\mathbb{\Lambda} - \delta x_p C_p\dot{x}_p - \delta\mathbb{W}^T\mathbb{C}\dot{\mathbb{W}}. \end{aligned} \tag{2.53}$$

The $\mathcal{H}$ variational principle can now be applied to derive the equations of motion of host structure attached to the PSOA. Recall that the equations of motion must satisfy the $\mathcal{H}$ variational principle we discussed in Subsection A.1. After substituting T, $\mathcal{V}_{\mathcal{H}}$ and δW_{nc} into Equation 2.34, the variational statement yields

$$\begin{aligned}
&\int_{t_0}^{t_1}\Big\{M_{pp}\left(\dot{x}_p-\dot{\mathfrak{z}}\right)\delta\left(\dot{x}_p-\dot{\mathfrak{z}}\right)+\mathbb{M}_p^T\dot{\mathbb{W}}\delta\left(\dot{x}_p-\dot{\mathfrak{z}}\right)+\left(\dot{x}_p-\dot{\mathfrak{z}}\right)\mathbb{M}_p^T\delta\dot{\mathbb{W}}+\delta\dot{\mathbb{W}}^T\mathbb{M}\dot{\mathbb{W}}\Big\}dt\\
&\quad-\int_{t_0}^{t_1}\Big\{\delta\mathbb{W}^T\mathbb{K}\mathbb{W}-\delta\mathbb{V}^T\mathbb{B}^T\mathbb{W}-\delta\mathbb{W}^T\mathbb{B}\mathbb{V}-\delta\mathbb{V}^T\mathbb{D}\mathbb{V}-\delta\mathbb{V}^T\boldsymbol{\mathcal{C}}\mathbb{V}+K_px_p\delta x_p\Big\}dt\\
&\quad+\int_{t_0}^{t_1}\Big\{F_p\delta\left(x_p-\mathfrak{z}\right)-\dot{\mathbb{\Lambda}}^T\boldsymbol{\zeta}\delta\mathbb{\Lambda}-\delta\mathbb{W}^T\mathbb{C}\dot{\mathbb{W}}-\delta x_pC_p\dot{x}_p+\mathbb{i}^T\delta\mathbb{\Lambda}\Big\}dt=0.
\end{aligned}\tag{2.54}$$

The base motion $\mathfrak{z}$ is a prescribed input for this system. Hence, we have $\delta(x_p-\mathfrak{z})=\delta x_p$. Rearranging the terms in the above expression and integration by parts results in the variational expression

$$\begin{aligned}
\int_{t_0}^{t_1}\Big\{&\delta x_p\Big(-M_{pp}\left(\ddot{x}_p-\ddot{\mathfrak{z}}\right)-\mathbb{M}_p\ddot{\mathbb{W}}-C_p\dot{x}_p-K_px_p+F_p\Big)\\
&+\delta\mathbb{W}^T\Big(-\mathbb{M}_p\left(\ddot{x}_p-\ddot{\mathfrak{z}}\right)-\mathbb{M}\ddot{\mathbb{W}}-\mathbb{C}\dot{\mathbb{W}}-\mathbb{K}\mathbb{W}+\mathbb{B}\mathbb{V}\Big)\\
&+\delta\mathbb{\Lambda}^T\Big(-\mathbb{B}^T\dot{\mathbb{W}}-\mathbb{D}\dot{\mathbb{V}}-\boldsymbol{\zeta}\dot{\mathbb{\Lambda}}+\mathbb{i}-\boldsymbol{\mathcal{C}}\dot{\mathbb{V}}\Big)\Big\}dt\\
&+\text{variational BCs}=0,
\end{aligned}\tag{2.55}$$

which must hold for all admissible variations δx_p, $\delta\mathbb{W}$ and $\delta\mathbb{\Lambda}$. It is shown in [82] that the variational boundary conditions above are zero. Finally, the equations of motion of the system under consideration are

$$\begin{bmatrix}\mathbb{M}&\mathbb{M}_p\\ \mathbb{M}_p^T&M_{pp}\end{bmatrix}\begin{Bmatrix}\ddot{\mathbb{W}}\\ \ddot{x}_p-\ddot{\mathfrak{z}}\end{Bmatrix}+\begin{bmatrix}\mathbb{C}&\mathbf{0}\\ \mathbf{0}^T&C_p\end{bmatrix}\begin{Bmatrix}\dot{\mathbb{W}}\\ \dot{x}_p\end{Bmatrix}+\begin{bmatrix}\mathbb{K}&\mathbf{0}\\ \mathbf{0}^T&K_p\end{bmatrix}\begin{Bmatrix}\mathbb{W}\\ x_p\end{Bmatrix}-\begin{bmatrix}\mathbb{B}\\ \mathbf{0}\end{bmatrix}\mathbb{V}=\begin{bmatrix}\mathbf{0}\\ F_{p_2}\end{bmatrix},\tag{2.56}$$

or

$$\begin{bmatrix} \mathbb{M} & \mathbb{M}_p \\ \mathbb{M}_p^T & M_{pp} \end{bmatrix} \begin{Bmatrix} \ddot{\mathbb{W}} \\ \ddot{x}_p \end{Bmatrix} + \begin{bmatrix} \mathbb{C} & \mathbf{0} \\ \mathbf{0}^T & C_p \end{bmatrix} \begin{Bmatrix} \dot{\mathbb{W}} \\ \dot{x_p} \end{Bmatrix} + \begin{bmatrix} \mathbb{K} & \mathbf{0} \\ \mathbf{0}^T & K_p \end{bmatrix} \begin{Bmatrix} \mathbb{W} \\ x_p \end{Bmatrix} - \begin{bmatrix} \mathbb{B} \\ \mathbf{0} \end{bmatrix} \mathbb{V} = \begin{bmatrix} \hat{F}_{p_1} \\ \hat{F}_{p_2} \end{bmatrix}, \tag{2.57}$$

where $\hat{F}_{p_1} = \mathbb{M}_p \ddot{\mathfrak{z}}$, $\hat{F}_{p_2} = F_p + M_{pp}\ddot{\mathfrak{z}}$ and

$$\mathbb{B}^T \dot{\mathbb{W}} + \mathbb{D}\dot{\mathbb{V}} + \boldsymbol{\zeta}\dot{\mathbb{\lambda}} - \mathbb{i} + \boldsymbol{\mathcal{C}}\dot{\mathbb{V}} = \mathbf{0}. \tag{2.58}$$

E Closed Form Expression for Frequency Response Function

The current section is focused on deriving the frequency response function from the force input F_p to the displacement x_p of the primary structure. The transfer function from the force input to the displacement of a host structure attached to a PSOA with capacitive shunt is given by Equation 2.15. Evaluating this transfer function along the imaginary axis can find the required FRF. However, we seek a FRF that is similar in form to the expression in Equation 2.1 [11]. To achieve this, we introduce a change of variables

$$\begin{Bmatrix} \mathbb{W} \\ x_p \end{Bmatrix} = \underbrace{\begin{bmatrix} I & -\boldsymbol{\alpha} \\ \mathbf{0}^T & 1 \end{bmatrix}}_{\Gamma} \begin{Bmatrix} \mathbb{X}_s \\ x_p \end{Bmatrix} \tag{2.59}$$

in Equation 2.15 and premultiply the same equation by Γ^T. This change in variables removes the mass coupling in the transfer function. In Equation 2.59, $\boldsymbol{\alpha} := \mathbb{M}^{-1}\mathbb{M}_p$, and $\mathbb{X}_s$ is analogous to the absolute displacement of the piezoelectric beam. After the change in

variables in Equation 2.15, we have

$$\begin{bmatrix} \mathbb{M}s^2 + \mathbb{C}s + \hat{\mathbb{K}} & -(\mathbb{C}s + \hat{\mathbb{K}})\boldsymbol{\alpha} \\ -((\mathbb{C}s + \hat{\mathbb{K}})\boldsymbol{\alpha})^T & \bar{M}_{pp}s^2 + \bar{C}_p s + \bar{K}_p \end{bmatrix} \begin{Bmatrix} \mathbb{X}_s \\ x_p \end{Bmatrix} = \begin{Bmatrix} \mathbf{0} \\ f_p(s) \end{Bmatrix}, \tag{2.60}$$

where the terms $\bar{M}_{pp}$, $\bar{C}_p$, $\bar{K}_p$ have the definitions $\bar{M}_{pp} := (M_{pp} - \boldsymbol{\alpha}^T \mathbb{M}_p)$, $\bar{C}_p := (C_p + \boldsymbol{\alpha}^T \mathbb{C}\boldsymbol{\alpha})$, $\bar{K}_p := (K_p + \boldsymbol{\alpha}^T \hat{\mathbb{K}}\boldsymbol{\alpha})$. From Equation 2.60, we have the relations

$$\mathbb{X}_s = (\mathbb{M}s^2 + \mathbb{C}s + \hat{\mathbb{K}})^{-1}(\mathbb{C}s + \hat{\mathbb{K}})\boldsymbol{\alpha} x_p, \tag{2.61}$$

$$-((\mathbb{C}s + \hat{\mathbb{K}})\boldsymbol{\alpha})^T \mathbb{X}_s + [\bar{M}_{pp}s^2 + \bar{C}_p s + \bar{K}_p] x_p = f_p(s). \tag{2.62}$$

Equation 2.61 represents the relation between the motion of the primary mass and motion of the substructures. The transfer function from the applied force to the displacement of the primary structure is obtained by substituting Equation 2.61 into Equation 2.62. As is well known, using modal or Fourier shape functions yields matrices and sub-matrices $\mathbb{M}$, $\mathbb{K}$, $\mathbb{C}$, $\mathbb{B}$ and $\mathbb{D}$ that are diagonal. As defined in the earlier sections, the elements of $\mathbb{M}$, $\mathbb{M}_p$, $\mathbb{K}$, $\mathbb{C}$ and $\mathbb{B}$ are $\boldsymbol{M}_{nn}$, $\boldsymbol{M}_{np}$, $\boldsymbol{K}_{nn}$, $\boldsymbol{C}_{nn}$ and $\boldsymbol{B}_n$, respectively. With single mode approximation these elements reduce to scalars which are denoted by M_{nn}, M_{np}, K_{nn}, C_{nn} and B_n, respectively. With these assumptions, it is easier to derive the transfer function which is given by

$$\frac{x_p(s)}{f_p(s)} = \Bigg\{ M_{pp}s^2 + C_p s + K_p + \sum_{n=1}^{N} \left[-\alpha_n M_{np} s^2 + \alpha_n^2 C_{nn} s + \alpha_n^2 \hat{K}_{nn} - \frac{(C_{nn}\alpha_n s + \hat{K}_{nn}\alpha_n)^2}{M_{nn}s^2 + C_{nn}s + \hat{K}_{nn}} \right] \Bigg\}^{-1}. \tag{2.63}$$

The transfer function in the case of multi-mode approximation will look very similar to Equation 2.63 and can be derived using the same procedure shown above. Substituting

$s = i\omega$ into Equation 2.63 results in an expression for the frequency response function

$$\frac{x_p(i\omega)}{f_p(i\omega)} = \Bigg\{ -M_{pp}\omega^2 + iC_p\omega + K_p + \sum_{n=1}^{N} \left[\alpha_n M_{np}\omega^2 + \alpha_n^2 \left[iC_{nn}\omega + \hat{K}_{nn} - \frac{(iC_{nn}\omega + \hat{K}_{nn})^2}{-M_{nn}\omega^2 + iC_{nn}\omega + \hat{K}_{nn}} \right] \right] \Bigg\}^{-1}. \quad (2.64)$$

Bibliography

[1] Daniel J Inman. Engineering Vibration. *Vibration Fundamentals and Practice*, page 560, 2001. ISSN 0137 2614. doi: 10.1016/B978-0-12-387000-1.01001-9. URL http://www.mendeley.com/research/engineering-vibration/.

[2] L. Kitis, B.P. P Wang, and W.D. D Pilkey. Vibration reduction over a frequency range. *Journal of Sound and Vibration*, 89(4):559–569, 1983. ISSN 0022460X. doi: 10.1016/0022-460X(83)90357-7.

[3] Roberto Villaverde. Reduction seismic response with heavily-damped vibration absorbers. *Earthquake Engineering & Structural Dynamics*, 13(1):33–42, January 1985. ISSN 0098-8847. doi: 10.1002/eqe.4290130105. URL https://doi.org/10.1002/eqe.4290130105.

[4] A G Thompson. Optimum tuning and damping of a dynamic vibration absorber applied to a force excited and damped primary system. *Journal of Sound and Vibration*, 77(3): 403–415, 1981. ISSN 0022-460X. doi: https://doi.org/10.1016/S0022-460X(81)80176-9. URL http://www.sciencedirect.com/science/article/pii/S0022460X81801769.

[5] S E Randall, I I I Halsted D. M., and D L Taylor. Optimum Vibration Absorbers for Linear Damped Systems. *Journal of Mechanical Design*, 103(4):908–913, October 1981. ISSN 1050-0472. URL http://dx.doi.org/10.1115/1.3255005.

[6] E Pennestrí. AN APPLICATION OF CHEBYSHEV'S MINâ MAX CRITERION TO THE OPTIMAL DESIGN OF A DAMPED DYNAMIC VIBRATION ABSORBER. *Journal of Sound and Vibration*, 217(4):757–765, 1998. ISSN 0022-460X. doi: https:

//doi.org/10.1006/jsvi.1998.1805. URL http://www.sciencedirect.com/science/article/pii/S0022460X98918053.

[7] M Strasberg and D Feit. Vibration damping of large structures induced by attached small resonant structures. *The Journal of the Acoustical Society of America*, 99(1): 335–344, 1996. doi: 10.1121/1.414545. URL https://doi.org/10.1121/1.414545.

[8] Adnan Akay, Zhaoshun Xu, Antonio Carcaterra, and I. Murat Koc. Experiments on Vibration Absorption using Energy Sinks. *The Journal of the Acoustical Society of America*, 118(5):3043, 2005. ISSN 00014966. doi: 10.1121/1.2046767.

[9] Lei Zuo and Samir A. Nayfeh. Optimization of the Individual Stiffness and Damping Parameters in Multiple-Tuned-Mass-Damper Systems. *Journal of Vibration and Acoustics*, 127(1):77, 2005. ISSN 07393717. doi: 10.1115/1.1855929. URL http://vibrationacoustics.asmedigitalcollection.asme.org/article.aspx?articleid=1470725.

[10] A. Carcaterra, A. Akay, and C. Bernardini. Trapping of vibration energy into a set of resonators: Theory and application to aerospace structures. *Mechanical Systems and Signal Processing*, 26(1):1–14, 2012. ISSN 08883270. doi: 10.1016/j.ymssp.2011.05.005. URL http://dx.doi.org/10.1016/j.ymssp.2011.05.005.

[11] Joseph F Vignola, John A Judge, and Andrew J Kurdila. Shaping of a system's frequency response using an array of subordinate oscillators. *The Journal of the Acoustical Society of America*, 126(1):129–139, July 2009. ISSN 0001-4966. doi: 10.1121/1.3143783. URL http://asa.scitation.org.ezproxy.lib.vt.edu/doi/pdf/10.1121/1.3143783https://doi.org/10.1121/1.3143783.

[12] H T 1940-(Harvey Thomas) Banks, R C (Ralph Charles) Smith, and Y (Yun) Wang.

Smart material structures: modeling, estimation, and control. Wiley, Chichester;New York;Paris;. ISBN 9782225852145;9780471970248;0471970247;2225852146;.

[13] Roy R Craig and Andrew J Kurdila. *Fundamentals of structural dynamics*. John Wiley & Sons, 2006. ISBN 0471430447.

[14] Joseph Vignola, Aldo Glean, John Judge, and Teresa Ryan. Optimal Apparent Damping as a Function of the Bandwidth of an Array of Vibration Absorbers. *The Journal of the Acoustical Society of America*, 134:1067–1070, 2013. doi: 10.1121/1.4812777. URL https://doi.org/10.1121/1.4812777.

[15] Joseph Vignola, John Judge, John Sterling, Teresa Ryan, Andrew Kurdila, Sai Tej Paruchuri, and Aldo Glean. On the Use of Shunted Piezo Actuators for Mitigation of Distribution Errors in Resonator Arrays. In *Proceedings of the 22nd International Congress on Acoustics*, 2016.

[16] G. Maidanik. Induced Damping By a Nearly Continuous Distribution of Nearly Undamped Oscillators: Linear Analysis. *Journal of Sound and Vibration*, 240(4):717–731, 2001. ISSN 0022460X. doi: 10.1006/jsvi.2000.3262. URL http://linkinghub.elsevier.com/retrieve/pii/S0022460X00932620.

[17] R Nagem. Vibration Damping By a Continuous Distribution of Undamped Oscillators. *Journal of Sound and Vibration*, 207(3):429–434, 1997. ISSN 0022460X. doi: 10.1006/jsvi.1997.1162. URL http://linkinghub.elsevier.com/retrieve/pii/S0022460X97911627.

[18] Nesbitt W Hagood, Walter H Chung, and Andreas Von Flotow. Modelling of Piezoelectric Actuator Dynamics for Active Structural Control. *Journal of Intelligent Material Systems and Structures*, 1(3):327–354, July 1990. ISSN 1045-389X. doi: 10.1177/1045389X9000100305. URL https://doi.org/10.1177/1045389X9000100305.

[19] A J Fleming, S Behrens, and S O R Moheimani. Synthetic impedance for implementation of piezoelectric shunt-damping circuits. *Electronics Letters*, 36(18):1525–1526, 2000. ISSN 0013-5194 VO - 36. doi: 10.1049/el:20001083.

[20] A Tylikowski. Distributed Piezoelectric Vibration Absorbers. *ZAMM - Journal of Applied Mathematics and Mechanics / Zeitschrift für Angewandte Mathematik und Mechanik*, 80(S2):305–306, January 2000. ISSN 0044-2267. doi: 10.1002/zamm.20000801424. URL https://doi.org/10.1002/zamm.20000801424.

[21] A Tylikowski. Control of circular plate vibrations via piezoelectric actuators shunted with a capacitive circuit. *Thin-Walled Structures*, 39(1):83–94, 2001. ISSN 0263-8231. doi: https://doi.org/10.1016/S0263-8231(00)00055-0. URL http://www.sciencedirect.com/science/article/pii/S0263823100000550.

[22] J J (John J.) Granier, R J (R. Jason) Haundhausen, and G E (Gabriel E.) Gaytan. Passive modal damping with piezoelectric shunts. United States, 2001. URL https://www.osti.gov/servlets/purl/975785.

[23] M Al-Ahmad, N Rolland, and P . Rolland. Piezoelectric-based tunable microstrip shunt resonator. In *2006 Asia-Pacific Microwave Conference*, pages 653–656, 2006. ISBN 2165-4727 VO -. doi: 10.1109/APMC.2006.4429505.

[24] Filippo Casadei, Lorenzo Dozio, Massimo Ruzzene, and Kenneth A Cunefare. Periodic shunted arrays for the control of noise radiation in an enclosure. *Journal of Sound and Vibration*, 329(18):3632–3646, 2010. ISSN 0022-460X. doi: https://doi.org/10.1016/j.jsv.2010.04.003. URL http://www.sciencedirect.com/science/article/pii/S0022460X10002415.

[25] L Airoldi and M Ruzzene. Wave Propagation Control in Beams Through Periodic Multi-Branch Shunts. *Journal of Intelligent Material Systems and Structures*, 22(14):

1567–1579, September 2011. ISSN 1045-389X. doi: 10.1177/1045389X11408372. URL https://doi.org/10.1177/1045389X11408372.

[26] L Airoldi Ruzzene and M. Design of tunable acoustic metamaterials through periodic arrays of resonant shunted piezos. *New Journal of Physics*, 13(11):113010, 2011. ISSN 1367-2630. URL http://stacks.iop.org/1367-2630/13/i=11/a=113010.

[27] Gang Wang Wen, Shengbing Chen, and Jihong. Low-frequency locally resonant band gaps induced by arrays of resonant shunts with Antoniou's circuit: experimental investigation on beams. *Smart Materials and Structures*, 20(1):15026, 2011. ISSN 0964-1726. URL http://stacks.iop.org/0964-1726/20/i=1/a=015026.

[28] Benjamin S Beck, Kenneth A Cunefare, Manuel Collet, and Massimo Ruzzene. Active vibration control of a stiffened panel through application of negative capacitance shunts. In *Proc.SPIE*, volume 7977, April 2011. URL https://doi.org/10.1117/12.880418.

[29] O Thomas Deü, J Ducarne, and J-F. Performance of piezoelectric shunts for vibration reduction. *Smart Materials and Structures*, 21(1):15008, 2012. ISSN 0964-1726. URL http://stacks.iop.org/0964-1726/21/i=1/a=015008.

[30] Y Lu and J Tang. Electromechanical tailoring of structure with periodic piezoelectric circuitry. *Journal of Sound and Vibration*, 331(14):3371–3385, 2012. ISSN 0022-460X. doi: https://doi.org/10.1016/j.jsv.2012.02.029. URL http://www.sciencedirect.com/science/article/pii/S0022460X12001769.

[31] Filippo Casadei, Benjamin S Beck, Kenneth A Cunefare, and Massimo Ruzzene. Vibration control of plates through hybrid configurations of periodic piezoelectric shunts. *Journal of Intelligent Material Systems and Structures*, 23(10):1169–1177, May 2012. ISSN 1045-389X. doi: 10.1177/1045389X12443014. URL https://doi.org/10.1177/1045389X12443014.

[32] Shengbing Chen, Gang Wang, Jihong Wen, and Xisen Wen. Wave propagation and attenuation in plates with periodic arrays of shunted piezo-patches. *Journal of Sound and Vibration*, 332(6):1520–1532, 2013. ISSN 0022-460X. doi: https://doi.org/10.1016/j.jsv.2012.11.005. URL http://www.sciencedirect.com/science/article/pii/S0022460X12008383.

[33] Filippo Casadei and Katia Bertoldi. Wave propagation in beams with periodic arrays of airfoil-shaped resonating units. *Journal of Sound and Vibration*, 333(24):6532–6547, 2014. ISSN 0022-460X. doi: https://doi.org/10.1016/j.jsv.2014.07.008. URL http://www.sciencedirect.com/science/article/pii/S0022460X14005823.

[34] K M Guo and J Jiang. Independent modal resonant shunt for multimode vibration control of a truss-cored sandwich panel. *International Journal of Dynamics and Control*, 2(3):326–334, 2014. ISSN 2195-2698. doi: 10.1007/s40435-013-0036-7. URL https://doi.org/10.1007/s40435-013-0036-7.

[35] B Lossouarn, J-F Deü, M Aucejo, and K A Cunefare. Multimodal vibration damping of a plate by piezoelectric coupling to its analogous electrical network. *Smart Materials and Structures*, 25(11):115042, 2016. ISSN 0964-1726. doi: 10.1088/0964-1726/25/11/115042. URL http://dx.doi.org/10.1088/0964-1726/25/11/115042.

[36] W Larbi, J.-F. Deü, and R Ohayon. Finite element reduced order model for noise and vibration reduction of double sandwich panels using shunted piezoelectric patches. *Applied Acoustics*, 108:40–49, 2016. ISSN 0003-682X. doi: https://doi.org/10.1016/j.apacoust.2015.08.021. URL http://www.sciencedirect.com/science/article/pii/S0003682X15002443.

[37] B Lossouarn, M Aucejo, J.-F. Deü, and B Multon. Design of inductors with high inductance values for resonant piezoelectric damping. *Sensors and Actuators A: Physical*,

259:68–76, 2017. ISSN 0924-4247. doi: https://doi.org/10.1016/j.sna.2017.03.030. URL http://www.sciencedirect.com/science/article/pii/S0924424716309785.

[38] William W Clark. Semi-active vibration control with piezoelectric materials as variable-stiffness actuators. volume 3672, pages 3672–3678, 1999. URL https://doi.org/10.1117/12.349775.

[39] Claude Richard, Daniel Guyomar, David Audigier, and Gil Ching. Semi-passive damping using continuous switching of a piezoelectric device. volume 3672, pages 3672–3678, 1999. URL https://doi.org/10.1117/12.349773.

[40] William W. Clark. Vibration Control with State-Switched Piezoelectric Materials. *Journal of Intelligent Material Systems and Structures*, 11(4):263–271, April 2000. ISSN 1045-389X. doi: 10.1106/18CE-77K4-DYMG-RKBB. URL http://jim.sagepub.com/cgi/doi/10.1106/18CE-77K4-DYMG-RKBBhttps://doi.org/10.1106/18CE-77K4-DYMG-RKBB.

[41] Kenneth A Cunefare, Sergio de Rosa, Nader Sadegh, and Gregg Larson. State-Switched Absorber for Semi-Active Structural Control. *Journal of Intelligent Material Systems and Structures*, 11(4):300–310, April 2000. ISSN 1045-389X. doi: 10.1106/U0K2-70FU-DR0W-MWU3. URL https://doi.org/10.1106/U0K2-70FU-DR0W-MWU3.

[42] Ronald A Morgan and Kon-Well Wang. Multifrequency piezoelectric vibration absorber for variable frequency harmonic excitations. volume 4331, pages 4311–4331, 2001. URL https://doi.org/10.1117/12.432697.

[43] Mark Holdhusen, Kenneth Cunefare, and Gregg D Larson. Role of damping in state-switched absorber for vibration control. volume 4326, pages 4311–4326, 2001. URL https://doi.org/10.1117/12.436477.

[44] Kenneth A Cunefare. State-Switched Absorber for Vibration Control of Point-Excited Beams. *Journal of Intelligent Material Systems and Structures*, 13(2-3):97–105, February 2002. ISSN 1045-389X. doi: 10.1177/104538902761402495. URL https://doi.org/10.1177/104538902761402495.

[45] Mark H Holdhusen and Kenneth A Cunefare. Optimization of a state-switched absorber applied to a continuous vibrating system. volume 5386, pages 5310–5386, 2004. URL https://doi.org/10.1117/12.539876.

[46] A Badel, G Sebald, D Guyomar, M Lallart, E Lefeuvre, C Richard, and J Qiu. Piezoelectric vibration control by synchronized switching on adaptive voltage sources: Towards wideband semi-active damping. *The Journal of the Acoustical Society of America*, 119(5):2815–2825, April 2006. ISSN 0001-4966. doi: 10.1121/1.2184149. URL https://doi.org/10.1121/1.2184149.

[47] Dominik Niederberger and Manfred Morari. An autonomous shunt circuit for vibration damping. *Smart Materials and Structures*, 15(2):359–364, 2006. ISSN 0964-1726. doi: 10.1088/0964-1726/15/2/016. URL http://dx.doi.org/10.1088/0964-1726/15/2/016.

[48] Hongli Ji, Jinhao Qiu, Adrien Badel, and Kongjun Zhu. Semi-active Vibration Control of a Composite Beam using an Adaptive SSDV Approach. *Journal of Intelligent Material Systems and Structures*, 20(4):401–412, September 2008. ISSN 1045-389X. doi: 10.1177/1045389X08095182. URL https://doi.org/10.1177/1045389X08095182.

[49] Jinhao Qiu, Hongli Ji, and Kongjun Zhu. Semi-active vibration control using piezoelectric actuators in smart structures. *Frontiers of Mechanical Engineering in China*, 4(3):242–251, 2009. ISSN 1673-3592. doi: 10.1007/s11465-009-0068-z. URL https://doi.org/10.1007/s11465-009-0068-z.

[50] Hongli Ji. Semi-Active Vibration Control Based on Switched Piezoelectric Transducers. page Ch. 10. IntechOpen, Rijeka, 2010. doi: 10.5772/10146. URL https://doi.org/10.5772/10146.

[51] Jun Cheng, Hongli Ji, Jinhao Qiu, and Toshiyuki Takagi. Semi-active vibration suppression by a novel synchronized switch circuit with negative capacitance. *International Journal of Applied Electromagnetics & Mechanics*, 37(4):291–308, December 2011. ISSN 13835416. URL http://login.ezproxy.lib.vt.edu/login?url=http://search.ebscohost.com/login.aspx?direct=true{&}db=a9h{&}AN=67478657{&}site=eds-live{&}scope=site.

[52] Bilal Mokrani, Gonçalo Rodrigues, Burda Ioan, Renaud Bastaits, and Andre Preumont. Synchronized switch damping on inductor and negative capacitance. *Journal of Intelligent Material Systems and Structures*, 23(18):2065–2075, January 2012. ISSN 1045-389X. doi: 10.1177/1045389X11433493. URL https://doi.org/10.1177/1045389X11433493.

[53] Christopher L Davis, George Andre Lesieutre, and Jeffrey J Dosch. Tunable electrically shunted piezoceramic vibration absorber. In *Proceedings of SPIE*, volume 3045, pages 3045–3049, 1997. doi: 10.1117/12.274188. URL http://dx.doi.org/10.1117/12.274188.

[54] Christopher L Davis and George Andre Lesieutre. Actively tuned solid state piezoelectric vibration absorber. volume 3327, pages 3314–3327, 1998. URL https://doi.org/10.1117/12.310681.

[55] Christopher L Davis and George A Lesieutre. An Actively Tuned Solid-State Vibration Absorber Using Capacitive Shunting of Piezoelectric Stiffness. *Journal of Sound and Vibration*, 232(3):601–617, 2000. ISSN 0022-460X. doi: https://doi.org/10.

1006/jsvi.1999.2755. URL http://www.sciencedirect.com/science/article/pii/S0022460X99927554.

[56] Mark Holdhusen and Kenneth A Cunefare. Optimization of location and tuning of a state-switched absorber for controlling beam vibration. volume 5049, pages 5010–5049, 2003. URL https://doi.org/10.1117/12.484014.

[57] J Ducarne, O Thomas, and J.-F. Deü. Placement and dimension optimization of shunted piezoelectric patches for vibration reduction. *Journal of Sound and Vibration*, 331(14): 3286–3303, 2012. ISSN 0022-460X. doi: https://doi.org/10.1016/j.jsv.2012.03.002. URL http://www.sciencedirect.com/science/article/pii/S0022460X12001976.

[58] Luciano Pereira da Silva, Walid Larbi, and Jean-François Deü. Topology optimization of shunted piezoelectric elements for structural vibration reduction. *Journal of Intelligent Material Systems and Structures*, 26(10):1219–1235, June 2014. ISSN 1045-389X. doi: 10.1177/1045389X14538533. URL https://doi.org/10.1177/1045389X14538533.

[59] Na Kong, Dong Sam Ha, Alper Erturk, and Daniel J Inman. Resistive Impedance Matching Circuit for Piezoelectric Energy Harvesting. *Journal of Intelligent Material Systems and Structures*, 21(13):1293–1302, January 2010. ISSN 1045-389X. doi: 10.1177/1045389X09357971. URL https://doi.org/10.1177/1045389X09357971.

[60] Yaowen Yang and Lihua Tang. Equivalent Circuit Modeling of Piezoelectric Energy Harvesters. *Journal of Intelligent Material Systems and Structures*, 20(18):2223–2235, October 2009. ISSN 1045-389X. doi: 10.1177/1045389X09351757. URL https://doi.org/10.1177/1045389X09351757.

[61] David Charnegie. *FREQUENCY TUNING CONCEPTS FOR PIEZOELECTRIC CANTILEVER BEAMS*. PhD thesis, 2007.

[62] Xu Wang and Liwei Lin. Dimensionless optimization of piezoelectric vibration energy harvesters with different interface circuits. *Smart Materials and Structures*, 22(8), 2013. ISSN 09641726. doi: 10.1088/0964-1726/22/8/085011.

[63] Daniel Motter, Felipe Aguiar Dias, and Samuel Silva. Vibration Energy Harvesting Using Piezoelectric Transducer and Non- Controlled Rectifiers Circuits. 2006.

[64] A. Badel, D. Guyomar, E. Lefeuvre, and C. Richard. Efficiency enhancement of a piezoelectric energy harvesting device in pulsed operation by synchronous charge inversion. *Journal of Intelligent Material Systems and Structures*, 16(10):889–901, 2005. ISSN 1045389X. doi: 10.1177/1045389X05053150.

[65] S. Adhikari, M. I. Friswell, and D. J. Inman. Piezoelectric energy harvesting from broadband random vibrations. *Smart Materials and Structures*, 18(11), 2009. ISSN 09641726. doi: 10.1088/0964-1726/18/11/115005.

[66] Woon Kyung Kim. *Design and Analysis of Switching Circuits for Energy Harvesting in Piezostrutures*. PhD thesis, Virginia Polytechnic Institute and State University, 2012. URL http://search.proquest.com.ezproxy.lib.vt.edu/docview/1512629030?pq-origsite=summon{&}accountid=14826.

[67] Ryan Lee Harne. *The study and development of distributed devices for concurrent vibration attenuation and energy harvesting*. PhD thesis, 2012.

[68] Yu-Yin Chen, Dejan Vasic, Yuan-Ping Liu, and François Costa. Study of a piezoelectric switching circuit for energy harvesting with bistable broadband technique by work-cycle analysis. *Journal of Intelligent Material Systems and Structures*, 24(2):180–193, September 2012. ISSN 1045-389X. doi: 10.1177/1045389X12460339. URL https://doi.org/10.1177/1045389X12460339.

[69] G K Ottman, H F Hofmann, and G A Lesieutre. Optimized piezoelectric energy harvesting circuit using step-down converter in discontinuous conduction mode. *IEEE Transactions on Power Electronics*, 18(2):696–703, 2003. ISSN 0885-8993 VO - 18. doi: 10.1109/TPEL.2003.809379.

[70] Sheng-Bing Chen, Ji-Hong Wen, Gang Wang, Xiao-Yun Han, and Xi-Sen Wen. Locally Resonant Gaps of Phononic Beams Induced by Periodic Arrays of Resonant Shunts. *Chinese Physics Letters*, 28(9):94301, 2011. ISSN 0256-307X. doi: 10.1088/0256-307x/28/9/094301. URL http://dx.doi.org/10.1088/0256-307X/28/9/094301.

[71] Jian-Wei Wang, Gang Wang, Sheng-Bing Chen, and Ji-Hong Wen. Broadband Attenuation in Phononic Beams Induced by Periodic Arrays of Feedback Shunted Piezoelectric Patches. *Chinese Physics Letters*, 29(6):64302, 2012. ISSN 0256-307X. doi: 10.1088/0256-307x/29/6/064302. URL http://dx.doi.org/10.1088/0256-307X/29/6/064302.

[72] Sheng-Bing Chen, Ji-Hong Wen, Gang Wang, and Xi-Sen Wen. Tunable band gaps in acoustic metamaterials with periodic arrays of resonant shunted piezos. *Chinese Physics B*, 22(7):74301, 2013. ISSN 1674-1056. doi: 10.1088/1674-1056/22/7/074301. URL http://dx.doi.org/10.1088/1674-1056/22/7/074301.

[73] T L Huang, M N Ichchou, O A Bareille, M Collet, and M Ouisse. Multi-modal wave propagation in smart structures with shunted piezoelectric patches. *Computational Mechanics*, 52(3):721–739, 2013. ISSN 1432-0924. doi: 10.1007/s00466-013-0844-9. URL https://doi.org/10.1007/s00466-013-0844-9.

[74] Hao Zhang, Ji-Hong Wen, Sheng-Bing Chen, Gang Wang, and Xi-Sen Wen. Flexural wave band-gaps in phononic metamaterial beam with hybrid shunting circuits. *Chinese*

Physics B, 24(3):36201, 2015. ISSN 1674-1056. doi: 10.1088/1674-1056/24/3/036201. URL http://dx.doi.org/10.1088/1674-1056/24/3/036201.

[75] Ziyang Lian, Shan Jiang, Hongping Hu, Longxiang Dai, Xuedong Chen, and Wei Jiang. An Enhanced Plane Wave Expansion Method to Solve Piezoelectric Phononic Crystal with Resonant Shunting Circuits. *Shock and Vibration*, 2016, 2016. ISSN 10709622. doi: 10.1155/2016/4015363.

[76] K Yi, M Collet, M Ichchou, and L Li. Flexural waves focusing through shunted piezoelectric patches. *Smart Materials and Structures*, 25(7):75007, 2016. ISSN 0964-1726. doi: 10.1088/0964-1726/25/7/075007. URL http://dx.doi.org/10.1088/0964-1726/25/7/075007.

[77] C Sugino, S Leadenham, M Ruzzene, and A Erturk. An investigation of electroelastic bandgap formation in locally resonant piezoelectric metastructures. *Smart Materials and Structures*, 26(5):55029, 2017. ISSN 0964-1726. doi: 10.1088/1361-665x/aa6671. URL http://dx.doi.org/10.1088/1361-665X/aa6671.

[78] Shan Jiang, Longxiang Dai, Hao Chen, Hongping Hu, Wei Jiang, and Xuedong Chen. Folding beam-type piezoelectric phononic crystal with low-frequency and broad band gap. *Applied Mathematics and Mechanics*, 38(3):411–422, 2017. ISSN 1573-2754. doi: 10.1007/s10483-017-2171-7. URL https://doi.org/10.1007/s10483-017-2171-7.

[79] Christopher Sugino, Massimo Ruzzene, and Alper Erturk. Dynamics of Hybrid Mechanical-Electromechanical Locally Resonant Piezoelectric Metastructures, 2017. URL http://dx.doi.org/10.1115/SMASIS2017-3948.

[80] Gang Wang, Jianqing Cheng, Jingwei Chen, and Yunze He. Multi-resonant piezoelectric shunting induced by digital controllers for subwavelength elastic wave attenuation in smart metamaterial. *Smart Materials and Structures*, 26(2):25031, 2017.

ISSN 0964-1726. doi: 10.1088/1361-665x/aa53ea. URL http://dx.doi.org/10.1088/1361-665X/aa53ea.

[81] H. F. Tiersten. *Linear Piezoelectric Plate Vibrations*. Springer US, Boston, MA, 1969. ISBN 978-1-4899-6221-8. doi: 10.1007/978-1-4899-6453-3. URL http://link.springer.com/10.1007/978-1-4899-6453-3.

[82] Andrew J Kurdila and Pablo Tarazaga. *Vibrations of Linear Piezostructures (In press)*. John Wiley & Sons, Inc., 2018. ISBN 9781119393405.

[83] B de Marneffe and A Preumont. Vibration damping with negative capacitance shunts: theory and experiment. *Smart Materials and Structures*, 17(3):35015, 2008. ISSN 0964-1726. doi: 10.1088/0964-1726/17/3/035015. URL http://dx.doi.org/10.1088/0964-1726/17/3/035015.

[84] Sai Tej Paruchuri, Andrew J Kurdila, John Sterling, Amelia Vignola, John Judge, Joe Vignola, and Teresa Ryan. Thermodynamic Variational Formulations of Subordinate Oscillator Arrays (SOA) With Linear Piezoelectrics. In *ASME. International Design Engineering Technical Conferences and Computers and Information in Engineering Conference, Volume 8: 29th Conference on Mechanical Vibration and Noise ():V008T12A068.*, 2017. doi: 10.1115/DETC2017-68056. URL http://dx.doi.org/10.1115/DETC2017-68056.

[85] Sai Tej Paruchuri, John Sterling, Andrew Kurdila, and Joseph Vignola. Piezoelectric composite subordinate oscillator arrays and frequency response shaping for passive vibration attenuation. In *2017 IEEE Conference on Control Technology and Applications (CCTA)*, pages 702–707. IEEE, August 2017. ISBN 978-1-5090-2182-6. doi: 10.1109/CCTA.2017.8062544. URL http://ieeexplore.ieee.org/document/8062544/.

[86] A. Preumont. *Mechatronics: Dynamics of Electromechanical and Piezoelectric Systems*. Springer, Dordrecht, 2006. ISBN 1402046952. doi: 10.1007/1-4020-4696-0. URL https://link-springer-com.ezproxy.lib.vt.edu/book/10.1007{%}2F1-4020-4696-0{#}authorsandaffiliationsbook.

[87] Yi-Yuan Yu. *Vibrations of Elastic Plates*. Springer New York, New York, NY, 1996. ISBN 978-1-4612-7509-1. doi: 10.1007/978-1-4612-2338-2. URL http://link.springer.com/10.1007/978-1-4612-2338-2.

[88] Jiashi Yang. *An Introduction to the Theory of Piezoelectricity*, volume 9 of *Advances in Mechanics and Mathematics*. Springer, Boston, MA, Boston, 2005. ISBN 978-0-387-23573-8. doi: https://doi-org.ezproxy.lib.vt.edu/10.1007/b101799. URL http://link.springer.com/10.1007/b101799.

[89] Donald J L Leo. *Engineering Analysis of Smart Material Systems*. John Wiley & Sons, Inc., 2007. ISBN 9780471684770. doi: 10.1002/9780470209721. URL http://doi.wiley.com/10.1002/9780470209721.

[90] Dean C Karnopp, Donald L Margolis, and Ronald C Rosenberg. *System Dynamics: Modeling, Simulation, and Control of Mechatronic Systems*. 2012. ISBN 9781118152812. doi: 10.1002/9781118152812.fmatter.

[91] Alper Erturk and Daniel J. Inman. *Piezoelectric Energy Harvesting*. John Wiley & Sons, Ltd, Chichester, UK, April 2011. ISBN 9781119991151. doi: 10.1002/9781119991151. URL http://doi.wiley.com/10.1002/9781119991151.

[92] Leonard. Meirovitch. *Methods of analytical dynamics*. McGraw-Hill, New York, 1970. ISBN 0070414556 9780070414556.

Chapter 3

RKHS Embedding for Estimation of Nonlinearities in Piezoelectrics

Abstract

Nonlinearities in piezoelectric systems can arise from internal factors such as nonlinear constitutive laws or external factors like realizations of boundary conditions. It can be difficult or even impossible to derive detailed models from the first principles of all the sources of nonlinearity in a system. This chapter introduces adaptive estimator techniques to approximate the nonlinearities that can arise in certain classes of piezoelectric systems. Here an underlying structural assumption is that the nonlinearities can be modeled as continuous functions in a reproducing kernel Hilbert space (RKHS). This approach can be viewed as a data-driven method to approximate the unknown nonlinear system. This chapter introduces the theory behind the adaptive estimator, discusses precise conditions that guarantee convergence of the function estimates, and studies the effectiveness of this approach numerically for a class of nonlinear piezoelectric composite beams.

3.1 Introduction

Researchers have studied piezoelectric systems extensively over the past three decades for applications to classical problems like vibration attenuation, which is described in general

treatises like [1, 2, 3, 4], as well as modern problems like energy harvesting [5, 6]. Even though many of these studies model piezoelectric oscillators as linear systems, piezoelectric systems are often inherently nonlinear. At low input amplitudes, the effect of nonlinearity is ordinarily not very pronounced. However, linear models can fail to capture the dynamics of piezoelectric systems that undergo large displacements, velocities, accelerations, or electric field strengths. Researchers have consequently also developed nonlinear models for many examples of piezoelectric oscillators. A general account of nonlinear field theory as it arises in modeling piezoelectric continua can be found in [7, 8, 9], while reference [10] gives a good account of how active nonlinear piezostructural components are incorporated in typical plate or shell models.

Some of the models that are perhaps the most relevant to the system considered in this chapter are [11, 12, 13, 14, 15, 16, 17, 18, 19]. In these studies, researchers investigate case-specific models that include higher-order polynomial terms in the constitutive laws. The models in the above publications by [11, 12, 13, 14, 15, 16, 17, 18, 19] are representative of methods that include higher-order (polynomial) terms in the electric enthalpy density to construct nonlinear piezoelectric system models. Using the extended Hamilton's principle, Lagrange's equations, or Lagrange density methods then gives a corresponding set of nonlinear equations of motion. We can think of all of these methods, in general, as approximations of the constitutive laws in terms of power series expansions of the nonlinear term. These methods are powerful tools and have been successfully implemented to model nonlinearities in piezoelectric devices, as illustrated in the articles cited above. Such methods for studying nonlinear systems that make explicit use of power series approximations and polynomial classes of nonlinearities have a long history. A general discussion of the theory underlying these approaches for nonlinear systems can be found in well-known texts such as those by [20, 21] for nonlinear systems theory, or [22] on perturbation methods. Much of the anal-

ysis carried out in using these methods relies expressly on knowing the exact form of the governing nonlinearity. When such knowledge is available, strong conclusions regarding the stability, the nature of bifurcations, the possibility of internal or parametric resonance, or even chaotic response of the system can often be made.

Nonlinearities in piezoelectric systems are not just limited to polynomials nonlinearities discussed above. There is a rich collection of literature that study history dependent modeling in piezoelectric systems and can be broadly classified into (1) rate-dependent and (2) rate-independent methods. General accounts of the theory on history dependent models can be found in [23, 24]. The former class of modeling approaches focuses on the relationship between the input control and output displacement. Examples of these methods include the Preisach model ([25, 26, 27]), Prandtl-Ishlinskii model ([28, 29, 30, 31]), Krasnoselskii-Pokrovskii model ([32, 33, 34]), and Maxwell model ([35, 36]). In the latter category of history dependent models for piezoelectric systems, rate-dependent methods include the Bouc-Wen Hysteresis model ([37, 38, 39]), Dahl model ([40, 41]), Duhem model ([42, 43]). A review of all these methods can be found in [44]. Overall, it should be noted that the nature of history dependent models in the above references varies substantially, much more so than the models that feature polynomial nonlinearities that appear in an ordinary differential equation. The equations governing history dependence in piezoelectrics may be cast in terms of functional differential equations, differential inclusions, or in terms of history dependent operators depending on the reference.

The above methods are highly effective for modeling piezoelectric system behavior when we know the form of the underlying nonlinearities. However, it is not always easy to determine this knowledge with a high level of certainty. Even for the narrow class of polynomial nonlinearities in the electric enthalpy, the choice of which polynomial terms to include for a particular material at hand can be subtle. If the form of the polynomial nonlinearity is

known, then the classical methods of attack such as in [20, 21, 22] can and should be applied: these approaches provide a framework for very strong conclusions. When a system at hand is poorly understood, or even unknown, data-driven identification methods have been developed to address such cases. To be sure, these techniques primarily focus on different types of conclusions than the methods that rely on precise knowledge of the form of the uncertainty. Data-driven estimation methods focus on conditions that ensure the convergence of a function estimate to the true unknown function, rate of convergence of the estimation error, and the study of types of uncertainties that can be estimated. Data-driven methods for linear systems are well-known, well-documented, and are described in classical texts like [45]. Some of these methods have been encoded in commercially available packages such as, for example, the LMS PolyMAX software. Data-driven modeling approaches developed explicitly for nonlinear systems are an area of increasing interest and as of yet to be fully developed. Researchers have used system identifications methods to estimate the parameters in the above class of conventional nonlinear modeling approaches discussed above [46, 47, 48]. On the other hand, data-driven approaches have also been used as standalone methods to model nonlinear system behavior. One example of such a technique is the Dynamic Mode Decomposition (DMD) method, which approximates Koopman modes to model the inherent dynamics [49, 50, 51, 52, 53, 54]. Another example would be the use of machine learning methods to identify the underlying nonlinearities in piezoelectric systems [55, 56, 57, 58, 59].

In this chapter, we introduce a novel data-driven approach for estimating nonlinearities in piezoelectric systems. This approach is based on embedding the unknown nonlinear function appearing in the governing equation in a reproducing kernel Hilbert space (RKHS). The unknown function is subsequently estimated through adaptive parameter estimation. Identification methods that use RKHS have been studied for problems like terrain measurement [60], control of dynamical systems [61, 62, 63], sensor selection [64], and learning

spatiotemporally-evolving systems [65, 66]. In this chapter, we extend the methodology initially developed in [60] to nonlinear piezoelectric systems, which are a type of nonautonomous system. The advantages are as follows:

1. Under some conditions, this technique provides a bound on the error between the actual and estimated unknown function.

2. There is a geometric interpretation of the error estimate, in terms of the positive limit set of the system equations, that describes the subset over which convergence is guaranteed. This is a newly observed property of the RKHS embedding method.

3. This technique not only gives us a nonlinear model but also estimates the underlying nonlinear function over a subspace of the state space.

4. Since the primary assumption is that the nonlinear function belongs to an RKHS, this technique can be implemented for a large class of nonlinearities.

5. Unlike conventional modeling techniques, the explicit structure of the uncertainty in the nonlinearity does not influence the estimation approach. If some portion of the nonlinearity is known, this knowledge can be used and only the unknown part of the nonlinearity needs to be estimated.

In this study, we take as a prototypical example of a piezoelectric system, a piezoelectric composite beam subject to base excitation, and we model its dynamics using an adaptive estimation technique based on the RKHS embedding method.

3.2 Nonlinear Piezoelectric Model

In this section, we derive the equations of motion of a piezoelectric bimorph beam shown in Figure 3.1. We assume that the beam is excited at its base by input z and the shunt circuit is open. The method given here represents the classical approach for deriving the governing equations for the target class of nonlinear piezoelectric composites. This section carefully describes the precise nature of some constitutive nonlinearities and reveals the limitations of the traditional linear models. In the current study, we have chosen the electric enthalpy density for nonlinear continua given in [11] to serve as the means to construct the governing equations and formulate the RKHS embedding approach. Note that the RKHS embedding techniques discussed in this chapter are not limited to this problem and can be adapted to model other types of similar nonlinear electromechanical composite oscillators.

3.2.1 Nonlinear Electric Enthalpy Density

The expression for electric enthalpy density for modeling linear piezoelectric continua is given by

$$\mathcal{H} = \frac{1}{2} C^E_{ijkl} S_{ij} S_{kl} - e_{mij} S_{ij} E_m - \frac{1}{2} \epsilon^S_{im} E_i E_m,$$

where C^E_{ijkl}, S_{ij}, e_{mij}, E_m, and ϵ^S_{im} are the Young's modulus, strain, piezoelectric coupling, electric field, and permittivity tensors, respectively. The quadratic form above is written using the summation convention. Based on thermodynamic considerations, the stress and electric displacement, T_{ij} and D_i, respectively, are defined in the relations

$$T_{ij} = \left. \frac{\partial \mathcal{H}}{\partial S_{ij}} \right|_{s,E}, \qquad -D_i = \left. \frac{\partial \mathcal{H}}{\partial E_i} \right|_{s,S}.$$

The associated constitutive laws of linear piezoelectricity have the form

$$\begin{Bmatrix} T_{ij} \\ D_m \end{Bmatrix} = \begin{bmatrix} C^E_{ijkl} & -e_{nij} \\ e_{mkl} & \epsilon^S_{mn} \end{bmatrix} \begin{Bmatrix} S_{kl} \\ E_n \end{Bmatrix},$$

where again the summation convention holds in the expression above. In the above equations, the superscripts on C^E_{ijkl} and ϵ^S_{mn} emphasize that these constants are measured when the electric field and strain are held constant. For piezoelectric beam bending models, consideration is restricted to constitutive laws that have the form

$$\begin{Bmatrix} T_x \\ D_z \end{Bmatrix} = \begin{bmatrix} C^E_{xx} & -e_{zx} \\ e_{zx} & \epsilon^S_{zz} \end{bmatrix} \begin{Bmatrix} S_x \\ E_z \end{Bmatrix},$$

where $x \sim 11$, $z \sim 3$ are the coordinate directions depicted in Figure 3.1. The coordinate x is measured along the neutral axis that extends along the length of the beams, and z is in the transverse bending displacement direction. The permittivity at constant strain can be related to that at constant stress using the relation

$$\epsilon^S_{zz} = \epsilon^T_{zz} - d^2_{zx} C^E_{xx}.$$

The piezoelectric strain coefficient d_{zx} is related to the piezoelectric coupling constant e_{zx} by the equation $e_{zx} = C^E_{xx} d_{zx}$. The constitutive laws for the piezoelectric composite are

$$\begin{aligned} T_x &= C^E_{xx} S_x - d_{zx} C^E_{xx} E_z, \\ D_z &= d_{zx} C^E_{xx} S_x + (\epsilon^T_{zz} - d^2_{zx} C^E_{xx}) E_z. \end{aligned}$$

A detailed discussion of this linear case can be found in [3, 67, 68].

For large values of the field variables, the effects of nonlinearity in the piezoelectric continua can become dominant. We account for these effects by adding higher order terms in the expression for the electric enthalpy density. The nonlinear dependence between C_{xx}^{E}, d_{zx} and S_x can be approximated using the relations [11]

$$C_{xx}^{E} = C_{xx}^{E(0)} + C_{xx}^{E(1)} S_x + C_{xx}^{E(2)} S_x^2,$$
$$d_{zx} = d_{zx}^{(0)} + d_{zx}^{(1)} S_x + d_{zx}^{(2)} S_x^2.$$

The corresponding electric enthalpy density has the form

$$\mathcal{H} = \frac{1}{2} C_{xx}^{E(0)} S_x^2 + \frac{1}{3} C_{xx}^{E(1)} S_x^3 + \frac{1}{4} C_{xx}^{E(2)} S_x^4 - \gamma_0 S_x E - \frac{1}{2} \gamma_1 S_x^2 E - \frac{1}{2} \nu_0 E^2 \tag{3.1}$$

with

$$\nu_0 = \epsilon^T - (d_{zx}^{(0)})^2 C_{xx}^{E(0)}, \quad \gamma_0 = C_{xx}^{E(0)} d_{zx}^{(0)},$$
$$\gamma_1 = C_{xx}^{E(0)} d_{zx}^{(1)} + C_{xx}^{E(1)} d_{zx}^{(0)}, \quad \gamma_2 = C_{xx}^{E(0)} d_{zx}^{(2)} + C_{xx}^{E(2)} d_{zx}^{(0)} + C_{xx}^{E(1)} d_{zx}^{(1)}.$$

Thus, the nonlinear constitutive laws, obtained using the relations shown above, have the form

$$T_x = C_{xx}^{E(0)} S_x + C_{xx}^{E(1)} S_x^2 + C_{xx}^{E(2)} S_x^3 - \gamma_0 E_z - \gamma_1 S_x E_z - \gamma_2 S_x^2 E_z,$$
$$D_z = \gamma_0 S_x + \frac{1}{2} \gamma_1 S_x^2 + \frac{1}{3} \gamma_2 S_x^3 + \nu_0 E_z.$$

See references [15, 16, 69, 70, 71] for other similar models that are used to represent the behavior of nonlinear piezoelectric systems.

3.2.2 Equations of Motion

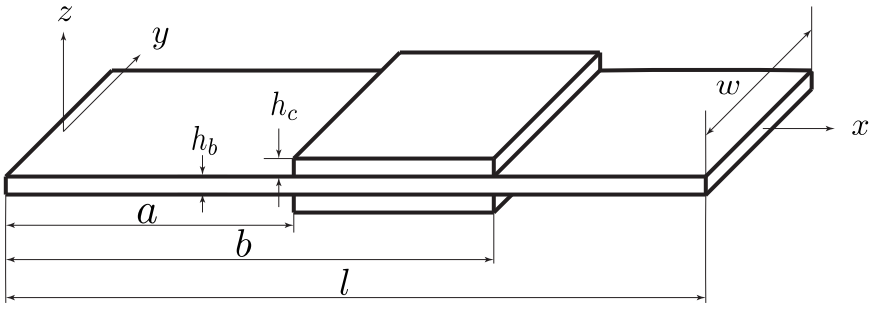

Figure 3.1: Dimensions of the cantilevered piezoelectric bimorph.

In this subsection, we derive the nonlinear equations of motion of the typical piezoelectric composite, the cantilevered bimorph, shown in Figure 3.1. The extended Hamilton's Principle states that of all the possible trajectories in the electromechanical configuration space, the actual motion satisfies the variational identity

$$\delta \int_{t_0}^{t_1} (T - \mathcal{V}_{\mathcal{H}})\, dt + \int_{t_0}^{t_1} \delta W dt = 0 \tag{3.2}$$

with kinetic energy T, electromechanical potential $\mathcal{V}_{\mathcal{H}}$ defined below, electromechanical virtual work δW, initial time t_0, and final time t_1. The kinetic energy of the nonlinear piezoelectric beam is expressed as

$$T = \frac{1}{2}\int_0^l m(x)(\dot{w} + \dot{\mathrm{z}})^2 dx = \frac{1}{2}\mathrm{m}\int_0^l (\dot{w} + \dot{\mathrm{z}})^2 dx \tag{3.3}$$

with $m(x)$ the mass per unit length of the beam and m defined as $\mathrm{m} = \rho_s h_s + 2\rho_p h_p$. In the above equation, $w = w(x,t)$ is the displacement from the neutral axis at location $x \in [0, l]$ at time t. The variable $\mathrm{z}(t)$ represents the displacement of the root of the beam, that is, it is the base motion that occurs in the z direction defined relative to the beam. The terms ρ and h represent the density and thickness, respectively. The subscript s represents the variables

corresponding to the substrate and the subscript p indicates those of the piezoceramic. The electric enthalpy for the nonlinear system is given by the relation

$$\mathcal{V}_{\mathcal{H}} = \int_V \mathcal{H} dV = \int_{V_b} \mathcal{H} dV_b + \int_{V_p} \mathcal{H} dV_p.$$

Substituting the expression for $\mathcal{H}$ in the above equation gives

$$\mathcal{V}_{\mathcal{H}} = \int_{V_b} \frac{1}{2} C_b S_x^2 dV_b + \int_{V_c} \left(\frac{1}{2} C_{xx}^{(0)} S_x^2 + \frac{1}{3} C_{xx}^{(1)} S_x^3 + \frac{1}{4} C_{xx}^{(2)} S_x^4 - \gamma_0 S_x E_z \right. \\ \left. - \frac{1}{2} \gamma_1 S_x^2 E_z - \frac{1}{3} \gamma_2 S_x^3 E_z - \frac{1}{2} \nu_0 E_z^2 \right) dV_p \tag{3.4}$$

with beam Young's modulus C_b, beam volume V_b and piezoelectric patch volume V_p. We recall that the approximation for bending strain in Euler-Bernoulli beam theory is given by

$$S_x(x, z, t) = -\frac{\partial^2 w(x,t)}{\partial x^2} z,$$

$\forall x \in [0, l], \qquad \forall z \in \left[-\frac{h_b}{2} - h_c, \frac{h_b}{2} + h_c\right]$. Consider the term $\int_{V_p} \frac{1}{2} C_{xx}^{(0)} S_x^2$ in the expression for electric enthalpy density. With the substitution of the expression for strain, we get

$$\int_{V_p} \frac{1}{2} C_{xx}^{(0)} S_x^2 = \frac{1}{2} C_{xx}^{(0)} \int_{V_p} [(w'')^2 z^2] dV = \frac{1}{2} C_{xx}^{(0)} \left(\int_a^b (w'')^2 dx \right) \left(\int_0^b dy \right) \left(2 \int_{\frac{h_b}{2}}^{\frac{h_b}{2} + h_c} z^2 dz \right) \\ = 2 \underbrace{\left[\frac{1}{6} C_{xx}^{(0)} b \left\{ \left(\frac{h_b}{2} + h_c \right)^3 - \left(\frac{h_b}{2} \right)^3 \right\} \right]}_{a_{(0,2)}} \int_a^b (w'')^2 dx = 2 a_{(0,2)} \int_a^b (w'')^2 dx.$$

The other terms in Equation 3.4 can be simplified in a similar manner. The expression for electric enthalpy density after simplification has the form

$$\mathcal{V}_{\mathcal{H}} = \frac{1}{2} C_b I_b \int_0^l (w'')^2 dx + 2 a_{(0,2)} \int_a^b (w'')^2 dx + 2 a_{(2,4)} \int_a^b (w'')^4 dx$$

$$+ 2b_{(1,1)} \left(\int_a^b w'' dx \right) E_z + 2b_{(3,1)} \left(\int_a^b (w'')^3 dx \right) E_z - 2b_{(0,2)} E_z^2, \tag{3.5}$$

where we define

$$a_{(0,2)} := \frac{1}{6} C_{xx}^{(0)} b \left[\left(\frac{h_b}{2} + h_c \right)^3 - \left(\frac{h_b}{2} \right)^3 \right], \quad a_{(2,4)} := \frac{1}{20} C_{xx}^{(2)} b \left[\left(\frac{h_b}{2} + h_c \right)^5 - \left(\frac{h_b}{2} \right)^5 \right],$$
$$b_{(1,1)} := \frac{1}{2} \gamma_0 b \left[\left(\frac{h_b}{2} + h_c \right)^2 - \left(\frac{h_b}{2} \right)^2 \right], \quad b_{(3,1)} := \frac{1}{12} \gamma_2 b \left[\left(\frac{h_b}{2} + h_c \right)^4 - \left(\frac{h_b}{2} \right)^4 \right],$$
$$b_{(0,2)} := \frac{1}{2} \nu_0 b h_c l_c.$$

For the time being, we omit the effects of damping in the following derivation. Following the details included in Appendix F, the variational statement of Hamilton's principle yields the pair of equations

$$\mathrm{m}\ddot{w} + C_b I_b w'''' + 4a_{(0,2)} \left(\chi_{[a,b]} w'' \right)'' + 8a_{(2,4)} (\chi_{[a,b]} (w'')^3)'' + 2b_{(1,1)} \chi''_{[a,b]} E_z$$
$$+ 6b_{(3,1)} (\chi_{[a,b]} (w'')^2)'' E_z = -\mathrm{m}\ddot{z}, \tag{3.6}$$
$$2b_{(1,1)} w'(b) - 2b_{(1,1)} w'(a) + 2b_{(3,1)} \left(\int_a^b (w'')^3 dx \right) + 4b_{(0,2)} E_z = 0, \tag{3.7}$$

where $\chi_{[a,b]}$ is the characteristic function of the interval $[a, b]$ defined as in Equation 3.23. These equations are subject to the corresponding variational boundary conditions

$$\left\{C_b I_b w'' + 4a_{(0,2)}\chi_{[a,b]}w'' + 8a_{(2,4)}\chi_{[a,b]}(w'')^3 + 2b_{(1,1)}\chi_{[a,b]}E_z + 6b_{(3,1)}\chi_{[a,b]}(w'')^2\right\}\delta w'\Big|_0^l = 0,$$
$$\left\{C_b I_b w''' + 4a_{(0,2)}\left(\chi_{[a,b]}w''\right)' + 8a_{(2,4)}\left(\chi_{[a,b]}(w'')^3\right)' + 2b_{(1,1)}\chi'_{[a,b]}E_z + 6b_{(3,1)}\left(\chi_{[a,b]}(w'')^2\right)'\right\}\delta w\Big|_0^l = 0,$$

and to the initial conditions $w(0) = w_0$ and $\dot{w}(0) = \dot{w}_0$.

We know that the effects of nonlinearity in oscillators become most noticeable near the natural frequency. Hence, we approximate the solutions of Equations 3.6 and 3.7 using a single-mode approximation $w(x,t) = \psi(x)u(t)$. Following the detailed analysis in Appendix G, the equations of motion are written

$$M\ddot{u}(t) + P\ddot{z}(t) + \underbrace{[K_b + K_p]}_{K}u(t) + K_N u^3(t) + [\mathcal{B} + Q_N u^2(t)]E_z = 0, \tag{3.8}$$

$$\mathcal{B}u(t) + \mathcal{B}_N u^3(t) = \mathcal{C}E_z \tag{3.9}$$

for constants $M, P, K_b, K_p, K_N, \mathcal{B}, Q_N, \mathcal{B}_N$, and $\mathcal{C}$ defined in Appendix G.

Note that the first equation defines the dynamics of the system and the second equation defines an algebraic relation between displacement and the electric field. From the second equation of motion, we get an expression for the electric field that has the form $E_z = [\mathcal{B}u(t) + \mathcal{B}_N u^3(t)]/\mathcal{C}$. Substituting this expression for electric field into the first equation of motion, we get

$$-P\ddot{z}(t) = M\ddot{u}(t) + \underbrace{\left[K + \frac{\mathcal{B}^2}{\mathcal{C}}\right]}_{\hat{K}}u(t) + \underbrace{\left[K_N + \frac{\mathcal{B}\mathcal{B}_N}{\mathcal{C}} + \frac{Q_N\mathcal{B}}{\mathcal{C}}\right]}_{\hat{K}_{N_1}}u^3(t) + \underbrace{\frac{Q_N\mathcal{B}_N}{\mathcal{C}}}_{\hat{K}_{N_2}}u^5(t),$$

$$-P\ddot{z}(t) = M\ddot{u}(t) + \hat{K}u(t) + \hat{K}_{N_1}u^3(t) + \hat{K}_{N_2}u^5(t).$$

After introducing a viscous damping term for the representation of energy losses, we have

$$M\ddot{u}(t) + C\dot{u}(t) + \hat{K}u(t) + \hat{K}_{N_1}u^3(t) + \hat{K}_{N_2}u^5(t) = -P\ddot{z}(t).$$

Let us define the state vector $\boldsymbol{x} = \{x_1, x_2\}^T = \{u, \dot{u}\}^T$. Now, we can write the first order form of the governing equations as

$$\begin{Bmatrix} \dot{x}_1 \\ \dot{x}_2 \end{Bmatrix} = \underbrace{\begin{bmatrix} 0 & 1 \\ -\frac{\hat{K}}{M} & -\frac{C}{M} \end{bmatrix}}_{A} \begin{Bmatrix} x_1 \\ x_2 \end{Bmatrix} + \underbrace{\begin{Bmatrix} 0 \\ -\frac{P}{M} \end{Bmatrix}}_{B} \underbrace{\ddot{z}(t)}_{\mathrm{u}(t)} + \underbrace{\begin{Bmatrix} 0 \\ 1 \end{Bmatrix}}_{B_N} \underbrace{\left(-\frac{\hat{K}_{N_1}}{M}x_1^3(t) - \frac{\hat{K}_{N_2}}{M}x_1^5(t) \right)}_{f(\boldsymbol{x}(t))}, \quad (3.10)$$

or

$$\dot{\boldsymbol{x}}(t) = A\boldsymbol{x}(t) + B\mathrm{u}(t) + B_N f(\boldsymbol{x}(t)).$$

We make several observations before proceeding to the adaptive estimation problem treated in the next section. Note that the specific form of function $f(\boldsymbol{x}) = f(x_1)$ that is given in Equation 10 above has been constructed assuming the only unknown terms are the nonlinearities arising from the constitutive laws. We allow for a wider class of uncertainty that can be expressed as $f(\boldsymbol{x}) = f(x_1, x_2)$. For instance, if the viscous damping coefficient is uncertain or unknown, the damping term should be subsumed into $f(x_1, x_2)$. With these considerations in mind, the derivations in the next section are carried out for the more general case when $f = f(x_1, x_2)$. However, when we prepare finite-dimensional approximations in Section 3.3.2 for the simulations in Sections 3.4 and 3.5, we specialize examples to the case $f = f(x_1)$ described above.

3.3 Adaptive Estimation in RKHS

In this section, we pose the estimation problem for the approximation of the unknown nonlinear function f and review the theory of RKHS adaptive estimation. The governing equation of the plant, the piezoelectric oscillator modeled in Section 3.2, has the general form

$$\dot{\boldsymbol{x}}(t) = A\boldsymbol{x}(t) + B\mathrm{u}(t) + B_N f(\boldsymbol{x}(t)). \tag{3.11}$$

We denote the state space of this evolution law by $X = \mathbb{R}^d$, so that $\boldsymbol{x}(t) \in X$. Under the assumption of full state observability, the problem of estimation of the states $\boldsymbol{x}(t)$ at a given time instant t is a classical state estimation problem. However, the problem of interest in this chapter is the estimation of the unknown function f. Problems of this type generally involve the definition of an estimator system that evolves in parallel with the actual plant. The model of the estimator for the plant defined by Equation 3.11 is taken in the form

$$\dot{\hat{\boldsymbol{x}}}(t) = A\hat{\boldsymbol{x}}(t) + B\mathrm{u}(t) + B_N \hat{f}(t, \boldsymbol{x}(t)). \tag{3.12}$$

In Equation 3.12, note that the estimate $\hat{f}$ of the function f depends not only on the actual (measured) states $\boldsymbol{x}(t)$ but also the time t. We want the function estimate $\hat{f}(t, \cdot)$ to converge in time to the actual function $f(\cdot)$ in some suitable function space norm as $t \to \infty$.

In addition to the estimator model, it is also important to define the hypothesis space, the space of functions in which the function f and the function estimate $\hat{f}$ live. In this chapter, we assume that the unknown nonlinear function f lives in the infinite dimensional RKHS $\mathcal{H}_X$ equipped with the reproducing kernel $\mathcal{K}_X : X \times X \to \mathbb{R}$. Recall that the reproducing property of the kernel states that, for any $\boldsymbol{x} \in X$ and $f \in \mathcal{H}_X$, $(\mathcal{K}(\boldsymbol{x}, \cdot), f)_{\mathcal{H}_X} = f(\boldsymbol{x})$. It is well known

that the existence of a reproducing kernel guarantees the boundedness of the evaluation functional $\mathcal{E}_{\boldsymbol{x}} : \mathcal{H}_X \to \mathbb{R}$, which is defined by the condition that $\mathcal{E}_{\boldsymbol{x}} f = (\mathcal{K}(\boldsymbol{x}, \cdot), f)_{\mathcal{H}_X}$. In this chapter, we restrict to RKHS in which the reproducing kernel is bounded by a constant. This implies that the injection $i : \mathcal{H}_X \to C(\Omega)$ from the RKHS $\mathcal{H}_X$ to the space of continuous function on Ω, $C(\Omega)$, is uniformly bounded [60]. This fact is used to prove the existence and uniqueness of the solution of the error system. A more detailed discussion about RKHS can be found in [72, 73, 74].

In addition to the estimator model, we also need an equation that defines the evolution (time derivative) of the function estimate. This is given by the learning law

$$\dot{\hat{f}}(t) = \Gamma^{-1}(B_N \mathcal{E}_{\boldsymbol{x}(t)})^* P(\boldsymbol{x}(t) - \hat{\boldsymbol{x}}(t)), \tag{3.13}$$

where $\Gamma \in \mathbb{R}^+$, $\mathcal{E}_{\boldsymbol{x}}$ is the evaluation functional at $\boldsymbol{x} \in X$, and the notation $(\cdot)^*$ denotes the adjoint of an operator. Further, the matrix $P \in \mathbb{R}^{d \times d}$ is the symmetric positive definite solution of the Lyapunov's equation $A^T P + PA = -Q$, where $Q \in \mathbb{R}^{d \times d}$ is an arbitrary but fixed symmetric positive definite matrix.

The existence and uniqueness of a solution for the estimator models given by Equations 3.12 and 3.13 can be proved under the assumption that the excitation input is continuous and we are working in an uniformly embedded RKHS as mentioned above. The following theorem proves this statement.

Theorem 3.1. *Define* $\mathbb{X} := \mathbb{R}^d \times \mathcal{H}_X$, *and suppose that* $\boldsymbol{x} \in C([0, T]; \mathbb{R}^d)$, $\mathrm{u} \in C([0, T]; \mathbb{R})$ *and that the embedding* $i : \mathcal{H}_X \hookrightarrow C(\Omega)$ *is uniform in the sense that there is a constant* $C > 0$ *such that for any* $f \in \mathcal{H}_X$,

$$\|f\|_{C(\Omega)} \equiv \|if\|_{C(\Omega)} \leq C\|f\|_{\mathcal{H}_X}.$$

Then for any $T > 0$, there is a unique mild solution $(\hat{\boldsymbol{x}}, \hat{f}) \in C([0,T], \mathbb{X})$ to

$$\begin{Bmatrix} \dot{\hat{\boldsymbol{x}}}(t) \\ \dot{\hat{f}}(t) \end{Bmatrix} = \begin{Bmatrix} A\hat{\boldsymbol{x}}(t) + B\mathrm{u}(t) + B_N \mathcal{E}_{\boldsymbol{x}(t)} \hat{f}(t) \\ \Gamma^{-1}(B_N \mathcal{E}_{\boldsymbol{x}(t)})^* P(\boldsymbol{x}(t) - \hat{\boldsymbol{x}}(t)) \end{Bmatrix}, \tag{3.14}$$

and the map $\hat{X}_0 \equiv (\hat{\boldsymbol{x}}_0, \hat{f}_0) \mapsto (\hat{\boldsymbol{x}}, \hat{f})$ is Lipschitz continuous from $\mathbb{X}$ to $C([0,T], \mathbb{X})$.

Proof. We set $X(t) := (\hat{x}(t), \hat{f}(t)) \in \mathbb{X}$. Equation 3.14 given above can be rewritten as

$$\begin{Bmatrix} \dot{\hat{\boldsymbol{x}}}(t) \\ \dot{\hat{f}}(t) \end{Bmatrix} = \underbrace{\begin{bmatrix} A & 0 \\ 0 & A_0 \end{bmatrix}}_{\mathcal{A}} \begin{Bmatrix} \hat{\boldsymbol{x}}(t) \\ \hat{f}(t) \end{Bmatrix} + \underbrace{\begin{Bmatrix} B\mathrm{u}(t) + B_N \mathcal{E}_{\boldsymbol{x}(t)} \hat{f}(t) \\ -A_0 \hat{f}(t) + \Gamma^{-1}(B_N \mathcal{E}_{\boldsymbol{x}(t)})^* P(\boldsymbol{x}(t) - \hat{\boldsymbol{x}}(t)) \end{Bmatrix}}_{\mathcal{F}(t, X(t))}, \tag{3.15}$$

$$\begin{Bmatrix} \hat{\boldsymbol{x}}(t_0) \\ \hat{f}(t_0) \end{Bmatrix} = \begin{Bmatrix} \hat{\boldsymbol{x}}_0 \\ \hat{f}_0 \end{Bmatrix},$$

where $-A_0$ is an arbitrary bounded linear operator from $\mathcal{H}_X$ to $\mathcal{H}_X$. It is clear from the above equation that $\mathcal{A}$ is a bounded linear operator. We know that every bounded linear operator is the infinitesimal generator of a C_0-semigroup on $\mathbb{X} := \mathbb{R}^d \times \mathcal{H}_X$ (Theorem 1.2, Chapter 1 of [75]). Now, consider the function $\mathcal{F}$. For each $t \geq 0$, we have

$$\begin{aligned} \|\mathcal{F}(t, \hat{X}) - \mathcal{F}(t, \hat{Y})\| &= \left\| \begin{Bmatrix} B_N \mathcal{E}_{\boldsymbol{x}(t)} (\hat{f}_{\hat{x}}(t) - \hat{f}_{\hat{y}}(t)) \\ -A_0 (\hat{f}_{\hat{x}}(t) - \hat{f}_{\hat{y}}(t)) + \Gamma^{-1}(B_N \mathcal{E}_{\boldsymbol{x}(t)})^* P(\hat{y}(t) - \hat{x}(t)) \end{Bmatrix} \right\| \\ &\leq D \|\hat{X} - \hat{Y}\|, \end{aligned}$$

where $\hat{X} := (\hat{x}, \hat{f}_{\hat{x}})$, $\hat{Y} := (\hat{y}, \hat{f}_{\hat{y}})$, and $D \geq 0$ is a constant. Note that we are able to achieve the above bound because of uniform boundedness of the evaluation functional $\mathcal{E}_{x(t)}$. Thus, for each $t \geq 0$, the map $\hat{X} \mapsto \mathcal{F}(t, \hat{X})$ is uniformly globally Lipschitz continuous. We also

note that the map $t \mapsto \mathcal{F}(t, \hat{X})$ is continuous for each $\hat{X} \in \mathbb{X}$ since u is continuous. Using Theorem 1.2 in Chapter 6 of [75], we can conclude that the above initial value problem has a unique mild solution, and the map $\hat{X}_0 \equiv (\hat{\boldsymbol{x}}_0, \hat{f}_0) \mapsto (\hat{\boldsymbol{x}}, \hat{f})$ is Lipschitz continuous from $\mathbb{X}$ to $C([0,T], \mathbb{X})$. □

Suppose that $\tilde{\boldsymbol{x}}(t) := \boldsymbol{x}(t) - \hat{\boldsymbol{x}}(t)$ and $\tilde{f}(t,\cdot) := f(\cdot) - \hat{f}(t,\cdot)$ denote the state error and the function error, respectively. Equations 3.11, 3.12 and 3.13 can now be expressed in terms of the error equation

$$\begin{Bmatrix} \dot{\tilde{\boldsymbol{x}}}(t) \\ \dot{\tilde{f}}(t) \end{Bmatrix} = \begin{bmatrix} A & B_N \mathcal{E}_{\boldsymbol{x}(t)} \\ -\Gamma^{-1}(B_N \mathcal{E}_{\boldsymbol{x}(t)})^* P & 0 \end{bmatrix} \begin{Bmatrix} \tilde{\boldsymbol{x}}(t) \\ \tilde{f}(t) \end{Bmatrix}. \tag{3.16}$$

Note, the above equation evolves in $\mathbb{R}^d \times \mathcal{H}_X$. Also, even though the original Equation 3.11 and the estimator Equation 3.12 are not the same as in Reference [60], the above error equation does have the same form as that studied in [60]. The existence and uniqueness of a solution for this equation are given by the following theorem.

Theorem 3.2. *Define $\mathbb{X} := \mathbb{R}^d \times \mathcal{H}_X$, and suppose that $\boldsymbol{x} \in C([0,T]; \mathbb{R}^d)$ and that the embedding $i : \mathcal{H}_X \hookrightarrow C(\Omega)$ is uniform in the sense that there is a constant $C > 0$ such that for any $f \in \mathcal{H}_X$,*

$$\|f\|_{C(\Omega)} \equiv \|if\|_{C(\Omega)} \leq C\|f\|_{\mathcal{H}_X}.$$

Then for any $T > 0$, there is a unique mild solution $(\tilde{\boldsymbol{x}}, \tilde{f}) \in C([0,T], \mathbb{X})$ to Equations 3.16 and the map $X_0 \equiv (\tilde{\boldsymbol{x}}_0, \tilde{f}_0) \mapsto (\tilde{\boldsymbol{x}}, \tilde{f})$ is Lipschitz continuous from $\mathbb{X}$ to $C([0,T], \mathbb{X})$.

The proof for this theorem is very similar to the proof of Theorem 3.1 and is given in [60]. Note that the above theorem does not study the stability nor the asymptotic stability of the

error system. In other words, the convergence of the state error and the function error to the origin is not addressed by this theorem. This aspect is addressed in the following subsection.

3.3.1 Persistence of Excitation

The convergence of state and function errors is guaranteed by additional conditions, commonly referred to as the persistence of excitation (PE) conditions [76, 77, 78]. These have been extended to the RKHS framework in [79, 80]. This section reviews the persistence of excitation conditions for adaptive estimators on RKHS in detail.

Before taking a look at the PE conditions for the adaptive estimator in the RKHS, it is important to note that they are defined over a set $\Omega \subseteq X$. Now, we can define $\mathcal{H}_\Omega := \overline{\{\mathcal{K}(\boldsymbol{x}, \cdot) | \boldsymbol{x} \in \Omega\}}$. Note that $\mathcal{H}_\Omega$ is a subspace of $\mathcal{H}_X$. The following definitions give us two closely related versions of the PE condition on the set Ω.

Definition 3.3. (**PE. 1**) The trajectory $\boldsymbol{x} : t \mapsto \boldsymbol{x}(t) \in \mathbb{R}^d$ persistently excites the indexing set Ω and the RKHS $\mathcal{H}_\Omega$ provided there exist positive constants T_0, γ, δ, and Δ, such that for each $t \geq T_0$ and any $g \in \mathcal{H}_X$, there exists $s \in [t, t + \Delta]$ such that

$$\left| \int_s^{s+\delta} \mathcal{E}_{\boldsymbol{x}(\tau)} g d\tau \right| \geq \gamma \|\Pi_\Omega g\|_{\mathcal{H}_X} > 0.$$

Definition 3.4. (**PE. 2**) The trajectory $\boldsymbol{x} : t \mapsto \boldsymbol{x}(t) \in \mathbb{R}^d$ persistently excites the indexing set Ω and the RKHS $\mathcal{H}_\Omega$ provided there exist positive constants T_0, γ, and Δ such that

$$\int_t^{t+\Delta} \left(\mathcal{E}^*_{\boldsymbol{x}(\tau)} \mathcal{E}_{\boldsymbol{x}(\tau)} g, g \right)_{\mathcal{H}_X} d\tau \geq \gamma \|\Pi_\Omega g\|^2_{\mathcal{H}_X} > 0$$

for all $t \geq T_0$ and any $g \in \mathcal{H}_X$.

In the above definitions, the term Π_Ω represents the orthogonal projection operator from the RKHS $\mathcal{H}_X$ to its subspace $\mathcal{H}_\Omega$. Notice that both the PE conditions are defined on the set Ω. It would be ideal if $\Omega = X$, the space on which the nonlinear function is defined. However, in most practical applications, the set Ω is a subset of the state space X. The following theorem relates both the PE conditions given above.

Theorem 3.5. *The PE condition in Definition PE. 3.3 implies the one in Definition PE. 3.4. Further, if the family of functions defined by* $\{g(\boldsymbol{x}(\cdot)) : t \mapsto g(\boldsymbol{x}(t)) | g \in \mathcal{H}_X\}$ *is uniformly equicontinuous, then the PE condition in Definition PE. 3.4 implies the one in Definition PE. 3.3.*

With the PE conditions defined, the following theorem addresses the convergence of the states of the error system to the origin.

Theorem 3.6. *Suppose the trajectory* $\boldsymbol{x} : t \mapsto \boldsymbol{x}(t)$ *persistently excites the RKHS* $\mathcal{H}_\Omega$ *in the sense of Definition PE. 3.3. Then the estimation error system in Equation 3.16 is uniformly asymptotically stable at the origin. In particular, we have*

$$\lim_{t\to\infty} \|\tilde{\boldsymbol{x}}(t)\| = 0, \qquad \lim_{t\to\infty} \|\Pi_\Omega \tilde{f}(t)\|_{\mathcal{H}_X} = 0.$$

The proof for this theorem can be found in [79, 80]. Intuitively, the second PE condition implies that the state trajectory should repeatedly enter every neighborhood of all the points in the set Ω infinitely many times. To satisfy this, it makes sense to pick the set Ω to be the positive limit set $\omega^+(\boldsymbol{x}_0)$ or one of its subsets. The following theorem from [81] affirms that the persistently excited sets are in fact contained in the positive limit set.

Theorem 3.7. *Let* $\mathcal{H}_X$ *be the RKHS of functions over* X *and suppose that this RKHS*

includes a rich family of bump functions. If the PE condition in Definition PE. 3.4 holds for Ω, then $\Omega \subseteq \omega^+(\boldsymbol{x}_0)$, the positive limit set corresponding to the initial condition $\boldsymbol{x}_0$.

3.3.2 Finite Dimensional Approximation

As mentioned above, the evolution of the error equation and the learning law for the RKHS adaptive estimator is in $\mathbb{R} \times \mathcal{H}_X$. In essence, the learning law constitutes a distributed parameter system since $\tilde{f}(t)$ evolves in a infinite-dimensional space. Thus, to implement this adaptive estimator, the persistently excited infinite-dimensional space $\mathcal{H}_\Omega$ is approximated by a nested, dense collection $\{\mathcal{H}_n\}_{n\in\mathbb{N}}$ of finite-dimensional subspaces. Recall that even though the particular nonlinear function f based on the choice of constitutive nonlinearities in Equation 3.1 is a function $f = f(x_1)$, we have elected to cast the problem in terms of the more general nonlinear function $f = f(x_1, x_2)$. In this section, we will continue with the analysis of finite-dimensional approximation for the more general unknown nonlinear function $f = f(x_1, x_2)$, which results in Equations 3.17 and 3.18 below. Modifications of these equations to study the particular case in which $f = f(x_1)$ are straightforward, and we summarize this specific case at the beginning of Section 3.5. We leave the details to the reader. Let Π_n represent the projection operator from infinite-dimensional $\mathcal{H}_X$ to the finite-dimensional $\mathcal{H}_n$. Now, the finite-dimensional approximations of the adaptive estimator equations can be expressed as

$$\dot{\hat{\boldsymbol{x}}}_n(t) = A\hat{\boldsymbol{x}}_n(t) + B\mathrm{u}(t) + B_N\mathcal{E}_{\boldsymbol{x}(t)}\Pi_n^*\hat{f}_n(t), \tag{3.17}$$

$$\dot{\hat{f}}_n(t) = \Gamma^{-1}\left(B_N\mathcal{E}_{\boldsymbol{x}(t)}\Pi_n^*\right)^* P\tilde{\boldsymbol{x}}_n(t), \tag{3.18}$$

where $\tilde{\boldsymbol{x}}_n := \boldsymbol{x} - \hat{\boldsymbol{x}}_n$.

Theorem 3.8. *Suppose that $\boldsymbol{x} \in C([0,T],\mathbb{R}^d)$ and that the embedding $i : \mathcal{H}_X \hookrightarrow C(\Omega)$ is*

uniform in the sense that

$$\|f\|_{C(\Omega)} \equiv \|if\|_{C(\Omega)} \leq C\|f\|_{\mathcal{H}_X}.$$

Then for any $T > 0$,

$$\|\hat{\boldsymbol{x}} - \hat{\boldsymbol{x}}_n\|_{C([0,T];\mathbb{R}^d)} \to 0,$$
$$\|\hat{f} - \hat{f}_n\|_{C([0,T];\mathbb{R}^d)} \to 0,$$

as $n \to \infty$.

The proof of the above theorem can be found in [60]. As noted earlier, the estimator equations considered in [60] are different from the ones considered in this chapter. However, the error equations for $\hat{\boldsymbol{x}} - \hat{\boldsymbol{x}}_n$ and $\hat{f} - \hat{f}_n$ still have the same form as in [60], and the proof of the above theorem will remain the same.

3.4 RKHS Adaptive Estimator Implementation

The previous section discussed the theory behind estimators that evolve in an RKHS. This section presents the algorithm for the implementation of the theory. Figure 3.2 shows the block diagram of the adaptive estimator. The actual model shown in the figure corresponds to the true system excited by the input u, and we assume that we can measure all the states $\boldsymbol{x}(t)$ of this true system. The estimator and learning law blocks in the diagram are what we implement on the computer. Let us first take a look at the estimator model. The operator Π_n^* in the estimator model is the adjoint of the orthogonal projection/approximation operator Π_n. It is equivalent to the inclusion map that maps an element of $\mathcal{H}_n$ space to the same element in the $\mathcal{H}_X$ space. Thus, the term $\mathcal{E}_{x(t)}\Pi_n^*\hat{f}_n(t)$ in the estimator model is the same as

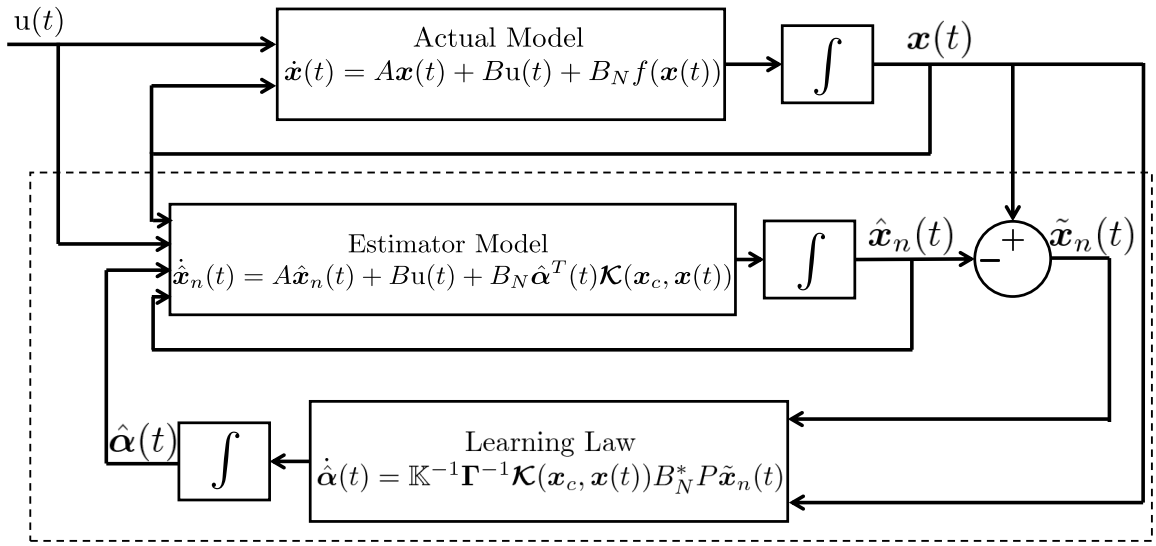

Figure 3.2: Adaptive Parameter Estimator Block Diagram.

$\mathcal{E}_{\boldsymbol{x}(t)}\hat{f}_n(t) = \hat{f}_n(t, \boldsymbol{x}(t))$.

Now, let us take a look at the learning law given in Equation 3.18. It is a derivative of a function, and we cannot directly implement it on a computer. To convert it to a form that is solvable using numerical methods, we take the inner product of the learning law with $\mathcal{K}(\boldsymbol{x}_i, \cdot)$. Before proceeding with this step, let us recall that the finite-dimensional function estimate $\hat{f}_n(t, \cdot)$ can be expressed as $\hat{f}_n(t, \cdot) = \sum_{j=1}^n \hat{\alpha}_j(t)\mathcal{K}(\boldsymbol{x}_j, \cdot) = \hat{\boldsymbol{\alpha}}^T(t)\boldsymbol{\mathcal{K}}(\boldsymbol{x}_c, \cdot)$. Thus, for $i = 1, \ldots, n$,

$$\left(\mathcal{K}(\boldsymbol{x}_i, \cdot), \dot{\hat{f}}_n(t)\right)_{\mathcal{H}_X} = \left(\mathcal{K}(\boldsymbol{x}_i, \cdot), \Gamma^{-1}\left(B_N\mathcal{E}_{\boldsymbol{x}(t)}\Pi_n^*\right)^* P\tilde{\boldsymbol{x}}_n(t)\right)_{\mathcal{H}_X},$$

which implies

$$\sum_{j=1}^n \mathcal{K}(\boldsymbol{x}_i, \boldsymbol{x}_j)\dot{\hat{\alpha}}_j(t) = \Gamma^{-1}\left(B_N\mathcal{E}_{\boldsymbol{x}(t)}\mathcal{K}(\boldsymbol{x}_i, \cdot), P\tilde{\boldsymbol{x}}_n(t)\right)_{\mathcal{H}_X}.$$

Thus, if $\hat{\boldsymbol{\alpha}}(t) := \{\hat{\alpha}_1(t), \ldots, \hat{\alpha}_n(t)\}^T$, its time derivative is given by the expression

$$\dot{\hat{\boldsymbol{\alpha}}}(t) = \mathbb{K}^{-1}\boldsymbol{\Gamma}^{-1}\boldsymbol{\mathcal{K}}(\boldsymbol{x}_c, \boldsymbol{x}(t))B_N^* P\tilde{\boldsymbol{x}}_n(t),$$

where $\mathbb{K}$ is the symmetric positive definite Grammian matrix whose ij^{th} element is defined as $\mathbb{K}_{ij} := \mathcal{K}(\boldsymbol{x}_i, \boldsymbol{x}_j)$, $\boldsymbol{\Gamma} := \Gamma\mathbb{I}_n$ is the gain matrix, and

$$\boldsymbol{\mathcal{K}}(\boldsymbol{x}_c, \boldsymbol{x}(t)) := \Big\{\mathcal{K}(\boldsymbol{x}_1, \boldsymbol{x}(t)), \ldots, \mathcal{K}(\boldsymbol{x}_n, \boldsymbol{x}(t))\Big\}^T.$$

The above equation gives us an expression for the rate at which the coefficients of the kernels change with time. Therefore, the implementation of the adaptive estimator amounts to integration of the equations

$$\dot{\hat{\boldsymbol{x}}}_n(t) = A\hat{\boldsymbol{x}}_n(t) + B\mathrm{u}(t) + B_N\hat{\boldsymbol{\alpha}}^T(t)\boldsymbol{\mathcal{K}}(\boldsymbol{x}_c, \boldsymbol{x}(t)), \tag{3.19}$$

$$\dot{\hat{\boldsymbol{\alpha}}}(t) = \mathbb{K}^{-1}\boldsymbol{\Gamma}^{-1}\boldsymbol{\mathcal{K}}(\boldsymbol{x}_c, \boldsymbol{x}(t))B_N^* P\tilde{\boldsymbol{x}}_n(t). \tag{3.20}$$

From the discussion in Subsection 3.3.1, it is clear that the persistence of excitation is sufficient to ensure parameter convergence. However, it is hard and sometimes impossible to check if a given space is persistently exciting. The following theorem from [82] gives us a sufficient condition for the persistence of excitation that is easy to verify. However, this theorem is only applicable to cases where radial basis functions over $\mathbb{R}^d$ generate the RKHS. Furthermore, we can only use this sufficient condition to check the persistence of excitation of finite-dimensional spaces. However, since all implementation is in the finite-dimensional spaces, the following theorem provides us a powerful tool to verify the convergence of parameters in practical applications.

Theorem 3.9. *Let* $\epsilon < \frac{1}{2}\min_{i\neq j}\|\boldsymbol{x}_i - \boldsymbol{x}_j\|$, *where* $\boldsymbol{x}_i$ *and* $\boldsymbol{x}_j$ *are the kernel centers* $\{\boldsymbol{x}_1, \ldots, \boldsymbol{x}_n\}$.

For every $t_0 \geq 0$ and $\delta > 0$, define

$$I_i = \{t \in [t_0, t_0 + \delta] : \|\boldsymbol{x}(t) - \boldsymbol{x}_i\| \leq \epsilon\}.$$

If there exists a δ such that the measure of I_i is bounded below by a positive constant that is independent of t_0 and the kernel center $\boldsymbol{x}_i$, and if the measure of $[t_0, t_0 + \delta]$ less than or equal to δ, then the space $\mathcal{H}_n$ is persistently exciting in the sense of Definition PE. 3.4.

Algorithm 1: RKHS adaptive estimator implementation

Input: $\boldsymbol{x}(t)$,$w^+(\boldsymbol{x}_0)$

Output: $\hat{f}_n(T, \cdot)$

1 Choose the RKHS $\mathcal{H}_X$ and the corresponding reproducing kernel $\mathcal{K}(\cdot, \cdot)$.

2 Choose kernel centers $\boldsymbol{x}_i$, for $i = 1, \ldots, n$ uniformly distributed on $w^+(\boldsymbol{x}_0)$,

if X is equal to the state space, choose kernels centers on $w^+(\boldsymbol{x}_0)$,

if X is a proper subset of the state space, choose kernel centers on the projection of $w^+(\boldsymbol{x}_0)$ on to the space X.

3 Run the adaptive estimator until the parameters converge.

Integrate

$$\dot{\hat{\boldsymbol{x}}}_n(t) = A\hat{\boldsymbol{x}}_n(t) + B\mathrm{u}(t) + B_N\hat{\boldsymbol{\alpha}}^T(t)\boldsymbol{\mathcal{K}}(\boldsymbol{x}_c, \boldsymbol{x}(t)),$$
$$\dot{\hat{\boldsymbol{\alpha}}}(t) = \mathbb{K}^{-1}\boldsymbol{\Gamma}^{-1}\boldsymbol{\mathcal{K}}(\boldsymbol{x}_c, \boldsymbol{x}(t))B_N^* P\tilde{\boldsymbol{x}}_n(t)$$

over the interval $[0, T]$.

4 Define $\hat{f}_n(T, \cdot) := \hat{\boldsymbol{\alpha}}^T(T)\boldsymbol{\mathcal{K}}(\boldsymbol{x}_c, \cdot)$.

We have to note that the persistence of excitation of $\mathcal{H}_n$ does not imply the convergence of error to 0 since the function f belongs to the infinite-dimensional space $\mathcal{H}_X$. However, it can

be shown that $\limsup_{t\to\infty} \left\| \Pi_n \left(f - \hat{f}_n(t) \right) \right\|_{\mathcal{H}_X}$ is bounded above by a positive constant when, for any t, the function $\left(f - \hat{f}_n(t) \right)$ belongs to a family of uniformly equicontinuous functions and $\boldsymbol{x}$ is uniformly continuous. We refer the reader to [82] for a more detailed discussion on the convergence of parameters in finite-dimensional spaces.

Algorithm 1 gives a step by step procedure for implementing the RKHS adaptive estimator.

3.5 Numerical Simulation Results

In this section, we consider the prototypical piezoelectric oscillator example modeled in Section 3.2 to study the effectiveness of an RKHS adaptive estimator and make qualitative studies of convergence. As emphasized above, the finite-dimensional Equations 3.17 and 3.18 are stated for the general analysis when the unknown function $f = f(x_1, x_2)$. In this section, we study qualitative convergence properties in the specific case that $f = f(x_1)$. For this specific example, it is straightforward to show that the finite-dimensional equations have the form

$$\begin{aligned} \dot{\hat{\boldsymbol{x}}}_n(t) &= A\hat{\boldsymbol{x}}_n(t) + B\mathrm{u}(t) + B_N \mathcal{E}_{x_1(t)} \Pi_n^* \hat{f}_n(t), \\ \dot{\hat{f}}_n(t) &= \Gamma^{-1} \left(B_N \mathcal{E}_{x_1(t)} \Pi_n^* \right)^* P \tilde{\boldsymbol{x}}_n(t). \end{aligned}$$

These equations evolve in $\mathbb{R}^d \times \mathcal{H}_n$, where

$$\mathcal{H}_n = span\{\mathcal{K}(x_{1,i}, \cdot)\}$$

is defined in terms of the kernel on $\mathbb{R}$, $\mathcal{K} : \mathbb{R} \times \mathbb{R} \to \mathbb{R}$ and displacement samples $\boldsymbol{x}_c = \{x_{1,i}\}_{i=1}^n = \Omega_n \subseteq \Omega \subseteq \mathbb{R}$. With this interpretation and the definition $\mathcal{K}(\boldsymbol{x}_c, \boldsymbol{x}(t)) := \{\mathcal{K}(x_{1,1}, x_1(t)), \ldots, \mathcal{K}(x_{1,n}, x_1(t))\}^T$, the specific governing equations still have the form shown

in Equations 3.19, 3.20, and Algorithm 1 applies. Tables 3.1 and 3.2 list the numerical values of the parameters used to build the actual model shown in Equation 3.10. We used the shape function corresponding to the first cantilever beam mode while modeling the system to get Equations 3.8 and 3.9. Table 3.2 also shows the input used to drive the actual system.

Table 3.1: Piezoceramic parameters used in simulations

	Parameter	Value
Piezoceramic (PIC 151)	ρ_p	7790 (kg/m^3)
	h_p	0.001 (m)
	a	0
	b	l
	$d_{31,0}$	-2.1e-10 (m/V)
	$d_{31,1}$	-36.9746 (m/V)
	$d_{31,2}$	-0.03596 (m/V)
	E_{p0}	0.667e+11 (Pa)
	E_{p1}	-3.328e-12 (Pa)
	E_{p2}	-1.4e+18 (Pa)
	ϵ_{33}	2.12e-8 (F/m)

Table 3.2: Other parameters of the actual system used in simulations

	Parameter	Value
Substrate	Material	St 37
	ρ_b	7800 (kg/m^3)
	C_b	2.089e+11 (Pa)
	l	0.4 (m)
	b	0.025 (m)
	h	0.003 (m)
Damping	α	0.1
	β	1e-3
Input	u(t)	$A\sin(\omega t)$
	Amplitude A	1 (m/s^2)
	Frequency ω	22.5 (rad/s)

Figure 3.3 shows the steady-state response of the actual piezoelectric system. This figure gives us an estimate of maximum and minimum displacement. Under the assumption that the unknown nonlinear term is a function of displacement only, it is clear that the set $\Omega \subseteq \mathbb{R}$. For this problem, the set Ω is the closed interval from minimum displacement to the maximum displacement. For the adaptive estimator, the reproducing kernel implemented in

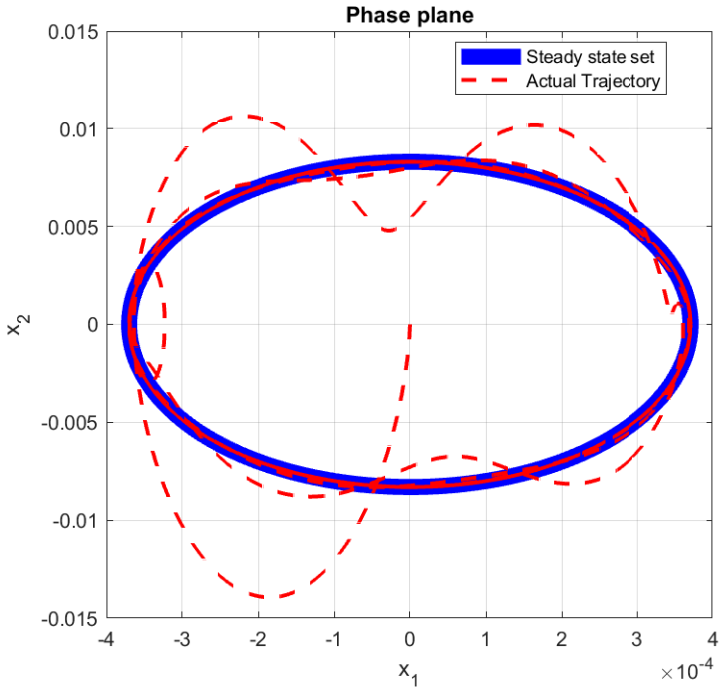

Figure 3.3: The trajectory in the phase plane starting at $[0,0]^T$ eventually converges to the steady-state set.

the simulation was selected to be the popular exponential function

$$\mathcal{K}(x,y) = e^{-\frac{||x-y||^2}{2\sigma^2}}.$$

Thus, $\mathcal{H}_\Omega$ is the set defined as

$$\mathcal{H}_\Omega := \overline{\{\mathcal{K}(x,\cdot) = e^{-\frac{||x-\cdot||^2}{2\sigma^2}} | x \in \Omega \subseteq \mathbb{R}\}},$$

where σ is the standard deviation of the radial basis function. For the simulations, we used $\sigma = 1e{-}9$. As shown in Figure 3.4, a total of 24 equidistant points were chosen in the interval $\Omega = [-0.00037018, 0.00037026]$ and the kernel functions were centered at these points. It is clear from the state-state trajectory in Figure 3.3 that the hypotheses for the sufficient condition given in Theorem 3.9 are satisfied.

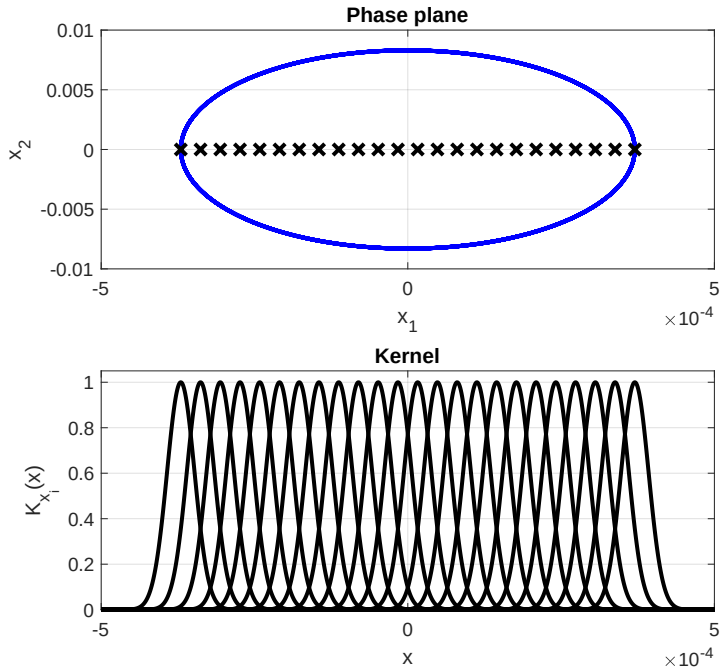

Figure 3.4: Radial basis functions centered at equidistant points in Ω.

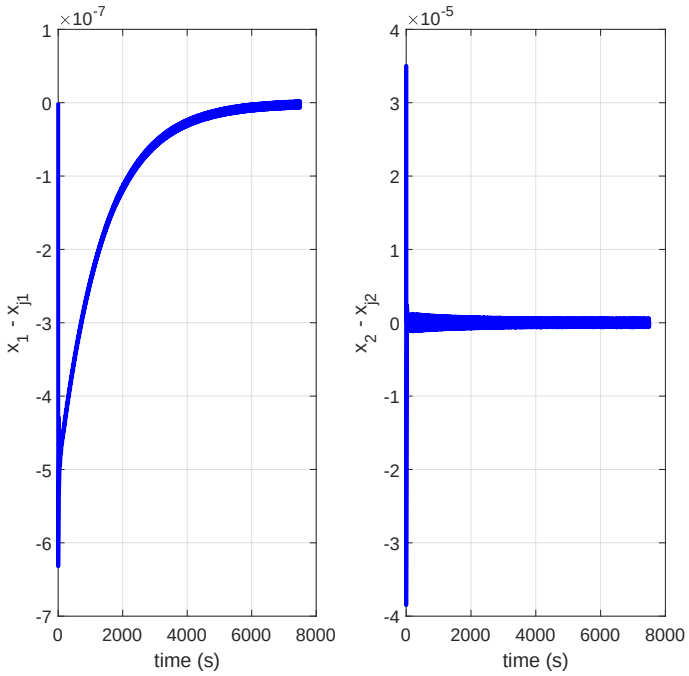

Figure 3.5: Evolution of state error with time.

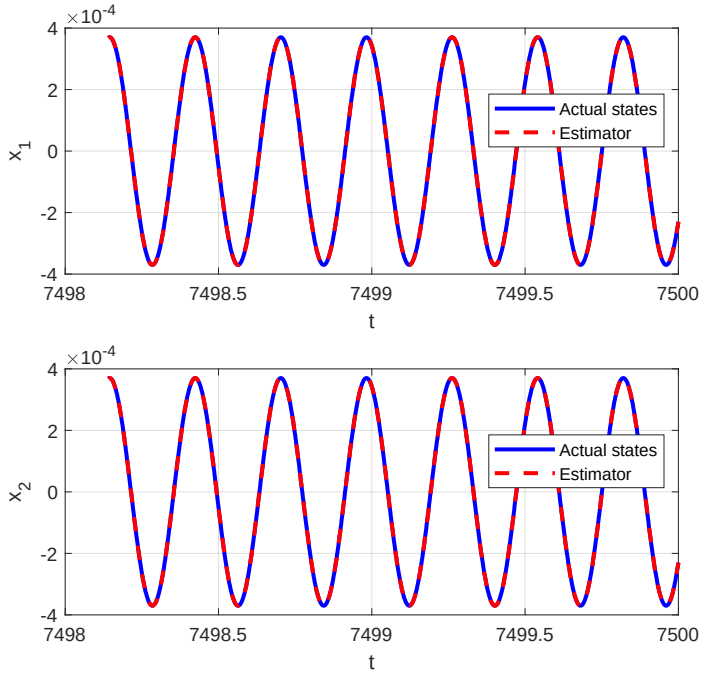

Figure 3.6: Actual states and state estimate - final 500 timesteps

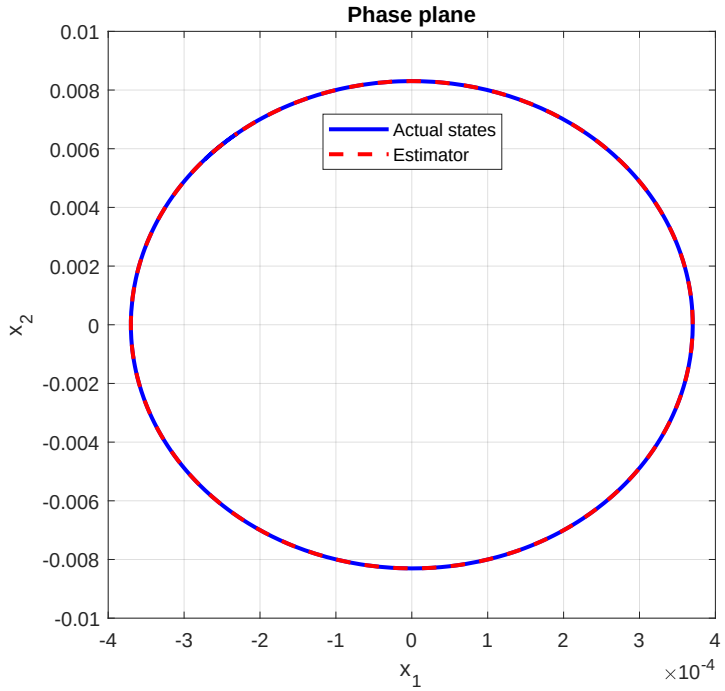

Figure 3.7: Actual states and state estimates in phase plane after convergence of state error.

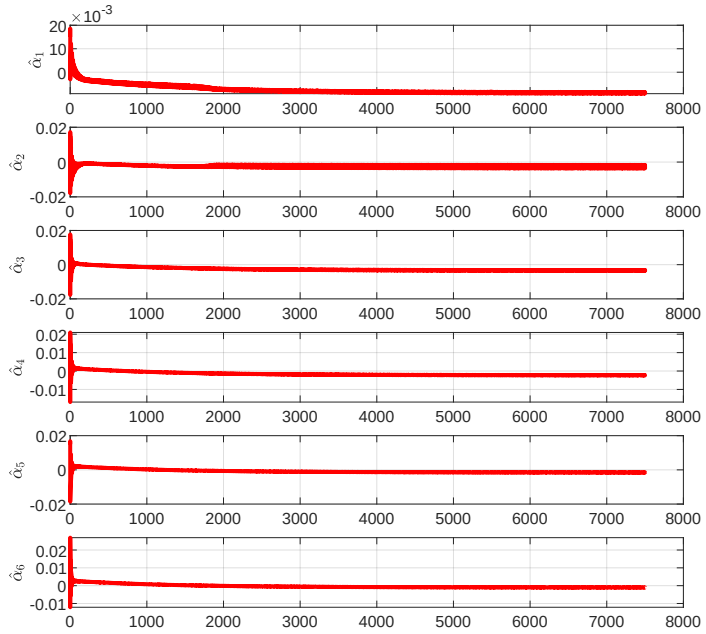

Figure 3.8: Evolution of the parameter estimates $\hat{\alpha}_1 - \hat{\alpha}_6$ with time.

Figure 3.5 shows the time history of the state errors. As expected, the state errors eventually converge to zero. Figure 3.6 shows the final 500-time-steps of the actual states and the estimated states. Figure 3.7 shows the corresponding phase plot. It is clear from these plots that the estimator tracks the actual states with almost no error.

Figures 3.8, 3.9, 3.10 and 3.11 show the evolution of the parameters. It is clear from the figures that the estimated parameters converge to a constant as time $t \to \infty$.

The plot of the actual function f and estimated function $\hat{f}_i$ evaluated on $\mathbb{R}$ can be seen in Figure 3.12. Figure 3.13 shows the pointwise error between the actual and estimated functions. The figures shows that the actual and estimated functions agree on Ω. Recall that convergence of the function error is guaranteed on the set Ω in the norm on $\mathcal{H}_X$ essentially. This amounts to a guarantee of the pointwise error over the set Ω. No guarantee is made

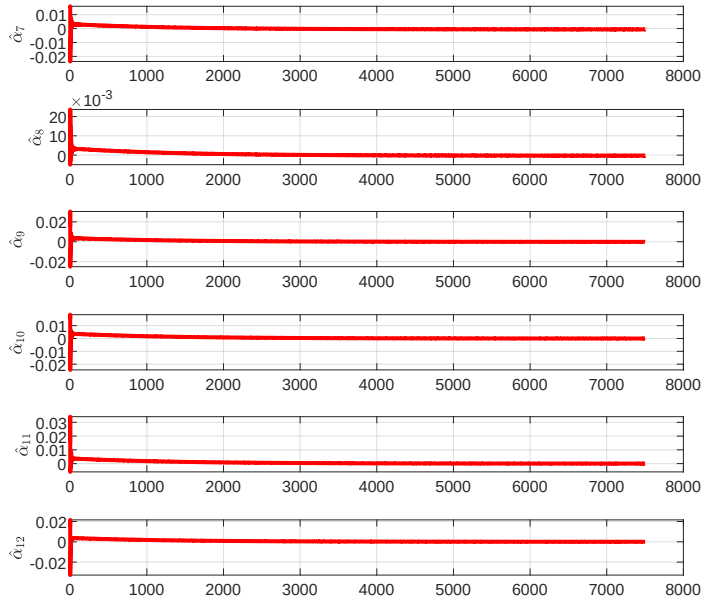

Figure 3.9: Evolution of the parameter estimates $\hat{\alpha}_7 - \hat{\alpha}_{12}$ with time.

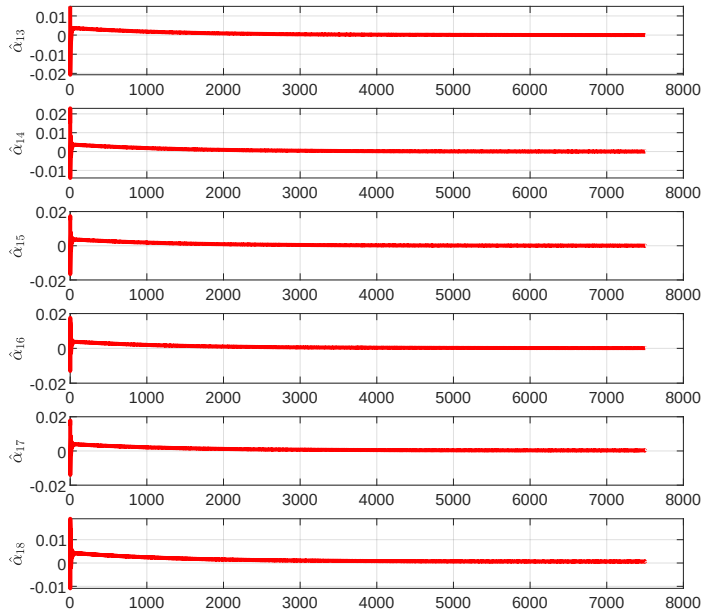

Figure 3.10: Evolution of the parameter estimates $\hat{\alpha}_{13} - \hat{\alpha}_{18}$ with time.

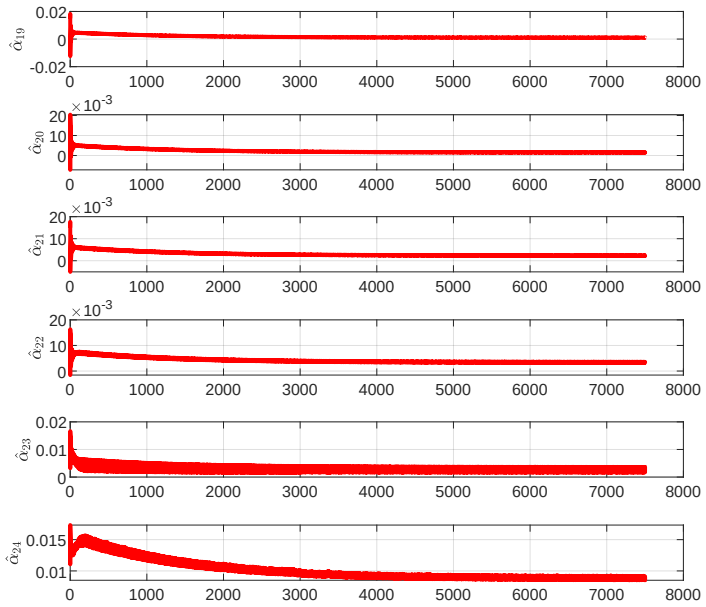

Figure 3.11: Evolution of the parameter estimates $\hat{\alpha}_{19} - \hat{\alpha}_{24}$ with time.

for values outside Ω. See [79, 80, 81] for more details on the convergence.

3.6 Conclusion

This chapter has introduced a novel approach to model and estimate uncertain nonlinear piezoelectric oscillators, and the effectiveness of the approach has been validated by testing it on a nonlinear piezoelectric bimorph beam. The nonlinear function used in the numerical study depended only on the displacement, but much of the theory applies to more complex uncertainties. It would be of interest to study the effectiveness of such estimators on more complex oscillators, ones for which unknown nonlinearities depend on all the states. The algorithm discussed in this chapter follows a general framework and can be adapted easily to model many other nonlinearities. Robustness of the current algorithm and its effectiveness in the presence of noise would be of great interest and remains to be explored and would

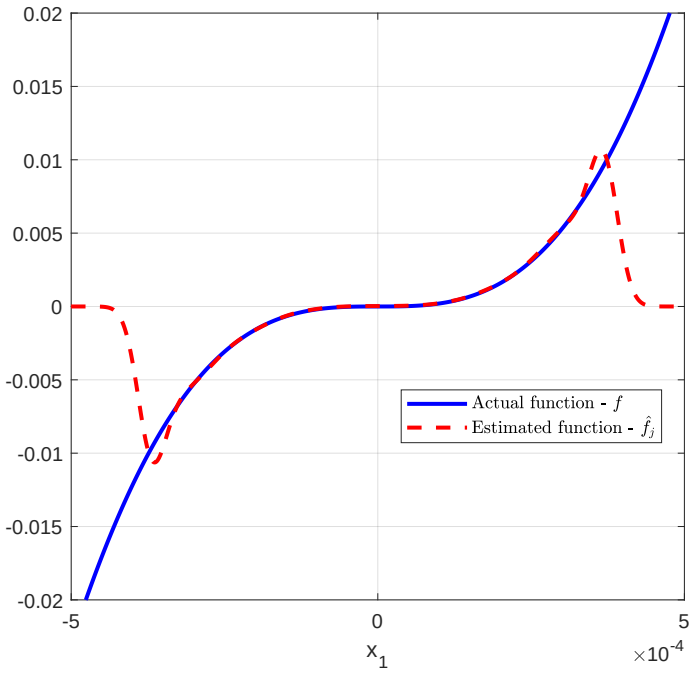

Figure 3.12: Actual function and function estimate on $\mathbb{R}$.

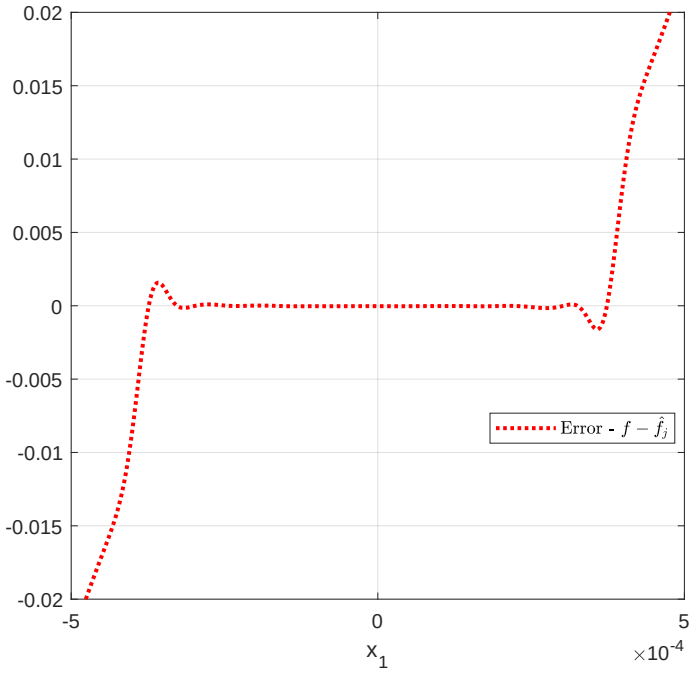

Figure 3.13: Error between actual function and function estimate on $\mathbb{R}$.

complement the findings in the current study.

F Piezoelectric Oscillator - Governing Equations

In this section, we go over the detailed steps involved in the derivation of the infinite-dimensional governing equation of the piezoelectric oscillator shown in Figure 3.1. The kinetic energy and the electric potential are given by Equation 3.3 and Equation 3.5, respectively. Using Hamilton's principle, we get the variational identity

$$\begin{aligned}\delta\int_{t_0}^{t_1}(T-\mathcal{V}_{\mathcal{H}})dt = \delta\int_{t_0}^{t_1}\Bigg\{&\left[\frac{1}{2}\mathrm{m}\int_0^l(\dot{w}+\dot{z})^2dx\right]\\ &-\left[\frac{1}{2}C_bI_b\int_0^l(w'')^2dx+2a_{(0,2)}\int_a^b(w'')^2dx\right.\\ &+2a_{(2,4)}\int_a^b(w'')^4dx+2b_{(1,1)}\left[\int_a^b w''dx\right]E_z\\ &\left.+2b_{(3,1)}\left[\int_a^b(w'')^3dx\right]E_z-2b_{(0,2)}E_z^2\right]\Bigg\}dt=0.\end{aligned} \tag{3.21}$$

The above variational statement can be rewritten as

$$\begin{aligned}\delta\int_{t_0}^{t_1}(T-\mathcal{V}_{\mathcal{H}})dt = \int_{t_0}^{t_1}\Bigg\{&\int_0^l(\mathrm{m}\dot{w}\delta\dot{w}+\mathrm{m}\dot{z}\delta\dot{w})dx\\ &-\int_0^l C_bI_bw''\delta w''dx-4a_{(0,2)}\int_a^b w''\delta w''dx\\ &-8a_{(2,4)}\int_a^b(w'')^3\delta w''dx-2b_{(1,1)}\left(\int_a^b(\delta w'')dx\right)E_z\\ &-2b_{(1,1)}\left(\int_a^b w''dx\right)\delta E_z-6b_{(3,1)}\left(\int_a^b(w'')^2\delta w''dx\right)E_z\\ &-2b_{(3,1)}\left(\int_a^b(w'')^3dx\right)\delta E_z+4b_{(0,2)}E_z\delta E_z\Bigg\}dt=0\end{aligned} \tag{3.22}$$

After integrating the above statement by parts, we get

$$\begin{aligned}
\int_{t_0}^{t_1} \Bigg\{ &- \int_0^l \Big[\mathrm{m}\ddot{w} + \mathrm{m}\ddot{z} + C_b I_b w'''' + 4a_{(0,2)} \left(\chi_{[a,b]} w''\right)'' + 8a_{(2,4)} (\chi_{[a,b]} (w'')^3)'' \\
&\qquad + 2b_{(1,1)} \chi''_{[a,b]} E_z + 6b_{(3,1)} (\chi_{[a,b]} (w'')^2)'' E_z \Big] \delta w dx \\
&- \left[2b_{(1,1)} \left(\int_0^l \chi_{[a,b]} w'' dx \right) + 2b_{(3,1)} \left(\int_0^l \chi_{[a,b]} (w'')^3 dx \right) - 4b_{(0,2)} E_z \right] \delta E_z \\
&- \left\{ C_b I_b w'' + 4a_{(0,2)} \chi_{[a,b]} w'' + 8a_{(2,4)} \chi_{[a,b]} (w'')^3 + 2b_{(1,1)} \chi_{[a,b]} E_z + 6b_{(3,1)} \chi_{[a,b]} (w'')^2 \right\} \delta w' \Big|_0^l \\
&+ \Big\{ C_b I_b w''' + 4a_{(0,2)} \left(\chi_{[a,b]} w''\right)' + 8a_{(2,4)} \left(\chi_{[a,b]} (w'')^3\right)' \\
&\qquad + 2b_{(1,1)} \chi'_{[a,b]} E_z + 6b_{(3,1)} \left(\chi_{[a,b]} (w'')^2\right)' \Big\} \delta w \Big|_0^l \Bigg\} dt = 0.
\end{aligned}$$

Note, in the above statement, the term $\chi_{[a,b]}$ is called the characteristic function of $[a, b]$ and is defined as

$$\chi_{[a,b]}(x) := \begin{cases} 1 & \text{if } x \in [a, b], \\ 0 & \text{if } x \notin [a, b]. \end{cases} \tag{3.23}$$

Since the variation of w and E_z are arbitrary, we can conclude that the equations of motion of the nonlinear piezoelectric cantilevered bimorph have the form shown in Equations 3.6 and 3.7.

G Single Mode Approximation of the Piezoelectric Oscillator Governing Equations

As mentioned earlier, the effects of nonlinearity in piezoelectric oscillators are most noticeable near the natural frequency of the system. Hence, single-mode models are sufficient to model the dynamics as long as the range of input excitation is restricted to a band around the first

natural frequency. Let us introduce the single-mode approximation $w(x,t) = \psi(x)u(t)$. To make calculations easier, let us introduce this approximation into the variational statement shown in Equation 3.22. Further, note that

$$\int_{t_0}^{t_1}\int_0^l \mathrm{m}\dot{w}\delta\dot{w}dxdt = -\int_{t_0}^{t_1}\int_0^l \mathrm{m}\ddot{w}\delta w dxdt,$$
$$\int_{t_0}^{t_1}\int_0^l \mathrm{m}\dot{z}\delta\dot{w}dxdt = -\int_{t_0}^{t_1}\int_0^l \mathrm{m}\ddot{z}\delta w dxdt.$$

After introducing the approximation for $w(x,t)$ into the variational statement in Equation 3.22 and using the equations shown above, we get the variational statement

$$\begin{aligned}0 = \int_{t_0}^{t_1}\Bigg\{ &-\Bigg[\mathrm{m}\left(\int_0^l \psi^2(x)dx\right)\ddot{u} + \mathrm{m}\left(\int_0^l \psi(x)dx\right)\ddot{z} + C_bI_b\left(\int_0^l \left(\psi''(x)\right)^2 dx\right)u \\ &+ 4a_{(0,2)}\left(\int_0^l \chi_{[a,b]}\left(\psi''(x)\right)^2\right)u + 8a_{(2,4)}\left(\int_0^l \chi_{[a,b]}\left(\psi''(x)\right)^4 dx\right)u^3 \\ &+ 2b_{(1,1)}E_z\left(\int_0^l \chi_{[a,b]}\psi''(x)dx\right) + 6b_{(3,1)}\left(\int_0^l \chi_{[a,b]}\left(\psi''(x)\right)^3\right)u^2E_z\Bigg]\delta u \\ &-\left[2b_{(1,1)}\left(\int_0^l \chi_{[a,b]}\psi''(x)dx\right)u + 2b_{(3,1)}\left(\int_0^l \chi_{[a,b]}\left(\psi''(x)\right)^3\right)u^3 - 4b_{(0,2)}E_z\right]\delta E_z\Bigg\}dt\end{aligned}$$

Thus, the approximated equation of motion are

$$\begin{aligned}&\underbrace{\mathrm{m}\left(\int_0^l \psi^2(x)dx\right)}_{M}\ddot{u} + \underbrace{\mathrm{m}\left(\int_0^l \psi(x)dx\right)}_{P}\ddot{z} \\ &\quad + \underbrace{C_bI_b\left(\int_0^l \left(\psi''(x)\right)^2 dx\right)}_{K_b}u + \underbrace{4a_{(0,2)}\left(\int_0^l \chi_{[a,b]}\left(\psi''(x)\right)^2\right)}_{K_p}u \\ &\quad + \underbrace{8a_{(2,4)}\left(\int_0^l \chi_{[a,b]}\left(\psi''(x)\right)^4 dx\right)}_{K_N}u^3 + \underbrace{2b_{(1,1)}\left(\int_0^l \chi_{[a,b]}\psi''(x)dx\right)}_{\mathcal{B}}E_z\end{aligned}$$

$$+ \underbrace{6b_{(3,1)}\left(\int_0^l \chi_{[a,b]}\left(\psi''(x)\right)^3\right)}_{Q_N} u^2 E_z = 0,$$

$$\underbrace{2b_{(1,1)}\left(\int_0^l \chi_{[a,b]}\psi''(x)dx\right)}_{\mathcal{B}} u(t) + \underbrace{2b_{(3,1)}\left(\int_0^l \chi_{[a,b]}\left(\psi''(x)\right)^3\right)}_{\mathcal{B}_N} u^3(t) = \underbrace{4b_{(0,2)}}_{\mathcal{C}} E_z.$$

These calculations generate the approximated Equations 3.8 and 3.9.

Bibliography

[1] H T Banks, R C Smith, and Y Wang. *Smart material structures: modeling, estimation, and control*. Wiley, Chichester;New York;Paris;, 1996. ISBN 9782225852145;9780471970248;0471970247;2225852146;.

[2] Ralph C Smith. *Smart material systems: model development*. SIAM, 2005. ISBN 0898715830.

[3] Donald J L Leo. *Engineering Analysis of Smart Material Systems*. John Wiley & Sons, Inc., 2007. ISBN 9780471684770. doi: 10.1002/9780470209721. URL http://doi.wiley.com/10.1002/9780470209721.

[4] A. Preumont. *Mechatronics: Dynamics of Electromechanical and Piezoelectric Systems*. Springer, Dordrecht, 2006. ISBN 1402046952. doi: 10.1007/1-4020-4696-0. URL https://link-springer-com.ezproxy.lib.vt.edu/book/10.1007{%}2F1-4020-4696-0{#}authorsandaffiliationsbook.

[5] Alper Erturk and Daniel J. Inman. *Piezoelectric Energy Harvesting*. John Wiley & Sons, Ltd, Chichester, UK, April 2011. ISBN 9781119991151. doi: 10.1002/9781119991151. URL http://doi.wiley.com/10.1002/9781119991151.

[6] Shashank Priya and Daniel J. Inman. *Energy harvesting technologies*. 2009. ISBN 9780387764634. doi: 10.1007/978-0-387-76464-1.

[7] Gérard A Maugin. *Nonlinear electromechanical effects and applications*, volume 1. World Scientific Publishing Company, 1986. ISBN 9813104007.

[8] Jiashi Yang. *Analysis of piezoelectric devices*. World Scientific, 2006. ISBN 9812773185.

[9] Jiashi Yang. *An introduction to the theory of piezoelectricity*, volume 9 of *Advances in Mechanics and Mathematics*. Springer, Boston, 2005. ISBN 978-0-387-23573-8. doi: https://doi-org.ezproxy.lib.vt.edu/10.1007/b101799. URL http://link.springer.com/10.1007/b101799.

[10] Yi-Yuan Yu. *Vibrations of elastic plates: linear and nonlinear dynamical modeling of sandwiches, laminated composites, and piezoelectric layers*. Springer Science & Business Media, 2012. ISBN 1461223385.

[11] U von Wagner and P Hagedorn. Piezo–beam systems subjected to weak electric field: experiments and modelling of non-linearities. *Journal of Sound and Vibration*, 256(5): 861–872, 2002. ISSN 0022-460X. doi: https://doi.org/10.1006/jsvi.2002.5024. URL http://www.sciencedirect.com/science/article/pii/S0022460X02950248.

[12] Utz von Wagner and Peter Hagedorn. Nonlinear Effects of Piezoceramics Excited by Weak Electric Fields. *Nonlinear Dynamics*, 31(2):133–149, 2003. ISSN 1573-269X. doi: 10.1023/A:1022093428599. URL https://doi.org/10.1023/A:1022093428599.

[13] Utz von Wagner. Non-linear longitudinal vibrations of piezoceramics excited by weak electric fields. *International Journal of Non-Linear Mechanics*, 38(4):565–574, 2003. ISSN 0020-7462. doi: https://doi.org/10.1016/S0020-7462(01)00113-5. URL http://www.sciencedirect.com/science/article/pii/S0020746201001135.

[14] Utz von Wagner. Non-linear longitudinal vibrations of non-slender piezoceramic rods. *International Journal of Non-Linear Mechanics*, 39(4):673–688, 2004. ISSN 0020-7462. doi: https://doi.org/10.1016/S0020-7462(03)00108-2. URL http://www.sciencedirect.com/science/article/pii/S0020746203001082.

[15] Samuel C Stanton, Alper Erturk, Brian P Mann, and Daniel J Inman. Nonlinear piezoelectricity in electroelastic energy harvesters: Modeling and experimental identifi-

cation. *Journal of Applied Physics*, 108(7):74903, October 2010. ISSN 0021-8979. doi: 10.1063/1.3486519. URL https://doi.org/10.1063/1.3486519.

[16] Samuel C Stanton, Alper Erturk, Brian P Mann, Earl H Dowell, and Daniel J Inman. Nonlinear nonconservative behavior and modeling of piezoelectric energy harvesters including proof mass effects. *Journal of Intelligent Material Systems and Structures*, 23 (2):183–199, January 2012. ISSN 1045-389X. doi: 10.1177/1045389X11432656. URL https://doi.org/10.1177/1045389X11432656.

[17] K Wolf and O Gottlieb. Nonlinear dynamics of a noncontacting atomic force microscope cantilever actuated by a piezoelectric layer. *Journal of Applied Physics*, 91(7):4701–4709, March 2002. ISSN 0021-8979. doi: 10.1063/1.1458056. URL https://doi.org/10.1063/1.1458056.

[18] Tim Usher and Alec Sim. Nonlinear dynamics of piezoelectric high displacement actuators in cantilever mode. *Journal of Applied Physics*, 98(6):64102, September 2005. ISSN 0021-8979. doi: 10.1063/1.2041844. URL https://doi.org/10.1063/1.2041844.

[19] Angela Triplett and D Dane Quinn. The Effect of Non-linear Piezoelectric Coupling on Vibration-based Energy Harvesting. *Journal of Intelligent Material Systems and Structures*, 20(16):1959–1967, August 2009. ISSN 1045-389X. doi: 10.1177/1045389X09343218. URL https://doi.org/10.1177/1045389X09343218.

[20] John Guckenheimer and Philip Holmes. *Nonlinear oscillations, dynamical systems, and bifurcations of vector fields*, volume 42. Springer Science & Business Media, 2013. ISBN 1461211409.

[21] Stephen Wiggins. *Introduction to applied nonlinear dynamical systems and chaos*, volume 2. Springer Science & Business Media, 2003. ISBN 0387001778.

[22] Ali H Nayfeh. *Introduction to perturbation techniques*. John Wiley & Sons, 2011. ISBN 3527618457.

[23] Augusto Visintin. *Differential models of hysteresis*, volume 111. Springer Science & Business Media, 2013. ISBN 3662115573.

[24] Martin Brokate and Jürgen Sprekels. *Hysteresis and phase transitions*, volume 121. Springer Science & Business Media, 2012. ISBN 1461240484.

[25] Ping Ge and Musa Jouaneh. Modeling hysteresis in piezoceramic actuators. *Precision Engineering*, 17(3):211–221, 1995. ISSN 0141-6359. doi: https://doi.org/10.1016/0141-6359(95)00002-U. URL http://www.sciencedirect.com/science/article/pii/014163599500002U.

[26] H Hu and R Ben Mrad. On the classical Preisach model for hysteresis in piezoceramic actuators. *Mechatronics*, 13(2):85–94, 2003. ISSN 0957-4158. doi: https://doi.org/10.1016/S0957-4158(01)00043-5. URL http://www.sciencedirect.com/science/article/pii/S0957415801000435.

[27] S Xiao and Y Li. Modeling and High Dynamic Compensating the Rate-Dependent Hysteresis of Piezoelectric Actuators via a Novel Modified Inverse Preisach Model. *IEEE Transactions on Control Systems Technology*, 21(5):1549–1557, 2013. ISSN 1558-0865 VO - 21. doi: 10.1109/TCST.2012.2206029.

[28] M Rakotondrabe. Classical Prandtl-Ishlinskii modeling and inverse multiplicative structure to compensate hysteresis in piezoactuators. In *2012 American Control Conference (ACC)*, pages 1646–1651, 2012. ISBN 2378-5861 VO -. doi: 10.1109/ACC.2012.6314620.

[29] Y Qin, Y Tian, D Zhang, B Shirinzadeh, and S Fatikow. A Novel Direct Inverse Modeling Approach for Hysteresis Compensation of Piezoelectric Actuator in Feedforward

Applications. *IEEE/ASME Transactions on Mechatronics*, 18(3):981–989, 2013. ISSN 1941-014X VO - 18. doi: 10.1109/TMECH.2012.2194301.

[30] Wei Tech Ang, F A Garmon, P K Khosla, and C N Riviere. Modeling rate-dependent hysteresis in piezoelectric actuators. In *Proceedings 2003 IEEE/RSJ International Conference on Intelligent Robots and Systems (IROS 2003) (Cat. No.03CH37453)*, volume 2, pages 1975–1980 vol.2, 2003. ISBN VO - 2. doi: 10.1109/IROS.2003.1248937.

[31] Y L Zhang, M L Han, M Y Yu, C Y Shee, and W T Ang. Automatic Hysteresis Modeling of Piezoelectric Micromanipulator in Vision-Guided Micromanipulation Systems. *IEEE/ASME Transactions on Mechatronics*, 17(3):547–553, 2012. ISSN 1941-014X VO - 17. doi: 10.1109/TMECH.2011.2106136.

[32] Z Li, J Shan, and U Gabbert. Inverse Compensation of Hysteresis Using Krasnoselskii-Pokrovskii Model. *IEEE/ASME Transactions on Mechatronics*, 23(2):966–971, 2018. ISSN 1941-014X VO - 23. doi: 10.1109/TMECH.2018.2805761.

[33] H T Banks, A J Kurdila, and G Webb. Identification of hysteretic control influence operators representing smart actuators part I: Formulation. *Mathematical Problems in Engineering*, 3:723495, 1997. ISSN 1024-123X. doi: 10.1155/S1024123X97000586. URL https://doi.org/10.1155/S1024123X97000586.

[34] William S Galinaitis and Robert C Rogers. Control of a hysteretic actuator using inverse hysteresis compensation. In *Proc.SPIE*, volume 3323, July 1998. doi: 10.1117/12.316308. URL https://doi.org/10.1117/12.316308.

[35] M Goldfarb and N Celanovic. Modeling piezoelectric stack actuators for control of micromanipulation. *IEEE Control Systems Magazine*, 17(3):69–79, 1997. ISSN 1941-000X VO - 17. doi: 10.1109/37.588158.

[36] Yanfang Liu, Jinjun Shan, Ulrich Gabbert, and Naiming Qi. Hysteresis and creep modeling and compensation for a piezoelectric actuator using a fractional-order Maxwell resistive capacitor approach. *Smart Materials and Structures*, 22(11):115020, 2013. ISSN 0964-1726. doi: 10.1088/0964-1726/22/11/115020. URL http://dx.doi.org/10.1088/0964-1726/22/11/115020.

[37] Wei Zhu and Xiao-Ting Rui. Hysteresis modeling and displacement control of piezoelectric actuators with the frequency-dependent behavior using a generalized Bouc–Wen model. *Precision Engineering*, 43:299–307, 2016. ISSN 0141-6359. doi: https://doi.org/10.1016/j.precisioneng.2015.08.010. URL http://www.sciencedirect.com/science/article/pii/S0141635915001555.

[38] M Rakotondrabe. Bouc–Wen Modeling and Inverse Multiplicative Structure to Compensate Hysteresis Nonlinearity in Piezoelectric Actuators. *IEEE Transactions on Automation Science and Engineering*, 8(2):428–431, 2011. ISSN 1558-3783 VO - 8. doi: 10.1109/TASE.2010.2081979.

[39] T S Low and W Guo. Modeling of a three-layer piezoelectric bimorph beam with hysteresis. *Journal of Microelectromechanical Systems*, 4(4):230–237, 1995. ISSN 1941-0158 VO - 4. doi: 10.1109/84.475550.

[40] Qingsong Xu and Yangmin Li. Dahl Model-Based Hysteresis Compensation and Precise Positioning Control of an XY Parallel Micromanipulator With Piezoelectric Actuation. *Journal of Dynamic Systems, Measurement, and Control*, 132(4), June 2010. ISSN 0022-0434. doi: 10.1115/1.4001712. URL https://doi.org/10.1115/1.4001712.

[41] S K Shome, M Prakash, A Mukherjee, and U Datta. Dither control for Dahl model based hysteresis compensation. In *2013 IEEE International Conference on Signal Processing,*

Computing and Control (ISPCC), pages 1–6, 2013. ISBN VO -. doi: 10.1109/ISPCC.2013.6663460.

[42] Chih-Jer Lin and Po-Ting Lin. Tracking control of a biaxial piezo-actuated positioning stage using generalized Duhem model. *Computers & Mathematics with Applications*, 64 (5):766–787, 2012. ISSN 0898-1221. doi: https://doi.org/10.1016/j.camwa.2011.12.015. URL http://www.sciencedirect.com/science/article/pii/S0898122111010583.

[43] W Xie, J Fu, H Yao, and C . Su. Observer based control of piezoelectric actuators with classical Duhem modeled hysteresis. In *2009 American Control Conference*, pages 4221–4226, 2009. ISBN 2378-5861 VO -. doi: 10.1109/ACC.2009.5159851.

[44] Jinqiang Gan and Xianmin Zhang. A review of nonlinear hysteresis modeling and control of piezoelectric actuators. *AIP Advances*, 9(4):40702, April 2019. doi: 10.1063/1.5093000. URL https://doi.org/10.1063/1.5093000.

[45] David J Ewins. *Modal testing: theory and practice*, volume 15. Research studies press Letchworth, 1984.

[46] Chih-Cheng Kao and Rong-Fong Fung. Using the modified PSO method to identify a Scott-Russell mechanism actuated by a piezoelectric element. *Mechanical Systems and Signal Processing*, 23(5):1652–1661, 2009. ISSN 0888-3270. doi: https://doi.org/10.1016/j.ymssp.2008.12.003. URL http://www.sciencedirect.com/science/article/pii/S0888327008003166.

[47] Rong-Fong Fung, Yi-Lung Hsu, and Ming-Shyan Huang. System identification of a dual-stage XY precision positioning table. *Precision Engineering*, 33(1):71–80, 2009. ISSN 0141-6359. doi: https://doi.org/10.1016/j.precisioneng.2008.04.002. URL http://www.sciencedirect.com/science/article/pii/S0141635908000391.

[48] Ching-Ming Chen, Yen-Chun Hsu, and Rong-Fong Fung. System identification of a Scott–Russell amplifying mechanism with offset driven by a piezoelectric actuator. *Applied Mathematical Modelling*, 36(6):2788–2802, 2012. ISSN 0307-904X. doi: https://doi.org/10.1016/j.apm.2011.09.064. URL http://www.sciencedirect.com/science/article/pii/S0307904X11006238.

[49] J Kutz, S Brunton, B Brunton, and J Proctor. *Dynamic Mode Decomposition: Data-Driven Modeling of Complex Systems*. Society for Industrial and Applied Mathematics, November 2016. ISBN 978-1-61197-449-2. doi: doi:10.1137/1.9781611974508. URL https://doi.org/10.1137/1.9781611974508.

[50] Jonathan H Tu, Clarence W Rowley, Dirk M Luchtenburg, Steven L Brunton, and J Nathan Kutz. On dynamic mode decomposition: Theory and applications. *Journal of Computational Dynamics*, 1(2):391–421, 2014. ISSN 2158-2491_2014_2_391. doi: 10.3934/jcd.2014.1.391. URL http://aimsciences.org//article/id/1dfebc20-876d-4da7-8034-7cd3c7ae1161.

[51] Nikolas Bravo, Ralph C Smith, and John Crews. Surrogate model development and feedforward control implementation for PZT bimorph actuators employed for robobee. In *Proc.SPIE*, volume 10165, April 2017. URL https://doi.org/10.1117/12.2259948.

[52] Nikolas Bravo, Ralph C Smith, and John Crews. Data-Driven Model Development and Feedback Control Design for PZT Bimorph Actuators, 2017. URL http://dx.doi.org/10.1115/SMASIS2017-3847.

[53] Nikolas Bravo and Ralph C Smith. Parameter-dependent surrogate model development for PZT bimorph actuators employed for micro-air vehicles. In *Proc.SPIE*, volume 10968, March 2019. URL https://doi.org/10.1117/12.2514246.

[54] Andrew J. Kurdila and Parag Bobade. Koopman Theory and Linear Approximation Spaces. November 2018. URL https://arxiv.org/abs/1811.10809.

[55] Helon V Hultmann Ayala, Didace Habineza, Micky Rakotondrabe, Carlos E Klein, and Leandro S Coelho. Nonlinear Black-box System Identification through Neural Networks of a Hysteretic Piezoelectric Robotic Micromanipulator. *IFAC-PapersOnLine*, 48(28): 409–414, 2015. ISSN 2405-8963. doi: https://doi.org/10.1016/j.ifacol.2015.12.162. URL http://www.sciencedirect.com/science/article/pii/S240589631502786X.

[56] S M Yang and G S Lee. System Identification of Smart Structures Using Neural Networks. *Journal of Intelligent Material Systems and Structures*, 8(10):883–890, October 1997. ISSN 1045-389X. doi: 10.1177/1045389X9700801008. URL https://doi.org/10.1177/1045389X9700801008.

[57] M Mohammadzaheri, S Grainger, M Bazghaleh, and P Yaghmaee. Intelligent modeling of a piezoelectric tube actuator. In *2012 International Symposium on Innovations in Intelligent Systems and Applications*, pages 1–6, 2012. ISBN VO -. doi: 10.1109/INISTA.2012.6246980.

[58] Morteza Mohammadzaheri, Steven Grainger, and Mohsen Bazghaleh. A comparative study on the use of black box modelling for piezoelectric actuators. *The International Journal of Advanced Manufacturing Technology*, 63(9):1247–1255, 2012. ISSN 1433-3015. doi: 10.1007/s00170-012-3987-5. URL https://doi.org/10.1007/s00170-012-3987-5.

[59] Shuanghe Yu, G Alici, B Shirinzadeh, and J Smith. Sliding Mode Control of a Piezoelectric Actuator with Neural Network Compensating Rate-Dependent Hysteresis. In *Proceedings of the 2005 IEEE International Conference on Robotics and Automation*, pages 3641–3645, 2005. ISBN 1050-4729 VO -. doi: 10.1109/ROBOT.2005.1570674.

[60] Parag Bobade, Suprotim Majumdar, Savio Pereira, Andrew J. Kurdila, and John B. Ferris. Adaptive estimation for nonlinear systems using reproducing kernel Hilbert spaces. *Advances in Computational Mathematics*, 45(2):869–896, 2019. ISSN 1572-9044. doi: 10.1007/s10444-018-9639-z. URL https://doi.org/10.1007/s10444-018-9639-z.

[61] G Joshi and G Chowdhary. Adaptive Control using Gaussian-Process with Model Reference Generative Network. In *2018 IEEE Conference on Decision and Control (CDC)*, pages 237–243, 2018. ISBN 2576-2370 VO -. doi: 10.1109/CDC.2018.8619431.

[62] A M Axelrod, H A Kingravi, and G V Chowdhary. Gaussian process based subsumption of a parasitic control component. In *2015 American Control Conference (ACC)*, pages 2888–2893, 2015. ISBN 0743-1619 VO -. doi: 10.1109/ACC.2015.7171173.

[63] G Chowdhary, H A Kingravi, J P How, and P A Vela. A Bayesian nonparametric approach to adaptive control using Gaussian Processes. In *52nd IEEE Conference on Decision and Control*, pages 874–879, 2013. ISBN 0191-2216 VO -. doi: 10.1109/CDC.2013.6759992.

[64] H Maske, H A Kingravi, and G Chowdhary. Sensor Selection via Observability Analysis in Feature Space. In *2018 Annual American Control Conference (ACC)*, pages 1058–1064, 2018. ISBN 2378-5861 VO -. doi: 10.23919/ACC.2018.8431625.

[65] Joshua Whitman and Girish Chowdhary. Learning Dynamics Across Similar Spatiotemporally-Evolving Physical Systems. In Sergey Levine, Vincent Vanhoucke, and Ken Goldberg, editors, *Proceedings of the 1st Annual Conference on Robot Learning*, volume 78 of *Proceedings of Machine Learning Research*, pages 472–481. PMLR, 2017. URL http://proceedings.mlr.press/v78/whitman17a.html.

[66] H A Kingravi, H Maske, and G Chowdhary. Kernel controllers: A systems-theoretic approach for data-driven modeling and control of spatiotemporally evolving processes.

In *2015 54th IEEE Conference on Decision and Control (CDC)*, pages 7365–7370, 2015. ISBN VO -. doi: 10.1109/CDC.2015.7403382.

[67] Andrew J Kurdila and Pablo Tarazaga. *Vibrations of Linear Piezostructures (In press)*. John Wiley & Sons, Inc., 2018. ISBN 9781119393405.

[68] H. F. Tiersten. *Linear Piezoelectric Plate Vibrations*. Springer US, Boston, MA, 1969. ISBN 978-1-4899-6221-8. doi: 10.1007/978-1-4899-6453-3. URL http://link.springer.com/10.1007/978-1-4899-6453-3.

[69] F Cottone, L Gammaitoni, H Vocca, M Ferrari, and V Ferrari. Piezoelectric buckled beams for random vibration energy harvesting. *Smart Materials and Structures*, 21 (3):35021, 2012. ISSN 0964-1726. doi: 10.1088/0964-1726/21/3/035021. URL http://dx.doi.org/10.1088/0964-1726/21/3/035021.

[70] Michael I Friswell, S Faruque Ali, Onur Bilgen, Sondipon Adhikari, Arthur W Lees, and Grzegorz Litak. Non-linear piezoelectric vibration energy harvesting from a vertical cantilever beam with tip mass. *Journal of Intelligent Material Systems and Structures*, 23(13):1505–1521, August 2012. ISSN 1045-389X. doi: 10.1177/1045389X12455722. URL https://doi.org/10.1177/1045389X12455722.

[71] M Rakotondrabe, Y Haddab, and P Lutz. Quadrilateral Modelling and Robust Control of a Nonlinear Piezoelectric Cantilever. *IEEE Transactions on Control Systems Technology*, 17(3):528–539, 2009. ISSN 2374-0159 VO - 17. doi: 10.1109/TCST.2008.2001151.

[72] N Aronszajn. Theory of Reproducing Kernels. *Transactions of the American Mathematical Society*, 68(3):337–404, 1950. ISSN 00029947. doi: 10.2307/1990404. URL http://www.jstor.org/stable/1990404.

[73] Alain Berlinet and Christine Thomas-Agnan. *Reproducing kernel Hilbert spaces in probability and statistics*. Springer Science & Business Media, 2011. ISBN 1441990968.

[74] Krikamol Muandet, Kenji Fukumizu, Bharath Sriperumbudur, and Bernhard Schölkopf. Kernel mean embedding of distributions: A review and beyond. *Foundations and Trends® in Machine Learning*, 10(1-2):1–141, 2017. ISSN 1935-8237.

[75] Amnon Pazy. *Semigroups of linear operators and applications to partial differential equations*, volume 44. Springer Science & Business Media, 2012. ISBN 1461255619.

[76] P. A. Ioannou and Jing Sun. *Robust Adaptive Control*. Dover Publications Inc., 1996. ISBN 0486498174.

[77] Shankar Sastry and Marc Bodson. *Adaptive control: stability, convergence and robustness*. Courier Corporation, 2011. ISBN 0486482022.

[78] Kumpati S Narendra and Anuradha M Annaswamy. *Stable adaptive systems*. Courier Corporation, 2012. ISBN 048614142X.

[79] Jia Guo, Sai Tej Paruchuri, and Andrew J. Kurdila. Persistence of Excitation in Uniformly Embedded Reproducing KernelHilbert (RKH) Spaces (ACC). In *American Control Conference*, 2020.

[80] Jia Guo, Sai Tej Paruchuri, and Andrew J. Kurdila. Persistence of Excitation in Uniformly Embedded Reproducing Kernel Hilbert (RKH) Spaces. *Systems & Control Letters*, 2019.

[81] Andrew J. Kurdila, Jia Guo, Sai Tej Paruchuri, and Parag Bobade. Persistence of Excitation in Reproducing Kernel Hilbert Spaces, Positive Limit Sets, and Smooth Manifolds. September 2019. URL http://arxiv.org/abs/1909.12274.

[82] A J Kurdila, Francis J Narcowich, and Joseph D Ward. Persistency of excitation in identification using radial basis function approximants. *SIAM journal on control and optimization*, 33(2):625–642, 1995. ISSN 0363-0129.

Chapter 4

Kernel Center Adaptation in the Reproducing Kernel Hilbert Space Embedding Method

Abstract

The performance of adaptive estimators that employ embedding in reproducing kernel Hilbert spaces (RKHS) depends on the choice of the location of basis kernel centers. Parameter convergence and error approximation rates depend on where and how the kernel centers are distributed in the state-space. In this chapter, we develop the theory that relates parameter convergence and approximation rates to the position of kernel centers. We develop criteria for choosing kernel centers in a specific class of systems - ones in which the state trajectory regularly visits the neighborhood of the positive limit set. Two algorithms, based on centroidal Voronoi tessellations and Kohonen self-organizing maps, are derived to choose kernel centers in the RKHS embedding method. Finally, we implement these methods on two practical examples and test their effectiveness.

4.1 Introduction

Adaptive estimation of unknown nonlinearities appearing in dynamical systems is a topic that has been studied over the past four decades. The finite-dimensional versions of such problems are described in classical texts like [1, 2, 3]. The goal of these methods is to estimate an unknown term appearing in the governing ordinary differential equations (ODEs). A common assumption in such problems is that all the states are available for measurement. Many of these methods also assume that the unknown function belongs to some hypothesis space of functions. The particular class of adaptive estimators studied in this chapter assumes that the hypothesis space is a reproducing kernel Hilbert space (RKHS). An RKHS $\mathcal{H}_{\mathbb{R}^d}$ is a Hilbert space of functions on the state-space $\mathbb{R}^d$ that is defined in terms of a positive-definite kernel $\mathcal{K} : \mathbb{R}^d \times \mathbb{R}^d \to \mathbb{R}$. An example of an RKHS is the space generated by the Gaussian radial basis kernels that have the form $\mathcal{K}(x, y) := e^{-\zeta \|x-y\|^2}$, where ζ is positive. The additional structure induced by the kernel $\mathcal{K}$ on $\mathcal{H}_{\mathbb{R}^d}$ enables the proof of crucial convergence results, even for the infinite-dimensional cases. The finite-dimensional version of the RKHS adaptive estimators have been studied in [4, 5]. However, the results for the infinite-dimensional adaptive estimation cases are relatively new and were investigated by Bobade et al. in [6].

In both the finite and infinite-dimensional cases, the unknown function $f \in \mathcal{H}$ has the form $f(\cdot) = \sum_i \alpha_i \mathfrak{K}_{\boldsymbol{x}_i}(\cdot)$, where $\mathfrak{K}_{\boldsymbol{x}_i}(\cdot) := \mathcal{K}(\boldsymbol{x}_i, \cdot)$ with $\boldsymbol{x}_i \in \mathbb{R}^d$. Note, the index $i \in \{1, \ldots, n\}$ for the n-dimensional case while $i \in \mathbb{N}$ for the infinite-dimensional case. We refer to $\mathfrak{K}_{\boldsymbol{x}_i} \in \mathcal{H}$ as the kernel function centered at $\boldsymbol{x}_i$ or the regressor function. Thus, we express the unknown function f as a linear combination of kernels centered at different points in the state-space. When the set of centers are fixed or held constant, the analysis in [1, 2, 3] are applicable. This chapter specifically studies how such centers can be chosen adaptively in the RKHS embedding method.

The general problem of center selection is familiar in both adaptive estimation and in machine learning methods based on radial basis functions (RBF) networks. Roughly speaking, the primary difference between the problem of center selection in these two applications is that computations are usually static or offline in machine learning, whereas they are recursive or online in adaptive estimation. One of the most common unsupervised learning methods for choosing the kernel centers in RBF networks is the k-mean clustering or Lloyd's algorithm [7, 8]. Researchers in the machine learning community have developed sophisticated methods for center selection/adaptation to optimize RBF networks. Some of the early accounts of such methods can be found in [9, 10, 11]. Self-organizing maps are another alternative for clustering data and thereby determining the kernel centers. The technique in [12] relies on adding kernels such that the sum of squared error is minimized. Lin and Chen describe a method that combines Kohonen self-organizing maps and RBF networks in [13]. Kernel centers are chosen based on the condition number of the sensitivity matrix in [14].

Variants of self-organizing RBF networks have also been implemented for dynamical system identification and control. Lian et al. develop a self-organizing RBF network that tunes the RBF network parameters based on an adaptation law. [15] They used this method for real-time approximation of dynamical systems. Han et al. describe a version of self-organizing RBF networks that use a growing and pruning algorithm in [16]. They illustrate the effectiveness of such networks and their variants [17] for dynamical system identification and model predictive control. [18, 19, 20]

Researchers have also studied the application of radial basis function networks to control problems. Some of these studies do not explicitly deal with the problem of center selection. However, the center adaptation or the kernel adaptation problems are often indirectly addressed to improve performance. In some cases, even parameter convergence is achieved. An account of common methods can be found in [21]. Sanner and Slotine implement Gaussian

networks for direct adaptive control in [22]. The neuro-control technique discussed in [23] and [24] uses a fixed set of basis functions or kernel centers. On the other hand, in the controller using neural networks proposed in [25], the kernel centers are chosen such that linear independence of $\mathfrak{K}_{\boldsymbol{x}_i}$ is maintained. As per the algorithm given in [26], the kernel parameters are chosen to approximate the nonlinear inversion error over a compact set. Reference [27] presents the advantages of adapting the kernel parameters and presents a theory for static as well as dynamic problems.

An important feature of this chapter is the study of how the center selection problem in RKHS embedding is related to parameter convergence in adaptive estimation. In adaptive estimation, we ordinarily use sufficient conditions, referred to as *persistence of excitation* (PE) conditions, to ensure parameter convergence. [1, 2, 3] The kernel center selection algorithms in the articles cited above do not take persistence of excitation into consideration. In most practical cases, the PE conditions are difficult to ensure *a priori*. They often do not play a constructive role in coming up with practical algorithms. For this reason, several authors have studied adaptive estimation methods which ensure parameter convergence without PE. In [28], Chowdhary and Johnson show that if the chosen regressors evaluated at measured data are linearly independent, then we get parameter convergence. Kamalapurkar et al. extended this work in [29] to relax the assumptions and developed a concurrent learning technique that implements a dynamic state-derivative estimator. Kingravi et al. in [5] propose a real-time regressors update algorithm that uses the regressors linear independence test. In [30], Modares et al. show that parameter convergence can be ensured by checking for linear independence of the filtered regressor. An alternative class of methods uses Gaussian processes for adaptive estimation and adaptive control. [31, 32, 33, 34] In these methods, the kernel centers are chosen at the points corresponding to the measured output data. An introduction to this theory with examples is given in [35].

The conventional PE condition is linked to the richness of the regressor functions that are used to represent the unknown function. In the RKHS embedding method, the modified PE conditions, studied in [36, 37], are directly related to the kernel center positions in the state-space. Recent results have shown that the idea of persistence of excitation can be associated with positive limit sets contained in the state-space. We review this theory rigorously in Section 4.2. This theory, along with the sufficient condition presented in [4], give us explicitly what sets in the state-space are persistently excited. Thus, for a particular class of RKHS adaptive estimators, we can choose kernel centers from these sets. The recent results in [38] establish that the accuracy of the RKHS embedding method can be shown to depend on the fill distance of samples in an uniform manifold. As the fill distance decreases to zero, the finite-dimensional approximation of function estimate converges to the infinite-dimensional function estimate. At the same time, it is also known that the condition number of the Grammian matrix that must be inverted to implement the RKHS embedding method is bounded by the minimal separation of samples that define the space of approximants. These two observations suggest that strategies to control the distribution of samples in practical simulations are needed.

In this chapter, we first prove that the infinite-dimensional PE condition implies uniform convergence of the parameter error in the PE sets (Corollary 4.4). This proof strengthens the results in [36, 37] in that it provides an intuitive insight into the implications of the PE condition in the infinite-dimensional RKHS embedding method. We then discuss the theory behind approximation of the infinite-dimensional adaptive estimator and prove that choosing kernel centers in PE sets implies convergence of the function estimates at the kernel centers (Theorem 4.10). This results also strengthens the early results in [6] and provides insights that connect convergence in the RKHS norm to practical observable results in computation. Based on these results and the theory in [6, 36, 37, 38], we develop criteria for choosing

kernel centers (Subsection 4.2.6). We present two kernel center selection algorithms that satisfy these criteria for certain classes of nonlinear systems. They apply to systems in which the neighborhoods of points in the positive limit sets are visited regularly by the state trajectory. In the limited literature on adaptive estimation by RKHS embedding, such algorithms are yet to be explored to the best of the authors' knowledge. The first algorithm is based on constructing centroidal Voronoi tessellations (CVT) of a polygon that surrounds the measured data. The second approach is based on Kohonen self-organizing maps. The advantages of these methods are as follows:

1. These algorithms choose kernel centers directly from the state-space. Such methods work for a large class of regressor functions, or types of kernels that define the RKHS.

2. We do not need explicit equations for the persistently exciting sets, which is the case in most practical applications. In the absence of such knowledge, it is hard to pick kernel centers that are evenly distributed in the persistently exciting set.

3. There are commercially available software for computing CVT and Kohonen self-organizing maps. This makes both methods simple to implement.

We organize the sections in this chapter as follows. In Section 4.2, we present the theory of adaptive estimation in infinite-dimensional RKHS and basic properties of persistence of excitation. We also discuss the relation between the approximation rates and distribution of samples in the state-space. Finally, we present the criteria for center selection and illustrate the effectiveness of the criteria using an example. In Section 4.3, we present the first method and theory of CVT based kernel center selection. We also prove theorems on convergence in this section. Section 4.4 presents the method based on Kohonen self-organizing maps. Finally, we present two examples that illustrate the effectiveness of both methods in Section 4.5.

4.2 RKHS Embedding for Adaptive Estimation

4.2.1 Reproducing Kernel Hilbert Space

A reproducing kernel Hilbert space $\mathcal{H}_X$ is a Hilbert space associated with a positive-definite kernel $\mathcal{K} : X \times X \to \mathbb{R}$. See [39, 40] for axiomatic definitions of what constitutes an admissible kernel. The kernel satisfies two properties, (1) $\mathcal{K}(\boldsymbol{x}, \cdot) \in \mathcal{H}$ for all $\boldsymbol{x} \in X$, and (2) the reproducing property: for all $\boldsymbol{x} \in X$ and $f \in \mathcal{H}_X$, $(\mathcal{K}(\boldsymbol{x}, \cdot), f)_{\mathcal{H}_X} = \mathcal{E}_{\boldsymbol{x}} f = f(\boldsymbol{x})$. Here, the notation $(\cdot, \cdot)_{\mathcal{H}_X}$ denotes the inner product associated with the Hilbert space $\mathcal{H}_X$. The term $\mathcal{E}_{\boldsymbol{x}}$ is the evaluation functional, which is a bounded linear operator. Throughout this chapter, we consider RKHS generated by kernels which satisfy the condition that $\mathcal{K}(\boldsymbol{x}, \boldsymbol{x}) \leq \bar{k}^2 < \infty$. This condition implies that the RKHS is continuously embedded in the space of continuous functions $C(X)$. [6] Many reproducing kernels used in practice satisfy the above condition. Given a positive-definite kernel, the RKHS $\mathcal{H}_X$ is generated by

$$\mathcal{H}_X := \overline{span\{\mathcal{K}(\boldsymbol{x}, \cdot) | \boldsymbol{x} \in X\}}.$$

Note that if the set X is infinite-dimensional, then the RKHS it generates is also infinite-dimensional. Given a subset $\Omega \subseteq X$, we define the associated RKHS $\mathcal{H}_\Omega \subseteq \mathcal{H}_X$ by

$$\mathcal{H}_\Omega := \overline{span\{\mathcal{K}(\boldsymbol{x}, \cdot) | \boldsymbol{x} \in \Omega\}}.$$

The above-mentioned reproducing property endows the RKHS with a structure that makes calculations easier. A detailed list of properties of RKHS can be found in [39, 40]. In this chapter, we are particularly interested in the properties of projection operators that act on an RKHS. We let P_Ω be the $\mathcal{H}_X$ orthogonal projection operator $P_\Omega : \mathcal{H}_X \to \mathcal{H}_\Omega$. From Hilbert space theory, we know that the operator P_Ω decomposes the Hilbert space $\mathcal{H}_X$ into

$\mathcal{H}_\Omega \bigoplus \mathcal{V}_\Omega$, where $\mathcal{V}_\Omega$ is the space of elements orthogonal to the elements of the space $\mathcal{H}_\Omega$. Since the space $\mathcal{H}_X$ is an RKHS, the reproducing property implies that for any $h \in \mathcal{V}_\Omega$, we have $h(\boldsymbol{x}) = 0$ for all $\boldsymbol{x} \in \Omega$. Another important property we use in this chapter is that for any discrete finite set Ω_n, the projection operator P_{Ω_n} coincides with the interpolation operator over Ω_n, i.e., for all $h \in \mathcal{H}_X$, and $\boldsymbol{x} \in \Omega_n$, we have $h(\boldsymbol{x}) = (P_{\Omega_n} h)(\boldsymbol{x})$. [41]

4.2.2 Adaptive Estimation in RKHS

Consider a nonlinear system governed by the ordinary differential equation

$$\dot{\boldsymbol{x}}(t) = A\boldsymbol{x}(t) + Bf(\boldsymbol{x}(t)),$$

where $\boldsymbol{x}(t) \in \mathbb{R}^d$ is the state, $A \in \mathbb{R}^{d\times d}$ is a known Hurwitz matrix, $B \in \mathbb{R}^d$ is a known vector and $f : \mathbb{R}^d \to \mathbb{R}$ is the unknown (nonlinear) function. Note, if the original system equations do not contain the term $A\boldsymbol{x}(t)$, we can add and subtract a known Hurwitz matrix and redefine the unknown nonlinear function to have the form shown above. As noted in [6] and discussed in more detail there, more general systems can addressed in the analysis that follows via analogy to the model problem above.

We assume that the unknown function f lives in the RKHS $\mathcal{H}_X$, where $X = \mathbb{R}^d$ is the state-space of the system. In other words, we assume that the unknown f has the form $f(\cdot) = \sum_{i\in\mathbb{I}}^{\infty} \alpha_i \mathcal{K}_{\boldsymbol{x}_i}(\cdot)$ for some $\{\boldsymbol{x}_i\}_{i\in\mathbb{I}}$ with $\mathbb{I}$ either finite or infinite. We now define an estimator model of the form

$$\dot{\hat{\boldsymbol{x}}}(t) = A\hat{\boldsymbol{x}}(t) + B\hat{f}(t, \boldsymbol{x}(t)),$$

where $\hat{\boldsymbol{x}}(t) \in \mathbb{R}^d$ is the state estimate and $\hat{f}(t, \boldsymbol{x}(t))$ is the function estimate. For each t, the function estimate $\hat{f}(t)$ is an element of the space $\mathcal{H}_X$. In this chapter, we assume full-state

measurement. This assumption allows us to define a function estimate $\hat{f}(t)$ that depends on the actual states $\boldsymbol{x}(t)$. Note that the function estimate also explicitly depends on the time t. The goal of adaptive estimation is make $\hat{f}(t) \to f$ as $t \to \infty$. To achieve this, we define the rate of evolution of the function estimate by the learning law

$$\dot{\hat{f}}(t) = \Gamma^{-1}(B\mathcal{E}_{\boldsymbol{x}(t)})^* P(\boldsymbol{x}(t) - \hat{\boldsymbol{x}}(t)),$$

where $\Gamma \in \mathbb{R}, \Gamma > 0$. The notation $(\cdot)^*$ represents the adjoint of an operator. Additionally, the term P is a symmetric positive-definite matrix in $\mathbb{R}^{d\times d}$ that solves the Lyapunov equation $A^T P + PA = -Q$, where $Q \in \mathbb{R}^{d\times d}$ is an arbitrarily chosen symmetric positive-definite matrix.

If we define the state and function errors as $\tilde{\boldsymbol{x}}(t) := \boldsymbol{x}(t) - \hat{\boldsymbol{x}}(t)$ and $\tilde{f}(t) := f - \hat{f}(t)$, the error evolution equations can be expressed as

$$\begin{Bmatrix} \dot{\tilde{\boldsymbol{x}}}(t) \\ \dot{\tilde{f}}(t) \end{Bmatrix} = \underbrace{\begin{bmatrix} A & B\mathcal{E}_{\boldsymbol{x}(t)} \\ -\Gamma^{-1}(B\mathcal{E}_{\boldsymbol{x}(t)})^* P & 0 \end{bmatrix}}_{\mathbb{A}(t)} \begin{Bmatrix} \tilde{\boldsymbol{x}}(t) \\ \tilde{f}(t) \end{Bmatrix}. \tag{4.1}$$

Note, in the above error equation, the term $\mathbb{A}(t)$ is a uniformly bounded linear operator, and the states $\begin{Bmatrix} \tilde{\boldsymbol{x}}(t) & \tilde{f}(t) \end{Bmatrix}^T$ evolve in the infinite-dimensional space $\mathbb{R}^d \times \mathcal{H}_X$.

Standard stability analysis using the Lyapunov's theorem and Barbalat's lemma shows that the norm of the state error $\|\tilde{\boldsymbol{x}}(t)\|_{\mathbb{R}^d} \to 0$ as $t \to \infty$. [6, 36, 37]

4.2.3 Parameter Convergence, PE and Positive Limit Sets

As mentioned earlier, persistence of excitation (PE) conditions are used to prove convergence of the function estimate to the actual function. Two different definitions of PE in RKHS are

available in the recent literature on RKHS embedding methods. [36, 37] They are as follows.

Definition 4.1. (**PE. 1**) The trajectory $\boldsymbol{x} : t \mapsto \boldsymbol{x}(t) \in \mathbb{R}^d$ persistently excites the indexing set Ω and the RKHS $\mathcal{H}_\Omega$ provided there exist positive constants T_0, γ, δ, and Δ, such that for each $t \geq T_0$ and any $g \in \mathcal{H}_X$, there exists $s \in [t, t + \Delta]$ such that

$$\left| \int_s^{s+\delta} \mathcal{E}_{\boldsymbol{x}(\tau)} g d\tau \right| \geq \gamma \|P_\Omega g\|_{\mathcal{H}_X} > 0.$$

Definition 4.2. (**PE. 2**) The trajectory $\boldsymbol{x} : t \mapsto \boldsymbol{x}(t) \in \mathbb{R}^d$ persistently excites the indexing set Ω and the RKHS $\mathcal{H}_\Omega$ provided there exist positive constants T_0, γ, and Δ such that

$$\int_t^{t+\Delta} \left(\mathcal{E}^*_{\boldsymbol{x}(\tau)} \mathcal{E}_{\boldsymbol{x}(\tau)} g, g \right)_{\mathcal{H}_X} d\tau \geq \gamma \|P_\Omega g\|^2_{\mathcal{H}_X} > 0$$

for all $t \geq T_0$ and any $g \in \mathcal{H}_X$.

Note that the PE condition given in Definition 4.2 structurally resembles the classical PE conditions defined using regressors in finite-dimensional spaces. [1, 2, 3] Recall that the term P_Ω in the above definitions is the orthogonal projection operator that maps elements from $\mathcal{H}_X$ to $\mathcal{H}_\Omega$. The following theorem is a special case of the results from [36, 37] and shows how these two PE conditions are related. Note that the notion of parameter convergence in the infinite-dimensional case is given with respect to PE condition in Definition 4.1 only.

Theorem 4.3. *The PE condition in Definition PE. 4.1 implies the one in Definition PE. 4.2. Further, if $X = \Omega$ is a discrete finite set, the state trajectory $t \mapsto \boldsymbol{x}(t)$ is uniformly continuous and maps to a compact set, and the family of functions defined by $\{g(\boldsymbol{x}(\cdot)) : t \mapsto g(\boldsymbol{x}(t)) | g \in \mathcal{H}_X, \|g\| = 1\}$ is uniformly equicontinuous, then the PE condition in Definition PE. 4.2 implies the one in Definition PE. 4.1.*

Furthermore, if the trajectory $\boldsymbol{x} : t \mapsto \boldsymbol{x}(t)$ *persistently excites the RKHS* $\mathcal{H}_\Omega$ *in the sense of Definition PE. 4.1. Then*

$$\lim_{t\to\infty} \|\tilde{\boldsymbol{x}}(t)\| = 0, \qquad \lim_{t\to\infty} \|P_\Omega \tilde{f}(t)\|_{\mathcal{H}_X} = 0.$$

We can view the term $P_\Omega \tilde{f}(t)$ as an element of the space $\mathcal{H}_\Omega$. Thus, the above statement implies that $P_\Omega \tilde{f}(t)$ converges to the zero element in the $\mathcal{H}_\Omega$ space. However, this statement does not imply the convergence or even the existence of the limit of $\tilde{f}(t) \in \mathcal{H}_X$.

The statement $\lim_{t\to\infty} \|P_\Omega \tilde{f}(t)\|_{\mathcal{H}_X} = 0$ is hard to interpret intuitively. The following corollary of the above theorem gives us the intuition about where the convergence is achieved.

Corollary 4.4. *If the trajectory* $\boldsymbol{x} : t \mapsto \boldsymbol{x}(t)$ *persistently excites the set* Ω *and the RKHS* $\mathcal{H}_\Omega$ *in the sense of Definition PE. 4.1, then* $\hat{f}(t)$ *converges uniformly to* f *on the set* Ω *as* $t \to \infty$.

Proof. Suppose the projection operator P_Ω decomposes the function $\tilde{f}(t)$ into $\tilde{f}(t) = P_\Omega \tilde{f}(t) + v(t)$, where $P_\Omega(\tilde{f}(t)) \in \mathcal{H}_\Omega$ and $v(t) \in \mathcal{V}_\Omega$. Since $v(t, \boldsymbol{x}) = 0$ for all $\boldsymbol{x} \in \Omega$, we have $\tilde{f}(t) = P_\Omega \tilde{f}(t, \boldsymbol{x})$. Thus, for all $\boldsymbol{x} \in \Omega$, we have

$$|\tilde{f}(t)| = |P_\Omega \tilde{f}(t, \boldsymbol{x})| = |\mathcal{E}_{\boldsymbol{x}} P_\Omega \tilde{f}(t)| \leq \|\mathcal{E}_{\boldsymbol{x}}\| \|P_\Omega \tilde{f}(t)\|_{\mathcal{H}_X}.$$

But we have assumed in this chapter that the kernel $\mathcal{K}$ that induces $\mathcal{H}_X$ satisfies $\mathcal{K}(\boldsymbol{x}, \boldsymbol{x}) \leq \bar{k}^2 < \infty$ for all $\boldsymbol{x} \in X$. Since the evaluation functional is consequently uniformly bounded, the above inequality holds for all $\boldsymbol{x} \in \Omega$. Taking the limit $t \to \infty$ and using Theorem 4.3 gives us the desired result. □

The above corollary clearly shows that, if the PE condition holds and *the kernel satisfies* $\mathcal{K}(\boldsymbol{x}, \boldsymbol{x}) \leq \bar{k}^2 < \infty$, then $\hat{f}(t, \boldsymbol{x}) \to f(\boldsymbol{x})$ for all $\boldsymbol{x} \in \Omega$. Generally, we would prefer the whole space to be persistently exciting, i.e. $\Omega = X$. However, this is not the case in most practical applications. Furthermore, the above PE definitions are hard to understand intuitively and difficult, if not impossible, to verify in real applications. The following theorem from [42] shows us exactly where to look for persistently exciting sets in the state-space. The theorem assumes that the RKHS space separates closed sets.

Definition 4.5. We say the RKHS $\mathcal{H}_X$ separates a set $A \subseteq X$ if for each $\boldsymbol{b} \notin A$, there is a function $f \in \mathcal{H}_X$ such that $f(\boldsymbol{a}) = 0$ for all $\boldsymbol{a} \in A$ and $f(\boldsymbol{b}) \neq 0$.

The RKHS generated by the Gaussian kernel, which is extensively used for RKHS based adaptive estimation and machine learning, does not satisfy the above condition for all closed sets. A detailed account for RKHS that separate closed sets can be found in [43]. In this chapter, we use the Sobolev-Matern kernels, which satisfy the above condition. A sufficient condition for an RKHS to separate closed sets is that it contains a rich family of bump functions.

Theorem 4.6. *Let $\mathcal{H}_X$ be the RKHS of functions over X and suppose that this RKHS includes a rich family of bump functions. If the PE condition in Definition PE. 4.2 holds for Ω, then $\Omega \subseteq \omega^+(\boldsymbol{x}_0)$, the positive limit set corresponding to the initial condition $\boldsymbol{x}_0$.*

This theorem gives us a necessary condition for a set to be persistently excited. While designing a adaptive estimator, this necessary condition can tell us where to look for persistently excited sets in the state-space.

4.2.4 Approximations, Convergence Rates and Sufficient Condition

For practical implementation, we approximate the infinite-dimensional adaptive estimator equations given in the previous subsection. Let $\{\Omega_n\}_{n\in\mathbb{N}}$ be a finite nested sequence of subsets of Ω, Further, let $\{\mathcal{H}_{\Omega_n}\}_{n\in\mathbb{N}}$ be the corresponding subspaces of $\mathcal{H}_X$ generated by the finite sets Ω_n. Now, define P_{Ω_n} as the orthogonal projection operator from $\mathcal{H}_X$ to the subspace $\mathcal{H}_{\Omega_n}$ such that $\lim_{n\to\infty} P_{\Omega_n} f = f$ for all $f \in \mathcal{H}_X$. With this definition of approximation, we write the finite-dimensional adaptive estimator model and the learning law as

$$\dot{\hat{\boldsymbol{x}}}_n(t) = A\hat{\boldsymbol{x}}_n(t) + B\mathcal{E}_{\boldsymbol{x}(t)}\Pi_n^*\hat{f}_n(t),$$
$$\dot{\hat{f}}_n(t) = \Gamma^{-1}\left(B\mathcal{E}_{\boldsymbol{x}(t)}\Pi_n^*\right)^* P\tilde{\boldsymbol{x}}_n(t)$$

with $\tilde{\boldsymbol{x}}_n := \boldsymbol{x} - \hat{\boldsymbol{x}}_n$. Since the RKHS $\mathcal{H}_{\Omega_n}$ is finite-dimensional, the basis of $\mathcal{H}_{\Omega_n}$ is the set $\{\mathfrak{K}_{\boldsymbol{x}_i} | \boldsymbol{x}_i \in \Omega_n\}$. We now note that the finite-dimensional function estimate $\hat{f}_n(t)$ has the form $\hat{f}_n(t) := \sum_{i=1}^n \hat{\alpha}_i(t)\mathfrak{K}_{\boldsymbol{x}_i}$. Using the reproducing property of the kernel, we rewrite the above finite-dimensional learning law as

$$\dot{\hat{\boldsymbol{\alpha}}}(t) = \mathbb{K}^{-1}\boldsymbol{\Gamma}^{-1}\boldsymbol{\mathcal{K}}(\boldsymbol{x}_c, \boldsymbol{x}(t))B^*P\tilde{\boldsymbol{x}}_n(t), \tag{4.2}$$

where $\hat{\boldsymbol{\alpha}}(t) := \{\hat{\alpha}_1(t), \ldots, \hat{\alpha}_n(t)\}^T$, $\mathbb{K}$ is the symmetric positive definite Grammian matrix whose ij^{th} element is defined as $\mathbb{K}_{ij} := \mathcal{K}(\boldsymbol{x}_i, \boldsymbol{x}_j)$, $\boldsymbol{\Gamma} := \Gamma\mathbb{I}_n$ is the gain matrix, and

$$\boldsymbol{\mathcal{K}}(\boldsymbol{x}_c, \boldsymbol{x}(t)) := \left\{\mathcal{K}(\boldsymbol{x}_1, \boldsymbol{x}(t)), \ldots, \mathcal{K}(\boldsymbol{x}_n, \boldsymbol{x}(t))\right\}^T.$$

The new learning law defines the rate of evolution of the coefficients, as opposed to the old learning law which defines the rate of evolution of the function $\hat{f}_n(t)$. This step is essential

for implementation purposes. We refer the reader to [44] for the intermediate steps involved in the derivation.

Note, the PE condition implies the convergence of the infinite-dimensional function estimate $\hat{f}(t)$ to f. It does not imply anything about the convergence of the approximation of the function estimate $\hat{f}_n(t)$ to f. On the other hand, the following theorem, proved in [6], shows that the term $\hat{f}_n(t)$ to $\hat{f}(t)$ as $n \to \infty$.

Theorem 4.7. *Suppose that $\boldsymbol{x} \in C([0,T], \mathbb{R}^d)$ and that the embedding $i : \mathcal{H}_X \hookrightarrow C(\Omega)$ is uniform in the sense that*

$$\|f\|_{C(\Omega)} \equiv \|if\|_{C(\Omega)} \leq C\|f\|_{\mathcal{H}_X}.$$

Then for any $T > 0$ and $t \in [0,T]$,

$$\|\hat{\boldsymbol{x}} - \hat{\boldsymbol{x}}_n\|_{C([0,T];\mathbb{R}^d)} \to 0,$$
$$\|\hat{f}(t) - \hat{f}_n(t)\|_{C([0,T];\mathbb{R}^d)} \to 0,$$

as $n \to \infty$.

Thus, as we choose denser finite discrete sets in Ω, the approximation of the function estimate $\hat{f}_n(t)$ gets closer to the function estimate $\hat{f}(t)$, which in turn converges to the actual function f as $t \to \infty$ if the PE condition holds. The above theorem does not explicitly tell us how to choose the set $\Omega_n \subseteq \Omega$. However, when the set Ω is a compact smooth Riemannian manifold embedded in $\mathbb{R}^d$ with metric d, the rate at which $\hat{f}_n(t)$ converges to the $\hat{f}(t)$ depends on how the elements of the set Ω_n are distributed in the set Ω. This distribution is defined in terms

of the *fill distance*

$$h_{\Omega_n,\Omega} := \sup_{x\in\Omega} \min_{\xi_i\in\Omega_n} d(x,\xi_i).$$

Theorem 4.8. *Let $\Omega \subseteq X := \mathbb{R}^d$ be a k-dimensional smooth manifold, and let the native space $\mathcal{H}_X$ be continuously embedded in a Sobolev space $W^{\tau,2}(X)$ with $\tau > d/2$, so that $\|f\|_{W^{\tau,2}(\mathbb{R}^d)} \lesssim \|f\|_{\mathcal{H}_X}$. Define $s = \tau - (d-k)/2$ and let $0 \leq \mu \leq \lceil s \rceil - 1$. Then there is a constant h_Ω such that if $h_{\Omega_n,\Omega} \leq h_\Omega$, then for all $f \in \boldsymbol{R}_\Omega(\mathcal{H}_X)$ we have*

$$\|(I - P_{\Omega_n})\hat{f}(t)\|_{W^{\mu,2}(\Omega)} \lesssim h^{s-\mu}_{\Omega_n,\Omega} \|\hat{f}(t)\|_{\boldsymbol{R}_\Omega(\mathcal{H}_X)}.$$

In the above theorem, the notation $\boldsymbol{R}_\Omega(\mathcal{H}_X)$ represents the restriction of the space $\mathcal{H}_X$ to the set Ω, and the notation $a \lesssim b$ implies that there exists a positive constant c such that $a \leq cb$. This theorem requires a lot of technical details and we direct interested readers to [38] for the detailed explanation of the rigorous theory and proofs. In this chapter, we are interested in the implications of the theorem. The theorem states that the fill distance $h_{\Omega_n,\Omega}$ defines the rate at which the norm of the error $\hat{f}(t) - \hat{f}_n(t)$ converges to zero.

Sufficient Condition

In all the discussion above, we assume that we have knowledge of the persistently excited set Ω. In most practical cases, it is impossible to determine this set. However, there is a much more practical and intuitive way for selecting the kernel centers in the set Ω_n when the RKHS is generated by a strictly positive definite kernel. For the precise hypothesis of the theorem below, the reader should see [45]: the context of the following theorem is rather detailed.

Theorem 4.9. *Suppose the RKHS is generated by a strictly positive definite kernel and the*

hypotheses of [45] hold. Let $\epsilon < \frac{1}{2}\min_{i\neq j}\|\boldsymbol{x}_i - \boldsymbol{x}_j\|$, *where* $\boldsymbol{x}_i$ *and* $\boldsymbol{x}_j$ *are the kernel centers* $\{\boldsymbol{x}_1, \ldots, \boldsymbol{x}_n\} \subseteq \omega^+(\boldsymbol{x}_0)$. *For every* $t_0 \geq 0$ *and* $\delta > 0$, *define*

$$I_i := I_{i,\epsilon,\delta} := \{t \in [t_0, t_0 + \delta] : \|\boldsymbol{x}(t) - \boldsymbol{x}_i\| \leq \epsilon\}.$$

If there exists a $\delta = \delta(\epsilon)$ *such that the measure of* I_i *is bounded below by a positive constant that is independent of* t_0 *and the kernel center* $\boldsymbol{x}_i$, *and if the measure of* $[t_0, t_0 + \delta]$ *is less than or equal to* δ, *then the space* $\mathcal{H}_n$ *is persistently exciting in the sense of PE 4.2.*

Intuitively, the above theorem states that the neighborhoods of the points in the finite PE set Ω_n are visited by the state trajectory infinitely many times, and the time of visitation is bounded below in a certain sense. Note that the above sufficient condition implies PE 4.2. When the hypotheses of Theorem 4.3 hold, we can conclude that the sufficient condition given in Theorem 4.9 implies PE 4.1. While implementing the adaptive estimator, if we only know that the actual function $f \in \mathcal{H}_X$ with X an infinite set, (as usual) the sufficient condition given in Theorem 4.9 only implies ultimate boundedness of the function estimate instead of convergence, in particular when we use the dead zone gradient law. Notice that this ultimate bound actually implies a stronger result than the one in the conventional analysis in Euclidean space: here, the ultimate bound is explicit in terms of the approximation space error. [45]

4.2.5 Center Selection Problem and Example

In the last section, we made no assumption about the space in which function estimate $\hat{f}(t)$ lives. The function estimate $\hat{f}(t)$ can live in $\mathcal{H}_X$ and is not restricted to $\mathcal{H}_\Omega$. This leads us to ask the question of why it is necessary for the kernel centers (elements of the set Ω_n) to be contained in the set Ω. It is indeed possible to approximate the function $\hat{f}(t)$ using kernel

centers that are outside of the set Ω. However, if the centers are contained in the set Ω, the function estimate will converge to the actual function values at those centers. Before we take a look at the next theorem, note that the basis of the space $\mathcal{H}_{\Omega_n}$ is the set $\{\mathfrak{K}_{\boldsymbol{x}_i} | \boldsymbol{x}_i \in \Omega_n\}$. This implies that the functions $P_{\Omega_n} f$ and $\hat{f}_n(t)$ have the form $P_{\Omega_n} f = \sum_{i=1}^n \alpha_i \mathfrak{K}_{\boldsymbol{x}_i}$ and $\hat{f}_n(t) = \sum_{i=1}^n \hat{\alpha}_i(t) \mathfrak{K}_{\boldsymbol{x}_i}$.

Theorem 4.10. *Suppose the set Ω is persistently exciting, and the set $\Omega_n \subseteq \Omega$. Then $\lim_{t\to\infty} \hat{f}_n(t, \boldsymbol{x}_i) = f(\boldsymbol{x}_i)$ for all $\boldsymbol{x} \in \Omega_n$ and $i \in \{1, \ldots, n\}$. Furthermore, for $i \in \{1, \ldots, n\}$, $\hat{\alpha}_i(t) \to \alpha_i$ as $t \to \infty$.*

Proof. Recall that $\hat{f}_n(t) := P_{\Omega_n} \hat{f}(t)$, where $P_{\Omega_n} : \mathcal{H}_X \to \mathcal{H}_{\Omega_n}$. The set Ω_n is discrete and finite. In RKHS, the projection operator from infinite-dimensional space to a finite-dimensional space coincides with the interpolation operator. In other words, for a given t, we have $\hat{f}_n(t, \boldsymbol{x}_i) = \hat{f}(t, \boldsymbol{x}_i)$ for all $\boldsymbol{x}_i \in \Omega_n$. From Corollary 4.4, we have $\lim_{t\to\infty} \hat{f}_n(t, \boldsymbol{x}_i) = f(\boldsymbol{x}_i)$ for all $\boldsymbol{x}_i \in \Omega_n$. This in turn implies that, for $i \in \{1, \ldots, n\}$, the coefficients $\hat{\alpha}_i(t)$ converge to α_i as $t \to \infty$ since the set $\{\mathfrak{K}_{\boldsymbol{x}_i} | \boldsymbol{x}_i \in \Omega_n\}$ forms the basis of the space $\mathcal{H}_{\Omega_n}$. □

The above theorem shows that selecting kernel centers in the PE set Ω will result in the approximated function estimate $\hat{f}_n(t)$ approaching the actual function value at the kernel centers. In addition to this fact, the theory on approximation rates holds only when the kernel centers are contained in the set Ω. This makes it advantageous to choose $\Omega_n \subseteq \Omega$. The following example helps us understand what happens when the kernel center is not exactly in the persistently excited set. The example considers the case where Ω is a singleton set. The analysis for more general PE sets is analogous to the one given below.

Example 4.11. Suppose the persistently excited set $\Omega = \{\boldsymbol{\xi}\}$. Suppose the kernel center is at $\Omega_n = \{\hat{\boldsymbol{\xi}}\}$. According to Corollary 4.4, given $\epsilon > 0$, there exists a T_0 such that for

any $t > T_0$, $|f(\boldsymbol{\xi}) - \hat{f}(t, \boldsymbol{\xi})| < \epsilon$. Suppose we stop the adaptive estimator at $T > T_0$. We know that by the properties of RKHS, $\hat{f}(T, \hat{\boldsymbol{\xi}}) = \hat{f}_n(T, \hat{\boldsymbol{\xi}})$. Since $\hat{f}$ and $\hat{f}_n$ are continuous, given $\epsilon > 0$, there exists δ such that if $\|\boldsymbol{\xi} - \hat{\boldsymbol{\xi}}\| < \delta$, then $|\hat{f}(T, \boldsymbol{\xi}) - \hat{f}(T, \hat{\boldsymbol{\xi}})| < \epsilon$ and $|\hat{f}_n(T, \boldsymbol{\xi}) - \hat{f}_n(T, \hat{\boldsymbol{\xi}})| < \epsilon$. Thus, we conclude that if $\|\boldsymbol{\xi} - \hat{\boldsymbol{\xi}}\| < \delta$, then $|f(\boldsymbol{\xi}) - \hat{f}_n(T, \boldsymbol{\xi})| < 3\epsilon$. Note, as $\hat{\boldsymbol{\xi}} \to \boldsymbol{\xi}$, $|f(\boldsymbol{\xi}) - \hat{f}_n(T, \boldsymbol{\xi})|$ approaches a value that is strictly less than ϵ.

4.2.6 Center Selection Criteria

Based on the theory presented in the previous subsections, we list the following criteria for choosing the kernel centers.

(C1) The kernel centers should be contained in or be as close as possible to the positive limit set based on Theorem 4.6.

(C2) The kernel centers should be evenly distributed when possible. There are two reasons for selecting this criteria.

  (i) The linear dependency of the kernels will be high if the centers are placed too close to each other. This will increase the condition number of the Grammian matrix in Equation 4.2.

  (ii) On the other hand, if the centers are too far apart, the fill distance increases, which in turn reduces the approximation rates based on Theorem 4.8.

(C3) The neighborhood of the centers should be visited by the state trajectory regularly. This is to satisfy the sufficient condition for PE based on Theorem 4.9.

Note: The above listed criteria assumes knowledge of the positive limit set and the state-trajectory.

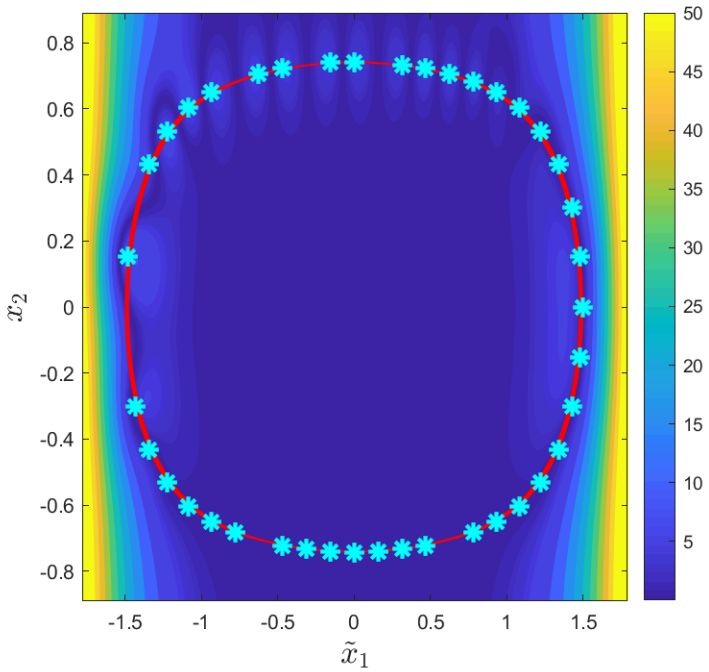

Figure 4.1: Random Centers - Pointwise error $|f(\boldsymbol{x}) - \hat{f}_n(T, \boldsymbol{x})|$. The marker $*$ and the red line represent the kernel centers and the limit set, respectively.

4.2.7 Example: The case when we have a priori knowledge of positive limit set

We test the above listed criteria on a simple practical example. We consider a nonlinear single-mode undamped piezoelectric oscillator with no input to test the above criteria. The governing equations have the form

$$\begin{Bmatrix} \dot{x}_1 \\ \dot{x}_2 \end{Bmatrix} = \underbrace{\begin{bmatrix} 0 & 1 \\ -\frac{\hat{K}}{M} & -\frac{C}{M} \end{bmatrix}}_{A} \begin{Bmatrix} x_1 \\ x_2 \end{Bmatrix} + \underbrace{\begin{Bmatrix} 0 \\ -\frac{P}{M} \end{Bmatrix}}_{\mathcal{B}} \underbrace{\ddot{z}(t)}_{u(t)} + \underbrace{\begin{Bmatrix} 0 \\ 1 \end{Bmatrix}}_{B} \underbrace{\left(-\frac{\hat{K}_{N_1}}{M} x_1^3(t) - \frac{\hat{K}_{N_2}}{M} x_1^5(t) \right)}_{f(\boldsymbol{x}(t))}, \quad (4.3)$$

where $M, \hat{K}, C, P$ are the modal mass, modal stiffness, modal damping, and modal input contribution term of the piezoelectric oscillator. The variables $\hat{K}_{N_1}, \hat{K}_{N_2}$ are the nonlinear

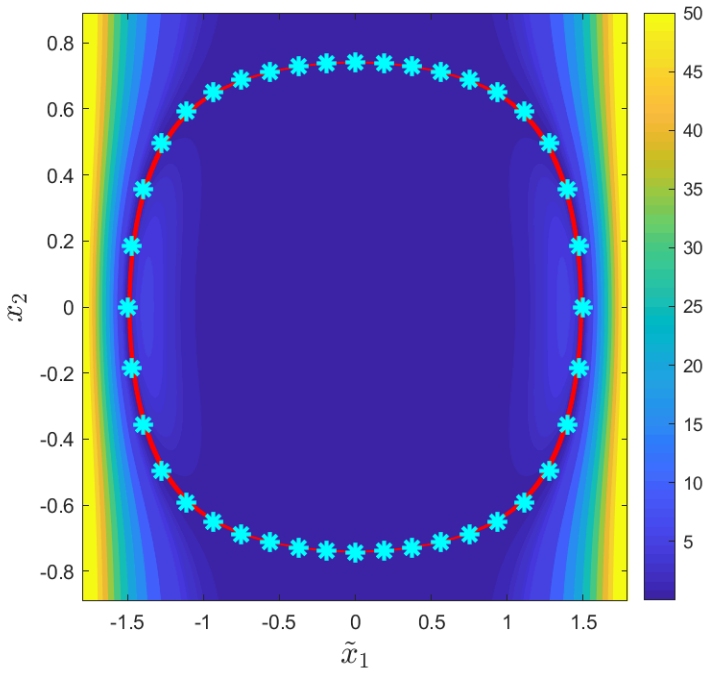

Figure 4.2: Uniform Centers - Pointwise error $|f(\boldsymbol{x}) - \hat{f}_n(T, \boldsymbol{x})|$. The marker $*$ and the red line represent the kernel centers and the limit set, respectively.

stiffness terms. The terms x_1, x_2 and z are the modal displacement, modal velocity and base displacement of the oscillator, respectively. The steps involved in deriving the above governing equations can be found in [44]. Typically, the magnitudes of the velocity and displacement values are not of the same order. In such cases, we have to use kernels that are skewed in a particular direction. Alternatively, we scale one of the states as $x_1 = S\tilde{x}_1$, where S is a positive constant. Note, after scaling, $\boldsymbol{x}(t) := \{\tilde{x}_1(t), x_2(t)\}^T$. In our simulations, we choose $M = 0.9745$, $\hat{K} = 329.9006$, $\hat{K}_{N_1} = -1.2901 \times 10^5$ and $\hat{K}_{N_2} = 1.2053 \times 10^9$. For the undamped, no input case, i.e., $C = 0$ and $P = 0$, the total energy is conserved. In other words, the trajectory is always contained in the limit set $\omega^+(\boldsymbol{x}_0)$, where $\boldsymbol{x}_0 \in \mathbb{R}^2$ is the initial condition. Note that any arbitrary discrete finite set in $\omega^+(\boldsymbol{x}_0)$ is visited by the state trajectory infinitely many times. Since we have a priori knowledge of the limit set $\omega^+(\boldsymbol{x}_0)$ for a given initial condition, we choose kernel centers in the set Ω and integrate the

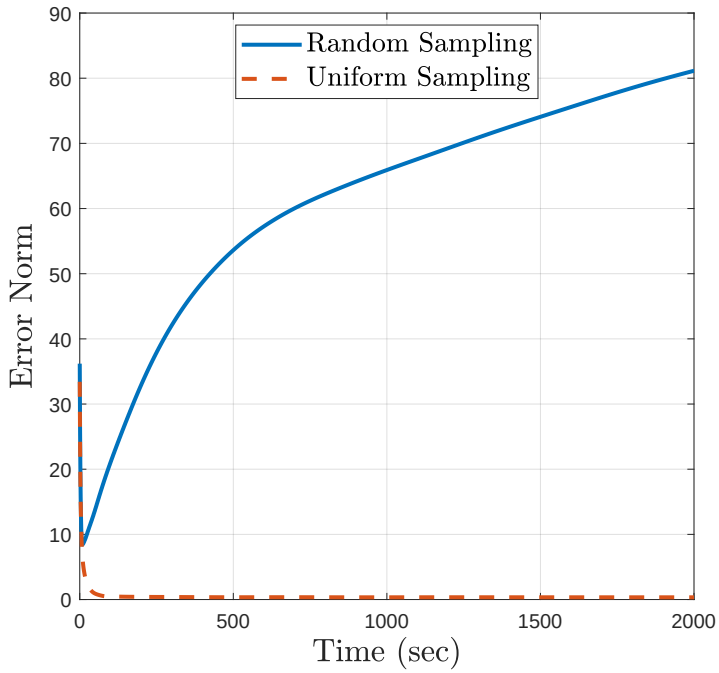

Figure 4.3: Variation of $\|\boldsymbol{\alpha} - \hat{\boldsymbol{\alpha}}(t)\|_{\mathbb{R}^n}$ with time.

equations

$$\dot{\hat{\boldsymbol{x}}}_n(t) = A\hat{\boldsymbol{x}}_n(t) + B\hat{\boldsymbol{\alpha}}^T(t)\boldsymbol{\mathcal{K}}(\boldsymbol{x}_c, \boldsymbol{x}(t)),$$
$$\dot{\hat{\boldsymbol{\alpha}}}(t) = \mathbb{K}^{-1}\boldsymbol{\Gamma}^{-1}\boldsymbol{\mathcal{K}}(\boldsymbol{x}_c, \boldsymbol{x}(t))B^*P\tilde{\boldsymbol{x}}_n(t)$$

over the interval $[0, T]$ for some $T > 0$. In all our simulations, we use the Sobolev-Matern $3, 2$ kernel, which has the form

$$\mathcal{K}_{3,2}(\boldsymbol{x}, \boldsymbol{y}) = \left(1 + \frac{\sqrt{3}\|\boldsymbol{x} - \boldsymbol{y}\|}{l}\right) \exp\left(-\frac{\sqrt{3}\|\boldsymbol{x} - \boldsymbol{y}\|}{l}\right),$$

where l is the scaling factor of length. [46]

To analyze the above-listed criteria's effectiveness, we tested the adaptive estimator with a

random and a deterministic, uniform collection of kernel centers. We set $S = 0.02$, $l = 0.2$, $\Gamma = 0.001$ and $n = 40$. The states and the parameters are initialized at $\boldsymbol{x}_0 = \{1.5, 0\}^T$ and $\alpha_i(0) = 1$ for $i = 1, \ldots, n$, respectively. For the uniform kernel center selection, we first calculate the distance between two adjacent kernel centers l_n when they are distributed uniformly in the positive limit set. Since we know the exact equation of the positive limit set, [36] we can calculate the total length and hence the length of the arc between two adjacent kernel centers. Given a kernel center, we choose the adjacent kernel center at a distance l_n. We repeat this procedure until we choose the required number of kernel centers that are distributed uniformly in the positive limit set. For choosing the kernel centers for the random case, we first ran the uniform center selection algorithm for $n = 48$ case, and then used the MATLAB function randperm to select $n = 40$ kernel centers randomly. Note that the MATLAB function randperm uses a uniform pseudorandom number generator algorithm.

Figures 4.1 and 4.2 show the pointwise error $|f(\boldsymbol{x}) - \hat{f}_n(T, \boldsymbol{x})|$ after running the adaptive estimator for $T = 2000$ seconds for a paritcular case of random and uniform selection of kernel centers. It is clear from the figures that the pointwise error is low in the case of uniform sampling. Figure 4.3 shows how the norm $\|\boldsymbol{\alpha} - \hat{\boldsymbol{\alpha}}(t)\|_{\mathbb{R}^n}$ varies with time t for both the random and uniform center selection methods. From Theorem 4.10, we know that $\hat{\boldsymbol{\alpha}}(t) \to \boldsymbol{\alpha}$, where $\boldsymbol{\alpha} = \{\alpha_1, \ldots, \alpha_n\}^T$ and $\hat{\boldsymbol{\alpha}}(t) = \{\hat{\alpha}_1(t), \ldots, \hat{\alpha}_n(t)\}^T$. It is clear from Figure 4.3 that the coefficient error norm converges rapidly to zero for the uniform centers case. For the random centers case, the error norm does not even start converging in the first 2000 seconds.

In the above problem, it is assumed that we have an explicit equation for the positive limit set $\omega^+(\boldsymbol{x}_0)$ for a given initial condition $\boldsymbol{x}_0$. Furthermore, the state trajectory is contained in the set $\omega^+(\boldsymbol{x}_0)$. This makes it possible to choose kernel centers that are uniformly distributed. In most practical examples, we cannot derive an explicit expression for the set $\omega^+(\boldsymbol{x}_0)$. We

only have samples of the state-trajectory that is contained in or converges to the positive limit set $\omega^+(\boldsymbol{x}_0)$. In the following two sections, we present kernel center selection methods that can be implemented when we do not have explicit knowledge of the positive limit set or when the state trajectory is not contained in the positive limit set. Both methods are applicable to systems for which the state trajectory visits the neighborhoods of all the points in the positive limit set $\omega^+(\boldsymbol{x}_0)$. We next consider algorithms that do not rely on a priori knowledge of the positive limit set $\omega^+(\boldsymbol{x}_0)$.

4.3 Method 1: Based on CVT and Lloyd's Algorithm

The first method we propose is based on building centroidal Voronoi tessellations (CVT) around the positive limit set. This method relies on samples taken in the positive limit set. We implement this approach for systems where the state-trajectory is contained in the positive limit set or converges to the same in finite time. We assume that there is a dense sampling Ξ of the positive limit set, i.e. $\overline{\Xi} = \omega^+(\boldsymbol{x}_0)$. Let $\{\Xi_m\}_{m=1}^{\infty}$ be a sequence of finite subsets of Ξ such that $\Xi_m \subset \Xi_{m+1}$ for all $m \in \mathbb{N}$ and $\cup_{m=1}^{\infty}\Xi_m = \Xi$, where $\Xi_m = \{\boldsymbol{\xi}_1, \ldots, \boldsymbol{\xi}_{q_m}\}$. The term q_m represents the number of samples in the set Ξ_m. Given a set of samples Ξ_m, we construct a region Q_m that is assumed to enclose the positive limit set. Before we go into the details of implementation, let us take a look at the theory behind Voronoi partitions.

4.3.1 Voronoi Partition

Suppose the state-space X is endowed with the metric $d(\cdot, \cdot)$. In this chapter, we use the Euclidean metric. Let $Q_m \subseteq X$ be a convex polytope and let $P_m = \{\boldsymbol{p}_{m,1}, \ldots, \boldsymbol{p}_{m,n_m}\}$ be a set of n_m points. The Voronoi partition $\mathcal{V}(P_m)$ generated by the set of points P_m is the

collection of n_m polytopes, $P_{m,1}, \ldots, P_{m,n_m}$, defined by

$$P_{m,i} = \{\boldsymbol{x} \in Q_m \mid d(\boldsymbol{x}, \boldsymbol{x}_i) \leq d(\boldsymbol{x}, \boldsymbol{x}_j), \text{ for } j = 1, \ldots, n_m, j \neq i\}$$

for $i = 1, \ldots, n_m$. An edge of the polytope $P_{m,i}$ is the region $P_{m,i} \cap P_{m,j}$ or $P_{m,i} \cap \partial Q_m$ for some $j \neq i$. We say that two polytopes are adjacent when they share a common edge. The notation ∂Q_m denotes the boundary of the region Q_m. We use the notation $\mathbb{E}(\mathcal{V}(P_m), Q_m)$ to denote the union of all edges of the polytopes in $\mathcal{V}(P_m)$. If $R \subseteq Q_m$, then $\mathbb{E}(\mathcal{V}(P_m), R) = \mathbb{E}(\mathcal{V}(P_m), Q_m) \cap R$. A particular class of Voronoi partitions are the *centroidal Voronoi partitions* or *centroidal Voronoi tessellations*, where each point generating the polytope is also its centroid. We use the notation $C_{P_{m,j}}$ to denote the centroid that generates the polytope $P_{m,j}$. Note, given a region $Y \subseteq X$, its centroid C_Y is defined as

$$C_Y = \frac{1}{M_Y} \int_Y \boldsymbol{y} \rho(\boldsymbol{y}) d\boldsymbol{y},$$

where $M_Y := \int_Y \rho(\boldsymbol{y}) d\boldsymbol{y}$ is the total mass of Y, and $\rho(\boldsymbol{y})$ is the mass density function over Y. When the polytope Q_m is convex, the partitions are also convex. This in turn implies that the centroid of each partition is contained inside the polytope. For a fixed number of partitions n_m, a convex polytope Q_m can have more than one centroidal Voronoi partition. While implementing this method for kernel center selection, the term n_m corresponds to the number of centers. The subscript m corresponds to the sampling subset Ξ_m. The number of kernel centers depends on the samples collected in this method.

4.3.2 Lloyd's algorithm

Lloyd's algorithm is used to construct the centroidal Voronoi tessellations for a given convex polytope Q_m and a fixed number of partitions n_m. It involves the following steps,

(i) Choose an initial set of points P_m.

(ii) Calculate the Voronoi partitions $\mathcal{V}(P_m)$ for the n_m points.

(iii) Calculate the set of centroids $\{C_{P_{m,1}}, \ldots, C_{P_{m,n_m}}\}$ of the Voronoi partitions.

(iv) Set $P_m = \{C_{P_{m,1}}, \ldots, C_{P_{m,n_m}}\}$ and go back to the second step.

The above set of steps are evaluated until convergence of centroids is achieved. The convergence of the algorithm for the convex case is proved in [47].

4.3.3 Implementation

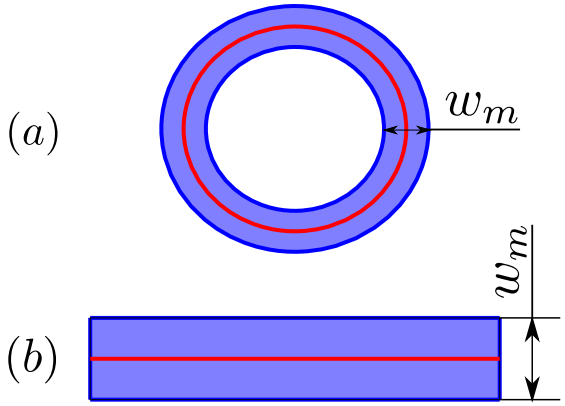

Figure 4.4: Examples of region Q_m constructed around the $\Xi_m \subseteq \omega^+(\boldsymbol{x}_0)$. The red curves are formed by connecting the samples Ξ_m. The blue region represents the region Q_m.

The idea behind this approach is that we have a finite sampling Ξ_m of the positive limit set $\omega^+(\boldsymbol{x}_0)$. We use this finite sampling Ξ_m to construct a region Q_m that encloses the positive limit set $\omega^+(\boldsymbol{x}_0)$. We then calculate the centroidal Voronoi partitions of the polygon and choose the kernel centers as the centroids of the partitions. In our implementation, we assume the mass density function as $\rho(\boldsymbol{q}) = 1$ for all $\boldsymbol{q} \in Q_m$ and $\rho(\boldsymbol{q}) = 0$ elsewhere. In the following discussion, we formalize this implementation.

Examples of the region Q_m for two different positive limit sets is shown in Figure 4.4. In the

case (b) where the positive limit set $\omega^+(\boldsymbol{x}_0)$ is straight line, the region Q_m is nothing but the rectangle enclosing the set. For the case (a) where the positive limit set $\omega^+(\boldsymbol{x}_0)$ is a closed curve that is symmetric about the origin in the figure, the region Q_m is first formed by the joining the samples of the positive limit set to form a closed curve. The closed curve is then scaled to form a larger and smaller closed curves. We choose Q_m to be the region enclosed by the larger and smaller closed curves. As evident from Figure 4.4, the region Q_m is not always convex. Thus, the theory in the previous subsection is not strictly applicable. Let Q'_m be the convex hull of the polytope Q_m. We know that the Lloyd's algorithm converges for the convex case. [47] The mass density function is still equal to 1 on Q_m and 0 elsewhere. Suppose we choose n_m points in Q'_m and run the Lloyd's algorithm. As a result, we get a set of centroids P'_m that generate the centroidal Voronoi partition $\mathcal{V}(P'_m)$. Now we define the collection $\mathcal{V}(P_m) := \{P'_{m,1} \cap Q_m, \ldots, P'_{m,n_m} \cap Q_m\}$. It is easy to see that $\mathcal{V}(P_m)$ is a centroidal Voronoi partition of the region Q_m generated by the centroids $P_m = P'_m$.

Thus, the Lloyd's algorithm indeed converges for the case in question. However, the polytopes in $\mathcal{V}(P_m)$ are not necessarily convex. And hence, the centroid $p_{m,i} \in P_m$ need not be contained in the polytope $P'_{m,i} \cap Q_m$ for $i = 1, \ldots, n_m$. The centers need not even be contained in the region Q_m. This is certainly not desirable when implementing Lloyd's algorithm and CVT for problems like sensor location or multirobot coordination. [48] However, the goal of our problem is to choose kernel centers that are close to the positive limit set. In the following analysis, we show that with sufficient number of samples and careful selection of the the region Q_m, we can often choose centers close to the positive limit set.

4.3.4 Convergence for Restricted Cases

We restrict the following analysis to positive limit sets contained in $\mathbb{R}^2$ that are homeomorphic to a line or a circle. In other words, the positive limit set is an open or closed curve.

With careful selection of Q_m, it is possible to show that we can choose kernel centers that approximate the positive limit set. The region Q_m is constructed such that the following conditions holds.

Condition 4.12. Associated with each Ξ_m is a region Q_m such that

1. the maximum width w_m of the region satisfies $w_m < r_m$, where $0 < r_m < r_{m-1}$ for all $m \in \mathbb{N}$,

2. the region Q_m is nested in Q_{m-1} for all $m \in \mathbb{N}$,

3. the sequence $\{r_m\}_{n=1}^{\infty}$ converges to 0,

4. for each r_m, there is an integer n_m such that the polytope $P_{m,j} \subseteq B_{cr_m}(C_{P_{m,j}})$ for all $j = 1, \ldots, n_m$. Here, the term $B_{cr_m}(C_{P_{m,j}})$ is the closed ball of radius cr_m centered at the centroid $C_{P_{m,j}}$ that generates the polytope $P_{m,j}$ with c a fixed positive constant.

We can think of the maximum width w_m of the region Q_m given in Figure 4.4 (a) as the Hausdorff distance between the inner and outer boundaries of the region Q_m. In the case of the region given in Figure 4.4 (b), the maximum width w_m corresponds to the Hausdorff distance between the two boundaries of the region Q_m that are parallel to the positive limit set.

Theorem 4.13. *Suppose Condition 4.12 holds. Then* $d(\omega^+(\boldsymbol{x}_0), P_m) \to 0$ *as* $m \to \infty$, *where* $d(\cdot, \cdot)$ *is the Hausdorff distance,* $\omega^+(\boldsymbol{x}_0)$ *is the positive limit set and* $P_m = \{C_{P_{m,1}}, \ldots, C_{P_{m,nm}}\}$ *is the set of centroids that generate the CVT* $\mathcal{V}(P_m)$.

Proof. We fist note that the centroid of each polytope is contained in $B_{cr_m}(C_{P_{m,j}})$ since the ball is convex. Since the maximum width of the region w_m satisfies $w_m < r_m$, it is clear that

$d(\omega^+(\boldsymbol{x}_0), Q_m) < r_m$. On the other hand, since the ball $B_{cr_m}(C_{P_{m,j}})$ contains the polytope $P_{m,j}$, we have $d(P_{m,j}, \{C_{P_{m,j}}\}) < cr_m$ for any $j = 1, \ldots, n_m$. Note that the bound cr_m on $d(P_{m,j}, \{C_{P_{m,j}}\})$ is uniform. Also, recall that $Q_m = \cup_{j=1}^{n_m} P_{m,j}$, and $P_m = \cup_{j=1}^{n_m} \{C_{P_{m,j}}\}$. Thus, we have $d(Q_m, P_m) < cr_m$. Using triangle inequality, we get $d(\omega^+(\boldsymbol{x}_0), P_m) < (1 + c)r_m$. Since $r_m \to 0$ as $m \to \infty$, we conclude that the centroids approach the positive limit set as $m \to \infty$. □

The assumptions in the above theorem are very strong because of Condition 4.12. It is possible to relax some of the assumptions by considering the geometric properties of the partitions. But, from a practical standpoint, the maximum number of samples of the positive limit set is limited by the measurement equipment. This theorem provides a framework for an implementation that agrees with intuition - if new samples of the positive limit set are measured, choose Q_m such that r_m is reduced and number of kernel centers n_m are increased. For a given r_m, the number of kernel centers cannot be indefinitely increased. Consider the example in Figure 4.5. Due to numerical errors, the Lloyd's algorithm converges to a CVT in which the kernel centers do not lie on the positive limit set when n_m is large. On the other hand, the term r_m cannot be decreased indefinitely, since the region Q_m, built based on finite number of samples, may no longer contain the positive limit set. Thus, the number of samples collected restrict the effectiveness of this method.

To avoids CVTs that are similar to the one given in Figure 4.5 (b), we introduce the following condition. Let $\bar{Q}$ represent the outer rectangle that is contained in $\mathbb{R}^2$ in Figure 4.5 and let $\bar{\mathcal{V}}_l$ represent the CVT made up of l horizontally stacked identical rectangles. Figure 4.5 (a) depicts the CVT $\bar{\mathcal{V}}_5$ of $\bar{Q}$. The following condition inherently ensures that the kernel centers are evenly distributed in or near the positive limit set.

Condition 4.14. Let $l = 1, \ldots, n_m$. For any possible l, consider an arbitrary collection of

l polytopes $P_{m,i_1}, \ldots, P_{m,i_l}$ in the partition $\mathcal{V}(P_m)$ such that each polytope is adjacent to at least one other polytope in the collection. The union of edges $\mathbb{E}(\mathcal{V}(P_m), P_{m,i_1} \cup \ldots \cup P_{m,i_l})$ is homeomorphic to the union of edges $\mathbb{E}(\bar{\mathcal{V}}_l, \bar{Q})$ of the CVT $\bar{\mathcal{V}}_l$.

Algorithm 2: CVT based kernel center selection

Input: Ξ_m, n_m

Output: P_m

1 Choose the constant r_m. Construct region Q_m such that the positive limit set $\omega^+(\boldsymbol{x}_0)$ is contained in Q_m.

2 Choose n_m separate points in the convex hull of Q_m.

3 Run the Lloyd's algorithm using the points chosen in Step 2 as the initial points.

(i) Calculate the Voronoi partitions $\mathcal{V}(P_m)$ for the n_m points.

(ii) Calculate the centroids $C_{P_{m,1}}, \ldots, C_{P_{m,n_m}}$ of the Voronoi partitions $\mathcal{V}(P_m)$.

(iii) Set $P_m = \{C_{P_{m,1}}, \ldots, C_{P_{m,n_m}}\}$ and go back to the Step 3 (i).

4 The above steps are repeated until convergence is achieved.

5 If the CVT from Step 4 does not satisfy Condition 4.14, choose a constant s_m such that $s_m < r_m$. Set $r_m = s_m$ and go back to Step 2.

If the CVT satisfies Condition 4.14, choose the set of centroids of the CVT P_m as the kernel centers for the adaptive estimator.

Algorithm 2 shows the steps involved in implementing this method. Step 4 in the algorithm can be implemented using commercially available tools like MATLAB, which makes the algorithm extremely straightforward for implementation. The inputs to the algorithm are the samples Ξ_m and the number of kernel centers n_m. We iteratively choose r_m in the algorithm until Condition 4.14 is satisfied. The output of the algorithm is the set of kernel centers, which can be implemented in the adaptive estimator algorithm.

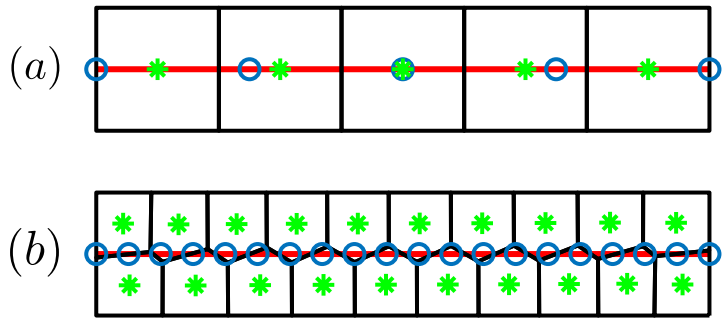

Figure 4.5: Increasing the number of kernel centers leads to completely different types of CVT while using the same Lloyds algorithm. The markers o and $*$ represent the initial positions and final converged positions of the kernel centers, respectively. The red line represents the limit set.

4.4 Method 2: Based on Kohonen Self-Organizing Maps

The second approach presented in this chapter is based on Kohonen self-organizing maps (SOMs), which were first introduced by Teuvo Kohonen. [49] Self-organizing maps are typically used for applications like clustering data, dimensionality reduction, pattern recognition, and visualization. Thus, given a set of samples in the input space, these maps can be used to produce a collection of neurons on a low-dimensional manifold that represents the samples' distribution. In our problem, the input space is the state-space, and the samples are the state measurements. The neurons on the low-dimensional manifold are the kernels centers. The position of the kernel centers in the state-space are represented by the weight vectors that the SOM algorithm generates.

One of the critical features of self-organizing maps is that the underlying topology between the input space (the original dataset) and the output space is maintained. Intuitively, points that are close in the original dataset are mapped to neurons that are close to each other (in some predefined metric). For our problem, we want the kernel centers to be evenly spaced in the state-space in addition to being close to the measurement samples. To ensure this, we choose the initial set of kernel centers on a manifold that is homeomorphic to the positive

limit set. This requires knowledge of the topology of the positive limit set. Before going over the details, let us take a look at the theory of Kohonen self-organizing maps.

Suppose we have the set of samples $\Xi_m = \{\boldsymbol{\xi}_{m,1}, \ldots, \boldsymbol{\xi}_{m,q_m}\}$. In the context of this chapter, the set Ξ_m is the set of samples of the positive limit set $\omega^+(\boldsymbol{x}_0)$. Let n_m represent the number of kernel centers $\boldsymbol{p}_{m,1}, \ldots, \boldsymbol{p}_{m,n_m}$ we want to choose. We associate the i^{th} kernel center with a weight vector $\boldsymbol{p}_{m,i}(t) \in \mathbb{R}^d$ for $i = 1, \ldots, n_m$. Note that the weight vectors depend on time and at any given instant in time t, the weight vector is an element of $\mathbb{R}^d$. The neighborhood function $\mathcal{N}_j$ defines neighbors of the center j. The choice of the neighborhood function depends on the topology we want to define on the kernel centers. The neurons (or the kernel centers) are often chosen in the form of a linear grid or a $2D$ grid, and the neighbors in such grids are naturally defined. The Kohonen self-organizing map's implementation involves the following steps. We first randomly choose a sample $\boldsymbol{\xi}_{m,k}$ from the sample set Ξ_m, where $k \in \{1, \ldots, q_m\}$. We then determine the winning neuron - the kernel center that is closest to the sample $\boldsymbol{\xi}_{m,k}$. The winning neuron i at a given instant t is the one which satisfies the condition

$$d(\boldsymbol{\xi}_{m,k}, \boldsymbol{p}_{m,i}(t)) \leq d(\boldsymbol{\xi}_{m,k}, \boldsymbol{p}_{m,j}(t)) \tag{4.4}$$

for $j = 1, \ldots, n_m$. We now update the weight vectors using the evolution equation

$$\frac{d\boldsymbol{p}_{m,j}(t)}{dt} = \beta_j(t)\mathcal{N}_j(t,i)\left(\boldsymbol{\xi}_{m,k} - \boldsymbol{p}_{m,j}(t)\right) \tag{4.5}$$

for $j = 1, \ldots, n_m$. In the above equation, $0 \leq \beta_j(t) < 1$ defines the rate of convergence of the center j. The neighborhood function determines which neighbors of the node i get updated. For convergence, we require that $\beta_j(t) \to 0$ and $\mathcal{N}_j(t,i) \to 0$ as $t \to \infty$, for any $i, j \in \{1, \ldots, n_m\}$. While implementing this algorithm, we can observe the SOM goes

through a *topological ordering phase* during which the grid of neurons try to match the patterns if the sample in the input space before convergence.

Note: The self-organizing map algorithm is easy to implement. However, many theoretical aspects of these maps, like convergence, remain unanswered for the general case. Researchers have studied and proved the theory for the 1D linear array case, when the nodes are arranged on a line. A review of some of the theoretical results are in [50].

4.4.1 Implementation

To implement Kohonen self-organizing maps for kernel center selection, we modify the above-discussed algorithm. In some dynamical systems, the trajectory approaches the positive limit set but is never contained in the set. In such cases, we only have measurements of the states and not the samples of positive limit set. Furthermore, arbitrary selection of state-samples might result in picking points away from the positive limit set. This in turn affects the convergence of the kernel centers to points inside the positive limit set. Hence, as opposed to choosing random samples $\boldsymbol{\xi}_{m,j}$ from the set Ξ_m, we use the state measurement $\boldsymbol{x}(t)$ at a given time instant to determine the winning node. We replace the term $\boldsymbol{\xi}_{m,j}$ with $\boldsymbol{x}(t)$ in Equations 4.4 and 4.5. This change enables us to implement this method for a more general class of systems in real-time.

A Kohonen self-organizing map algorithm gives a low-dimensional representation of all samples (which include the ones that are outside the limit set). On the other hand, the objective of our problem is to choose kernel centers on the positive limit set such that they are spaced as uniformly as possible. To ensure this, we choose the topology of the output space to match that of the positive limit set. In other words, we choose the initial kernel centers and the neighborhood function such that the topology is homeomorphic to the positive limit set.

For example, if the positive limit set is a closed curve in $\mathbb{R}^2$, the initial weight vectors can be points on the unit circle, and the neighborhood function can be defined as

$$\mathcal{N}_j(t,i) = \begin{cases} 1 & \text{if } j \in \mathcal{T}, \\ 0 & \text{if } j \notin \mathcal{T}, \end{cases} \tag{4.6}$$

where the set $\mathcal{T}$ is defined as $\mathcal{T} = \{i-1, i, i+1\}$ for $i \neq 1, n_m$. For $i = 1$ and $i = n_m$, we choose $\mathcal{T} = \{n_m, 1, 2\}$ and $\mathcal{T} = \{n_m - 1, n_m, 1\}$, respectively.

On top of the above modifications, we enforce the condition that, when we have samples of the positive limit set, the number of kernel centers or neurons n_m should be strictly less than q_m, the number of samples in the set Ξ_n. When n_m is equal to q_m, the kernel centers can converge to the samples. In the case where the positive limit set is a closed curve, this can be interpreted as a solution to the traveling salesman problem. [51] To avoid convergence to the samples, we impose the above dimensionality reduction condition.

Algorithm 3 shows the steps involved in implementing this method. We present the algorithm for the case where the positive limit set is a closed curve. However, the algorithm can be extended easily for other types of positive limit sets. The neighborhood function for this case, defined by Equation 4.6, is inherently accounted in the algorithm.

Recall that in the case of CVT based method presented in the previous section, the samples are contained in the positive limit set, which meant the trajectory was contained in the positive limit set or converged to the set in finite time. Since we use the state measurement for the Kohonen SOM based approach, we can relax some of the requirements of the CVT based method. It is sufficient for the trajectory to converge to the positive limit set as $t \to \infty$. However, it is important to choose $\beta_j(t)$ such that the state trajectory converges to the positive limit set faster than the rate at which $\beta_j(t) \to 0$. If this is violated, the kernel

centers will not converge to the positive limit set.

Algorithm 3: Kohonen SOM based Kernel Center Selection - Closed Curve Case

---

Input: $\boldsymbol{x}(t)$, q_m

Output: $\{\boldsymbol{p}_{m,1}(T), \ldots, \boldsymbol{p}_{m,n_m}(T)\}$

1 Choose the number of kernel centers n_m such that $n_m < q_m$. If $p_m = 0$, choose a positive integer for n_m.

2 Choose β_j such that $0 \leq \beta_j(t) < 1$ for $t \in [0, \infty)$ and $\beta_j(t) \to 0$ as $t \to \infty$ for all $j = 1, \ldots, n_m$.

3 Initialize the weight vectors $\boldsymbol{p}_{m,j}$ as the points on a circle contained inside the closed curve.

4 Implement the Kohonen SOM algorithm for $t \in [0, T]$ for some $T > 0$.

(i) At time t, determine the winning neuron i that satisfies the condition

$$d(\boldsymbol{x}(t) - \boldsymbol{p}_{m,i}(t)) \leq d(\boldsymbol{x}(t) - \boldsymbol{p}_{m,j}(t))$$

for $j = \{1, \ldots, n_m\}$.

(ii) Define the set $\mathcal{T}$ as $\mathcal{T} = \{i-1, i, i+1\}$ for $i \neq 1, n_m$. For $i = 1$ and $i = n_m$, choose $\mathcal{T} = \{n_m, 1, 2\}$ and $\mathcal{T} = \{n_m - 1, n_m, 1\}$, respectively.

(iii) Update the weight vectors based on

$$\frac{d\boldsymbol{p}_{m,j}(t)}{dt} = \begin{cases} \beta_j(t)\left(\boldsymbol{x}(t) - \boldsymbol{p}_{m,j}(t)\right) & \text{if } j \in \mathcal{T} \\ 0 & \text{if } j \notin \mathcal{T} \end{cases}$$

for $j = 1, \ldots, n_m$. This update happens until next state measurement. Go back to Step 4 (i) after the update.

Note, in the Lloyd's algorithm, the distance between any two kernel centers is inherently ensured to remain uniform by the algorithm. This can be attributed to the way partitions are defined and the selection of the mass density function. On the other hand, the distribution of the converged kernel centers from the Kohonen SOM based algorithm depends on the distribution of the sampled measurements. If the state measurements are concentrated on a particular neighborhood of the positive limit set, implementing Algorithm 3 will result in the kernel centers being concentrated in or near the neighborhood.

4.5 Numerical Illustration of Center Selection Methods

We illustrate the effectiveness of the two approaches explained above for two examples in this section. The first example is the undamped piezoelectric oscillator example considered in Section 4.2.7. The positive limit set in this case is almost symmetric about the axis after scaling of the states. The second example is a nonlinear oscillator which has a nonsymmetric positive limit set. We implement the above discussed methods for both cases and use the resulting kernel centers in the adaptive estimators. We use MATLAB lloydsAlgorithm function, developed by Aaron T. Becker's Robot Swarm Lab, for implementing Step 4 of Algorithm 2. The function expects the boundary of a polygon as input and hence we approximate the region Q_m using a polygon as shown in Figures 4.6 and 4.9. In the adaptive estimator simulations, we use the Sobolev-Matern $3, 2$ kernel given in Subsection 4.2.7.

4.5.1 Example 1: Nonlinear Piezoelectric Oscillator

The first example we consider is the undamped nonlinear piezoelectric oscillator whose motion is governed by the Equation 4.3. We use the same values for the structural parameters as

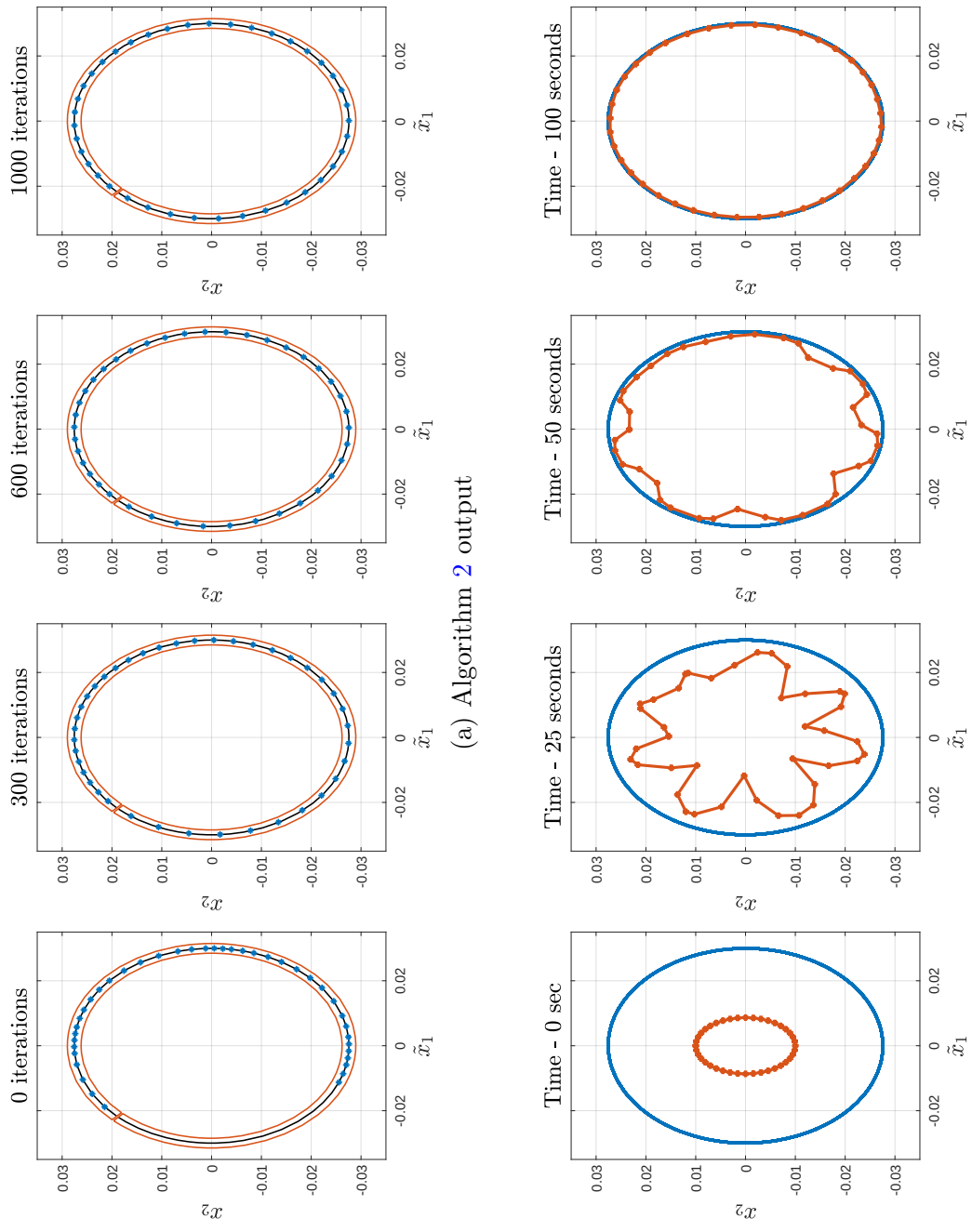

(a) Algorithm 2 output

(b) Algorithm 3 output

Figure 4.6: Algorithm outputs of Example 4.5.1. The marker $*$ and the blue line represent the kernel centers and the limit set, respectively.

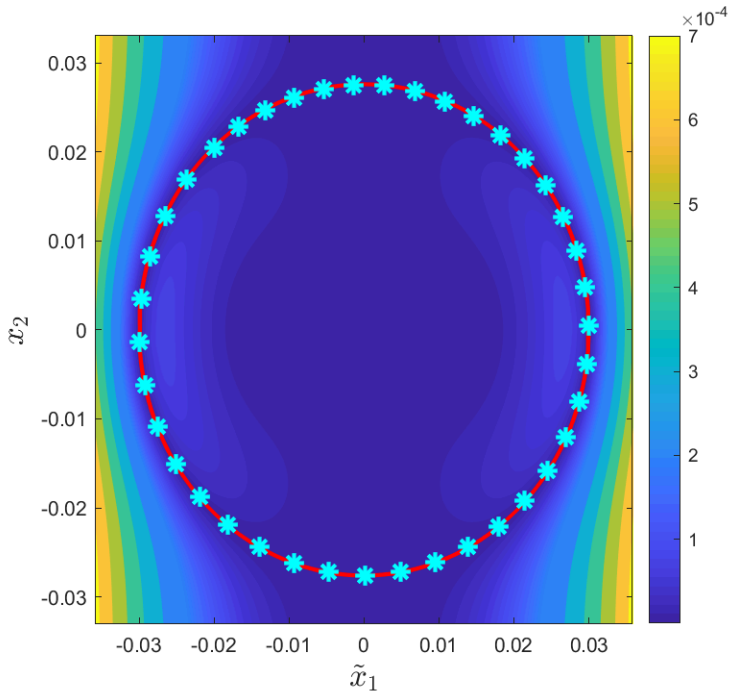

Figure 4.7: Kernel centers for Example 4.5.1 selected using Algorithm 2 - Pointwise error $|f(\boldsymbol{x}) - \hat{f}_n(T, \boldsymbol{x})|$ obtained from adaptive estimator. The marker $*$ and the red line represent the kernel centers and the limit set, respectively.

the ones used in the example in Section 4.2.7. We set the scaling factor $S = 0.02$ and initialized the states at $\boldsymbol{x}_0 = \{\tilde{x}_1(0), x_2(0)\}^T = \{0.03, 0\}^T$. Figure 4.6 shows how the kernel centers evolve while using Algorithms 2 and 3. We set the number of kernel centers as $n_m = 40$ for both of the algorithms. For implementing Algorithm 2, we first collect the set of samples Ξ_m of the positive limit set $\omega^+(\boldsymbol{x}_0)$. By connecting the samples in Ξ_m with straight lines, we form a closed curve which is represented by the blue line in Figure 4.6a. We then scale the closed curve by a factor of 1.1 and 0.9, thus forming concentric larger and smaller closed curves. We chose the region between these two closed curves as Q_m. Dividing the region Q_m as shown in Figure 4.6a results in a polygon, thus enabling us to use the lloydsAlgorithm function in MATLAB. While implementing Algorithm 2, we chose $\beta_j(t) = 0.99$ for $t \leq 1000$ s and $\beta_j(t) = 0$ for $t > 1000$ s for all j. As evident from Figure 4.6, the CVT based approach

and the Kohonen SOM based approach take 1000 iterations and 100 seconds, respectively to converge. It is clear that the kernel centers are more uniformly spaced than those picked arbitrarily in the example in Subsection 4.2.7. We subsequently use the converged kernel centers and simulate the adaptive estimator algorithm for $T = 300$ seconds. For the adaptive estimator, we set $l = 0.006$, $\Gamma = 0.001$ and initialized the parameters at $\alpha_i(t) = 0.0001$ for $i = 1 \ldots, n_m$. Figures 4.7 and 4.8 shows the pointwise error $|f(\boldsymbol{x}) - \hat{f}(T, \boldsymbol{x})|$ obtained after using the kernel centers from the CVT and Kohonen SOM based approach. As expected, both the plots show that the error is $\mathcal{O}(10^{-4})$ over the positive limit set.

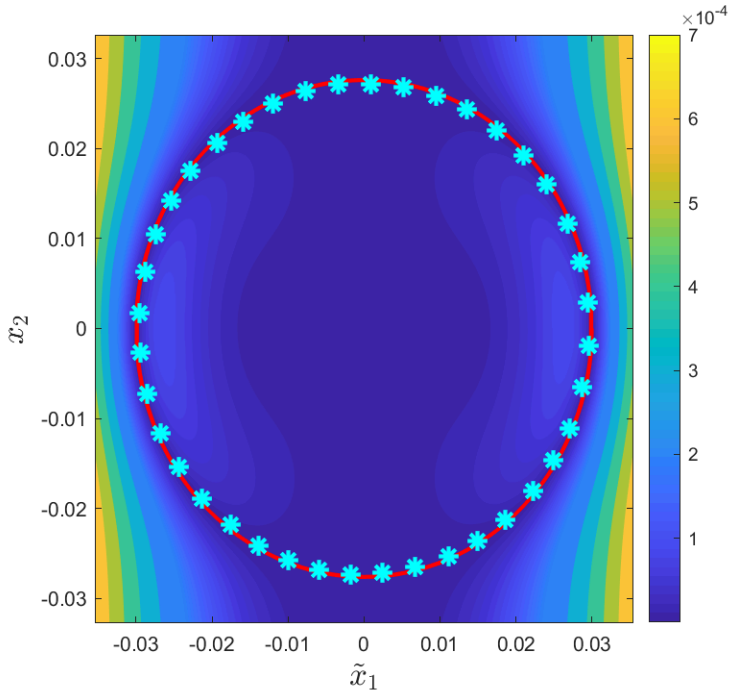

Figure 4.8: Kernel centers for Example 4.5.1 selected using Algorithm 3 - Pointwise error $|f(\boldsymbol{x}) - \hat{f}_n(T, \boldsymbol{x})|$ obtained from adaptive estimator. The marker $*$ and the red line represent the kernel centers and the limit set, respectively.

4.5.2 Example 2: Nonlinear Oscillator

For the second example, we consider a nonlinear oscillator whose motion is governed by the equation

$$\begin{Bmatrix} \dot{x}_1 \\ \dot{x}_2 \end{Bmatrix} = \underbrace{\begin{bmatrix} 0 & 1 \\ -1 & 0.5 \end{bmatrix}}_{A} \begin{Bmatrix} x_1 \\ x_2 \end{Bmatrix} + \underbrace{\begin{Bmatrix} 0 \\ 1 \end{Bmatrix}}_{B} \underbrace{\left(-x_1^2 x_2\right)}_{f(\boldsymbol{x}(t))}. \tag{4.7}$$

This system exhibits a more complex behavior than that in Example 4.5.1. Firstly, the state trajectory is not contained in the positive limit set $\omega^+(\boldsymbol{x}_0)$, which is depicted as the blue, solid line in Figure 4.9. Note that the positive limit set is not symmetric. Refer Example 9.2.2 in [52] for a detailed analysis of the nonlinear behavior of the oscillator. Here, we are interested in estimating the nonlinear function $f(\boldsymbol{x}(t)) = -x_1^2 x_2$. Figure 4.9 shows the implementation of the CVT based and Kohonen SOM based kernel center selection methods for this problem. In both cases, we fixed number of kernel center as $n_m = 40$ and initialized the states at $\boldsymbol{x}_0 = \{x_1(0), x_2(0)\}^T = \{0, 2\}^T$. The polygon in Figure 4.9a for the CVT based approach is built similar to the method used for Example 4.5.1. For the Kohonen SOM approach, we set $\beta_j(t) = 0.99$ for $t \leq 1000$ s and $\beta_j(t) = 0$ for $t > 1000$ s for all j. As evident from the figures, the CVT and Kohonen SOM methods take 600 iterations and 200 seconds, respectively for convergence of the kernel centers. It is clear that the kernel centers from the CVT based algorithm are more uniformly placed that the output of the Kohonen SOM algorithm. This can be attributed to the fact the state measurement samples are not uniformly distributed and to the fact that the CVT method makes strong assumptions about the structure of Q_m. Since the distribution of the state measurement affect the results of the Kohonen SOM based approach, the kernel centers are not uniform in this case. However, when the kernel centers from these algorithms are implemented in the adaptive estimator,

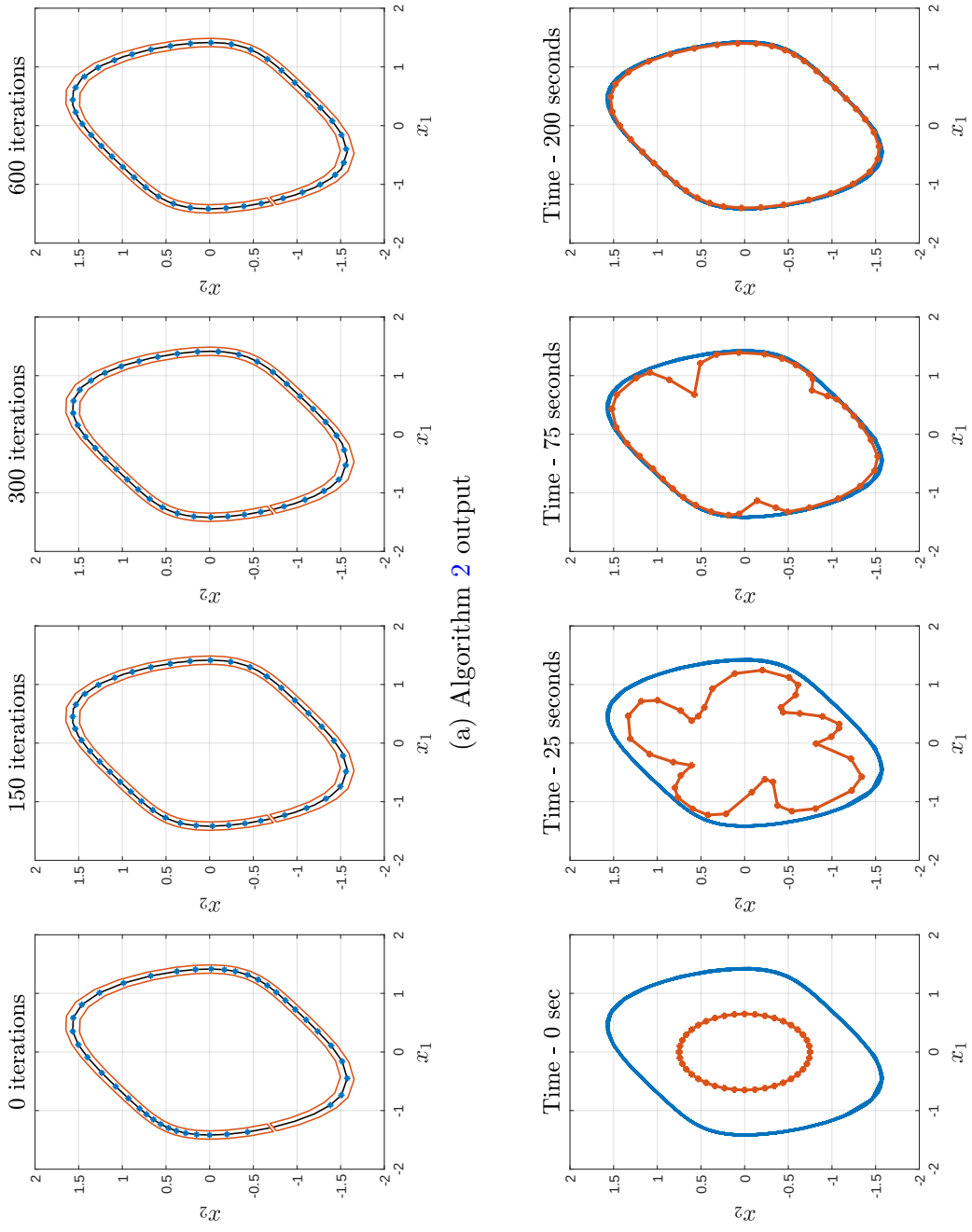

(a) Algorithm 2 output

(b) Algorithm 3 output

Figure 4.9: Algorithm outputs of Example 4.5.2. The marker $*$ and the blue line represent the kernel centers and the limit set, respectively.

we obtain convergence on the positive limit set. Figures 4.10 and 4.11 shows the pointwise error $|f(\boldsymbol{x}) - \hat{f}(T, \boldsymbol{x})|$ after implementing the adaptive estimator for $T = 300$ seconds using the kernel centers from the CVT and Kohonen SOM based kernel center selection approach, respectively. We set $l = 0.5$, $\Gamma = 0.001$ and initialized the parameters at $\alpha_i(t) = 0.0001$ for $i = 1 \ldots, n_m$. As in Example 4.5.1, the error is the smallest over the positive limit set.

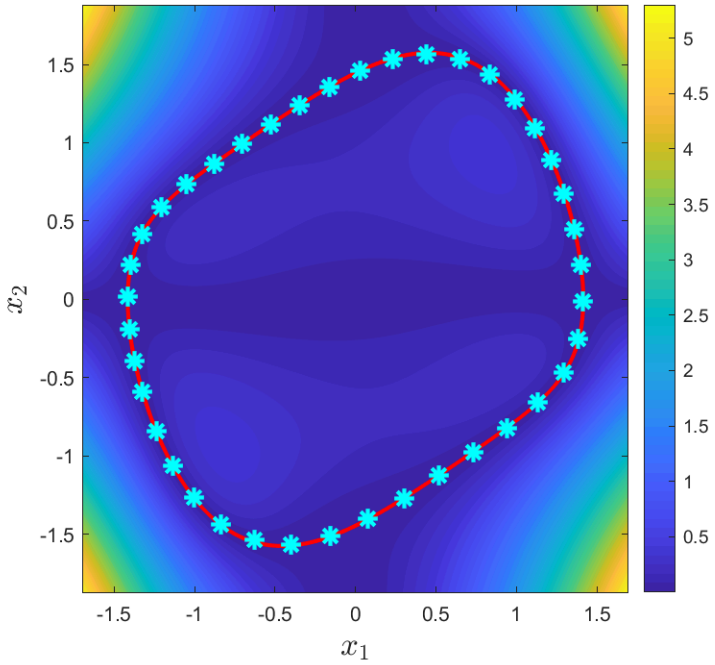

Figure 4.10: Kernel centers for Example 4.5.2 selected using Algorithm 2 - Pointwise error $|f(\boldsymbol{x}) - \hat{f}_n(T, \boldsymbol{x})|$ obtained from adaptive estimator. The marker $*$ and the red line represent the kernel centers and the limit set, respectively.

4.6 Conclusion

In this chapter, we developed criteria for kernel center selection based on the theory of infinite-dimensional adaptive estimation in reproducing kernel Hilbert spaces. We introduced two methods that use this criteria for kernel center selection. These methods provide a simple way to choose kernel centers for a specific class of nonlinear systems - systems in which state

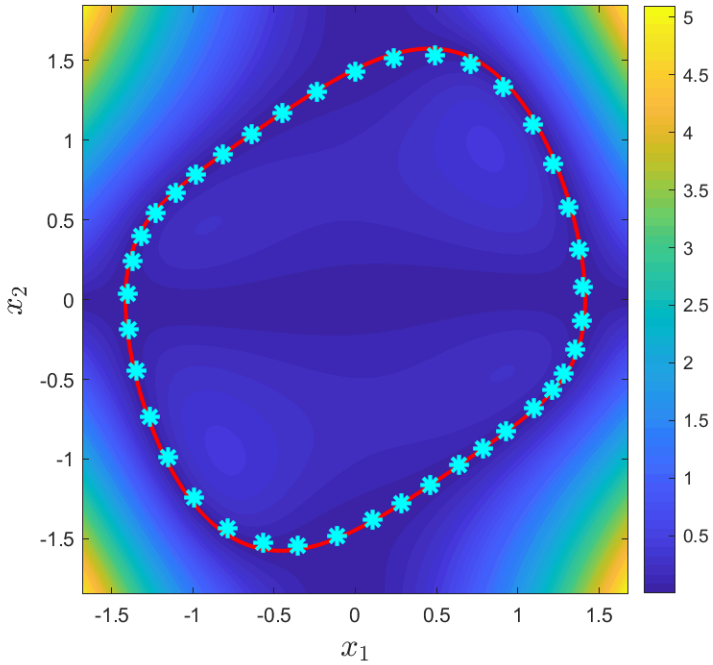

Figure 4.11: Kernel centers for Example 4.5.2 selected using Algorithm 3 - Pointwise error $|f(\boldsymbol{x}) - \hat{f}_n(T, \boldsymbol{x})|$ obtained from adaptive estimator. The marker $*$ and the red line represent the kernel centers and the limit set, respectively.

trajectory regularly visits the neighborhoods of the positive limit set. We illustrated the effectiveness of both algorithms using practical examples. The approaches discussed in this chapter assume a fixed number of kernel centers. It would be of great interest to develop techniques that iteratively add kernel centers in real-time while accounting for the persistence of excitation and fill-distance conditions.

Bibliography

[1] P. A. Ioannou and Jing Sun. *Robust Adaptive Control*. Dover Publications Inc., 1996. ISBN 0486498174.

[2] Shankar Sastry and Marc Bodson. *Adaptive control: stability, convergence and robustness*. Courier Corporation, 2011. ISBN 0486482022.

[3] Kumpati S Narendra and Anuradha M Annaswamy. *Stable adaptive systems*. Courier Corporation, 2012. ISBN 048614142X.

[4] A. J. Kurdila, Francis J. Narcowich, and Joseph D. Ward. Persistency of excitation in identification using radial basis function approximants. *SIAM journal on control and optimization*, 33(2):625–642, July 1995. ISSN 0363-0129. doi: 10.1137/S0363012992232555.

[5] H A Kingravi, G Chowdhary, P A Vela, and E N Johnson. Reproducing Kernel Hilbert Space Approach for the Online Update of Radial Bases in Neuro-Adaptive Control. *IEEE Transactions on Neural Networks and Learning Systems*, 23(7):1130–1141, 2012. ISSN 2162-2388 VO - 23. doi: 10.1109/TNNLS.2012.2198889.

[6] Parag Bobade, Suprotim Majumdar, Savio Pereira, Andrew J. Kurdila, and John B. Ferris. Adaptive estimation for nonlinear systems using reproducing kernel Hilbert spaces. *Advances in Computational Mathematics*, 45(2):869–896, 2019. ISSN 1572-9044. doi: 10.1007/s10444-018-9639-z. URL https://doi.org/10.1007/s10444-018-9639-z.

[7] Yaser S Abu-Mostafa, Malik Magdon-Ismail, and Hsuan-Tien Lin. *Learning From Data*. AMLBook, 2012. ISBN 1600490069.

[8] Junjie Wu. *Advances in K-means clustering: a data mining thinking*. Springer Science & Business Media, 2012. ISBN 3642298079.

[9] Mark J L Orr. Regularization in the Selection of Radial Basis Function Centers. *Neural Computation*, 7(3):606–623, May 1995. ISSN 0899-7667. doi: 10.1162/neco.1995.7.3.606. URL https://doi.org/10.1162/neco.1995.7.3.606.

[10] K Warwick, J D Mason, and E L Sutanto. Centre Selection for Radial Basis Function Networks BT - Artificial Neural Nets and Genetic Algorithms. pages 309–312, Vienna, 1995. Springer Vienna. ISBN 978-3-7091-7535-4.

[11] J Nie and D A Linkens. Learning control using fuzzified self-organizing radial basis function network. *IEEE Transactions on Fuzzy Systems*, 1(4):280–287, 1993. ISSN 1941-0034 VO - 1. doi: 10.1109/91.251928.

[12] G D Hager, M Dewan, and C V Stewart. Multiple kernel tracking with SSD. In *Proceedings of the 2004 IEEE Computer Society Conference on Computer Vision and Pattern Recognition, 2004. CVPR 2004.*, volume 1, pages I–I, 2004. ISBN 1063-6919 VO - 1. doi: 10.1109/CVPR.2004.1315112.

[13] Gwo-Fong Lin and Lu-Hsien Chen. Time series forecasting by combining the radial basis function network and the self-organizing map. *Hydrological Processes*, 19(10): 1925–1937, June 2005. ISSN 0885-6087. doi: 10.1002/hyp.5637. URL https://doi.org/10.1002/hyp.5637.

[14] Zhimin Fan, Ming Yang, Ying Wu, Gang Hua, and Ting Yu. Efficient Optimal Kernel Placement for Reliable Visual Tracking. In *2006 IEEE Computer Society Conference on Computer Vision and Pattern Recognition (CVPR'06)*, volume 1, pages 658–665, 2006. ISBN 1063-6919 VO - 1. doi: 10.1109/CVPR.2006.109.

[15] J Lian, Y Lee, S D Sudhoff, and S H Zak. Self-Organizing Radial Basis Function Network for Real-Time Approximation of Continuous-Time Dynamical Systems. *IEEE Transactions on Neural Networks*, 19(3):460–474, 2008. ISSN 1941-0093 VO - 19. doi: 10.1109/TNN.2007.909842.

[16] H Han and J Qiao. A Self-Organizing Fuzzy Neural Network Based on a Growing-and-Pruning Algorithm. *IEEE Transactions on Fuzzy Systems*, 18(6):1129–1143, 2010. ISSN 1941-0034 VO - 18. doi: 10.1109/TFUZZ.2010.2070841.

[17] H Han, W Lu, Y Hou, and J Qiao. An Adaptive-PSO-Based Self-Organizing RBF Neural Network. *IEEE Transactions on Neural Networks and Learning Systems*, 29(1): 104–117, 2018. ISSN 2162-2388 VO - 29. doi: 10.1109/TNNLS.2016.2616413.

[18] Hong-Gui Han, Qi-li Chen, and Jun-Fei Qiao. An efficient self-organizing RBF neural network for water quality prediction. *Neural Networks*, 24(7):717–725, 2011. ISSN 0893-6080. doi: https://doi.org/10.1016/j.neunet.2011.04.006. URL http://www.sciencedirect.com/science/article/pii/S0893608011001390.

[19] Hong-Gui Han, Jun-Fei Qiao, and Qi-Li Chen. Model predictive control of dissolved oxygen concentration based on a self-organizing RBF neural network. *Control Engineering Practice*, 20(4):465–476, 2012. ISSN 0967-0661. doi: https://doi.org/10.1016/j.conengprac.2012.01.001. URL http://www.sciencedirect.com/science/article/pii/S0967066112000020.

[20] Jun-Fei Qiao and Hong-Gui Han. Identification and modeling of nonlinear dynamical systems using a novel self-organizing RBF-based approach. *Automatica*, 48(8):1729–1734, 2012. ISSN 0005-1098. doi: https://doi.org/10.1016/j.automatica.2012.05.034. URL http://www.sciencedirect.com/science/article/pii/S0005109812002075.

[21] N Sundararajan, P Saratchandran, and Yan Li. *Fully tuned radial basis function neural networks for flight control*, volume 12. Springer Science & Business Media, 2013. ISBN 1475752865.

[22] R M Sanner and J . E Slotine. Gaussian networks for direct adaptive control. *IEEE Transactions on Neural Networks*, 3(6):837–863, 1992. ISSN 1941-0093 VO - 3. doi: 10.1109/72.165588.

[23] K Y Volyanskyy, W M Haddad, and A J Calise. A new neuroadaptive control architecture for nonlinear uncertain dynamical systems: Beyond σ- and e-modifications. In *2008 47th IEEE Conference on Decision and Control*, pages 80–85, 2008. ISBN 0191-2216 VO -. doi: 10.1109/CDC.2008.4739101.

[24] Y H Kim and F L Lewis. Neural network output feedback control of robot manipulators. *IEEE Transactions on Robotics and Automation*, 15(2):301–309, 1999. ISSN 2374-958X VO - 15. doi: 10.1109/70.760351.

[25] H D Patino, R Carelli, and B R Kuchen. Neural networks for advanced control of robot manipulators. *IEEE Transactions on Neural Networks*, 13(2):343–354, 2002. ISSN 1941-0093 VO - 13. doi: 10.1109/72.991420.

[26] Flavio Nardi. *Neural network based adaptive alogrithms for nonlinear control*. PhD thesis, 2000.

[27] Ransalu Senanayake, Anthony Tompkins, and Fabio Ramos. Automorphing Kernels for Nonstationarity in Mapping Unstructured Environments. In Aude Billard, Anca Dragan, Jan Peters, and Jun Morimoto, editors, *Proceedings of The 2nd Conference on Robot Learning*, volume 87 of *Proceedings of Machine Learning Research*, pages 443–455. PMLR, 2018. URL http://proceedings.mlr.press/v87/senanayake18a.html.

[28] G Chowdhary and E Johnson. Concurrent learning for convergence in adaptive control without persistency of excitation. In *49th IEEE Conference on Decision and Control (CDC)*, pages 3674–3679, 2010. ISBN 0191-2216 VO -. doi: 10.1109/CDC.2010.5717148.

[29] R Kamalapurkar, B Reish, G Chowdhary, and W E Dixon. Concurrent Learning for Parameter Estimation Using Dynamic State-Derivative Estimators. *IEEE Transactions on Automatic Control*, 62(7):3594–3601, 2017. ISSN 1558-2523 VO - 62. doi: 10.1109/TAC.2017.2671343.

[30] H Modares, F L Lewis, and M Naghibi-Sistani. Adaptive Optimal Control of Unknown Constrained-Input Systems Using Policy Iteration and Neural Networks. *IEEE Transactions on Neural Networks and Learning Systems*, 24(10):1513–1525, 2013. ISSN 2162-2388 VO - 24. doi: 10.1109/TNNLS.2013.2276571.

[31] Girish Chowdhary, Jonathan How, and Hassan Kingravi. Model Reference Adaptive Control using Nonparametric Adaptive Elements. In *AIAA Guidance, Navigation, and Control Conference*, Guidance, Navigation, and Control and Co-located Conferences. American Institute of Aeronautics and Astronautics, August 2012. doi: doi:10.2514/6.2012-5038. URL https://doi.org/10.2514/6.2012-5038.

[32] G Chowdhary, H A Kingravi, J P How, and P A Vela. Bayesian nonparametric adaptive control of time-varying systems using Gaussian processes. In *2013 American Control Conference*, pages 2655–2661, 2013. ISBN 2378-5861 VO -. doi: 10.1109/ACC.2013.6580235.

[33] R C Grande, G Chowdhary, and J P How. Nonparametric adaptive control using Gaussian Processes with online hyperparameter estimation. In *52nd IEEE Conference on Decision and Control*, pages 861–867, 2013. ISBN 0191-2216 VO -. doi: 10.1109/CDC.2013.6759990.

[34] Ali Abdollahi and Girish Chowdhary. Adaptive-optimal control under time-varying stochastic uncertainty using past learning. *International Journal of Adaptive Control and Signal Processing*, 33(12):1803–1824, December 2019. ISSN 0890-6327. doi: 10.1002/acs.3061. URL https://doi.org/10.1002/acs.3061.

[35] M Liu, G Chowdhary, B Castra da Silva, S Liu, and J P How. Gaussian Processes for Learning and Control: A Tutorial with Examples. *IEEE Control Systems Magazine*, 38 (5):53–86, 2018. ISSN 1941-000X VO - 38. doi: 10.1109/MCS.2018.2851010.

[36] Jia Guo, Sai Tej Paruchuri, and Andrew J. Kurdila. Persistence of Excitation in Uniformly Embedded Reproducing KernelHilbert (RKH) Spaces (ACC). In *American Control Conference*, 2020.

[37] Jia Guo, Sai Tej Paruchuri, and Andrew J. Kurdila. Persistence of Excitation in Uniformly Embedded Reproducing Kernel Hilbert (RKH) Spaces. February 2019. URL https://arxiv.org/abs/2002.07963.

[38] Jia Guo, Sai Tej Paruchuri, and Andrew J. Kurdila. Approximations of the Reproducing Kernel Hilbert Space (RKHS) Embedding Method over Manifolds. July 2020. URL http://arxiv.org/abs/2007.06163.

[39] N Aronszajn. Theory of Reproducing Kernels. *Transactions of the American Mathematical Society*, 68(3):337–404, 1950. ISSN 00029947. doi: 10.2307/1990404. URL http://www.jstor.org/stable/1990404.

[40] Alain Berlinet and Christine Thomas-Agnan. *Reproducing kernel Hilbert spaces in probability and statistics*. Springer Science & Business Media, 2011. ISBN 1441990968.

[41] Holger Wendland. *Scattered data approximation*, volume 17. Cambridge university press, 2004. ISBN 1139456652.

[42] Andrew J. Kurdila, Jia Guo, Sai Tej Paruchuri, and Parag Bobade. Persistence of Excitation in Reproducing Kernel Hilbert Spaces, Positive Limit Sets, and Smooth Manifolds. September 2019. URL http://arxiv.org/abs/1909.12274.

[43] Ernesto De Vito, Lorenzo Rosasco, and Alessandro Toigo. Learning Sets with Separating Kernels. April 2012. URL http://arxiv.org/abs/1204.3573.

[44] Sai Tej Paruchuri, Jia Guo, and Andrew J. Kurdila. RKHS Embedding for Estimating Nonlinear Piezoelectric Systems. February 2020. URL http://arxiv.org/abs/2002.07296.

[45] Sai Tej Paruchuri, Jia Guo, and Andrew Kurdila. Sufficient Conditions for Parameter Convergence over Embedded Manifolds using Kernel Techniques. September 2020. URL https://arxiv.org/abs/2009.02866.

[46] Carl Edward Rasmussen. Gaussian processes in machine learning. In *Summer School on Machine Learning*, pages 63–71. Springer, 2003.

[47] Jorge Cortes, Sonia Martinez, Timur Karatas, and Francesco Bullo. Coverage control for mobile sensing networks. *IEEE Transactions on robotics and Automation*, 20(2): 243–255, 2004. ISSN 1042-296X.

[48] A Breitenmoser, M Schwager, J Metzger, R Siegwart, and D Rus. Voronoi coverage of non-convex environments with a group of networked robots. In *2010 IEEE International Conference on Robotics and Automation*, pages 4982–4989, 2010. ISBN 1050-4729 VO -. doi: 10.1109/ROBOT.2010.5509696.

[49] Teuvo Kohonen. *Self-organization and associative memory*, volume 8. Springer Science & Business Media, 2012. ISBN 3642881637.

[50] M Cottrell, J C Fort, and G Pagès. Theoretical aspects of the SOM algorithm. *Neurocomputing*, 21(1):119–138, 1998. ISSN 0925-2312. doi: https://doi.org/10.1016/S0925-2312(98)00034-4. URL http://www.sciencedirect.com/science/article/pii/S0925231298000344.

[51] Łukasz Brocki and Danijel Koržinek. Kohonen Self-Organizing Map for the Traveling Salesperson Problem. pages 116–119, Berlin, Heidelberg, 2007. Springer Berlin Heidelberg. ISBN 978-3-540-73956-2.

[52] John H Hubbard and Beverly H West. *Differential equations: A dynamical systems approach: Ordinary differential equations*, volume 5. Springer, 2013. ISBN 1461209374.

Chapter 5

Sufficient Conditions for Parameter Convergence over Embedded Manifolds using Kernel Techniques

Abstract

The persistence of excitation (PE) condition is sufficient to ensure parameter convergence in adaptive estimation problems. Recent results on adaptive estimation in reproducing kernel Hilbert spaces (RKHS) introduce PE conditions for RKHS. This chapter presents sufficient conditions for PE for the particular class of uniformly embedded reproducing kernel Hilbert spaces (RKHS) defined over smooth Riemannian manifolds. This chapter also studies the implications of the sufficient condition in both finite and infinite-dimensional cases. When the RKHS is finite-dimensional, the sufficient condition implies parameter convergence as in the conventional analysis. On the other hand, when the RKHS is infinite-dimensional, the same condition implies that the function estimate error is ultimately bounded by a constant that depends on the approximation error of the infinite-dimensional RKHS. We illustrate the effectiveness of the sufficient condition in a practical example.

5.1 Introduction

Adaptive estimation of unknown nonlinearities arising in finite-dimensional autonomous dynamical systems is now a classical, or textbook, problem. [1, 2, 3] Typically, in such estimation problems, we assume that the unknown function is a linear combination of known basis functions, commonly referred to as regressors. We can guarantee parameter convergence in adaptive estimation problems by assuming that additional sufficient conditions on the regressors hold. In control theory parlance, we refer to these hypotheses as persistence of excitation (PE) conditions. It is important to observe that the definition of PE can vary depending on the type of problem or the algorithm implemented.

5.1.1 PE Conditions and Convergence

Some of the earliest accounts of PE conditions and their implications for parameter convergence in adaptive estimation are given in [4, 5]. In these studies, the authors pose the problem of parameter estimation as the stability analysis of a linear time-varying (LTV), finite-dimensional system and show that the LTV systems are asymptotically stable when the PE condition holds. In some cases, we can even guarantee exponential stability. [6, 7] When only a subspace is persistently excited, it is possible to show that the parameter error eventually becomes orthogonal to that subspace. [6] In other words, the estimates converge to the projection of the unknown function onto the subspace.

In [8, 9, 10, 11, 12], the authors generalize some of the existing notions of PE and extend the theory on the stability of LTV systems. The work by Farrell illustrates the effectiveness of local PE conditions for parameter convergence. [13] The PE condition in [14] ensures the convergence of parameter estimates of systems defined by the interconnection of LTI blocks and nonlinear functions. Yuan and Wang relate the learning speeds and constants that ap-

pear in the PE definition in [15]. In [16], Nikitin proposes a generalized PE definition that relaxes some of the conditions imposed on conventional PE conditions. An account of parameter estimation for distributed parameter systems and the corresponding notion of PE is given in [17, 18, 19, 20, 21, 22]. Recent articles on adaptive estimation in reproducing kernel Hilbert spaces (RKHS) extend the notion of partial PE to cases where the unknown function appearing in ordinary differential equations (ODEs) belongs to an infinite-dimensional RKHS. [23, 24, 25]

The PE condition is difficult, and sometimes impossible, to verify *a priori* in practical applications. To overcome this limitation, authors have studied simpler sufficient conditions that ensure PE. A few of the earliest accounts that analyze sufficient conditions for PE are [26, 27]. In these papers, the authors link the richness of the reference trajectory to the PE condition. This richness condition is much more intuitive than the PE condition. Kurdila et al. illustrate in [28, 29] that, in function spaces generated by radial basis functions, radial basis functions centered at points in state space that are *visited regularly* are persistently excited. The work by Gorinevsky and Lu et al., in which it is shown that inputs belonging to neighborhoods of radial basis function centers are PE, illustrates a similar result. [30, 31] In [32, 33], Wang et al. relax some of the hypotheses in [28, 29]. They derive a sufficient condition for PE for any recurrent trajectory contained in a regular lattice. In [34], Bamieh and Giarre pose a linear parameter varying identification problem as linear regression, which allows them to show that in some instances, the PE condition simplifies to an interpolation condition.

An alternative to developing sufficient conditions that ensure PE is to develop methods that ensure parameter convergence without PE. For example, Adetola and Guay prove in [35] that we can compute the unknown parameters once the regressor matrix becomes positive definite. The recent class of estimation techniques, referred to as concurrent learning, obviates the

need for persistently exciting signals by using a rich collection of recorded data. [36, 37, 38] Song et al. show asymptotic constancy of parameter estimates without the PE condition in [39]. In [40], Wang et al. propose a finite-time parameter estimation technique that uses the dynamic regressor extension and mixing methods to transform the estimation problem into a series of regression models. This transformation results in parameter convergence under non-PE conditions.

In most of the studies mentioned above, the states and the parameters evolve in Euclidean spaces (a notable exception being the family of related papers [17, 18, 19, 20, 21, 22], which treat distributed parameter systems). However, for a given initial condition in many such finite-dimensional systems, the state trajectory traverses only a subdomain of Euclidean space. Recent articles on adaptive estimation in RKHS provide a framework for adaptive estimation of dynamic systems whose states evolve in more generic spaces, including embedded manifolds. [23, 41] The corresponding PE conditions are given in [24, 25]. Guo et al. study the rate of convergence of the finite-dimensional approximations of reproducing kernel Hilbert spaces defined over manifolds in [42]. From an adaptive estimation perspective, this is equivalent to studying the rate at which the finite-dimensional function estimate $\hat{f}_n$ converges to the infinite-dimensional function estimate $\hat{f}$. However, to carryout the analysis in these studies, it is necessary to choose the RKHS that is persistently excited.

This requirement, in turn, suggests a need for sufficient conditions for PE that works in spaces that are more general than Euclidean spaces. In this chapter, we introduce a sufficient condition for PE of RKHS defined over embedded manifolds and study its implications in both finite and infinite-dimensional cases. In the typical situation in which the analysis in this chapter is applied, we assume that we are given an ODE (such as in the model problem Equation 5.1), and that the system admits an invariant submanifold M that is regularly embedded in the state space $\mathbb{R}^d$ for some given initial condition. The sufficient condition is

also applicable when, given an initial condition, the forward orbit is a subset of an invariant manifold and/or the embedded manifold is Euclidean space itself.

5.1.2 Summary of New Results

This chapter extends the results in the recent papers [23, 24, 25, 41, 42] in several fundamental ways. The first result states sufficient conditions that guarantee the PE condition for finite-dimensional RKHS over a manifold M that is defined in terms of a finite number of kernel basis functions. While this was carried out in [29] for radial basis functions over $\mathbb{R}^n$, here we treat the case where the native space is defined over a smooth manifold and the RKHS is generated by a continuous strictly positive definite kernel. As in [29], we see that the RKHS is PE if the trajectory repeatedly visits any (geodesic) neighborhoods of the kernel basis centers, and the time of visitation is bounded below in some sense. This result has direct applicability to finite-dimensional cases of the RKHS embedding methods discussed in [23, 24, 25, 41, 42]. It serves as a foundation for practical choices of PE subsets and spaces, which is not addressed in these references. The second principal result of this chapter is the study of the implications of the above sufficient condition when the RKHS is infinite-dimensional. We show that when the sufficient condition described above is valid, the function (parameter) error is eventually bounded above by a constant, which depends on the finite-dimensional approximation error of the infinite-dimensional RKHS. Researchers have investigated such cases for parameter estimation in Euclidean spaces using dead-zone gradient algorithm. [3, 43] The result in this chapter can be considered as a generalization of this approach to reproducing kernel Hilbert spaces of functions defined over manifolds.

The organization of this chapter is as follows. Section 5.2 reviews background material for the new results in Sections 5.3 and 5.4. It covers the theory of adaptive estimation in reproducing kernel Hilbert spaces and introduces two recent, different notions of the persistence

of excitation. We discuss when the two notions of PE are equivalent and when we can ensure parameter convergence. In Section 5.3, we derive one of the primary results of this chapter, a sufficient condition for PE in the finite-dimensional case. We show that this sufficient condition ensures convergence of parameters when the unknown function belongs to a known finite-dimensional space. In Section 5.4, we discuss the implications of this sufficient condition when we only know that the unknown function belongs to an infinite-dimensional space. We show that the projection (onto the persistently excited finite-dimensional subspace) of the function estimate error is bounded by a constant times the error of best approximation. Section 5.5 illustrates the theory using a numerical example. Section 5.6 concludes the chapter.

5.2 Review of Adaptive Estimation in RKHS

5.2.1 The Theory of RKHS

A reproducing kernel Hilbert space $\mathcal{H}_X$ is a Hilbert space of functions defined on the set X and that can be defined in terms of an associated continuous, positive-definite kernel $\mathcal{K} : X \times X \to \mathbb{R}$. In this chapter, we assume that the kernel is strictly positive-definite. For each $\boldsymbol{x} \in X$, the kernel basis centered at $\boldsymbol{x}$, denoted $\mathcal{K}(\boldsymbol{x}, \cdot)$, is a function in $\mathcal{H}_X$. Suppose $(\cdot, \cdot)_{\mathcal{H}_X}$ is the inner product associated with the space $\mathcal{H}_X$. The reproducing property of the RKHS states that for any $\boldsymbol{x} \in X$ and $f \in \mathcal{H}_X$, $(\mathcal{K}(\boldsymbol{x}, \cdot), f)_{\mathcal{H}_X} = \mathcal{E}_{\boldsymbol{x}} f = f(\boldsymbol{x})$. The operator $\mathcal{E}_{\boldsymbol{x}}$ is the evaluation functional. In the context of this chapter, we assume that the evaluation operator is *uniformly bounded*, that is $|\mathcal{E}_{\boldsymbol{x}} f| \leq c\|f\|_{\mathcal{H}_X}$ for all $\boldsymbol{x} \in X$ and $f \in \mathcal{H}_X$ and some fixed positive constant c. One sufficient condition for the uniform boundedness of all the evaluation functionals is that there exists a constant $\bar{k}$ such that $\mathcal{K}(\boldsymbol{x}, \boldsymbol{x}) \leq \bar{k}^2 < \infty$ for all $\boldsymbol{x} \in X$. This condition implies that the RKHS is continuously embedded in the space

of continuous functions $C(X)$ defined on X, that is, given any function $f \in \mathcal{H}_X$, we have $\|f\|_{C(X)} \leq c\|f\|_{\mathcal{H}_X}$ for some constant c. Given a positive definite kernel $\mathcal{K} : X \times X \to \mathbb{R}$, we generate the associated RKHS by

$$\mathcal{H}_X := \overline{span\{\mathcal{K}(\boldsymbol{x}, \cdot) | \boldsymbol{x} \in X\}},$$

where the inner product satisfies $\langle \mathcal{K}(\boldsymbol{x}, \cdot), \mathcal{K}(\boldsymbol{y}, \cdot) \rangle_{\mathcal{H}_X} = \mathcal{K}(\boldsymbol{x}, \boldsymbol{y})$. For any set $M \subseteq X$, the associated RKHS $\mathcal{H}_\Omega \subseteq \mathcal{H}_X$ is defined as

$$\mathcal{H}_\Omega := \overline{span\{\mathcal{K}(\boldsymbol{x}, \cdot) | \boldsymbol{x} \in M \subseteq X\}}.$$

Additionally, if Ω_n is a discrete finite set of n elements in X, the associated RKHS is an n-dimensional space. In this chapter, we use a subscript, as in Ω_n, to describe the number of elements in a discrete finite set. In addition to the above spaces, we are also interested in the space of restrictions $R_M(\mathcal{H}_X)$, where $M \subseteq X$. We define the space $R_M(\mathcal{H}_X)$ by

$$R_M(\mathcal{H}_X) := \{g : M \to \mathbb{R} \mid g = R_M f := f|_M \ \forall \ f \in \mathcal{H}_X\}.$$

The functions in $R_M(\mathcal{H}_X)$ are defined only on $M \subseteq X$, but those in $\mathcal{H}_X$ are defined everywhere in X. When $M = X$, the space $R_M(\mathcal{H}_X)$ is nothing but the space $\mathcal{H}_X$. The restricted space $R_M(\mathcal{H}_X)$ is itself an RKHS, [44, 45] and the associated reproducing kernel is given by

$$\mathcal{R}(\boldsymbol{x}, \boldsymbol{y}) = \mathcal{K}|_M(\boldsymbol{x}, \boldsymbol{y}) = \mathcal{K}(\boldsymbol{x}, \boldsymbol{y})$$

for all $\boldsymbol{x}, \boldsymbol{y} \in M$. The kernel $\mathcal{R}$ generates the space $R_M(\mathcal{H}_X)$ just as the kernel $\mathcal{K}$ generates $\mathcal{H}_X$.

In this chapter, the set X represents the state space $\mathbb{R}^d$ of the plant, and the set M is taken to be a smooth, Riemmanian, k-dimensional manifold that is regularly embedded in the state space X. The sets Ω and Ω_n are used to represent persistently excited subsets of X. The reproducing property mentioned above endows the RKHS $\mathcal{H}_X$ with many interesting properties which makes proving theorems easier. A detailed description of these properties is given in [44, 45, 46]. We describe the properties as and when we use them in this chapter.

5.2.2 RKHS Embedding for Adaptive Estimation

In this subsection and the next, we discuss several recent results that are critical to the new results derived in Sections 5.3 and 5.4. Interested readers are referred to [23, 24, 25] for more detailed discussions. Suppose we have a nonlinear system governed by the ordinary differential equation

$$\dot{\boldsymbol{x}}(t) = A\boldsymbol{x}(t) + Bf(\boldsymbol{x}(t)), \tag{5.1}$$

where $\boldsymbol{x}(t) \in X := \mathbb{R}^d$, $A \in \mathbb{R}^{d\times d}$ is known and Hurwitz, $B \in \mathbb{R}^d$ is known and $f : \mathbb{R}^d \to \mathbb{R}$ is the unknown (nonlinear) function, which is assumed to be an element of the RKHS $\mathcal{H}_X$. We also assume that we measure all the states $\boldsymbol{x}(t)$ of the system at each time $t \geq 0$. We define an estimator model of the form

$$\dot{\hat{\boldsymbol{x}}}(t) = A\hat{\boldsymbol{x}}(t) + B\hat{f}(t, \boldsymbol{x}(t)), \tag{5.2}$$

where $\hat{\boldsymbol{x}}(t) \in \mathbb{R}^d$ is the state estimate and $\hat{f}(t, \boldsymbol{x}(t))$ is the function estimate, which at each time t is an element of the RKHS $\mathcal{H}_X$. Our goal is to ensure that the function estimate $\hat{f}(t)$

approaches the true function f as $t \to \infty$. We use the gradient law, which is given by

$$\dot{\hat{f}}(t) = \Gamma^{-1}(B\mathcal{E}_{\boldsymbol{x}(t)})^* P(\boldsymbol{x}(t) - \hat{\boldsymbol{x}}(t)), \tag{5.3}$$

to define the rate of change of the function estimate. In the above equation, the term $\Gamma \in \mathbb{R}$ and the notation L^* represents the adjoint of the linear operator L. The matrix P is the symmetric positive definite solution of the Lyapunov's equation $A^T P + PA = -Q$, where $Q \in \mathbb{R}^{d \times d}$ is an arbitrary symmetric positive-definite matrix.

It is now possible to write down the error equations, which have the form

$$\begin{Bmatrix} \dot{\tilde{\boldsymbol{x}}}(t) \\ \dot{\tilde{f}}(t) \end{Bmatrix} = \begin{bmatrix} A & B\mathcal{E}_{\boldsymbol{x}(t)} \\ -\Gamma^{-1}(B\mathcal{E}_{\boldsymbol{x}(t)})^* P & 0 \end{bmatrix} \begin{Bmatrix} \tilde{\boldsymbol{x}}(t) \\ \tilde{f}(t) \end{Bmatrix}. \tag{5.4}$$

In the above equation, the terms $\tilde{\boldsymbol{x}}(t) := \boldsymbol{x}(t) - \hat{\boldsymbol{x}}(t)$ and $\tilde{f}(t, \cdot) := f(\cdot) - \hat{f}(t, \cdot)$ represent the state and function error, respectively. The error systems, governed by the above equations, evolves in the infinite-dimensional space $\mathbb{R}^d \times \mathcal{H}_X$. Lyapunov analysis and Barbalat's lemma can be used to show that the state error $\tilde{\boldsymbol{x}}(t)$ converges to zero. [24, 25] However, we cannot make any claims about the function error $\tilde{f}$ without additional assumptions.

5.2.3 Persistence of Excitation

As in the study of finite dimensional systems in [1, 2, 3], persistence of excitation conditions introduced in [24, 25] for RKHS embedding are sufficient to prove convergence of the function error $\tilde{f}(t) \to 0$. We discuss two notions of PE conditions.

Definition 5.1. (**PE** $\mathcal{H}_X$**-1**) The trajectory $\boldsymbol{x} : t \mapsto \boldsymbol{x}(t) \in \mathbb{R}^d$ persistently excites the indexing set Ω and the RKHS $\mathcal{H}_\Omega$ provided there exist positive constants T_1, γ_1, δ_1, and Δ_1,

such that for each $t \geq T_1$ and any $g \in \mathcal{H}_X$, there exists $s \in [t, t + \Delta_1]$ such that

$$\left| \int_s^{s+\delta_1} \mathcal{E}_{\boldsymbol{x}(\tau)} g d\tau \right| \geq \gamma_1 \|P_\Omega g\|_{\mathcal{H}_X} > 0.$$

Definition 5.2. (**PE $\mathcal{H}_X$-2**) The trajectory $\boldsymbol{x} : t \mapsto \boldsymbol{x}(t) \in \mathbb{R}^d$ persistently excites the indexing set Ω and the RKHS $\mathcal{H}_\Omega$ provided there exists positive constants T_2, γ_2, and Δ_2 such that

$$\int_t^{t+\Delta_2} \left\langle \mathcal{E}^*_{\boldsymbol{x}(\tau)} \mathcal{E}_{\boldsymbol{x}(\tau)} g, g \right\rangle_{\mathcal{H}_X} d\tau \geq \gamma_2 \|P_\Omega g\|^2_{\mathcal{H}_X} > 0$$

for all $t \geq T_2$ and any $g \in \mathcal{H}_X$.

The space $\mathcal{H}_X$ in the notation "PE $\mathcal{H}_X$-1" and "PE $\mathcal{H}_X$-2" refers to the space in which the functions g are contained. The operator P_Ω is the $\mathcal{H}_X$-orthogonal projection from the space $\mathcal{H}_X$ onto the closed subspace $\mathcal{H}_\Omega$. The following theorem shows that the function error converges over the PE set when the PE condition in Definition 5.1 holds.

Theorem 5.3. *If the trajectory $\boldsymbol{x} : t \mapsto \boldsymbol{x}(t)$ persistently excites the RKHS $\mathcal{H}_\Omega$ in the sense of Definition PE $\mathcal{H}_X-$ 5.1. Then*

$$\lim_{t\to\infty} \|\tilde{\boldsymbol{x}}(t)\| = 0, \qquad \lim_{t\to\infty} \|P_\Omega \tilde{f}(t)\|_{\mathcal{H}_X} = 0.$$

In the above theorem, we can additionally show that if $\lim_{t\to\infty} \|P_\Omega \tilde{f}(t)\|_{\mathcal{H}_X} = 0$, then $\lim_{t\to\infty} |f(\boldsymbol{x}) - \hat{f}(t, \boldsymbol{x})| = 0$ for all $\boldsymbol{x} \in \Omega$. In fact, the convergence is uniform over the set Ω since we assume that the evaluation functional is uniformly bounded.

Before proceeding further, let us note how the above definitions and theorem simplify when

the actual unknown function $f \in \mathcal{H}_{\Omega_n}$. In such cases, we can assume that the function $\hat{f}$ in the adaptive estimator equation and the functions g in Definitions 5.1 and 5.2 are in the space $\mathcal{H}_{\Omega_n}$ and revise the definitions of PE conditions to PE $\mathcal{H}_{\Omega_n}$-1 and PE $\mathcal{H}_{\Omega_n}$-2. Since the trajectory $\boldsymbol{x} : t \mapsto \boldsymbol{x}(t) \in \mathbb{R}^d$ persistently excites the space $\mathcal{H}_{\Omega_n}$ and all the functions are in $\mathcal{H}_{\Omega_n}$, the error equations can be recast in $\mathbb{R}^d \times \mathcal{H}_{\Omega_n}$, and the projection operator $P_\Omega \equiv P_{\Omega_n}$ disappears. On the other hand, when the evolution of the state trajectory is on a manifold M, we can treat the above problem solely as estimation of functions over the manifold M. In such cases, the persistently excited set Ω is a subset of the manifold and we replace the space $\mathcal{H}_X$ and $\mathcal{H}_{\Omega_n}$ with $R_M(\mathcal{H}_X)$ and $R_M(\mathcal{H}_{\Omega_n})$, respectively, in the above theorems and definitions.

5.2.4 Equivalence of PE conditions

In the previous subsection, we discussed two different notions of PE. PE $\mathcal{H}_X$-1 always implies PE $\mathcal{H}_X$-2.

Theorem 5.4. *The PE condition in Definition 5.1 implies the one in Definition 5.2.*

The proof of the above theorem is given in [24, 25]. Now, note that the hypotheses of Theorem 5.3 assumes that the PE condition in Definition 5.1 holds. On the other hand, the sufficient condition, given in next section, implies that the PE condition in Definition 5.2 holds. In particular, it implies that PE $\mathcal{H}_{\Omega_n}$ - **1** holds, where $\mathcal{H}_{\Omega_n}$ is a finite-dimensional RKHS. Thus, it is important to understand when the PE condition in Definition 5.2 implies the PE condition in Definition 5.1. The following theorem from [24, 25] explicitly states when the two notions of PE are equal.

Theorem 5.5. *If the family of functions defined by* $\mathbb{U}(\bar{S}_n) = \{g(\boldsymbol{x}(\cdot)) : t \mapsto g(\boldsymbol{x}(t)) | g \in \bar{S}_n := \mathcal{H}_{\Omega_n} \text{ such that } \|g\|_{\mathcal{H}_{\Omega_n}} = 1\}$ *is uniformly equicontinuous, then the PE* $\mathcal{H}_{\Omega_n}$ - *5.2*

implies PE $\mathcal{H}_{\Omega_n}$ - *5.1.*

The proof of a more general case of the above theorem is given in [24]. It is important to understand the family of functions $\mathbb{U}(\bar{S}_n)$ are equicontinuous. A sufficient condition for this is that the unit ball $\bar{S}_n = \{g : X \mapsto \mathbb{R} \in \mathcal{H}_{\Omega_n} \text{ such that } \|g\| = 1\}$ is uniformly equicontinuous and the state trajectory $t \mapsto \boldsymbol{x}(t)$ is uniformly continuous. If the state trajectory $t \mapsto \boldsymbol{x}(t)$ maps to a compact set V, then $\mathbb{U}(\bar{S}_n)$ is uniformly equicontinuous if $\bar{S}_n$ redefined as $\bar{S}_n = \{g : V \mapsto \mathbb{R} \in \mathcal{H}_{\Omega_n} \text{ such that } \|g\| = 1\}$ is uniformly equicontinuous and the state trajectory $t \mapsto \boldsymbol{x}(t)$ is uniformly continuous. We know that $\bar{S}_{V,n}$ is uniformly equicontinuous. Thus, if the state trajectory $t \mapsto \boldsymbol{x}(t)$ is uniformly continuous and maps to a compact set, the family of functions $\mathbb{U}(\bar{S}_n)$ is uniformly equicontinuous.

5.3 Sufficient Condition for PE

In this section, we derive the sufficient condition for persistence of excitation of the trajectory $\boldsymbol{x} : t \mapsto \boldsymbol{x}(t)$ in the sense of the PE $\mathcal{H}_{\Omega_n}$ - 5.2. We assume that the states evolves in a *smooth, compact, Riemmanian k-dimensional* manifold that is regularly embedded in X and endowed with the (Riemmanian) distance function $d_M(\cdot,\cdot) : M \times M \to \mathbb{R}^+ \cup \{0\}$. Note, by definition, $d_M(\boldsymbol{x}, \boldsymbol{y})$ is equal to the infimum of the lengths of all the smooth curves joining $\boldsymbol{x} \in M$ and $\boldsymbol{y} \in M$. The sufficient condition is valid for the case when $f \in R_M(\mathcal{H}_{\Omega_n}) \subseteq R_M(\mathcal{H}_X)$, where $\Omega_n = \{\boldsymbol{x}_1, \ldots, \boldsymbol{x}_n\}$ is a discrete finite set in M. We analyze the implications of relaxing this condition in the next section. In the following analysis, we assume that the kernel $\mathcal{R} : M \times M \to \mathbb{R}$ is a continuous, *strictly* positive-definite kernel. Many kernels are strictly positive definite (Matern/Sobolev, exponential, multiquadric).

Lemma 5.6. *Suppose $\boldsymbol{y}_i \in M$ for $i = 1, \ldots, n$. If*

$$S(\boldsymbol{y}_1, \ldots, \boldsymbol{y}_n) := \begin{pmatrix} \mathcal{R}(\boldsymbol{x}_1, \boldsymbol{y}_1) & \ldots & \mathcal{R}(\boldsymbol{x}_n, \boldsymbol{y}_1) \\ \vdots & \ddots & \vdots \\ \mathcal{R}(\boldsymbol{x}_1, \boldsymbol{y}_n) & \ldots & \mathcal{R}(\boldsymbol{x}_n, \boldsymbol{y}_n) \end{pmatrix}, \tag{5.5}$$

then there exists an $\epsilon > 0$ and a number $\theta(\epsilon, \boldsymbol{x}_1, \ldots, \boldsymbol{x}_n) > 0$ such that

$$\|S\boldsymbol{\alpha}\| \geq \theta \|\boldsymbol{\alpha}\|$$

for all $\boldsymbol{\alpha} \in \mathbb{R}^n$ and for every collection of $\boldsymbol{y}_i$'s that satisfy $d_M(\boldsymbol{x}_i, \boldsymbol{y}_i) \leq \epsilon$ for $i = 1, \ldots, n$.

Proof. The proof of this lemma follows easily by modifications of the arguments in [29] (which holds for radial basis functions in $\mathbb{R}^n$) to the case when the basis function is a continuous, *strictly* positive-definite kernel basis function defined on a manifold. We note that the eigenvalues of the matrix $S^T S$ vary continuously with $\boldsymbol{y}_i$ for $i = 1, \ldots, n$, since the eigenvalues are continuous functions of the elements of a matrix and the map $\boldsymbol{y} \to \mathcal{R}(\boldsymbol{x}, \boldsymbol{y})$ is continuous by hypothesis. Let $\lambda(\boldsymbol{y}_1, \ldots, \boldsymbol{y}_n)$ be the smallest eigenvalue of $S(\boldsymbol{y}_1, \ldots, \boldsymbol{y}_n)^T S(\boldsymbol{y}_1, \ldots, \boldsymbol{y}_n)$. Since the kernel is strictly positive definite, the smallest eigenvalue of $S(\boldsymbol{x}_1, \ldots, \boldsymbol{x}_n)^T S(\boldsymbol{x}_1, \ldots, \boldsymbol{x}_n)$ satisfies $\lambda(\boldsymbol{x}_1, \ldots, \boldsymbol{x}_n) > 0$. By continuity of eigenvalues, we choose an $\epsilon > 0$ such that

$$\lambda(\boldsymbol{y}_1, \ldots, \boldsymbol{y}_n) > \frac{1}{2}\lambda(\boldsymbol{x}_1, \ldots, \boldsymbol{x}_n) > 0$$

whenever $d_M(\boldsymbol{x}_i, \boldsymbol{y}_i) \leq \epsilon$ for $i = 1 \ldots, n$. (It is easy to see that such a choice is always possible. Since $y \mapsto \lambda(y)$ is continuous at x, for any $\gamma > 0$, there is an $\epsilon > 0$ such that if $d_M(x, y) < \epsilon$, then $|\lambda(y) - \lambda(x)| < \gamma$. Choose $\gamma := \frac{1}{2}\lambda(x)$, and pick an appropriate $\epsilon > 0$. Then the smallest that $\lambda(y)$ can be is greater than $\frac{1}{2}\lambda(x)$. So, $\lambda(y) \geq \frac{1}{2}\lambda(x) > 0$.) With this

choice of ϵ, finally set $\theta = \sqrt{\frac{1}{2}\lambda(\boldsymbol{x}_1, \ldots, \boldsymbol{x}_n)}$. We have

$$\|S(\boldsymbol{y}_1, \ldots, \boldsymbol{y}_n)\boldsymbol{\alpha}\|^2 \geq \lambda(\boldsymbol{y}_1, \ldots, \boldsymbol{y}_n)\boldsymbol{\alpha}^T\boldsymbol{\alpha} > \theta^2\|\boldsymbol{\alpha}\|^2.$$

□

For proving the next theorem, we enforce the following additional condition on ϵ in the previous lemma. Note, if a particular $\epsilon > 0$ works in the above lemma, any smaller positive value will satisfy the lemma.

Condition 5.7. Let $\boldsymbol{x}_i, \boldsymbol{x}_j \in \Omega_n$ for $i, j = 1, \ldots, n$. The choice of ϵ in Lemma 5.6 also satisfies

$$0 < \epsilon < \frac{1}{2}\min_{i \neq j} d_M(\boldsymbol{x}_i, \boldsymbol{x}_j).$$

Lemma 5.8. *Let I be a bounded, Lebesgue (μ) measurable subset of $[0, \infty)$, and also let*

$$I_i := \{s \in I | d_M(\boldsymbol{x}_i, \boldsymbol{x}(t)) \leq \epsilon \text{ for } i = 1, \ldots, n\},$$

where ϵ is as in Lemma 5.6 and satisfies Condition 5.7. If $\mu(I_i) \geq \tau_0$ for $1, \ldots, n$, then with θ as in Lemma 5.6,

$$\int_I \left(\mathcal{E}^*_{\boldsymbol{x}(\tau)}\mathcal{E}_{\boldsymbol{x}(\tau)}g, g\right)_{R_M(\mathcal{H}_X)} d\tau \geq \tau_0\theta^2\|\boldsymbol{\alpha}\|^2$$

holds for any $g \in R_M(\mathcal{H}_X)$ and $\boldsymbol{\alpha} = \{\alpha_1, \ldots, \alpha_n\}$ such that $g = \sum_{i=1}^n \alpha_i \mathcal{R}(\boldsymbol{x}_i, \cdot)$.

Proof. First, we note that

$$\left\langle \mathcal{E}^*_{\boldsymbol{x}(\tau)} \mathcal{E}_{\boldsymbol{x}(\tau)} g, g \right\rangle_{R_M(\mathcal{H}_X)} = \left\langle \mathcal{E}_{\boldsymbol{x}(\tau)} g, \mathcal{E}_{\boldsymbol{x}(\tau)} g \right\rangle_{\mathbb{R}} = \left(g(\boldsymbol{x}(\tau))\right)^2.$$

Moreover, the sets I_i are disjoint since the closed balls defined as $B_\epsilon(\boldsymbol{x}_i) := \{\boldsymbol{y} \in M | d_M(\boldsymbol{x}_i, \boldsymbol{y}) \leq \epsilon\}$ centered at x_i and radius ϵ do not intersect with each other when ϵ satisfies Condition 5.7. Furthermore, since $\cup_{i=1}^n I_i \subseteq I$, we have

$$\int_I \left\langle \mathcal{E}^*_{\boldsymbol{x}(\tau)} \mathcal{E}_{\boldsymbol{x}(\tau)} g, g \right\rangle_{R_M(\mathcal{H}_X)} d\tau \geq \sum_{i=1}^n \int_{I_i} \left(g(\boldsymbol{x}(\tau))\right)^2 d\tau. \tag{5.6}$$

The closed balls $B_\epsilon(\boldsymbol{x}_i)$ are compact since the manifold M is compact. Thus, the function $g \in R_M(\mathcal{H}_X) \subseteq C(M)$ attains its maximum and minimum at points in the manifold M, say $\overline{\boldsymbol{y}}_i, \underline{\boldsymbol{y}}_i \in M$, respectively. Thus, for each $i = 1, \ldots, n$, we get the inequality

$$\left(g(\underline{\boldsymbol{y}}_i)\right)^2 \mu(I_i) \leq \int_{I_i} \left(g(\boldsymbol{x}(\tau))\right)^2 d\tau \leq \left(g(\overline{\boldsymbol{y}}_i)\right)^2 \mu(I_i).$$

By definition of d_M, we know that the closed ball $B_\epsilon(\boldsymbol{x}_i)$ is connected. Using the generalized intermediate value theorem and the hypothesis that $\mu(I_i) \geq \tau_0$, we conclude that there exists a $\boldsymbol{y}_i \in B_\epsilon(\boldsymbol{x}_i)$ such that

$$\int_{I_i} \left(g(\boldsymbol{x}(\tau))\right)^2 d\tau = \left(g(\boldsymbol{y}_i)\right)^2 \mu(I_i) \geq \left(g(\boldsymbol{y}_i)\right)^2 \tau_0$$

for $i = 1, \ldots, n$. From the Inequality 5.6, we have

$$\int_I \left\langle \mathcal{E}^*_{\boldsymbol{x}(\tau)} \mathcal{E}_{\boldsymbol{x}(\tau)} g, g \right\rangle_{R_M(\mathcal{H}_X)} d\tau \geq \sum_{i=1}^n \left(\sum_{j=1}^n \alpha_j \mathcal{R}(\boldsymbol{x}_j, \boldsymbol{y}_i) \right)^2 \tau_0 = \|S\boldsymbol{\alpha}\|^2 \tau_0,$$

where $S = S(\boldsymbol{y}_1, \ldots, \boldsymbol{y}_n)$ is defined as in Equation 5.5. Since we choose ϵ as in Lemma 5.6,

using the lemma gives us the desired result. □

The above lemma plays a direct role in the proof of the sufficient conditions for PE given below.

Theorem 5.9. *Suppose that the manifold M is positive invariant under the state trajectory $t \mapsto \boldsymbol{x}(t)$ and $\Omega_n := \{\boldsymbol{x}_1, \ldots, \boldsymbol{x}_n\}$. Also suppose that the constant ϵ is chosen as in Lemma 5.6 and satisfies Condition 5.7. For every $t \geq 0$ and every $\Delta_2 > 0$, define*

$$I_i := \{s \in [t, t+\Delta_2] | d_M(\boldsymbol{x}_i, \boldsymbol{x}(t)) \leq \epsilon \text{ for } i = 1, \ldots, n\}.$$

If there exists a $T_2 \geq 0$ and $\Delta_2 > 0$ such that for all $t \geq T_2$, $\mu(I_i)$ is bounded below by a positive constant $\tau_0 > 0$ for all $i = 1, \ldots, n$ and t, then the trajectory $\boldsymbol{x} : t \to \boldsymbol{x}(t)$ persistently excites the indexing set Ω_n and the RKHS $R_M(\mathcal{H}_{\Omega_n})$ in the sense of PE $R_M(\mathcal{H}_{\Omega_n})$ - 5.2.

Proof. For a given $t \geq T_2$, we define $I := [t, t+\Delta_2]$. Since $\mu(I_i) \geq \tau_0$ for $i = 1, \ldots, n$, we apply Lemma 5.8 to get

$$\int_t^{t+\Delta_2} \left\langle \mathcal{E}^*_{\boldsymbol{x}(\tau)} \mathcal{E}_{\boldsymbol{x}(\tau)} g, g \right\rangle_{R_M(\mathcal{H}_X)} d\tau \geq \tau_0 \theta^2 \|\boldsymbol{\alpha}\|^2.$$

We note that the constant τ_0 is independent of t. Thus, the above inequality is valid for all $t \geq T_2$. Given $g = \sum_{i=1}^n \alpha_i \mathcal{R}(\boldsymbol{x}_i, \cdot) \in R_M(\mathcal{H}_X)$, its norm is given by

$$\|g\|^2_{R_M(\mathcal{H}_X)} = \left\langle \sum_{i=1}^n \alpha_i \mathcal{R}(\boldsymbol{x}_i, \cdot), \sum_{i=1}^n \alpha_i \mathcal{R}(\boldsymbol{x}_i, \cdot) \right\rangle_{R_M(\mathcal{H}_X)} = \boldsymbol{\alpha}^T S(\boldsymbol{x}_1, \ldots, \boldsymbol{x}_n) \boldsymbol{\alpha},$$

where $S(\boldsymbol{x}_1, \ldots, \boldsymbol{x}_n)$ is defined as in Equation 5.5 and is called the Grammian matrix. It is

straightforward to see that the norm in $S(\boldsymbol{x}_1, \ldots, \boldsymbol{x}_n)$ is equivalent to the norm in $\mathbb{R}^n$ since

$$\underline{\lambda}\|\boldsymbol{\alpha}\|^2 \leq \|g\|^2_{R_M(\mathcal{H}_X)} \leq \overline{\lambda}\|\boldsymbol{\alpha}\|^2,$$

where $\underline{\lambda}$ and $\overline{\lambda}$ are the minimum and maximum eigenvalues of the Grammian matrix $S(\boldsymbol{x}_1, \ldots, \boldsymbol{x}_n)$. Note that the Grammian matrix is a symmetric positive definite matrix, and hence all eigenvalues are real and positive. Using the above equivalence of norms, we get

$$\int_t^{t+\Delta_2} \left\langle \mathcal{E}^*_{\boldsymbol{x}(\tau)} \mathcal{E}_{\boldsymbol{x}(\tau)} g, g \right\rangle_{R_M(\mathcal{H}_X)} d\tau \geq \gamma_2 \|g\|^2_{R_M(\mathcal{H}_X)},$$

where $\gamma_2 = \frac{\tau_0 \theta^2}{\overline{\lambda}}$. □

Theorem 5.9 states that after a finite amount of time T_2, if there exists a constant Δ_2 such that in any time window $[t, t+\Delta_2] \subseteq [T_2, \infty)$, the state trajectory stays in the neighborhood of each of the centers $\boldsymbol{x}_1, \ldots, \boldsymbol{x}_n$ for at least a finite amount of time τ_0, then the state trajectory is persistently exciting in the sense of PE defined in the theorem. The example in Section 5.5 gives an intuitive illustration of the sufficient condition.

Corollary 5.10. *If the hypothesis of Theorem 5.9 holds and the family of functions $\mathbb{U}(\bar{S}_n)$, as defined in Subsection 5.2.4, are uniformly equicontinuous, then the trajectory $\boldsymbol{x} : t \to \boldsymbol{x}(t)$ persistently excites the indexing set Ω_n and the RKHS $R_M(\mathcal{H}_{\Omega_n})$ in the sense of PE $R_M(\mathcal{H}_{\Omega_n})$ - 5.1.*

Furthermore, if the unknown nonlinear function $f \in R_M(\mathcal{H}_{\Omega_n})$, then

$$\lim_{t\to\infty} \|\tilde{\boldsymbol{x}}(t)\| = 0,$$

$$\lim_{t\to\infty} \|\tilde{f}(t)\|_{R_M(\mathcal{H}_{\Omega_n})} = 0.$$

The proof of the above corollary follows directly from Theorem 5.9 and the discussion in Subsections 5.2.3 and 5.2.4.

5.4 Implications of the Sufficient Condition in Infinite Dimensions

In the previous section, we considered the case where the unknown nonlinear function f is in the finite-dimensional space $R_M(\mathcal{H}_{\Omega_n})$. In this section, we consider the case where it is only known that $f \in R_M(\mathcal{H}_X)$. Since functions in $R_M(\mathcal{H}_X)$ are defined only on the manifold M, we need the state trajectory $\boldsymbol{x}(t)$ to be contained in M for the governing equations to make sense. The implication of this change in hypotheses is that the function estimate error is ultimately bounded above by a constant which depends on the norm of the complementary projection.

In the following analysis, we use the subscript n to denote the terms associated with the finite-dimensional space $R_M(\mathcal{H}_{\Omega_n})$. Let $\mathbb{P}_{\Omega_n}$ be the projection operator from $R_M(\mathcal{H}_X)$ onto $R_M(\mathcal{H}_{\Omega_n})$. The projection operator decomposes the space $R_M(\mathcal{H}_X)$ into $R_M(\mathcal{H}_X) = R_M(\mathcal{H}_{\Omega_n}) \bigoplus R_M(\mathcal{V}_{\Omega_n})$. Note that space $R_M(\mathcal{V}_{\Omega_n})$ contains functions that are orthogonal to the functions in $R_M(\mathcal{H}_{\Omega_n})$. Using the reproducing property, it is easy to show that functions in $R_M(\mathcal{V}_{\Omega_n})$ vanish identically on the set Ω_n, i.e., for all $v \in R_M(\mathcal{V}_{\Omega_n})$, and $\boldsymbol{x} \in \Omega_n$, $v(\boldsymbol{x}) = 0$. With this definition, we rewrite the plant equation given in Equation 5.1, in which $f \in R_M(\mathcal{H}_X)$, in the form

$$\dot{\boldsymbol{x}}(t) = A\boldsymbol{x}(t) + Bf_n(\boldsymbol{x}(t)) + Bv_n(\boldsymbol{x}(t)),$$

where $\boldsymbol{x}(t) \in M$, $f_n = \mathbb{P}_{\Omega_n} f \in R_M(\mathcal{H}_{\Omega_n})$, $v_n \in R_M(\mathcal{V}_{\Omega_n})$ and $f = f_n + v_n$.

For practical applications, we want estimates that are finite-dimensional. We replace the infinite-dimensional estimate $\hat{f}$ in Equation 5.2 with the finite-dimensional estimate $\hat{f}_n := \hat{f}_n(t,\cdot) \in R_M(\mathcal{H}_{\Omega_n})$. The estimator equation has the form

$$\dot{\hat{\boldsymbol{x}}}(t) = A\hat{\boldsymbol{x}}(t) + B\hat{f}_n(t, \boldsymbol{x}(t)), \tag{5.7}$$

where $\hat{\boldsymbol{x}}(t) \in \mathbb{R}^d$ is the finite-dimensional state estimate. We use the dead-zone gradient learning law

$$\dot{\hat{f}}_n(t) = \Gamma^{-1}(B\mathcal{E}_{\boldsymbol{x}(t)}\mathbb{P}_{\Omega_n})^*\tilde{\boldsymbol{x}}_D(t), \tag{5.8}$$

where

$$\tilde{\boldsymbol{x}}_D(t) = \tilde{\boldsymbol{x}}(t) - \Phi\sigma(\tilde{\boldsymbol{x}}(t)).$$

In the above equation, $\Phi = \frac{\|B\|\|v_n\|_{C(U)}}{\lambda_A}$, and the other terms are defined as in Equation 5.3. The saturation function $\sigma : \mathbb{R}^d \to \mathbb{R}^d$ is defined as

$$\sigma_i(\boldsymbol{x}) = \begin{cases} \frac{\boldsymbol{x}_i}{\Phi} & \text{if } \left|\frac{\boldsymbol{x}_i}{\Phi}\right| \leq 1, \\ 1 & \text{if } \left|\frac{\boldsymbol{x}_i}{\Phi}\right| > 1 \end{cases}$$

for $i = 1, \ldots, d$ and $\sigma(\boldsymbol{x}) = \{\sigma_1(\boldsymbol{x}), \ldots, \sigma_d(\boldsymbol{x})\}^T$. Using the reproducing property, we can show that Equation 5.8 is equivalent to

$$\dot{\hat{\boldsymbol{\alpha}}}(t) = S(\boldsymbol{x}_1, \ldots, \boldsymbol{x}_n)^{-1}\boldsymbol{\Gamma}^{-1}\boldsymbol{\mathcal{R}}(\boldsymbol{x}_c, \boldsymbol{x}(t))B^T\tilde{\boldsymbol{x}}_D(t), \tag{5.9}$$

where $\boldsymbol{\mathcal{R}}(\boldsymbol{x}_c, \boldsymbol{x}(t)) := \{\boldsymbol{\mathcal{R}}(\boldsymbol{x}_1, \boldsymbol{x}(t)), \ldots, \boldsymbol{\mathcal{R}}(\boldsymbol{x}_n, \boldsymbol{x}(t))\}^T$, $S(\boldsymbol{x}_1, \ldots, \boldsymbol{x}_n)$ is defined as in Equation 5.5, and $\boldsymbol{\Gamma} := \Gamma\mathbb{I}_n$ is the gain matrix. [47] The term $\hat{\boldsymbol{\alpha}}(t) := \{\alpha_1(t), \ldots, \alpha_n(t)\}^T$ in the

above equation is the unknown parameter that satisfies $\hat{f}_n = \sum_{i=1}^{n} \alpha_i \mathcal{R}(\boldsymbol{x}_i, \cdot)$. The error equations are then

$$\begin{Bmatrix} \dot{\tilde{\boldsymbol{x}}}(t) \\ \dot{\tilde{f}}(t) \end{Bmatrix} = \begin{Bmatrix} A\tilde{\boldsymbol{x}}(t) + B\mathcal{E}_{\boldsymbol{x}(t)}\tilde{f}(t) \\ -\Gamma^{-1}(B\mathcal{E}_{\boldsymbol{x}(t)}\mathbb{P}_{\Omega_n})^*\tilde{\boldsymbol{x}}_D(t) \end{Bmatrix} \tag{5.10}$$

where $\tilde{\boldsymbol{x}}(t) := \boldsymbol{x}(t) - \hat{\boldsymbol{x}}(t)$ and $\tilde{f}(t) := f - \hat{f}_n(t)$. If we define $\tilde{f}_n(t) := \mathbb{P}_{\Omega_n} f - \hat{f}_n = f_n - \hat{f}_n(t)$, we get $\tilde{f}(t) := \tilde{f}_n(t) + v_n$. Since the function v_n is a constant, we have $\dot{\tilde{f}}(t) = \dot{\tilde{f}}_n(t)$.

The following theorem shows us that the sufficient condition given in Theorem 5.9 implies boundedness of the error by a constant proportional to $\|(I - \mathbb{P}_{\Omega_n})f\|_{C(U)}$, where U is a compact set in which the states are contained after a finite amount of time. The proof of the theorem is similar to that of Theorem 5.3. In the context of this theorem, we assume that the state trajectory $t \mapsto \boldsymbol{x}(t)$ is *bounded* and *uniformly continuous*. Generally speaking, we use both these assumptions in the proof of Theorem 5.9.

Theorem 5.11. *Suppose that the state trajectory $\boldsymbol{x}(t) \in M$, the function $f \in R_M(\mathcal{H}_X)$, and the class of functions $\mathbb{U}(\bar{S}_n)$ defined in Subsection 5.2.4 is uniformly equicontinuous. Also suppose that the constant ϵ is chosen as in Lemma 5.6 and satisfies Condition 5.7. If the sufficient condition given by Theorem 5.9 holds, and the evolution of $\hat{f}_n(t)$ is governed by Equation 5.8, then*

$$\limsup_{t\to\infty} \|\tilde{\boldsymbol{x}}(t)\| \leq \hat{c}\|v_n\|_{C(U)}, \qquad \limsup_{t\to\infty} \|\tilde{f}_n(t)\| \leq \check{c}\|v_n\|_{C(U)},$$

where $\hat{c} := \hat{c}(n)$ and $\check{c} := \check{c}(n)$ are constants and $\|v_n\|_{C(U)}$ denotes the uniform norm of the function v_n over the set $U = \overline{\{\boldsymbol{x}(\tau) | \tau \geq T_1\}}$ with T_1 is defined as in PE $R_M(\mathcal{H}_{\Omega_n})$-5.1.

Proof. Since the hypotheses of Corollary 5.10 holds, the state trajectory is persistently ex-

citing in the sense that there exist constants T_1, γ_1, δ_1 and Δ_1 such that the PE condition given in the corollary holds. Consider the Lyapunov function

$$V(t) = \langle \tilde{\boldsymbol{x}}_D(t), \tilde{\boldsymbol{x}}_D(t) \rangle + \left\langle \tilde{f}_n(t), \Gamma \tilde{f}_n(t) \right\rangle_{R_M(\mathcal{H}_X)}.$$

The time derivative of the Lyapunov equation is

$$\begin{aligned}\dot{V}(t) &= \left\langle \tilde{\boldsymbol{x}}_D(t), \left(I - \Phi \frac{\partial \sigma}{\partial \boldsymbol{x}}(\tilde{\boldsymbol{x}}(t)) \right) \dot{\tilde{\boldsymbol{x}}}(t) \right\rangle + \left\langle \tilde{f}_n(t), \dot{\tilde{f}}_n(t) \right\rangle \\ &= -\lambda_A \|\tilde{\boldsymbol{x}}_D(t)\|^2 - \lambda_A \Phi \|\tilde{\boldsymbol{x}}_D(t)\|_1 + \tilde{\boldsymbol{x}}_D(t)^T B v_n(\boldsymbol{x}(t)).\end{aligned}$$

In deriving the above equation, we assume that the matrix A has the form $A = -\lambda_A I$, where $\lambda_A > 0$. (There is not loss of generality in this assumption. If A does not satisfy this assumption, we can modify the estimator in Equation 5.7 by replacing the term $A\hat{\boldsymbol{x}}(t)$ with $A\boldsymbol{x}(t)$ and adding the term $\lambda_A I \tilde{\boldsymbol{x}}(t)$. Then the error equations have the same form as in Equation 5.10 and the analysis proceeds without change.) Since $\Phi = \frac{\|B\| \|v_n\|_{C(U)}}{\lambda_A}$, we conclude that

$$\dot{V}(t) \leq -\lambda_A \|\tilde{\boldsymbol{x}}_D(t)\|^2.$$

Thus, we conclude that $\tilde{\boldsymbol{x}}_D(t)$, $\tilde{\boldsymbol{x}}(t)$ are bounded and the family of functions $\{\tilde{f}_n(t)\}_{t \geq 0}$ is uniformly bounded.

Next note that $\dot{\tilde{\boldsymbol{x}}}(t)$ is bounded. This is evident from the equality

$$\|\dot{\tilde{\boldsymbol{x}}}\| \leq \|A\| \|\tilde{\boldsymbol{x}}(t)\| + \|B\| \|\mathcal{E}_{\boldsymbol{x}(t)}\| \left(\|\tilde{f}_n(t)\| + \|v_n\| \right).$$

Thus, $\tilde{\boldsymbol{x}}(t)$ is Lipschitz continuous in t, which implies that the same is uniformly continuous

in t. This in turn implies that $\tilde{\boldsymbol{x}}_D(t)$ is uniformly continuous in t. Next, notice that the function v_n is bounded and uniformly continuous on the set U, since v_n is continuous and U is compact. Furthermore, recall that the state trajectory is bounded and uniformly continuous in t. Thus, $\dot{V}(t)$ is uniformly continuous in t.

Since $V(t)$ is monotonically decreasing and bounded below, we have

$$\lim_{t\to\infty}\int_{t_0}^{t}\dot{V}(t)d\tau = \lim_{t\to\infty} V(t) - V(t_0) < \infty.$$

Using Barbalat's lemma for $\dot{V}$, we get

$$\lim_{t\to\infty}\|\tilde{\boldsymbol{x}}_D(t)\| = 0,$$

which implies

$$\limsup_{t\to\infty}\|\tilde{\boldsymbol{x}}(t)\| \leq \hat{c}\|v_n\|_{C(U)},$$

where $\hat{c} = \frac{\|B\|\sqrt{\bar{\lambda}n}}{\lambda_A}$, $\bar{\lambda}$ is the largest eigenvalue of the Grammian matrix $S(\boldsymbol{x}_1,\ldots,\boldsymbol{x}_n)$.

Next, we turn to the proof that $\limsup_{t\to\infty}\|\tilde{f}_n(t)\| \leq \check{c}\|v_n\|_{C(U)}$. Given $\varepsilon > 0$, there exists a T such that for all $t \geq T$, $\|\tilde{\boldsymbol{x}}_D(t)\| < \varepsilon$ or $\|\tilde{\boldsymbol{x}}(t)\| < \hat{c}\|v_n\|_{C(U)} + \varepsilon$. Without loss of generality, select the constant $T \geq T_1$. Let $s \in [T, T+\Delta_1]$. Since we know how the state error evolves, the norm of the state error at $s+\delta_1$ is bounded below by

$$\begin{aligned}\|\tilde{\boldsymbol{x}}(s+\delta_1)\| &= \left\|\tilde{\boldsymbol{x}}(s) + \int_s^{s+\delta_1} A\tilde{\boldsymbol{x}}(\tau) + B\mathcal{E}_{\boldsymbol{x}(\tau)}\tilde{f}(\tau)d\tau\right\|,\\ &\geq \underbrace{\left\|\int_s^{s+\delta_1} B\mathcal{E}_{\boldsymbol{x}(\tau)}\tilde{f}(T)d\tau\right\|}_{\text{term 1}} - \underbrace{\left\|\tilde{\boldsymbol{x}}(s) + \int_s^{s+\delta_1} A\tilde{\boldsymbol{x}}(\tau)d\tau\right\|}_{\text{term 2}}\end{aligned}$$

$$- \underbrace{\left\| \int_s^{s+\delta_1} B\mathcal{E}_{\boldsymbol{x}(\tau)}(\tilde{f}(\tau) - \tilde{f}(T))d\tau \right\|}_{\text{term 3}}.$$

Let us consider term 1. We have

$$\begin{aligned}\left\| \int_s^{s+\delta_1} B\mathcal{E}_{\boldsymbol{x}(\tau)}\tilde{f}(T)d\tau \right\| &= \|B\| \left| \int_s^{s+\delta_1} \mathcal{E}_{\boldsymbol{x}(\tau)}\tilde{f}(T)d\tau \right| = \|B\| \left| \int_s^{s+\delta_1} \mathcal{E}_{\boldsymbol{x}(\tau)} \left(\tilde{f}_n(T) + v_n \right) d\tau \right|, \\ &\geq \|B\| \left| \int_s^{s+\delta_1} \mathcal{E}_{\boldsymbol{x}(\tau)}\tilde{f}_n(T)d\tau \right| - \|B\| \left| \int_s^{s+\delta_1} v_n(\boldsymbol{x}(\tau))d\tau \right|.\end{aligned}$$

Since the PE condition for $R_M(\mathcal{H}_{\Omega_n})$ is valid, we have

$$\left\| \int_s^{s+\delta_1} B\mathcal{E}_{\boldsymbol{x}(\tau)}\tilde{f}(T)d\tau \right\| \geq \gamma_1 \|B\| \|\tilde{f}_n(T)\| - \delta_1 \|B\| \|v_n\|_{C(U)}.$$

Now consider term 2. We bound term 2 above by

$$\left\| \tilde{\boldsymbol{x}}(s) + \int_s^{s+\delta_1} A\tilde{\boldsymbol{x}}(\tau)d\tau \right\| \leq \|\tilde{\boldsymbol{x}}(s)\| + \int_s^{s+\delta_1} \|A\| \|\tilde{\boldsymbol{x}}(\tau)\| d\tau \leq (1 + \|A\|\delta)(\hat{c}\|v_n\|_{C(U)} + \varepsilon).$$

Before proceeding further, we consider the term $\tilde{f}(\tau) - \tilde{f}(T)$. Using the learning law gives us

$$\begin{aligned}\|\tilde{f}(\tau) - \tilde{f}(T)\|_{R_M(\mathcal{H}_X)} &= \left\| \int_T^{\tau} \Gamma^{-1}(B\mathcal{E}_{\boldsymbol{x}(\xi)}\mathbb{P}_{\Omega_n})^* \tilde{\boldsymbol{x}}_D(\xi)d\xi \right\|_{R_M(\mathcal{H}_X)}, \\ &\leq \int_T^{\tau} \Gamma^{-1} \|B\| \|\mathcal{E}_{\boldsymbol{x}(\xi)}\| \|\mathbb{P}_{\Omega_n}\| \|\tilde{\boldsymbol{x}}_D(\xi)\| d\xi \leq c_2(\tau - T)\varepsilon,\end{aligned} \tag{5.11}$$

where $c_2 = \Gamma^{-1}\|B\|\|\mathcal{E}_{\boldsymbol{x}(\xi)}\|$. Thus, since $T \leq s \leq T + \Delta$, Term 3 is bounded above by

$$\left\| \int_s^{s+\delta_1} B\mathcal{E}_{\boldsymbol{x}(\tau)}(\tilde{f}(\tau) - \tilde{f}(T))d\tau \right\| \leq \int_s^{s+\delta} \|B\| \|\mathcal{E}_{\boldsymbol{x}(\tau)}\| \|\tilde{f}(\tau) - \tilde{f}(T)\|_{R_M(\mathcal{H}_X)} d\tau \leq c_3\varepsilon,$$

where $c_3 = \|B\|\|\mathcal{E}_{\boldsymbol{x}(\tau)}\|c_2 \left(\frac{1}{2}\delta_1^2 + \Delta_1\delta_1 \right)$. Thus, the norm of the state error at $s+\delta_1$ is bounded

below by

$$\|\tilde{\boldsymbol{x}}(s+\delta_1)\| \geq \gamma_1\|B\|\|\tilde{f}_n(T)\| - \delta_1\|B\|\|v_n\|_{C(U)} - (1+\|A\|\delta_1)(\hat{c}\|v_n\|_{C(U)}+\varepsilon) - c_3\varepsilon.$$

Since $s+\delta_1 > s \geq T$, we know that $\|\tilde{\boldsymbol{x}}(s+\delta_1)\| < \hat{c}\|v_n\|_{C(U)} + \varepsilon$. Rearranging the terms in the above equation, we get

$$\|\tilde{f}_n(T)\| < \check{c}\|v_n\|_{C(U)} + \frac{(2+\|A\|\delta_1 + c_3)}{\gamma_1\|B\|}\varepsilon,$$

where $\check{c} = \frac{(2+\|A\|\delta_1)\hat{c}+\delta_1\|B\|}{\gamma_1\|B\|}$. In the argument above, T is such that $\|\tilde{x}_n(t)\| < \hat{c}\|v_n\|_{C(U)} + \varepsilon$ for all $t \geq T$. We can repeat the above analysis for a sequence of ε, $\{\bar{\varepsilon}_k\}_{k=1}^{\infty}$ such that $\bar{\varepsilon}_1 > \bar{\varepsilon}_2 > \ldots$, $\lim_{k\to\infty}\bar{\varepsilon}_k \to 0$. We can find an associated sequence of T, $\{\bar{T}_k\}_{k=1}^{\infty}$ such that $\bar{T}_1 < \bar{T}_2 < \ldots$, $\lim_{k\to\infty}\bar{T}_k \to \infty$. Note that for any τ such that $\bar{T}_k \leq \tau < \bar{T}_{k+1}$, we have

$$\|\tilde{f}_n(\tau)\| < \check{c}\|v_n\|_{C(U)} + \frac{(2+\|A\|\delta_1 + c_3)}{\gamma_1\|B\|}\bar{\varepsilon}_k.$$

Thus, we conclude that

$$\limsup_{t\to\infty}\|\tilde{f}_n(t)\| \leq \check{c}\|v_n\|_{C(U)}.$$

□

Remarks on Theorem 5.11:

1. The implication of Theorem 5.11 agrees with our intuition. The term $\|\tilde{f}_n(t)\|$ is eventually bounded by a constant that depends on the norm of the orthogonal component $v_n = (I - \mathbb{P}_{\Omega_n})f$ of the unknown function, the matrix A and the dimension n. In particular, the bound depends on the uniform norm of v_n on the set U.

2. By comparing Theorems 5.3 and 5.11, it is clear that both theorems rely on different notions of PE (PE $R_M(\mathcal{H}_X)$-2 and PE $R_M(\mathcal{H}_{\Omega_n})$-2, respectively), which leads to distinct results. The differing notions arise from the fact that the we assume that the actual function f is an element of $R_M(\mathcal{H}_{\Omega_n})$, as opposed to $R_M(\mathcal{H}_X)$, while proving the sufficient condition in Theorem 5.9.

3. In the above theorem, we can interpret v_n as process noise.

We next study in the following corollary a new error bound that is an immediate result of the sufficient condition derived in Theorem 5.9 and Theorem 5.11. Following the derivation of the corollary, we compare and contrast the nature of the new convergence rate with the results in [42].

Corollary 5.12. *Suppose that the hypothesis of Theorem 5.11 holds, and suppose that the set $U \subseteq \cup_{i=1}^{n} B_\eta(\boldsymbol{x}_i)$, where $B_\eta(\boldsymbol{x}_i)$ is the closed ball of radius η centered at $\boldsymbol{x}_i \in \Omega_n$. If the function v_n is Lipschitz continuous on $\cup_{i=1}^{n} B_\eta(\boldsymbol{x}_i)$, then*

$$\lim_{t\to\infty} \|\tilde{f}_n(t)\| \leq \check{c} L \eta,$$

where L is the Lipschitz constant and $\check{c} := \check{c}(n)$ is a constant defined as in Theorem 5.11.

Proof. We know that the function v_n vanishes identically on the set Ω_n since $v_n \in R_M(\mathcal{V}_{\Omega_n})$, i.e., $v_n(\boldsymbol{x}_i) = 0$ for all $\boldsymbol{x}_i \in \Omega_n$. Since v_n is Lipschitz continuous, we have

$$|v_n(\boldsymbol{y})| \leq L d_M(\boldsymbol{x}_i, \boldsymbol{y}) \leq L\eta,$$

where $\boldsymbol{x}_i \in \Omega_n$, $\boldsymbol{y} \in B_\eta(\boldsymbol{x}_i)$ for all $i = 1, \ldots, n$. Since the upper bound $L\eta$ is independent of

index i and the hypotheses of Theorem 5.11 hold, we have

$$\lim_{t\to\infty} \|\tilde{f}_n(t)\| \leq \check{c}L\eta.$$

□

Remarks on Corollary 5.12:

1. The corollary shows that if the function v_n is Lipschitz continuous and if $U \subseteq \cup_{i=1}^n B_\eta(\boldsymbol{x}_i)$, then the error bound for $\lim_{t\to\infty} \|\tilde{f}_n(t)\|$ depends on the radius η of the closed balls $B_\eta(\boldsymbol{x}_i)$. It is clear that the radius η depends on the maximum distance of the state $\boldsymbol{x}(t)$ from the kernel centers $\boldsymbol{x}_i \in \Omega_n$ for $t \geq T_1$. Thus, by choosing T_1 large enough, we can make the error bound small. However, we cannot make the error bound zero since the radius η depends on the distance between the neighboring kernel centers. If the distance between neighboring kernels centers is greater than 2η, then the exists a t such that $\boldsymbol{x}(t) \notin U \subseteq \cup_{i=1}^n B_\eta(\boldsymbol{x}_i)$. This suggests that we can try to reduce the error bound by choosing more kernel centers that are persistently excited. However, careful study of the constant $\check{c}$ shows that it depends on the number of kernel centers n, $\check{c} := \check{c}_n$. A rigorous treatment of this strategy will require the control of the product $\check{c}_n\eta_n$.

2. The notion of distance between kernel centers directly ties to the concept of fill distance $h_{\Omega_n,M}$ defined as

$$h_{\Omega_n,M} := \sup_{\boldsymbol{y}\in M} \min_{\boldsymbol{x}_i\in\Omega_n} d_M(\boldsymbol{x}_i, \boldsymbol{y}).$$

It is shown in [42] that for certain kernels, the rate of convergence of the finite-dimensional function estimate $\hat{f}_n$ to the infinite-dimensional function estimate $\hat{f}$ de-

pends on the fill distance. We can think of the infinite-dimensional estimate as the one that makes the error $P_\Omega \tilde{f}(t) \to 0$ as $t \to \infty$, where Ω is the PE set (that consists of infinite number of elements). By adding more centers, the finite-dimensional $\hat{f}_n(t) = P_{\Omega_n} \hat{f}(t)$ converges to the infinite-dimensional function estimate $P_\Omega \tilde{f}(t)$. This in turn implies that the bound on the error goes to zero as we add more centers.

3. In Corollary 5.12, we assumes that the function v_n is Lipschitz continuous on the set U. This condition is equivalent to assuming that the change of the function v_n is constrained in the set U. We can come up with conditions that ensure Lipschitz continuity in a variety of ways. Suppose that the kernel generates an RKHS $\mathcal{H}_X$ that is embedded in a Sobolev space $W^{s,2}(X)$. A well known example of such a kernel is the Sobolev-Matern kernel. If the Sobolev space is of high enough order, Sobolev embedding theorem implies that the space $W^{s,2}(X)$ is embedded in the Holder space $C^{(1,0)}(X)$. We know that functions in $C^{(1,0)}(X)$ are globally Lipschitz. This implies that the function v_n is Lipschitz continuous.

5.5 Numerical Example

To interpret and evaluate the implications of the sufficient condition, we consider the undamped, unforced version of the nonlinear piezoelectric oscillator studied in [47]. We show that the sufficient condition implies ultimate boundedness of the function error estimate when we implement a gradient learning law based adaptive estimator. The governing equations of this oscillator have the form

$$\begin{Bmatrix} \dot{x}_1(t) \\ \dot{x}_2(t) \end{Bmatrix} = \underbrace{\begin{bmatrix} 0 & 1 \\ -\frac{\hat{K}}{M} & 0 \end{bmatrix}}_{A} \underbrace{\begin{Bmatrix} x_1(t) \\ x_2(t) \end{Bmatrix}}_{\boldsymbol{x}(t)} + \underbrace{\begin{Bmatrix} 0 \\ 1 \end{Bmatrix}}_{B} \underbrace{\left(-\frac{\hat{K}_{N_1}}{M} x_1^3(t) - \frac{\hat{K}_{N_2}}{M} x_1^5(t) \right)}_{f(\boldsymbol{x}(t))}, \tag{5.12}$$

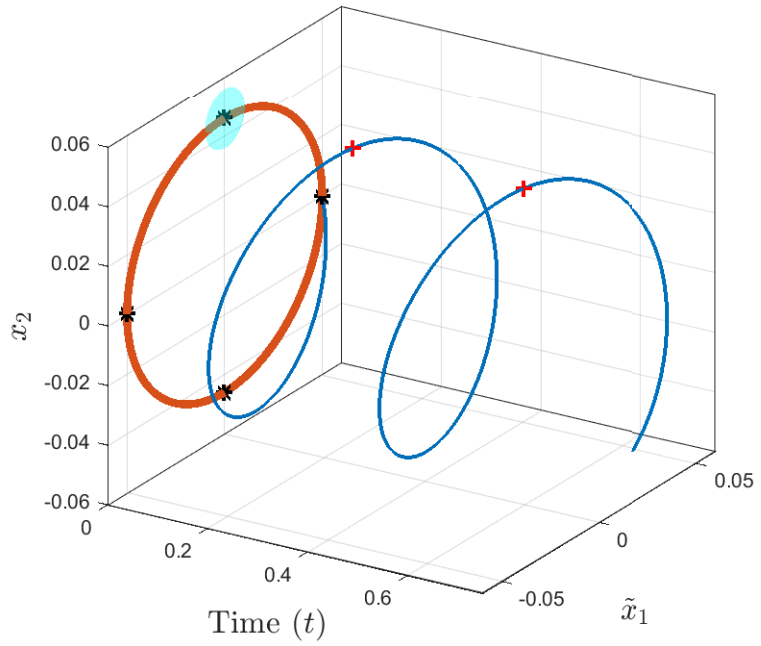

Figure 5.1: State trajectory of the nonlinear system governed by Equation 5.12, when the initial condition is $\boldsymbol{x}_0 = [0.05, 0]^T$. The red loop is the positive limit set. The cyan circle represents the closed ball centered at the point depicted by marker $*$ in the phase plane. Marker $+$ represents the point depicted by $*$ in the state trajectory.

where $M, \hat{K}$ are the modal mass and modal stiffness of the piezoelectric oscillator, respectively. The variables $\hat{K}_{N_1}, \hat{K}_{N_2}$ are constants derived from nonlinear piezoelectric constitutive laws. [47] The states $x_1(\cdot)$ and $x_2(\cdot)$ are the modal displacement and modal velocity, respectively. Typically, the two states are not of the same order of magnitude, which inspires the use of anisotropic kernel functions, i.e. those that are elongated in one direction. However, equivalently, it is much easier to introduce a scaling factor for the one of the states. We substitute $x_1(t) = s\tilde{x}_1(t)$ in the governing equations, where s is the scaling factor, and redefine $\boldsymbol{x}(t) := [\tilde{x}_1(t), x_2(t)]^T$. For our simulations, we choose $M = 0.9745$, $\hat{K} = 329.9006$, $\hat{K}_{N_1} = -1.2901e+05$, $\hat{K}_{N_2} = 1.2053e+09$ and $s = 0.02$. Furthermore, we choose the initial condition $\boldsymbol{x}_0 = [\tilde{x}_1(0), x_2(0)]^T = [0.05, 0]^T$.

Figure 5.1 shows the evolution of the states with time. It is clear that the positive limit set for the selected initial condition is a smooth, compact, Riemmanian, 1-dimensional manifold embedded in $X = \mathbb{R}^2$. In our simulations, we use the RKHS generated by the Sobolev-Matern $3, 2$ kernel, which has the form

$$\mathcal{R}_{3,2}(\boldsymbol{x}, \boldsymbol{y}) = \left(1 + \frac{\sqrt{3}\|\boldsymbol{x} - \boldsymbol{y}\|}{l}\right) \exp\left(-\frac{\sqrt{3}\|\boldsymbol{x} - \boldsymbol{y}\|}{l}\right), \tag{5.13}$$

where l is the scaling factor of length. [48]

The adaptive estimation equations are given by Equation 5.7, and

$$\dot{\hat{f}}_n(t) = \Gamma^{-1}(B\mathcal{E}_{\boldsymbol{x}(t)})^* P(\boldsymbol{x}(t) - \hat{\boldsymbol{x}}(t)). \tag{5.14}$$

Notice that the above equation specifies the derivative of the function estimate. Using the reproducing property, we can show that this evolution law is equivalent to

$$\dot{\hat{\boldsymbol{\alpha}}}(t) = S(\boldsymbol{x}_1, \ldots, \boldsymbol{x}_n)^{-1} \boldsymbol{\Gamma}^{-1} \boldsymbol{\mathcal{R}}(\boldsymbol{x}_c, \boldsymbol{x}(t)) B^T P \tilde{\boldsymbol{x}}(t), \tag{5.15}$$

where all the terms are defined as in Equation 5.9. To build the adaptive estimate, we fix n, then choose kernel centers $\boldsymbol{x}_1, \ldots, \boldsymbol{x}_n$ along with the gain parameter Γ, and integrate Equations 5.7 and 5.15.

Figure 5.1 depicts the state evolution with time as well as the positive limit set of our example. It is clear from the figure that the state trajectory is uniformly continuous. Our goal is to choose n kernel centers $\boldsymbol{x}_1, \ldots, \boldsymbol{x}_n$ that are persistently excited. First let us note that the trajectory is periodic. Set $\Delta_2 = 2t_p$, where t_p is the period of the state trajectory. Consider an arbitrary point $\boldsymbol{x}_1$ in the positive limit set. Consider the window $I_p = [t, t + 2t_p]$ for any arbitrary $t \geq 0$. It is clear that the time spent by the state trajectory in $B_\epsilon(\boldsymbol{x}_1)$

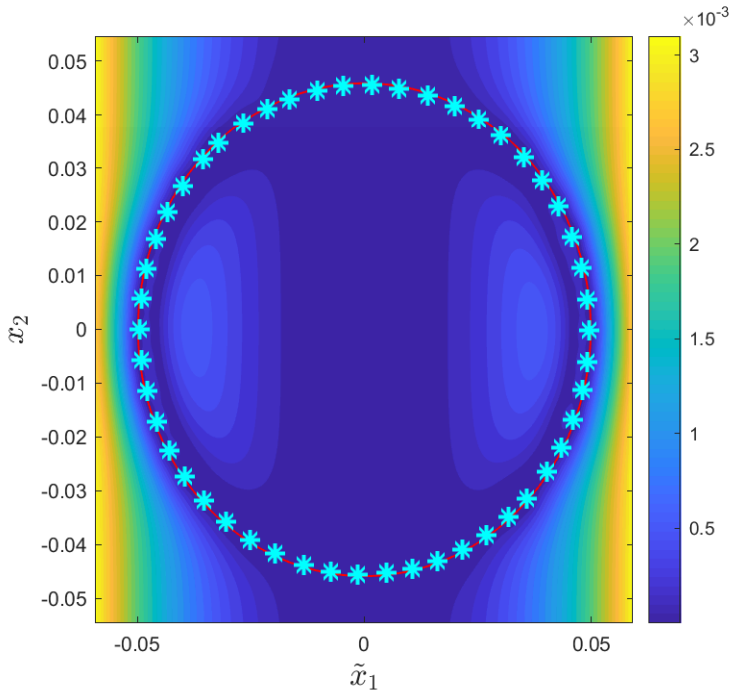

Figure 5.2: Pointwise error $|f(\boldsymbol{x}) - \hat{f}_n(t_e, \boldsymbol{x})|$. The marker $*$ and the red line represent the kernel centers and the limit set Ω, respectively.

during any window I_p is bounded below by a constant. In Figure 5.1, consider the (cyan) ball in the phase plane and any part of the state trajectory that is contained in a time window of $2t_p$. It is clear that the time spent by the trajectory in this ball is bounded below. Thus, using Corollary 5.10, we conclude that the point $\boldsymbol{x}_1$ is persistently excited. We repeat this analysis until n points are determined. For this specific problem, any discrete finite number of points in the positive limit set are persistently excited. Note that in our previous analysis, we did not explicitly calculate the radius ϵ. However, the above analysis is valid for a ball of any positive radius centered at a point in the positive limit set. For a point outside the positive limit set, we need explicit knowledge of ϵ that is as in Lemma 5.6 and satisfies Condition 5.7.

In the above analysis, we treat the state trajectory as elements contained in $\mathbb{R}^2$. However,

the state trajectory is contained in the positive limit set, which is a smooth, compact, Riemmanian 1-dimensional manifold M embedded in $X = \mathbb{R}^2$. We can treat the problem as evolution on a manifold and restrict the Hilbert space of function $\mathcal{H}_X$ to the manifold. Analysis similar to the one given above holds in this case. The primary difference is that we consider closed balls that are contained in the one-dimensional manifold M as opposed to ones contained in $\mathbb{R}^2$. We can determine the persistently excited points in M and combine our analysis given in [42] to determine approximation rates of convergence.

Figure 5.2 depicts the pointwise error $|f(\boldsymbol{x}) - \hat{f}_n(t_e, \boldsymbol{x})|$ after running the adaptive estimator for $t_e = 150$ seconds with 50 kernel centers initialized at $\alpha_i(0) = 0.001$ for all $i = 1, \ldots, 50$. In our simulations, we set $\Gamma = 0.001$ and $l = 0.005$. Note that the function $f(\boldsymbol{x})$ in Equation 5.12 is clearly not in the space of $\mathcal{H}_{\Omega_{50}}$, where Ω_{50} is the set of 50 kernel centers in the positive limit set denoted by the marker $*$ in Figure 5.2. No linear combination of kernels, given by Equation 5.13, centered at points in Ω_{50} will be equation to $f(\boldsymbol{x})$. Thus, based on our analysis in Section 5.4, we can only guarantee boundedness of the asymptotic function error in the neighborhood of the positive limit set. Figure 5.2 clearly shows that the pointwise error is bounded around the positive limit set. Note, in our theorems imply convergence in the $R_M(H_X)$ norm. However, in an RKHS, convergence in RKHS norm implies pointwise convergence. In fact, since we consider only RKHS that are uniformly bounded, convergence in RKHS norm implies uniform convergence.

5.6 Conclusion

In this chapter, we have derived a sufficient condition for different notions of PE in RKHS defined over embedded manifolds. This sufficient condition is valid for RKHS generated by continuous, strictly positive definite kernels. We have studied the implications of the

sufficient condition in the case when the RKHS is finite or infinite-dimensional. When the unknown function resides in a finite-dimensional RKHS, the sufficient condition implies convergence of function error estimate. In the more general case when we only know that the unknown function resides in an infinite-dimensional RKHS, the sufficient conditions implies ultimate boundedness of the function estimate error by a constant that depends on the approximation error. Finally, the numerical example has illustrated the practicality of the sufficient condition.

Bibliography

[1] Shankar Sastry and Marc Bodson. *Adaptive control: stability, convergence and robustness*. Courier Corporation, 2011. ISBN 0486482022.

[2] Kumpati S Narendra and Anuradha M Annaswamy. *Stable adaptive systems*. Courier Corporation, 2012. ISBN 048614142X.

[3] P. A. Ioannou and Jing Sun. *Robust Adaptive Control*. Dover Publications Inc., 1996. ISBN 0486498174.

[4] A Morgan and K Narendra. On the Uniform Asymptotic Stability of Certain Linear Nonautonomous Differential Equations. *SIAM Journal on Control and Optimization*, 15(1):5–24, January 1977. ISSN 0363-0129. doi: 10.1137/0315002. URL https://doi.org/10.1137/0315002.

[5] A P Morgan and K S Narendra. On the Stability of Nonautonomous Differential Equations $\dot{x} = [A + B(t)]x$, with Skew Symmetric Matrix $B(t)$. *SIAM Journal on Control and Optimization*, 15(1):163–176, January 1977. ISSN 0363-0129. doi: 10.1137/0315013. URL https://doi.org/10.1137/0315013.

[6] Stephen Boyd and Shankar Sastry. On parameter convergence in adaptive control. *Systems and Control Letters*, 3(6):311–319, December 1983. ISSN 01676911. doi: 10.1016/0167-6911(83)90071-3.

[7] B Anderson. Exponential stability of linear equations arising in adaptive identification. *IEEE Transactions on Automatic Control*, 22(1):83–88, 1977. ISSN 0018-9286 VO - 22. doi: 10.1109/TAC.1977.1101406.

[8] E Panteley, A Loria, and A Teel. Relaxed persistency of excitation for uniform asymptotic stability. *IEEE Transactions on Automatic Control*, 46(12):1874–1886, 2001. ISSN 1558-2523 VO - 46. doi: 10.1109/9.975471.

[9] Antonio Loria, Elena Panteley, Dobrivoje Popovic, and Andrew R. Teel. Persistency of excitation for uniform convergence in nonlinear control systems. January 2003. URL https://arxiv.org/abs/math/0301335.

[10] E Panteley and A Loria. Uniform exponential stability for families of linear time-varying systems. In *Proceedings of the 39th IEEE Conference on Decision and Control (Cat. No.00CH37187)*, volume 2, pages 1948–1953 vol.2, 2000. ISBN 0191-2216 VO - 2. doi: 10.1109/CDC.2000.912148.

[11] A Loria, R Kelly, and A R Teel. Uniform parametric convergence in the adaptive control of manipulators: a case restudied. In *2003 IEEE International Conference on Robotics and Automation (Cat. No.03CH37422)*, volume 1, pages 1062–1067 vol.1, 2003. ISBN 1050-4729 VO - 1. doi: 10.1109/ROBOT.2003.1241733.

[12] Elena Panteley and Antonio Loria. On global uniform asymptotic stability of nonlinear time-varying systems in cascade. *Systems & Control Letters*, 33(2):131–138, 1998. ISSN 0167-6911. doi: https://doi.org/10.1016/S0167-6911(97)00119-9. URL http://www.sciencedirect.com/science/article/pii/S0167691197001199.

[13] Jay A. Farrell. Persistence of excitation conditions in passive learning control. *Automatica*, 33(4):699–703, 1997. ISSN 00051098. doi: 10.1016/S0005-1098(96)00203-8.

[14] C. Novara, T. Vincent, K. Hsu, M. Milanese, and K. Poolla. Parametric identification of structured nonlinear systems. *Automatica*, 47(4):711–721, April 2011. ISSN 00051098. doi: 10.1016/j.automatica.2011.01.063.

[15] Chengzhi Yuan and Cong Wang. Persistency of excitation and performance of deterministic learning. *Systems & Control Letters*, 60(12):952–959, 2011. ISSN 0167-6911. doi: https://doi.org/10.1016/j.sysconle.2011.08.002. URL http://www.sciencedirect.com/science/article/pii/S0167691111001770.

[16] Sergey Nikitin. Generalized Persistency of Excitation. *International Journal of Mathematics and Mathematical Sciences*, 2007:69093, 2007. ISSN 0161-1712. doi: 10.1155/2007/69093. URL https://doi.org/10.1155/2007/69093.

[17] M A Demetriou and I G Rosen. Adaptive identification of second-order distributed parameter systems. *Inverse Problems*, 10(2):261–294, 1994. ISSN 0266-5611. doi: 10.1088/0266-5611/10/2/006. URL http://dx.doi.org/10.1088/0266-5611/10/2/006.

[18] M A Demetriou and I G Rosen. On the persistence of excitation in the adaptive estimation of distributed parameter systems. *IEEE Transactions on Automatic Control*, 39(5):1117–1123, 1994. ISSN 1558-2523 VO - 39. doi: 10.1109/9.284907.

[19] Michael A. Demetriou and Fariba Fahroo. Model reference adaptive control of structurally perturbed second-order distributed parameter systems. *International Journal of Robust and Nonlinear Control*, 16(16):773–799, November 2006. ISSN 1049-8923. doi: 10.1002/rnc.1100. URL https://doi.org/10.1002/rnc.1100.

[20] J Baumeister, W Scondo, M A Demetriou, and I G Rosen. On-Line Parameter Estimation for Infinite-Dimensional Dynamical Systems. *SIAM Journal on Control and Optimization*, 35(2):678–713, March 1997. ISSN 0363-0129. doi: 10.1137/S0363012994270928. URL https://doi.org/10.1137/S0363012994270928.

[21] Michael Böhm, M A Demetriou, Simeon Reich, and I G Rosen. Model Reference Adaptive Control of Distributed Parameter Systems. *SIAM Journal on Control and Optimiza-*

tion, 36(1):33–81, January 1998. ISSN 0363-0129. doi: 10.1137/S0363012995279717. URL https://doi.org/10.1137/S0363012995279717.

[22] Michael A Demetriou. *Adaptive parameter estimation of abstract parabolic and hyperbolic distributed parameter systems*. PhD thesis, University of Southern California, 1994. URL http://digitallibrary.usc.edu/cdm/ref/collection/p15799coll37/id/67220.

[23] Parag Bobade, Suprotim Majumdar, Savio Pereira, Andrew J. Kurdila, and John B. Ferris. Adaptive estimation for nonlinear systems using reproducing kernel Hilbert spaces. *Advances in Computational Mathematics*, 45(2):869–896, 2019. ISSN 1572-9044. doi: 10.1007/s10444-018-9639-z. URL https://doi.org/10.1007/s10444-018-9639-z.

[24] Jia Guo, Sai Tej Paruchuri, and Andrew J. Kurdila. Persistence of Excitation in Uniformly Embedded Reproducing KernelHilbert (RKH) Spaces (ACC). In *American Control Conference*, 2020.

[25] Jia Guo, Sai Tej Paruchuri, and Andrew J. Kurdila. Persistence of Excitation in Uniformly Embedded Reproducing Kernel Hilbert (RKH) Spaces. February 2019. URL https://arxiv.org/abs/2002.07963.

[26] E W Bai and S S Sastry. Persistency of excitation, sufficient richness and parameter convergence in discrete time adaptive control. *Systems & Control Letters*, 6(3):153–163, 1985. ISSN 0167-6911. doi: https://doi.org/10.1016/0167-6911(85)90035-0. URL http://www.sciencedirect.com/science/article/pii/0167691185900350.

[27] Stephen Boyd~ and S S Sastry. Necessary and Sufficient Conditions for Parameter Convergence in Adaptive Control*. Technical Report 6, 1986.

[28] Andrew J. Kurdila, Francis J. Narcowich, and Joseph D. Ward. Persistency of excitation, identification, and radial basis functions. In *Proceedings of the IEEE Conference on*

Decision and Control, volume 3, pages 2273–2278. IEEE, 1994. doi: 10.1109/cdc.1994.411479.

[29] A. J. Kurdila, Francis J. Narcowich, and Joseph D. Ward. Persistency of excitation in identification using radial basis function approximants. *SIAM journal on control and optimization*, 33(2):625–642, July 1995. ISSN 0363-0129. doi: 10.1137/S0363012992232555.

[30] D Gorinevsky. On the persistency of excitation in radial basis function network identification of nonlinear systems. *IEEE Transactions on Neural Networks*, 6(5):1237–1244, 1995. ISSN 1941-0093 VO - 6. doi: 10.1109/72.410365.

[31] Songwu Lu and T Basar. Robust nonlinear system identification using neural-network models. *IEEE Transactions on Neural Networks*, 9(3):407–429, 1998. ISSN 1941-0093 VO - 9. doi: 10.1109/72.668883.

[32] Cong Wang and David J. Hill. Learning from neural control. *IEEE Transactions on Neural Networks*, 17(1):130–146, January 2006. ISSN 10459227. doi: 10.1109/TNN.2005.860843.

[33] CONG WANG, TIANRUI CHEN, GUANRONG CHEN, and DAVID J HILL. DETERMINISTIC LEARNING OF NONLINEAR DYNAMICAL SYSTEMS. *International Journal of Bifurcation and Chaos*, 19(04):1307–1328, April 2009. ISSN 0218-1274. doi: 10.1142/S0218127409023640. URL https://doi.org/10.1142/S0218127409023640.

[34] Bassam Bamieh and Laura Giarr. Identification of linear parameter varying models. *INTERNATIONAL JOURNAL OF ROBUST AND NONLINEAR CONTROL Int. J. Robust Nonlinear Control*, 12:841–853, 2002. doi: 10.1002/rnc.706.

[35] Veronica Adetola and Martin Guay. Finite-time parameter estimation in adaptive control of nonlinear systems. *IEEE Transactions on Automatic Control*, 53(3):807–811, April 2008. ISSN 00189286. doi: 10.1109/TAC.2008.919568.

[36] Girish Chowdhary, Maximilian Mühlegg, and Eric Johnson. Exponential parameter and tracking error convergence guarantees for adaptive controllers without persistency of excitation. *International Journal of Control*, 87(8):1583–1603, August 2014. ISSN 13665820. doi: 10.1080/00207179.2014.880128.

[37] Kyriakos G. Vamvoudakis, Marcio Fantini Miranda, and João P. Hespanha. Asymptotically stable adaptive-optimal control algorithm with saturating actuators and relaxed persistence of excitation. *IEEE Transactions on Neural Networks and Learning Systems*, 27(11):2386–2398, November 2016. ISSN 21622388. doi: 10.1109/TNNLS.2015.2487972.

[38] Stefan Kersting and Martin Buss. Recursive estimation in piecewise affine systems using parameter identifiers and concurrent learning Recursive estimation in piecewise affine systems using parameter identifiers and concurrent learning. *International Journal of Control*, 92(6):1264–1281, 2019. ISSN 1366-5820. doi: 10.1080/00207179.2017.1390256.

[39] Yongduan Song, Kai Zhao, and Miroslav Krstic. Adaptive Control with Exponential Regulation in the Absence of Persistent Excitation. *IEEE Transactions on Automatic Control*, 62(5):2589–2596, May 2017. ISSN 00189286. doi: 10.1109/TAC.2016.2599645.

[40] Jian Wang, Denis Efimov, and Alexey A. Bobtsov. On Robust Parameter Estimation in Finite-Time without Persistence of Excitation. *IEEE Transactions on Automatic Control*, 65(4):1731–1738, April 2020. ISSN 15582523. doi: 10.1109/TAC.2019.2932960.

[41] Andrew J. Kurdila, Jia Guo, Sai Tej Paruchuri, and Parag Bobade. Persistence of Excitation in Reproducing Kernel Hilbert Spaces, Positive Limit Sets, and Smooth Manifolds. September 2019. URL http://arxiv.org/abs/1909.12274.

[42] Jia Guo, Sai Tej Paruchuri, and Andrew J. Kurdila. Approximations of the Reproducing Kernel Hilbert Space (RKHS) Embedding Method over Manifolds. July 2020. URL http://arxiv.org/abs/2007.06163.

[43] R M Sanner and J E Slotine. Stable Recursive Identification Using Radial Basis Function Networks. In *1992 American Control Conference*, pages 1829–1833, 1992. ISBN VO -. doi: 10.23919/ACC.1992.4792428.

[44] Alain Berlinet and Christine Thomas-Agnan. *Reproducing kernel Hilbert spaces in probability and statistics*. Springer Science & Business Media, 2011. ISBN 1441990968.

[45] Saburou Saitoh and Yoshihiro Sawano. *Theory of reproducing kernels and applications*. Springer, 2016. ISBN 9811005303.

[46] N Aronszajn. Theory of Reproducing Kernels. *Transactions of the American Mathematical Society*, 68(3):337–404, 1950. ISSN 00029947. doi: 10.2307/1990404. URL http://www.jstor.org/stable/1990404.

[47] Sai Tej Paruchuri, Jia Guo, and Andrew Kurdila. Reproducing kernel Hilbert space embedding for adaptive estimation of nonlinearities in piezoelectric systems. *Nonlinear Dynamics*, 2020. ISSN 1573-269X. doi: 10.1007/s11071-020-05812-2. URL https://doi.org/10.1007/s11071-020-05812-2.

[48] Carl Edward Rasmussen. Gaussian processes in machine learning. In *Summer School on Machine Learning*, pages 63–71. Springer, 2003.

Chapter 6

Conclusion

The work in this dissertation makes a number of novel contributions to the extensive research on piezoelectric systems. The first part of this dissertation introduces and describes a systematic approach for designing piezoelectric oscillator arrays for wide-band attenuation. Such oscillator arrays are advantageous in that they have a low mass ratio when compared to alternative, contemporary vibration attenuation solutions like meta-structures. A central concern of the techniques introduced in the dissertation is how theory and design can be used to treat when there is uncertainty in the host structure. The performance of the newly introduced theory and design methods are demonstrated using simulations as well as experiments, as discussed in Chapter 2.

The second substantial topic addressed in the dissertation is an analysis of the RKHS embedding method for adaptive estimation as it is applied for modeling nonlinearities in piezoelectric systems. The work in Chapter 3 develops the theory of RKHS embedding for adaptive estimation, and constructs an algorithm for estimating nonlinear functions in piezoelectric models. Chapter 4 presents two algorithms for kernel center selection that is necessary while implementing RKHS adaptive estimators for identifying functions of the type $f : \mathbb{R}^d \to \mathbb{R}$. Chapter 5 derives sufficient conditions for the persistence of excitation of RKHS, which is needed to ensure convergence of function estimates.

6.1 Scope for Further Research

The work in this dissertation naturally suggests a number of important, open, and interesting research questions. Some of the potential directions for future research motivated by this work are listed below.

6.1.1 Piezoelectric Subordinate Oscillator Arrays

The following is the list of potential research projects that expand on piezoelectric subordinate oscillator arrays' work in this dissertation.

1. The study of the energy harvesting capabilities of the PSOAs attached to a host structure.

2. The investigation of active piezoelectric oscillator arrays that tune the shunt capacitance in real-time to overcome the uncertainties in the system.

3. The analysis of the effect of using effective negative capacitance in conjunction with conventional capacitive circuits on performance recovery capabilities.

6.1.2 RKHS Embedding Methods for Adaptive Estimation

The following research problems related to RKHS embedding methods for adaptive estimation remain to be explored.

1. The experimental validation of the RKHS embedding methods for modeling nonlinear piezoelectric oscillators.

2. The investigation of interpolation of nonlinear RKHS models to increase the model's effectiveness across multiple disjoint persistently exciting sets.

3. The study of parallels between the persistence of excitation of RKHS as well the concept of generalized frames.